Mussel-inspired Polyglycerol Coatings for the Prevention of Biomaterial-related Fouling

Dissertation for the acquisition of the academic degree of

Doctor of Natural Sciences (Dr. rer. nat.)

Submitted by

Michaël Willem Kulka

From Roermond (Netherlands)

Institute for Organic Chemistry

Department of Biology, Chemistry, Pharmacy

Freie Universität Berlin

2020

The following work has been performed under the supervision of Prof. Dr. Rainer Haag from April 2016 till June 2020, at the department of chemistry and biochemistry of the Freie Universität Berlin. Parts of this thesis have been financially supported by collaborative research center "Multivalence as chemical organizational and action principle" (SFB 765) which was funded by the "Deutsche Forschungsgemeinschaft" (DFG). Furthermore, the work was financially supported by the German Federal Ministry of Education and Research (BMBF) via the "KMU-innovativ" program "GlycoVAD".

Hereby I declare that the following thesis was prepared autonomously and that no illegal help was used. Contributions of others, e.g., content, quotes, or figures are indicated by referring to the original work.

Berlin, 25.06.2020, _____ (Michaël Willem Kulka)

Direct Supervisor: Prof. Dr. Rainer Haag

Second Supervisor: Dr. Jens Dernedde

Date of Disputation: 25.06.2020

ACKNOWLEDGEMENTS

First, I would like to thank Prof. Dr. Rainer Haag for giving me the opportunity to conduct my doctoral work in his research group at the department for chemistry and biochemistry of the Freie Universität Berlin (FUB) (Berlin, Germany). Additionally, I would like to thank Prof. Dr. Michael Schirner, Dr. Katharina Achazi, Chuanxiong Nie, Yannic Kerkhoff, and Elisa Quaas of the FUB, and Dr. Jens Dernedde and Dr. Kim Silberreis of the Charité Universitätsmedizin (Berlin, Germany), for their assistance in the biological experiments that were conducted in my work. Furthermore, I would like to thank PD Dr. Kai Licha of the company FEW Chemicals GmbH (Bitterfeld-Wolfen, Germany) for his support considering organic synthesis. Besides, I would like to thank Dr. Luis Cuellar Camacho (FUB) for teaching me how to execute atomic force microscopy, and Anke Schindler (FUB) for teaching me how to perform scanning electron microscopy. I would also like to express my gratitude to Prof. Dr.-Ing. Klaus Affeld († 2019), PD Dr.-Ing. Ulrich Kertzscher, Tim Bierewirtz, Felix Hehnen, and Sarah Smatty of the biofluid mechanics lab at the Charité medical university (Berlin, Germany), who heavily supported this work with their expertise in biofluid mechanics. I also wish to thank my cooperation partners Dr. Lars I. Dahms, Dr. Lena Kaufmann, Sebastian Friedrich, and Valentin Kunz at Berlin Heart GmbH (Berlin, Germany), for supporting this work with their expertise in ventricular assist devices. I would also like to convey my gratitude to Prof. Dr. Ingo Grunwald of the City University of Applied Sciences Bremen (Bremen, Germany) and Dr. Dirk Salz of the Fraunhofer Institute for Manufacturing Technology and Advanced Materials (Bremen, Germany) for their technical support in the physical vapor deposition of titanium dioxide. Furthermore, I would like to thank Dr. Özlem Özcan, Dr. Wolgang Unger, Dr. Jörg Radnik, Nina Wurzler, and Jörg M. Stockmann of the Federal Institute for Materials Research and Testing (BAM) (Berlin, Germany) for their support in the streaming potential and X-ray photoelectron spectroscopy measurements. Additionally, I would like to thank Dr. Ievgen S. Donskyi and Philip Nickl of the FUB for their help in the fitting of all X-ray photo electron spectroscopy spectra. I would also like to acknowledge the technical assistance of the core facility BioSupraMol (FUB), which is financially supported by the Deutsche Forschungsgemeinschaft (DFG). Furthermore, I would like to thank the collaborative research center 765 (SFB 765) and the German Federal Ministry for Education and Research (BMBF) for their financial contributions to this doctoral work. I also wish to thank

Dr. Wiebke Fischer, Eike Ziegler, Lydia Alnajjar, and Katharina Tebel, for dealing with the bureaucratic and financial matters at the FUB. Additionally, I would like to thank Dr. Pam Winchester for proofreading the thesis and all the manuscripts.

I also thank my colleagues from the Haag group, with whom I had great discussions about work, as well as about private interests. Besides, I would like to thank all my non-work-related friends in both Berlin and the Netherlands, who always supported me throughout my doctoral work. Finally, my thanks go out to my family, especially my parents, sister, and grandmother who are always there for me whenever I need them.

CONTENT

1. INTRODUCTION

Cardiovascular diseases (CVDs) are the leading cause of mortality and are responsible for 3.9 million death per year in Europe as a whole (i.e., 45% of all deaths).[1] The application of ventricular assist devices (VADs) is often considered a last resort treatment and is commonly used as bridging therapy for severe CVD patients awaiting heart transplantations. VADs are electromechanical devices which support cardiac circulation or fully replace the function of a failing heart (**Figure 1**). However, users of VADs suffer from complications resulting from hemolysis and shear-induced thrombosis.[2] To overcome the issues considering VAD-associated thrombosis, there is a need for new durable surface coatings, which prevent the formation of shear-induced thrombi on the blood-contacting surfaces in VADs. However, this is challenging because of the wide variety of wall shear rates commonly encountered in VADs, which lead to biomaterial-induced thrombosis through various mechanisms.[3] Additionally, the potential wear effect of high wall shears can significantly compromise the stability of the coatings.

State-of-the-art techniques for preventing biomaterial-associated thrombosis either rely on bioactive coatings that interact with specific blood-components,[4] or on coatings that prevent the adhesion of protein and cells (i.e., organic or inorganic bioinert coatings).[5-8] Over the last decades, surface functionalization with polymeric coatings has become an interesting approach to introduce tailor-made properties (e.g., antithrombogenic bioactive or bioinert properties) to a material surface. Traditionally, thiol and siloxane chemistries are applied to modify noble metals and hydroxylated surfaces, respectively.[9-10] Alternatively, methods such as Langmuir-Blodgett deposition,[11] layer-by-layer (LbL) assembly,[12] irradiation-mediated grafting,[13-14] and electrostatic or hydrophobic adsorption are used for the effective immobilization of functional polymers on a surface.[15-16] However, most of these methods require specific chemical and/or physical properties of the substrate or the use of complex machinery, thus limiting their application. Therefore, there is a need for novel substrate-independent coating methods, which can extend the application of polymeric coatings to a broad range of substrate materials.

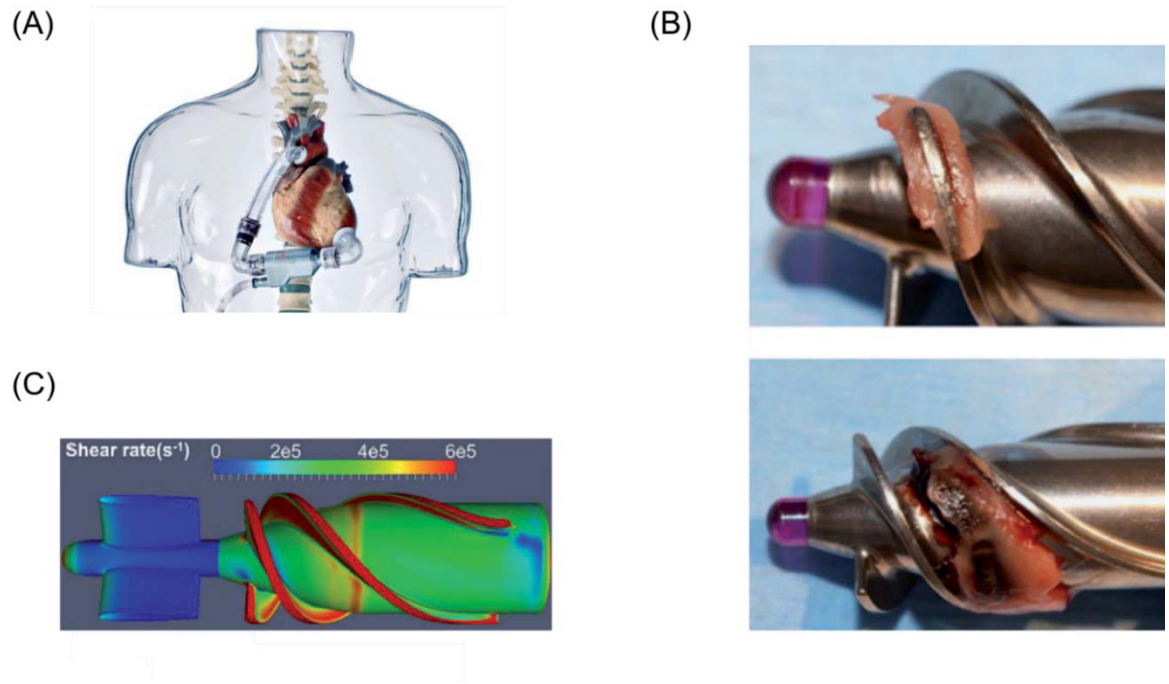

Figure 1. (A) The picture shows an INCOR® VAD by Berlin Heart GmbH (Berlin, Germany), which reaches rotation numbers between 5,000-10,000 rotations per minute (2-9 $lmin^{-1}$), leading to shear strain rates up to maximum 200,000 s^{-1}. The production of this specific model of VAD was terminated at the end of 2018. (B) Examples of thrombosis in the HeartMate II VAD system by Abbott laboratories (Abbott Park, Illinois, USA). The top image shows a pure fibrin clot resulting from high shear. The bottom images show a fibrin and blood clot. This figure was reproduced with permission from ref. 17 Copyright © 2014, Elsevier. (C) An in silico modulation of the shear rates within the model VAD. The red areas represent the areas with high shear, whereas the yellow, green, and blue areas represent the areas with lower wall shear stress. The blue top part represents the flow straightener that is used for fixation of the rotor. This figure was reproduced with permission from ref. 18 Copyright © 2016, Nature.

To achieve universal, stable, and substrate-independent coating behavior, the anchoring interactions between a polymeric coating material and a surface must be well designed. For instance, as no anchor group will be reactive to all types of substrates, the formation of chemical bonds between anchor groups of the polymer and functional groups of the substrate is not always preferred. The use of unspecific non-covalent interactions, such as electrostatic interactions, hydrogen bonds, hydrophobic interactions, and van der Waals interactions, is a promising alternative for the creation of substrate-independent coating behavior, because these interactions have proven to be strong enough to effectively tether polymer coatings to the

surface. Examples of non-covalently attached functional polymer films include the creation of electrodes coated with hemoglobin-octadecylamine films via Langmuir-Blodgett deposition,[19] the creation of cell adhesive substrates via the formation of polyelectrolyte films,[12] and the creation of protein repelling surfaces via the non-covalent adsorption of amphiphilic polymers to hydrophobic surfaces.[16] The coating stability can be enhanced by chemical crosslinking, amplifying the stabilizing intra-layer interactions.[20] Recently, mussel-inspired surface chemistry has been increasingly applied to the substrate-independent modification of biomaterials, as will be discussed in more detail later in this thesis.[21-22] Consequently, a multitude of antifouling and bioactive surfaces for the prevention of biomaterial-associated fouling and thrombosis have been developed.[6, 23-27] Most of these studies have ignored the critical role of shear forces in the substrate-induced formation of surface blood clots.

The aim of this doctoral thesis was to use mussel-inspired polymeric surface coatings to introduce antifouling and antithrombogenic surface properties to medically relevant titanium dioxide (TiO_2) surfaces and other blood contact materials. Furthermore, the focus of this thesis was on investigating the relation between wall shear stress and biomaterial-associated thrombosis (i.e., the antithrombotic effectiveness of the developed materials under low and high shear conditions).

2. THEORETICAL BACKGROUND

2.1. Biomaterial-induced Thrombosis

The use of biomaterials is essential in many medical treatments, such as hemodialysis,[28] bone and joint substitution,[29] and in vascular grafts.[30] When a biomaterial is exposed to a biological liquid (e.g., whole blood or lymph), proteins rapidly adhere to the surface in a dynamic process. The composition and development of this protein layer depend on the physical and chemical characteristics of the biomaterial, and determine the fate of the biomaterial in a biological environment. In blood-contacting biomaterials, the protein layer mediates the adhesion and activation of platelets and leukocytes, that adhere to the protein-coated surface via specific receptors. The protein layer can also develop over time into surface-bound protein complexes that trigger coagulation- or complement-activating reactions.[31]

2.1.1. Platelet Activation and Fibrinogen

Blood platelets are abundantly present in the blood and can circulate for 1-7 days in a quiescent state under physiological conditions.[32] Platelets are 1-3 μm sized lens-shaped fragments of cytoplasm that stop the bleeding of damaged blood vessels during hemostasis by clumping and clotting.[32-33] When a blood vessel is damaged, the endothelium of the vessel is interrupted and the underlaying collagen is exposed to the circulating platelets. The platelets then rapidly bind to the exposed collagen matrix, initiating the primary hemostasis.[34] The exposure of a biomaterial to whole blood can also result in the adhesion and activation of blood platelets (**Figure 2**), potentially leading to adverse biomaterial-induced thrombosis. Therefore, testing the platelet adhesive and activating properties of a blood-contacting biomaterial is important. Upon blood exposure, plasma proteins, including albumin, fibrinogen, fibronectin, vitronectin, and the von Willebrand factor (vWF) adhere to the biomaterial surface within seconds to minutes.[35] Fibrinogen has been identified as the most important protein in biomaterial-induced platelet adhesion,[36] and as little as 7 ng/cm^2 of immobilized fibrinogen has been reported to effectively induce platelet adhesion.[37] However, native fibrinogen does not mediate platelet activation in fluid blood, which indicates that platelet adhesion to fibrinogen requires biomaterial-induced configurational changes of fibrinogen. Besides fibrinogen, also fibronectin, vWF, and vitronectin can mediate the adhesion and activation of blood platelets. The adhesion of platelets to the surface-bound protein is mediated via specific cell membrane receptors, such as glycoprotein IIb and IIIa (GPIIb and GPIIIa, respectively).[38]

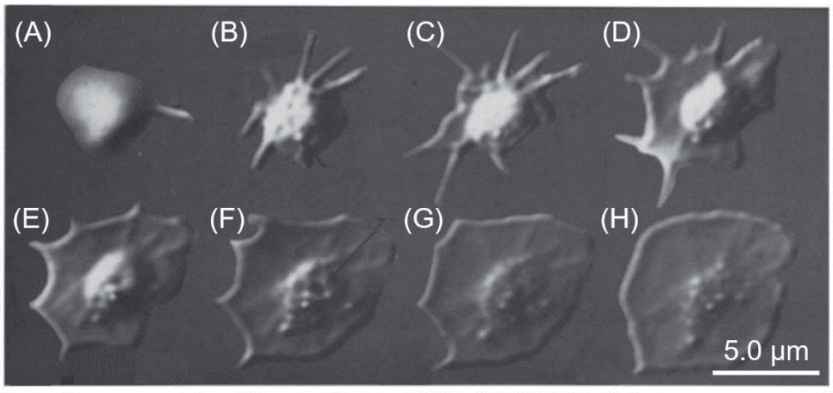

Figure 2. Various stages in the transformation of a human blood platelet, going from its inactive spheroidal form (A) to its activated fully spread form (H). In mammals, thrombocytes do not have a cell nucleus, but in other animal classes (such as birds and amphibians) thrombocytes can be found as intact mononuclear cells.[39] On a healthy endothelial cell

monolayer, platelet adhesion and activation is prevented by antithrombogenic properties of nitric oxide (NO) and prostaglandin I_2, which are both released from the endothelial surface.[32] This figure was reproduced with permission from ref. 40 Copyright © 1979, Rockefeller University Press.

Even though the specific mechanisms of the binding of platelets to fibrinogen remain to be elucidated, the influence of the amount of adherent fibrinogen and albumin on the blood-compatibility of biomaterials has been previously well investigated.[41-42] In contrast to fibrinogen, albumin is generally considered inert toward platelet adhesion and activation.[36] Therefore, the development of surfaces, which selectively adsorb albumin while rejecting fibrinogen has been proposed as an effective way to prevent biomaterial-induced platelet adhesion.[43-44] Besides the amount of protein, there is growing evidence that the conformation of the adherent fibrinogen influences biomaterial-induced platelet adhesion.[35, 45] For instance, Sivaraman et al. have observed that platelet adhesion is strongly correlated with the degree of adsorption-induced unfolding of fibrinogen, whereas no correlation to the amount of adsorbed fibrinogen was found.[45] Their study also indicated that –OH terminated self-assembled monolayers (SAMs) induce only little degradation of the secondary structure of native fibrinogen, whereas $–CH_3$ terminated SAMs clearly lead to concentration-dependent, substrate-induced changes. Interestingly, the changes in the secondary structure were pronounced more strongly at lower fibrinogen concentrations, explained by the higher surface area available per fibrinogen strand. At the low concentrations, the fibrinogen strand degraded as a result of the hydrophobic effect, after adhering to the surface in its native form. In contrast, at high concentrations the fibrinogen strands quickly saturated the surface, and the proteins were not able to unfold resulting from the lack of free space on the surface.[45] Several other studies have also focused on the relation between the conformation of fibrinogen and platelet adhesion/activation.[35, 46] Although this relation is not yet fully understood, the conformation of fibrinogen is now generally accepted as an important parameter in biomaterial-induced platelet adhesion.

The adhesion and activation of platelets are important in natural coagulation, which is the process in which liquid blood turns into a gel (i.e., forms a blood clot), leading to the cessation of blood loss from a damaged blood vessel. Coagulation includes the adhesion, activation, and aggregation of platelets (i.e., primary hemostasis), as well as the formation and

maturation of a fibrin film (i.e., secondary hemostasis).[39] The coagulation cascade can be divided in two pathways, an intrinsic pathway (or contact activated pathway) and an extrinsic pathway (or tissue-factor pathway) (**Figure 3**)[39, 47] that both finally result in the activation of thrombin, transforming soluble fibrinogen into the insoluble fibrin strands.[39] Both pathways consist of series of soluble zymogens (i.e., inactive precursors of enzymes), which activate each other in a cascade-like manner. The extrinsic pathway is activated when coagulation factor VII (FVII) is exposed to tissue factor (TF), which is found in the tissues of the subendothelium (in natural coagulation TF is released from the subendothelium upon vessel damage).[39] The resulting fibrin formation strengthens the platelet plug, that simultaneously forms at the site of endothelial damage.[39] The intrinsic pathway involves a series of protein cofactors and enzymes, which interact in reactions that take place on membrane surfaces. The intrinsic pathway will be discussed in more detail in the next chapter of this thesis.

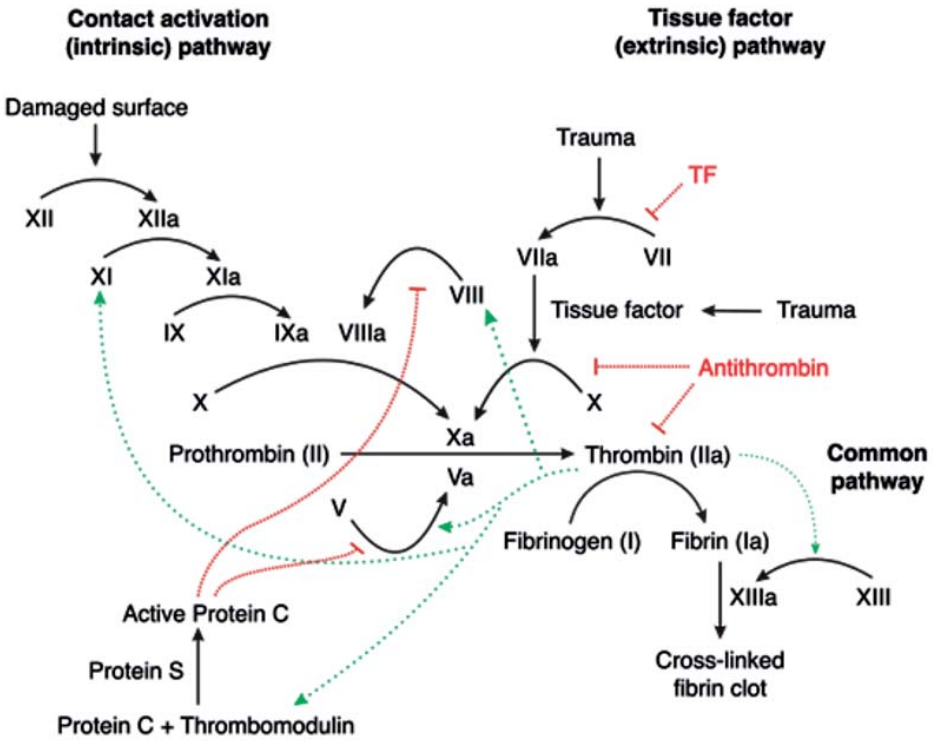

Figure 3. A schematic representation of the intrinsic and extrinsic pathways of the coagulation cascade. This figure was reproduced with permission from ref. 48 Copyright © 2019, Royal Society of Chemistry.

Multiple scientific studies have shown that platelet adhesion, activation, and aggregation are intertwined with the two pathways of the coagulation cascade. For instance, platelets can induce the activation of coagulation factor XII (FXII), hereby triggering the intrinsic pathway of the coagulation cascade,[49] and vice versa, thrombin can also activate the platelets.[50]

2.1.2. The Intrinsic Pathway of Blood Coagulation

Blood coagulation via the intrinsic pathway is especially relevant in biomaterial-associated coagulation.[31-32] FXII can bind to the surface, resulting in an auto-activating conformational change to FXIIa ("a" for activated). Subsequently, FXIIa further activates FXII (i.e., an autocatalytic feed-back loop is created). Besides, FXIIa transforms the protein prekallikrein (PK) to active kallikrein (KK), which activates further FXII (i.e., enhancing the positive feed-back loop). Once KK and FXIIa are formed, high molecular weight kininogen (HMWK) is cleaved, which results in the release of pro-inflammatory bradykinin (**Figure 4**).[51] FXIIa also activates coagulation factor XI (FXI), triggering the intrinsic coagulation pathway. The HMWK mediates the surface immobilization of PK and FXI via the formation of a non-covalently linked complexes in the blood plasma.[52]

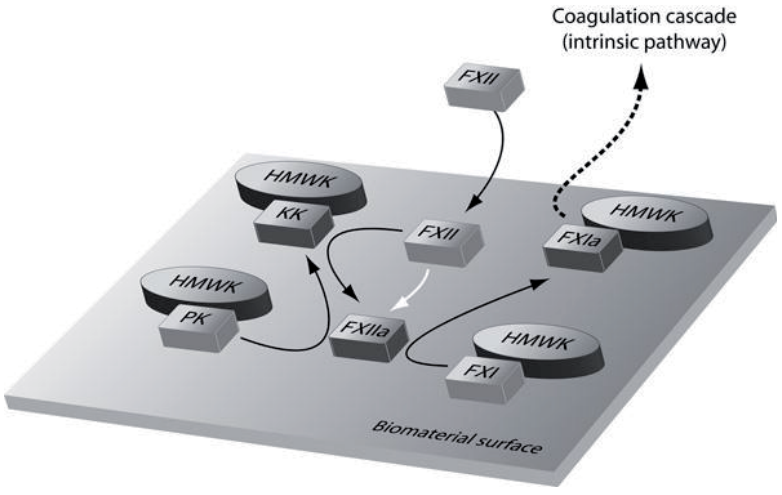

Figure 4. A schematic representation of the contact activation system on a biomaterial surface. Initially, FXII (also known as the Hageman factor) binds to the surface, where it undergoes a spontaneous transformation resulting in active FXIIa. Subsequently, FXIIa activates PK and FXI, finally resulting in activation of the coagulation cascade and the release of pro-inflammatory bradykinin.[53]

The intrinsic coagulation pathway is activated by exogenous negatively charged surfaces, such as glass,[54] silica,[55] dextran sulfate,[56-57] kaolin,[58] and nanoparticles.[59] More recent studies have also identified endogenous activators, such as polyphosphates,[60] collagen,[61] and misfolded protein aggregates.[62] Besides, physiologically negatively charged surfaces, such as cell membranes (i.e., both eukaryotic and prokaryotic) and virus particles, might also provide a sufficient negative charge for the activation of the contact-activated system.[63]

2.1.3. Activation of Leukocytes

Neutrophils (i.e., the most prominent class of leukocytes) can adhere to fibrinogen via transmembrane receptors.[64-65] Additionally, adherent platelets can promote the adhesion of neutrophils via receptor-mediated binding.[66] Upon surface immobilization, neutrophils promote the production of TF,[67-68] that activates the intrinsic pathways of the coagulation cascade. Furthermore, neutrophils promote platelet activation by the release of platelet activating substances, such as platelet-activating factor, interleukins, and tumor necrosis factor from their stored granules.[31] Vice versa, it has long been recognized that platelets can mediate the release of TF from neutrophils, thus indirectly coupling platelet adhesion/activation to the extrinsic coagulation pathway.[69]

2.1.4. Complement System Activation

The contact of artificial surfaces with blood leads to the immediate adsorption of serum protein onto the surface. Initially, more abundant and mobile protein (i.e., albumin, globulin, fibrinogen, and fibronectin) will adsorb to the surface.[31] Subsequently, these protein are replaced by less mobile proteins with higher affinity to the surface (such as FXII and HMWK) in a kinetic process called the Vroman effect.[70] Especially the complement protein C3 (and its spontaneously formed hydrolysis products) binds well to foreign surfaces, leading to activation of the complement system.[71] The complement system is a part of the innate immune system, which enhances the ability of antibodies and phagocytic cells to clear microbes and damaged cells from the host. The complement system consists of more than 30 serum proteins.[72] Some of them can be serially activated and participate in cascade reactions that finally lead to chemotaxis (i.e., inducing the movement of organisms/cells via chemical stimuli) and opsonizing reactions (i.e., reactions that enhance phagocytosis).[73] Furthermore, the complement system promotes inflammation and attacks the cell membranes of pathogen cells

via the formation of the so-called membrane attack complex (MAC).[74] The degree in which a biomaterial triggers the complement system is dependent on the chemical and physical properties of the biomaterial's surface. However, an earlier study has shown that hydrophobic surfaces are more likely to promote complement system activation than hydrophilic surfaces.[75]

Especially the complement factors C5a and C3a function as potent leukocyte chemo-attractants, which enhance leukocyte adhesion and activation, resulting in the release of coagulation-activating TF. This indirectly links the complement system to the extrinsic coagulation pathway (**Figure 5**).[31]

2.1.5. Other Thrombosis-inducing Factors

The implantation of a biomaterial can also lead to thrombosis unrelated to the properties of the biomaterial, i.e., through altered blood-flow parameters and turbulent flow.[76-77] Additionally, red blood cells can adhere to biomaterial surfaces in a passive process, where they can promote platelet activation by the release of adenosine diphosphate (ADP).[31] Besides, ADP and hemoglobin can be released upon rupture of the red blood cells in a process called hemolysis. The released hemoglobin acts as a scavenger molecule for NO, which effectively enhances platelet activation by overturning the inhibitory effect of NO on platelet activation.[78-79]

2.1.6. ISO Norms for Blood-contacting Materials

New commercial blood-contacting biomaterials are only allowed to the market when they have been tested for their interaction with the blood components according to a given set of tests. The International Organization for Standardization (ISO) (i.e., the international organization responsible for the creation of production norms) has summarized a selection of required testing methods (including their required design) for blood-contacting biomaterials in their norm ISO 10993. Although some scientific works have been conducted according to this ISO-norm,[80-84] the use of ISO 10993 is fairly uncommon in the development of novel biomaterials.

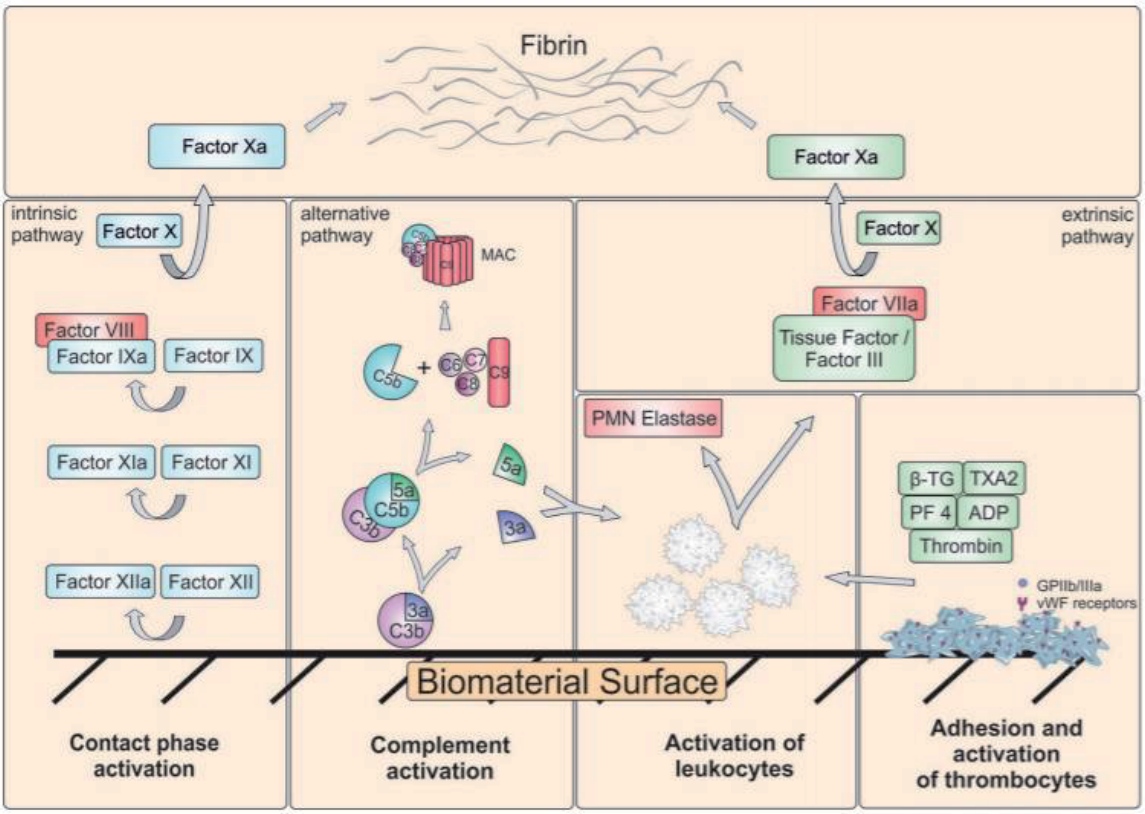

Figure 5. A schematic summary of all factors that trigger biomaterials-induced coagulation. Direct activation of the intrinsic coagulation cascade occurs via the biomaterial-induced transformation of FXII to FXIIa. Biomaterial-induced activation of the complement system via the alternative and classical pathways finally attracts leukocytes. Additionally, leukocytes are attracted by adherent platelets, via the release of β-thromboglobulin (β-TG) from the platelets' alpha granules. Subsequently, the leukocytes release TF, which activates the extrinsic pathway of the coagulation cascade. Besides β-TG, platelets release a variety of substances including ADP, GPIIb/IIIa, thromboxane A2 (TXA2), and platelet factor 4 (PF4). PMN = polymorphonuclear. This figure was reproduced with permission from ref. 32 Copyright © 2018, Weber, Steinle, Golombek, Hann, Schlensak, Wendel, and Avci-Adali.

2.2. Thrombus Formation Under High Shear Conditions

So far, several factors considering biomaterial-induced thrombosis were discussed under static or near static flow conditions. However, protein transport and wall shear stress are directly related to the blood's flowrate and must therefore be considered in the rational design of the blood-contacting materials, which are exposed to high wall shears. Furthermore, high-shear thrombus formation is mainly mediated by platelet aggregation, rather than by the coagulation

cascade.[85] The following sections will highlight the role of shear in biomaterial-induced thrombosis.

2.2.1. Shear Factors

Until now, the role of platelets, the complement system, leukocytes, and the coagulation cascade in biomaterial-induced thrombosis has been discussed. However, the coagulation cascade mainly dominates thrombus formation only at low shear rates (i.e., at shear rates < 50 s^{-1}), where it causes the formation of erythrocyte-rich thrombi, appearing as red blood clots. In contrast, at high shear rates (i.e., at shear rates > 5,000 s^{-1}) thrombus formation is mainly mediated via platelet aggregation, leading to the formation of white blood clots (**Figure 1**).[86]

Ex vivo and *in vitro* experiments have shown that high-shear thrombotic occlusion on biomaterials is a three-phase process (**Figure 6**).[87-88] In the first phase, platelets adhere to a non-endothelial surface. The first phase shows only limited thrombus growth and is therefore called the lag phase. Lag times can vary from 175 till 300 seconds for the initial shear rates of 500-5,000 s^{-1}.[89] The lag time is thought to represent the time needed for the deposition of plasma protein on the surface, which is required for subsequent platelet adhesion.[90] Additionally, the lag time includes the time needed for the gathering of a sufficient amount of non-activated platelets (i.e., the time prior to the shear activation of the platelets). In the second phase, the thrombus grows rapidly, which leads to the formation of the bulk of the occlusive thrombus. In this phase, the thrombus can grow up to 60 times faster than in the initial phase, depending on the magnitude of the applied shear rate.[91] The final third phase involves asymptotic coagulation thrombus growth, potentially leading to full occlusion of a blood vessel.

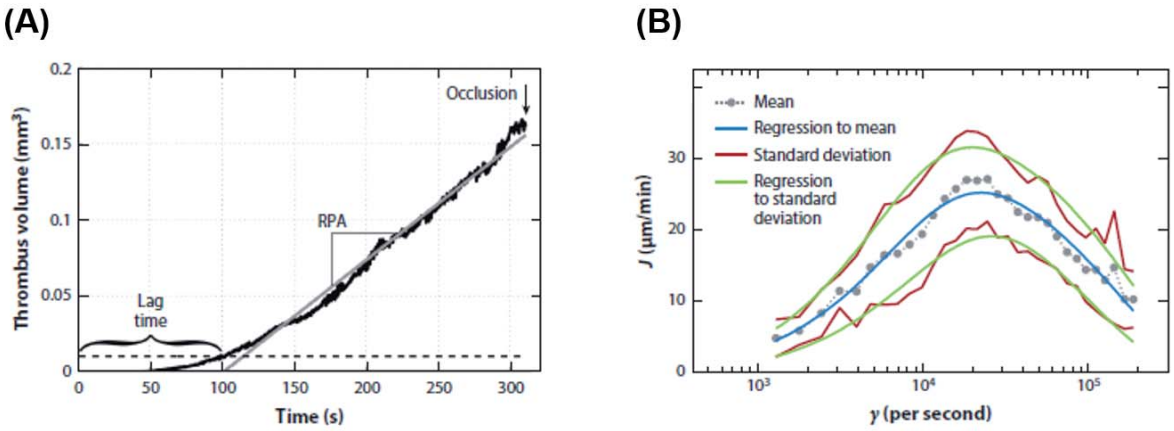

Figure 6. (A) A graphical representation of the thrombus volume in all three phases This figure was reproduced with permission from ref. 83 Copyright © 2015, Elsevier. (B) A graphical representation of the thrombus growth rate in the second phase. This figure was reproduced with permission from ref. 92 Copyright © 2016, Springer.

The first two phases depend on the shear rate in different manners. The duration of the first phase decreases with increasing shear, resulting from the increased transportation of protein to the surface.[93] Furthermore, increased shear leads to enhanced vWF activation and the increased mural activation of platelets.[94-95] The second phase shows a shear-dependent maximum around 25,000 s^{-1}. Nevertheless, thrombus formation can still occur at shear rates > 100,000 s^{-1}.[85] For rapid thrombus growth to occur, the blood constituents first need to reach the vessel wall or growing thrombus. Under flow, the presence of red blood cells and increased shear rates enhance the mass transport of whole blood in a phenomenon called enhanced diffusivity.[93, 96] This leads to an enhanced diffusivity of large proteins and furthermore enhances the platelet deposition rate, potentially contributing to rapid thrombus growth. Additionally, platelets migrate to the vessel wall in flowing blood, which can significantly enhance the concentration of near-wall platelets and thereby increase the risk of thrombus.[97]

2.2.2. The vWF and Shear

The vWF is a large multimeric glycoprotein that is found in platelet α-granules, the blood plasma, and in the subendothelial connective tissue.[98] Under high shear conditions, platelet adhesion is mediated by vWF rather than by fibrinogen (**Figure 7**).[99] At shear rates > 5,000 s^{-1}, the vWF undergoes a conformational change, leading to the exposure of additional

collagen- and platelet-binding sites (**Figure 8**).[94] When vWF is bound to the surface, it can bind inactivated platelets at shear rates > 10,000 s^{-1} in the presence of soluble vWF.[100] Additionally, the vWF forms long net-like structures under shear rates > 25,000 s^{-1}.[101] Furthermore, a previous study showed that thrombus formation was inhibited under high shear, when the vWF was diluted by 90%.[85] In contrast, thrombus formation continued in a blood analogous solution containing only 10% of the physiological platelet count, when having normal concentrations of vWF.[85] The combined results clearly illustrated the critical role of the vWF in coagulation. Therefore, it is important to prevent unspecific adhesion of the vWF to blood-contacting biomaterials, especially when these materials are experiencing high shear conditions (e.g., as in case of VADs).

3.3.3. Assessing Shear-Thrombosis Relations

As earlier discussed, shear plays an important role in (biomaterial-induced) thrombosis. Under both healthy and pathological conditions, a wide variety of shear rates is observed in the circulatory system.[3] Therefore, understanding the influence of shear on biomaterial-induced thrombosis is essential when developing blood-contacting biomaterials. *In vitro* methods for studying the relation between shear and biomaterial-induced thrombosis can be divided in static blood incubation models, agitated blood incubation models, and shear flow models.[32] In the static blood incubation models, the biomaterial is incubated with whole blood or platelet-rich plasma (PRP) without flow conditions,[102] which can quickly deliver information about the intrinsic thrombogenicity of the surface in the absence of shear. However, the static models provide little information about the general hemocompatibility of a biomaterial and suffer from cell sedimentation and platelet activation, resulting from protein aggregate formation at the air-blood interface.[103] Agitated blood incubation models commonly utilize a flat incubation chamber with the top and bottom faces made of the biomaterial of interest. The incubation chamber is subsequently filled with blood and incubated on a shaker or overhead rotator without directed flow.[104] The incubation chamber can also be rotated, preventing blood component or testing material sedimentation.[105] A wide variety of shear models have been developed, including tubular systems, such as the chandler loop and the roller pomp closed loop,[106-107] flat-plate flow chambers,[108] and parallel plate-and-cone platelet viscometers.[109] Furthermore, methods which utilize directed (microfluidic) flow channels for the characterization of platelet adhesion to biomaterial surfaces have been described in

literature.[110] However, these have limited diagnostic value, because of the constant shear conditions.

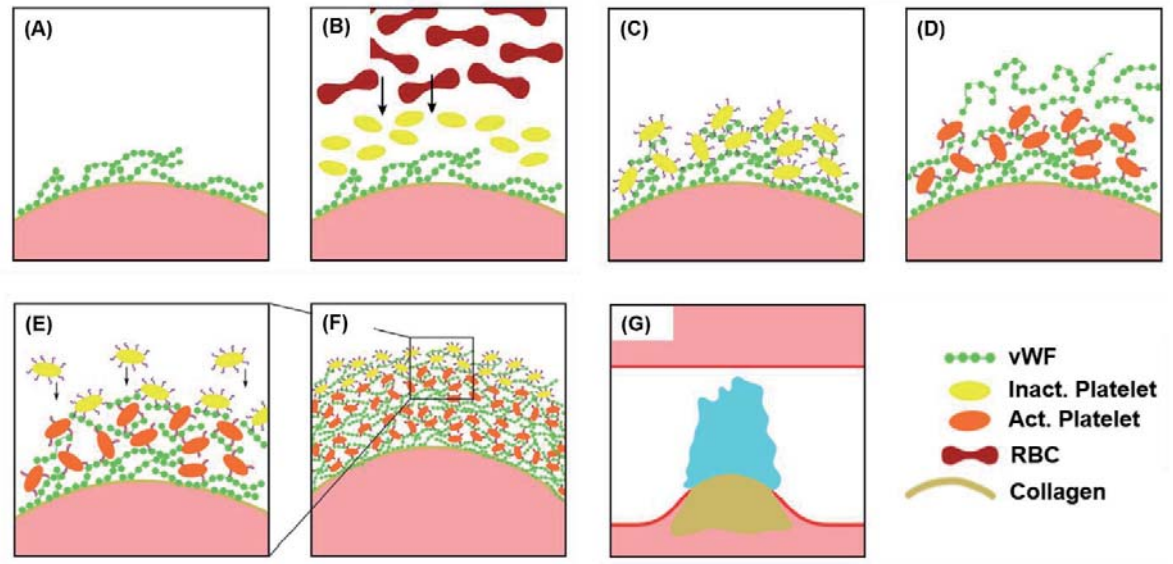

Figure 7. A schematic representation of thrombus formation under high shear conditions. (A) At high shear, the vWF unfolds and adheres to collagen of the damaged endothelium (e.g., as a result of a ruptured atherosclerotic plaque) or to the biomaterial's surface. (B) Platelets migrate to the surface and (C) the inactivated platelets subsequently adhere to the surface-bound vWF. (D) The platelet activation leads to the release of further vWF from the platelets α granules, promoting further adhesion. (E, F) Additional vWF bind to mural platelets and lead to further platelet aggregation. (G) Finally, a large-scale thrombus (light blue) forms on the exposed collagen or biomaterial's surface. RBC = red blood cells. This figure was reproduced with permission from ref. 85 Copyright © 2015, Elsevier.

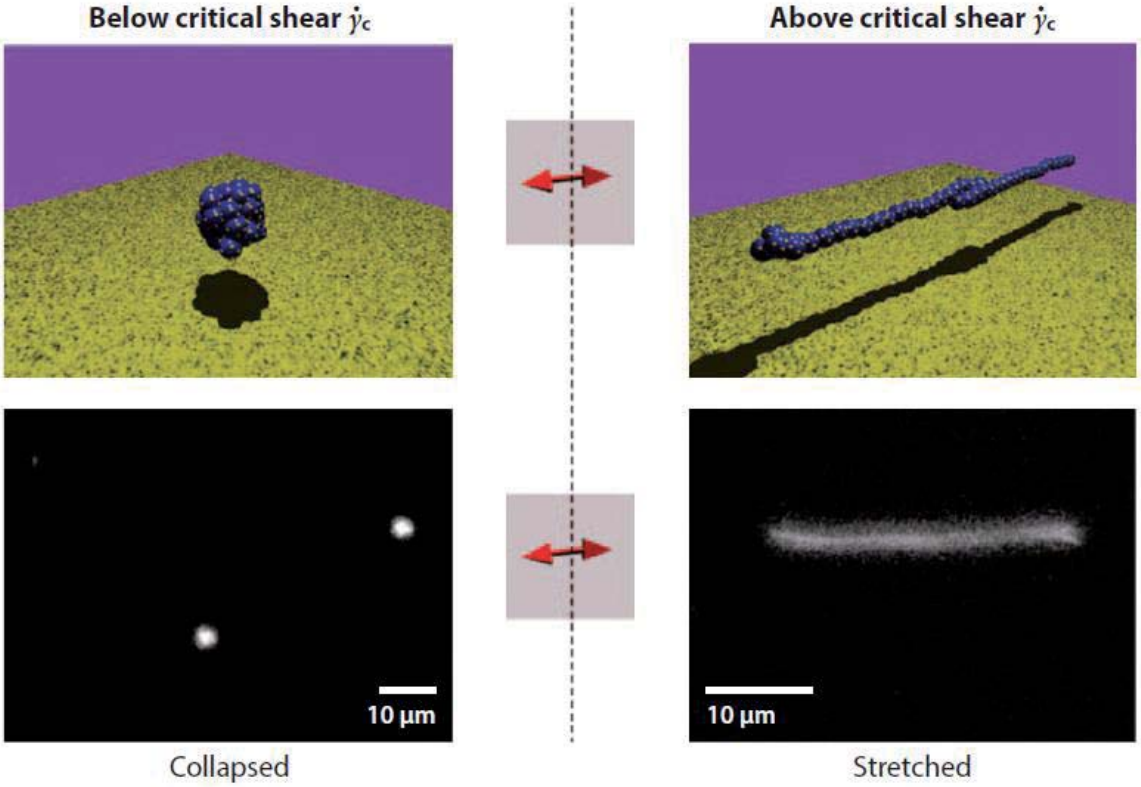

Figure 8. Unfolding of the vWF under varying shear rates, monitored by fluorescence microscopy. This figure was reproduced with permission from ref. 94 Copyright © 2007, National Academy of Sciences, U.S.A.

The use of stagnation point flow chambers has become prominent in the field of bio-fluid mechanics, in order to overcome the problems associated with the other model types.[111-114] Stagnation point flow models utilize a laminar flow in combination with radial spreading of the blood in customized flow chambers, resulting in radius-dependent wall shear rates. As a result, platelet adhesion can be investigated under a wide variety of wall shear rates in a single measurement. Affeld et al. developed a stagnation point flow model that was capable of visualizing and quantifying platelet adhesion at shear rates 0-180 s^{-1} in a single measurement (**Figure 9**).[111-114] The model utilized a laminar flow module and a custom-made flow chamber combined with an inverted fluorescence microscope and whole blood containing fluorescently labeled platelets.[112] The advantage of this model was the modular buildup of the custom flow-chamber, allowing for the placement of polymer-coated substrates (**Figure 10**). Furthermore, physical vapor deposition techniques could be applied to functionalize the glass substrates with metallic coatings of choice, given that the coated metal layer remained transparent. As a result,

the adhesion of platelets to a broad range of materials and polymeric coatings could easily be studied, utilizing the stagnation point flow model.

Surprisingly, the application of flow models with a broad spectrum of shear rates remains fairly uncommon in the field of blood-contacting biomaterials, where hemocompatibility and biocompatibility are still often considered under static conditions.[6, 115-119] However, as biomaterial-induced thrombosis is strongly linked to shear stress, there is a need for the use of more advanced shear models that further help to improve blood-contacting biomaterials.

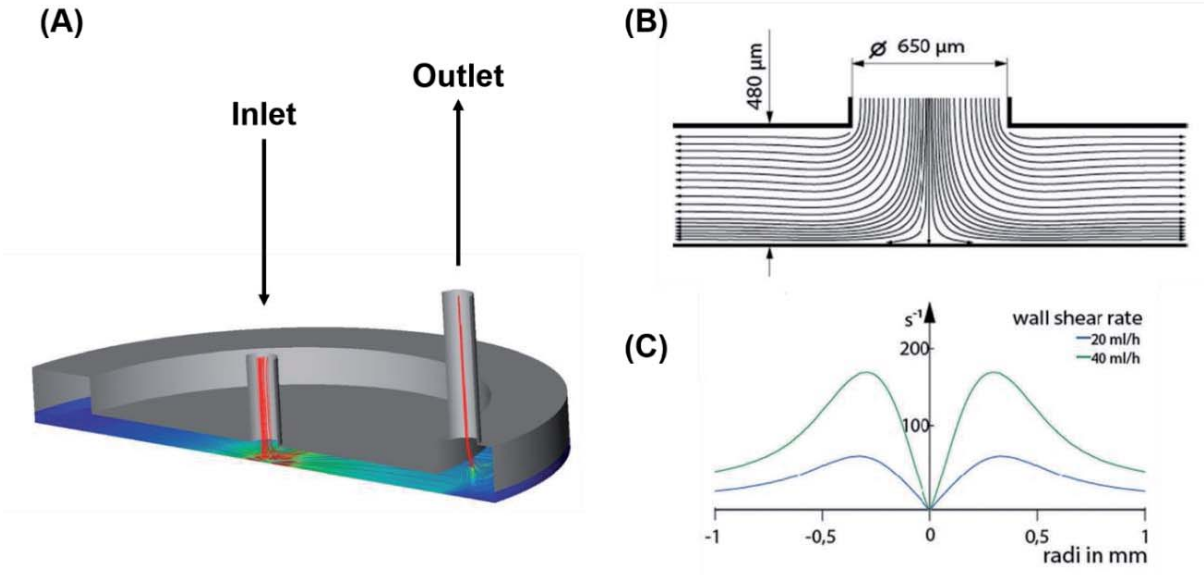

Figure 9. (A) A schematic representation of the wall shear in the stagnation point flow model developed by Affeld et al. The red color represents the areas with high shear, whereas blue represents the areas with low shear. (B) A schematic representation of the laminar flow within the flow chamber. (C) A graphical representation of the wall shear rate within the flow chamber at 20 mlh^{-1} (blue) and at 40 mlh^{-1} (green). This figure was reproduced with permission from ref. 120 Copyright © 2016, American Vacuum Society.

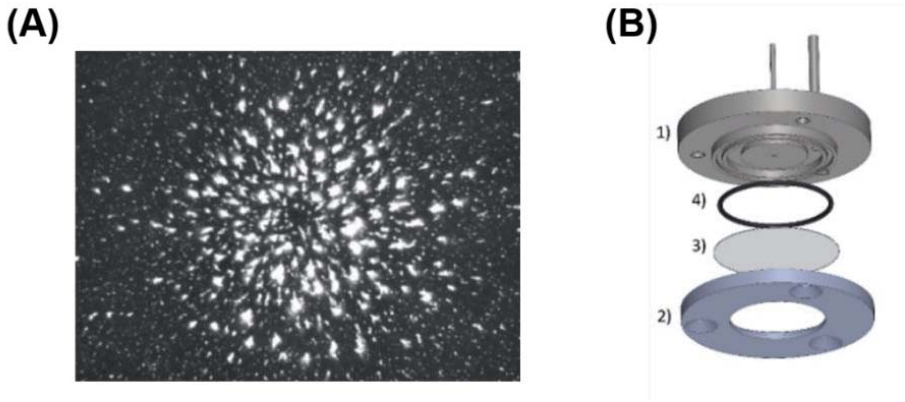

Figure 10. (A) A typical fluorescent microscopy image of platelet adhesion obtained from the stagnation point flow model. This figure was reproduced with permission from ref. 120 Copyright © 2016, American Vacuum Society. (B) A schematic representation of the stagnation point flow model: (1) The top plate with inlet and outlet, (2) the stainless steel bottom plate, (3) the (polymer or metal-coated) cover slip on which the platelet adhesion is visualized, and (4) a silicon ring to seal the system.

2.3. Bioactive Antithrombogenic Surfaces

Many publications have focused on the creation of bioactive biomaterials and coatings for the prevention of biomaterial-induced thrombosis, many of which were based on the immobilization of natural anticoagulant agents including heparin,[121-131] thrombomodulin,[132] corn trypsin inhibitor,[133] heparan sulfate,[134-135] hirudin,[136] bivalirudin,[137] boophilin,[136, 138] and argatroban.[139] Furthermore, major efforts have been invested in the direct grafting of biologically active moieties to the biomaterial to mimic the biological function of the natural anticoagulants.[140-141] Also polymeric mimics of natural anticoagulants have been introduced to the biomaterial surfaces via grafting-from and grafting-to approaches.[115, 142-144] Besides grafting, these bioactive polymers have been directly blended into the polymeric matrix of biomaterials, hereby enhancing their blood compatibility.[145] In addition, materials that have been inspired by the platelet-resistant endothelium, such as NO-releasing antithrombogenic polymeric coatings and elastin-based materials, have also been developed.[31, 146-149]

2.4. Bioinert Polymer Coatings

So far, all coatings discussed in this thesis have relied on biological interactions between specific blood components and bioactive components present in (or released by) the coating. An interesting alternative to bioactive coatings is the use of bioinert antifouling polymeric coatings that prevent the initial adhesion of protein to the surface. Biofouling (i.e., accumulation of protein, microorganisms, plants, algae, or small animals on wetted surfaces) has been detected in medical implants,[150] food packaging materials,[151] marine and industrial equipment,[152] and in materials for water purification systems.[153] In diagnostics, unspecific protein adsorption can reduce the sensitivity of immunological assays,[154] whereas, in case of *in vivo* implants, protein fouling might hamper the device's efficacy and induce thrombosis and/or implant-associated infections.[31, 155-156] Coatings that prevent the *in vivo* adhesion of proteins and cells could potentially lead to prolonged, more efficient, and safer use of blood-contacting biomaterials, and are therefore beneficial for patients' well-being. Furthermore, such coatings are also economically interesting because they might reduce the costs associated with repeated surgical interventions and prolonged hospitalization.

2.4.1. Hydrophilic Antifouling Coatings

In 1991, Whitesides et al. discovered the potent protein-repelling properties of oligo(ethylene glycol) (OEG) SAMs on gold.[157] Since then, Whitesides' findings led to the development of a wide variety of antifouling hydrophilic polymer coatings. In the current scientific literature, the immobilization of poly(ethylene glycol) (PEG) is considered the gold standard for the creation of surfaces with protein- and cell-repelling properties, and the immobilization of PEG has been performed through a wide variety of methods.[158-161] Although the mechanism underlaying the antifouling properties of PEG is currently not fully understood, the loss of polymeric entropy upon protein adsorption and the strong hydration of the PEG-chain in combination with charge neutrality are considered to be in a key role.[162] Furthermore, the polymeric grafting density has shown to influence the antifouling properties of PEG.[163] Besides, multiple studies have indicated that the polymeric chain length only has a minor effect on the antifouling properties of the surface.[164-165] However, there is no satisfying theoretical model predicting the antifouling properties of PEG and other polymeric structures with defined parameters.[166] Although PEG has been shown to be a versatile tool for the introduction of antifouling surface properties, its application has remained limited because of its immunological recognition in healthy subjects and limited *in vivo* and *in vitro* polymer stability.[162, 167-168] Additionally, a previous study by

Kizhakkedathu et al. has shown that high molecular weight PEG induces severe red blood cell aggregation, cell toxicity, and dose-dependent activation of blood coagulation, platelets, and complement system.[169] Therefore, there is a need for novel polymeric materials, that exhibit similar or superior antifouling properties to PEG, while showing higher thermal stability, oxidative stability, and biocompatibility under physiological conditions.

The work of Whitesides et al. has inspired the development of many antifouling coatings,[157] including coatings based on peptoids,[170] poly(saccharides),[171] poly(oxazolines),[172-174] poly(propylene sulfoxides),[175] poly(*N*-vinylpyrrolidones),[176-177] oligoglycerols,[178] and poly(glycerols).[179-181] The non-fouling properties of these systems are thought to arise from the formation of a surface hydration layer, that acts as a physical barrier for the prevention of unspecific protein adsorption (**Figure 11**).[162] The strength of the surface hydration is primarily determined by the physical and chemical properties of the material and the surface packing (i.e., film thickness, packing density, and chain conformation). The influence of the surface hydration on antifouling properties is clearly displayed by polyamide-, mannitol-, and PEG-coatings, which experience a transition from non-fouling to fouling upon decreased surface hydration,[182] increased packing density,[183] increased hydrophobicity of the surface-bound polymer chains,[184] and temperature rise.[185-186]

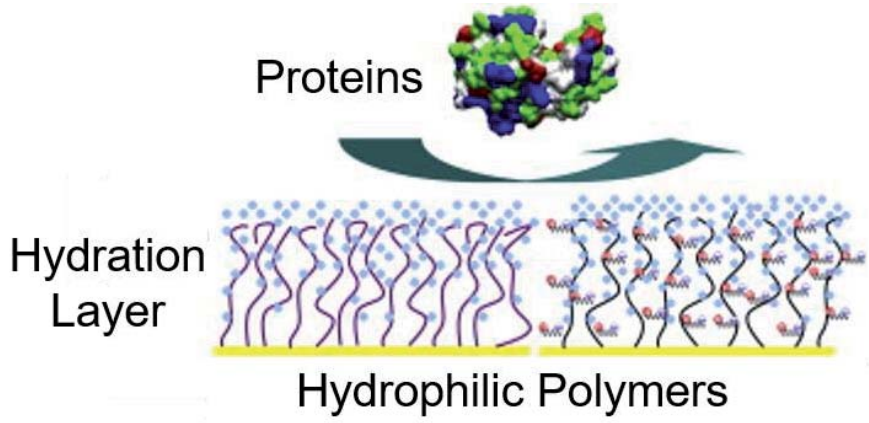

Figure 11. A schematic representation of hydrophilic antifouling surface coatings with an immobilized surface bound hydration layer (light blue) that prevents the adhesion of proteins. This figure was reproduced with permission from ref. 162 Copyright © 2010, Elsevier

Polyglycerol (PG) is an interesting biocompatible alternative to PEG,[187] with diverse molecular architectures (e.g., dendronized, hyperbranched, and linear structures can be obtained) and a controllable molecular weight (**Figure 12**).[188-191] A study by Haag et al. has shown the higher oxidative stability of bulk PG in comparison to PEG,[192] which is important for biomaterials that are exposed to high temperatures under aerobic conditions during sterilization.[193] PG-based structures have been detected to induce less blood platelet activation than PEG, which is a major advantage for the development of PG-functionalized blood contacting materials.[187] As the immobilization of PG dendrons, dendritic PG (dPG) (i.e., hyperbranched with low polydispersity), and linear polyglycerol (lPG) can successfully introduce antifouling surface properties,[181, 191, 194-195] the PG-based antifouling surface coatings constitute an attractive alternative to conventional PEG-based systems.

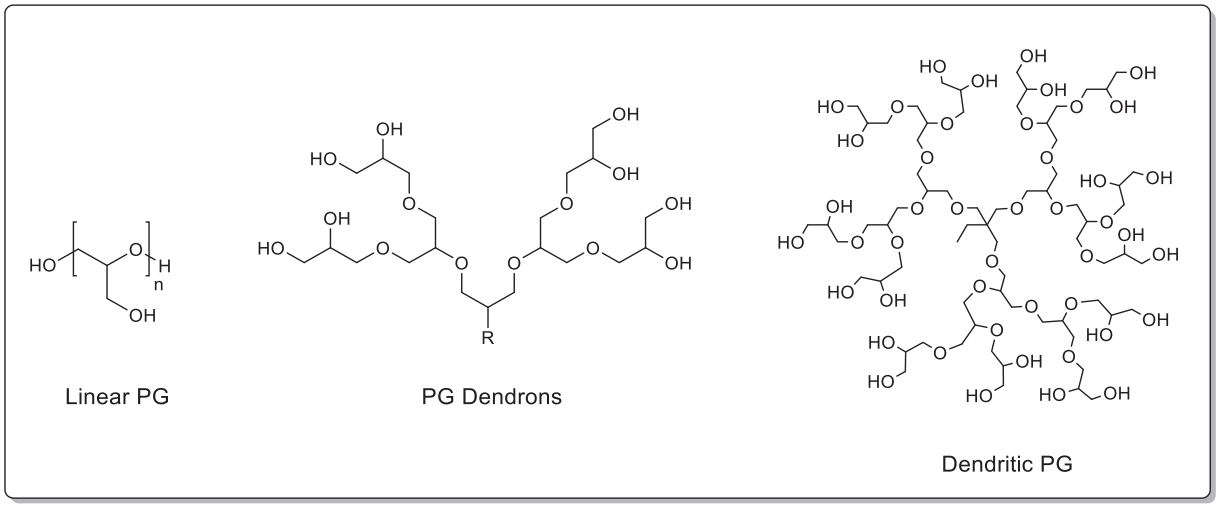

Figure 12. A schematic representation of the various molecular structures possible with PG backbones.

2.4.2. Zwitterionic Antifouling Coatings

Another important class of hydrophilic coatings are zwitterionic antifouling coatings, which commonly show even better antifouling properties than non-charged hydrophilic coatings, resulting from strong ionic solvation in the absence of net charge.[162] Zwitterionic coatings can be divided in polybetaines and polyampholytes. Polybetaines zwitterions carry a positive and negative charge in the same monomer (**Figure 13**),[196] whereas polyampholytes carry positive and negative charges in a 1:1 ratio in different monomeric units (**Figure 14**).[197] The control

over charge uniformity and distribution of two oppositely charged moieties on the surface are critical factors in the creation of antifouling polyzwitterionic materials. The optimization of these factors enables the maximal surface hydration resulting from electrostatic hydration, while minimizing the electrostatic interactions with protein. As an alternative to coatings based on polybetaine or polyampholyte zwitterions, highly antifouling surface coatings have been created via the formation of mixed charge SAMs (**Figure 15**). For instance, the 1:1 combination of thiol-terminated trimethylammonium moieties and thiol-terminated sulfonates on gold surfaces leads to the formation of a SAM in the absence of net-charge, while maximizing surface hydration (i.e., enhancing antifouling property).[198] Furthermore, SAMs containing phosphorylcholine (i.e., the hydrophilic head group found in some phospholipids) have also shown to effectively suppress the adhesion of protein.[199] Even though zwitterionic coatings have great potency for *in vivo* application, their antifouling properties are dependent of factors such as the pH,[200] packing density,[201] and ionic strength.[202] Therefore, there is a need for the further development of surface coatings that remain antifouling under a broad range of conditions.

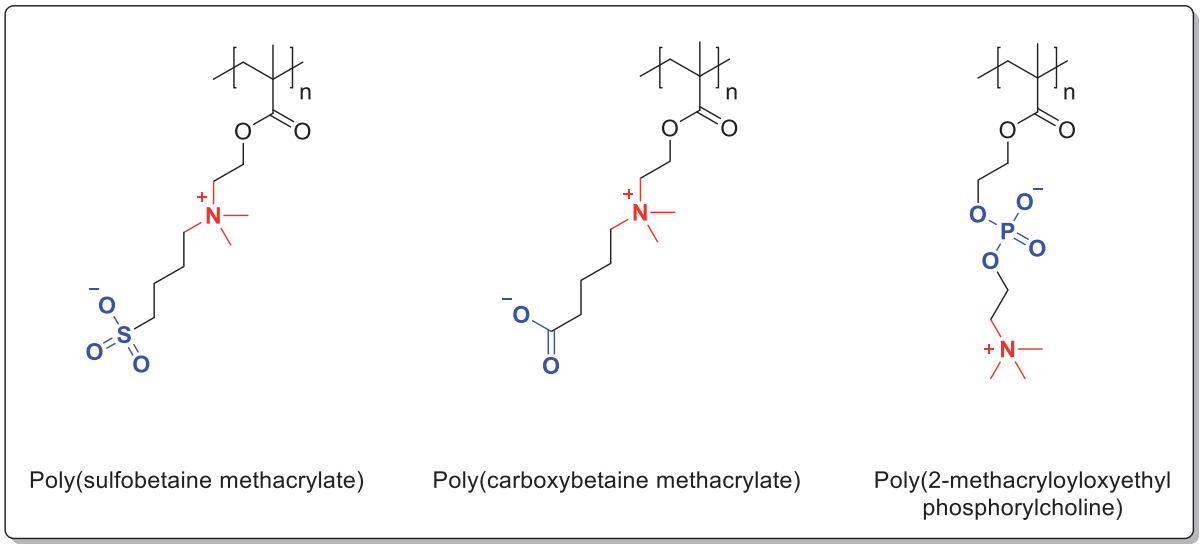

Figure 13. Three structures of polybetaines commonly used in surface modification: poly(sulfobetaine),[203] poly(carboxybetaine methacrylate),[204] and poly(2-methacryloloxyethyl phosphorylcholine).[205]

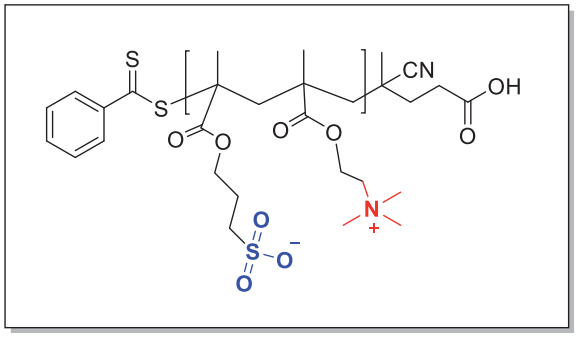

Figure 14. A polyampholyte structure synthesized via reversible addition-fragmentation chain transfer polymerization by Sponchioni et al.[206] The positive charge is depicted in red, whereas the negative charge is depicted in blue.

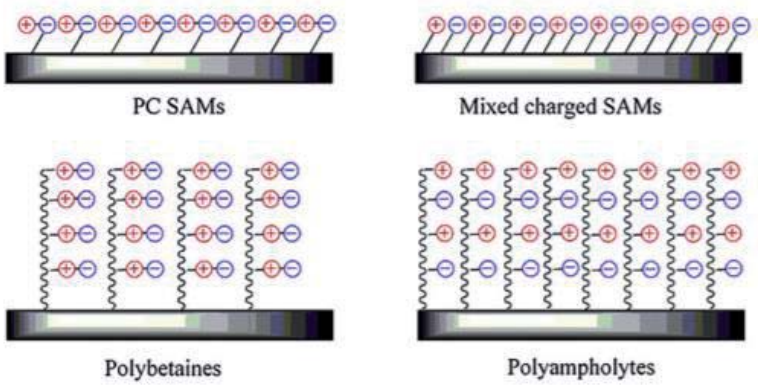

Figure 15. A schematic representation of the various types of zwitterionic antifouling surface modifications (blue = negative charge, red = positive charge). Although in principle not a zwitterionic system, mixed charged SAMs are included in this figure because of their related properties. This figure was reproduced with permission from ref. 162 Copyright © 2010, Elsevier.

2.4.3. Superhydrophobic Antifouling Coatings

Superhydrophobic surfaces (i.e., surfaces with a static water contact angle (CA) > 150°) repel water and other aqueous liquids by combining nano- and microscale surface topologies with low surface energies. Superhydrophobic surfaces found in nature include lotus leaves, rice leaves, and the wings of some species of insects (**Figure 16**).[207] In case of blood-contacting biomaterials, superhydrophobic coatings can enhance hemocompatibility of the biomaterial by reducing its effective area and the adhesion area exposed to platelets (i.e., creating a size

mismatch between platelets and topologically uniform areas).[208-211] Furthermore, they can alter the hydrodynamic properties of the biomaterial surface and reduce or alter protein adhesion, resulting in increased blood repellency. [212-213] The protein repellence on superhydrophobic surfaces is mediated by a surface-bound air-layer (i.e., the plastron), which is immobilized within the roughness of the surface. The plastron presents a physical barrier that prevents the adhesion of protein from the surrounding media. However, removal of the plastron can lead to the exposure of a high hydrophobic surface area, to which protein or cells readily adhere.[214] Although superhydrophobic surfaces can effectively reduce platelet and protein adhesion, they tend to lose their anti-platelet properties over time mainly resulting from their low mechanical durability.[215] Furthermore, the gradual dissolution of the surface-bound air layer reduces the stability of the plastron.[216] As the fabrication of superhydrophobic coatings is often also laborious, there is a need for easily producible superhydrophobic coatings that can effectively prevent biomaterial-induced thrombosis, protein adhesion, and bacterial infection and have a high plasmon stability and mechanical durability.

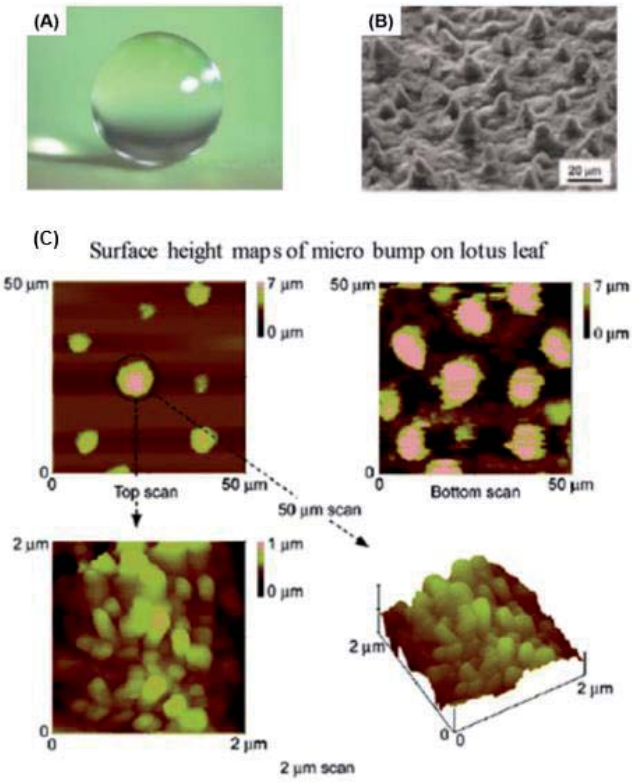

Figure 16. (A) A water droplet on a lotus leaf. (B) Scanning electron microscopy (SEM)-image of a lotus leaf, showing the micrometer-sized waxy pillars on the surface. (C) An atomic force

microscopy (AFM) image of the single pillars, showing the nanometer-sized roughness. This figure was reproduced with permission from ref. 207 Copyright © 2011, RCS Publishing.

2.5. Alternative Antithrombogenic Surfaces

Besides bioactive coatings and polymer-based bioinert coatings, alternative materials and methods have also been developed for the creation of antithrombogenic surfaces. Examples include but are not limited to the use of bioinert titanium nitride (TiN) (i.e., an inorganic bioinert surface), the use of diamond-like carbon coatings (DLC), and the use of alternating current (AC) polarized copper prosthesis materials.[8, 217] Furthermore, the application of (endothelial) cell linings for the introduction of thrombosis-inhibiting surface properties has also been investigated.[218-219]

Although multiple works have shown the high hemocompatibility of TiN coatings,[220-222] the application of these coatings has remained untouched in commercial VADs. TiN coatings can be produced via chemical or physical vapor deposition. The hemocompatibility of TiN is thought to arise as a result of the preferred adhesion of albumin over fibrinogen.[220] DLC coatings show higher hemocompatibility than TiN coatings, and have been used in some commercial VAD systems. DLC coatings can be deposited on a wide range of substrates using pulsed laser deposition, plasma-enhanced chemical vapor deposition, cathodic arc depositions, direct ion beam deposition, ion beam sputtering, and direct current/radiofrequency sputtering.[8] DLC coatings are chemically inert and have a high strength, low frictional coefficient, and a high thermal conductivity.[8] Furthermore, DLC coatings are highly bio- and hemocompatible, as a result of the high hydrophobicity and smoothness of these coatings.[8] However, a major risk of DLC coatings is the potential formation of microcracks.[8] The use of AC-polarized copper prosthesis materials has shown to be highly efficient in the prevention of surface blood clots on highly thrombogenic copper.[217] However, to the best of our knowledge the application of AC-polarized blood-contacting materials in VADs remains unexplored. A work by Scott-Burden et al. showed the effective reduction of platelet adhesion in an VAD system that was seeded with genetically modified smooth muscle cells. The cells were genetically engineered to produce antithrombotic NO.[219] Another work by Nikolaychik et al. showed the potency of endothelial cell linings in the creation of hemocompatible polyurethane cardiac prostheses.[218] Although the use of (endothelial) cell linings is showing its first clinical successes in the formation of vascular grafts,[223] their use in VAD systems has remained highly experimental.

2.6. Mussel-inspired Surface Chemistry

The great interest in controlled modification of physicochemical surface properties has resulted in the development of a wide range of universal (i.e., substrate-independent) polymeric coatings. Unlike conventional coating methods, such as the functionalization of hydroxylated surface with silanes and phosphonates,[224] or the functionalization of gold surfaces with thiols and disulfides,[225] universal polymeric coatings can be applied to a broad range of materials, independent of the chemical and physical properties of the underlaying substrate.[226] In general, surfaces can be functionalized via chemisorption or physisorption. In chemisorption, the coating binds to the substrates via the formation of covalent bonds, thus involving a chemical reaction between the surface and the adsorbate (e.g., the formation of thiol SAMs on gold and the functionalization of metal oxides with phosphonic acids and alkyl silanes).[224, 227] Additionally, in irradiative chemisorption surface radicals are created through irradiation to start surface-initiated polymerization of selected monomers.[228] Unlike in chemisorption, physisorption does not involve the formation of chemical bonds between the adsorbate and the surface. Instead, the surface-immobilization is mediated by reversible van der Waals interactions, electrostatic interactions, hydrophobic interactions, and hydrogen bonds. The physisorption can also be applied for the formation of multilayer systems,[229] whereas chemisorption leads to the formation of monolayers as a result of the depletion of reactive sites on the surface. As the physisorption does not rely on the formation of chemical bonds, it is suitable for the formation of universal coatings via various techniques, such as spin coating and the use of LbL assemblies.[229-230] However, due to the reversible binding interactions with low binding energies, intra-layer physical or chemical crosslinking of the adsorbate material is required for long-term stability of physisorbed coatings. Recently, various nature-inspired universal physisorbed coatings, such as coatings based on adhesion of blood protein,[231] plant polyphenols,[35, 232] and mussel-foot protein,[21] have been created.

2.6.1. Mussel Adhesion

Mussels can adhere to virtually all types of organic and inorganic surfaces, including surfaces which are classically categorized as non-fouling (e.g., polytetrafluoroethylene (PTFE)).[21] Mussels adhere themselves to the substrate using their byssal threads, which are tethered to the surface via an adhesive plaque. The proteins confined to the byssal threads and plaque include mussel-foot protein (mfp)-1, mfp-2, mfp-3, mfp-4, mfp-5 (**Figure 17A**), and mfp-6, which all contain the unusual amino acid 3,4–dihydroxyphenyl-L-alanine (i.e., DOPA) in varying

amounts (**Figure 17B**). Although DOPA is found in all mfps, its contents are significantly higher in the mfps that mediate surface binding (i.e., mainly mfp-3 and -5).[233]

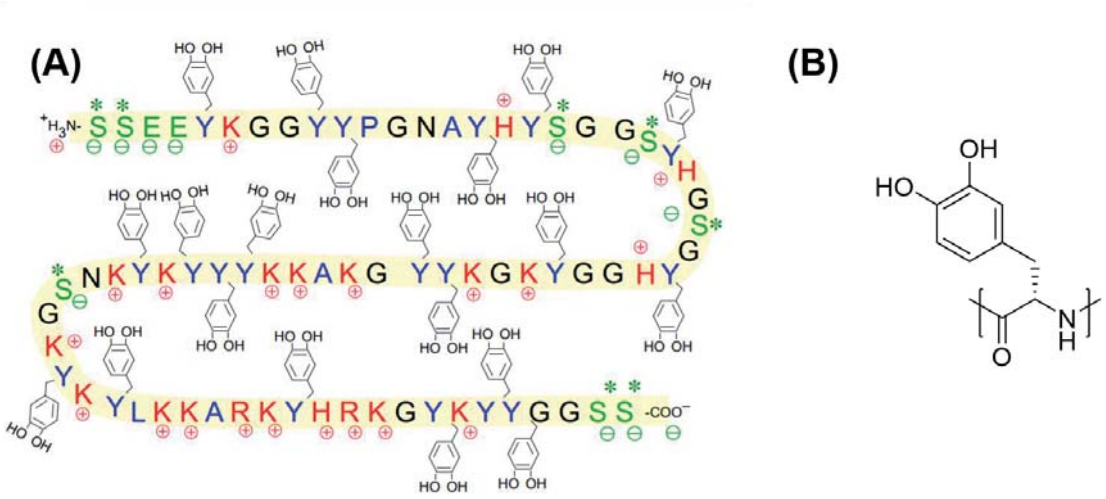

Figure 17. (A) A schematic representation of the mfp-5 protein as found in the plaque near to the interface. Y = DOPA, K = lysine, S = serine, G = glycine. (B) The molecular structure of the L-DOPA amino acid as found in mfp-3 and -5. Color key: tyrosine/DOPA: blue, cationic side chains: red, anionic side chains: green, thiols: purple. This figure was reproduced with permission from ref. 233 Copyright © 2017, The Company of Biologists.

In 1981, Waite et al. suggested the essential role of DOPA in the sticky properties of the mfps.[234] Since then, DOPA-mediated surface binding has been intensively studied and is now widely agreed to occur through hydrogen bonding, π–π interactions, and the formation of reversible coordination complex structures between the surface and DOPA's catechol moiety (**Figure 18A**). Especially in case of TiO_2, the binding of catechols via the formation of reversible coordination complexes was found to be exceptionally strong (with a single molecule interaction force of ca. 800 pN).[21, 235-236] When catechols are oxidized to their respective *o*-quinone form, their affinity towards metal oxides is significantly reduced. However, when the *o*-quinones are formed in presence of thiol- or amino-functionalized surfaces, they covalently immobilize to the surface (or crosslink on the surface) through the formation of Michael adducts and Schiff bases (**Figures 18A** and **18B**).[235]

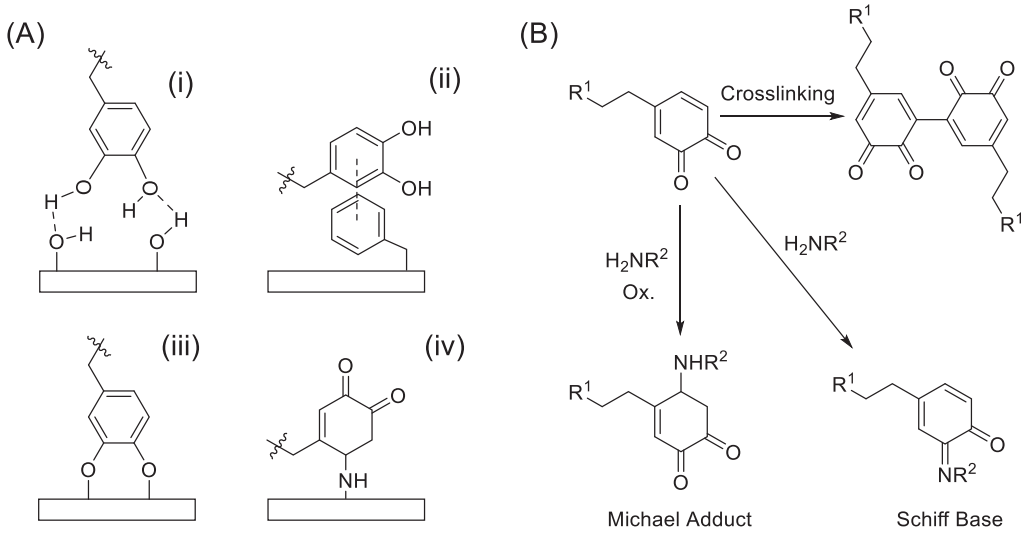

Figure 18. (A) A schematic display of the various catechol adhesion mechanisms. (i) On surfaces that display hydrogen bond donors/acceptors, catechols can bind the formation of hydrogen bonds, (ii) on surfaces that contain aromatic systems, catechols can bind via π–π interactions, (iii) catechols can tether to certain metal oxide surfaces (especially TiO_2) via the formation of strong but reversible metal complexes, (iv) finally, catechols can irreversibly bind to amine (and thiol) functionalized surfaces via the formation of Michael adducts.[237] (B) A schematic representation of the Michael-addition reactions and Schiff base formations between amines and *o*-quinones.[238] Furthermore, *o*-quinones can undergo crosslinking reactions.[239] In case of the Michael addition reaction to catechols, full understanding of the reaction mechanism has not been achieved yet. Furthermore, when catechols are reacted with primary amines in the presence of oxidizing agents such as $NaIO_4$, many side products are formed, most likely as a result of aryloxyl-phenol coupling reactions.[238] The Schiff base formation was found to only play a minor role when the reaction is performed under basic conditions (pH 11).[238]

Although DOPA was found to show strong and universal surface binding properties, the sole presence of DOPA did not explain the rapid polymerization of the mfps upon mussel adhesion. More recently, Waite et al. observed the close proximity of catechol- (i.e., DOPA) and amine-containing amino acids (i.e., lysine and histidine) in mfp-5, leading to the hypothesis that the coexistence of these groups was essential for rapid adhesive properties.[240] This led to the development of a variety of catechol-amine-including antifouling peptide sequences, containing a biomimetic anchoring block rich in DOPA and lysine amino acids,[170] catechol-

functionalized poly(ethylene amine),[241] and catechol-functionalized chitosan.[242] However, low molecular weight catechol amines were not considered prior to 2007.

2.6.2. Polydopamine and Catechol Chemistry

In 2007, Messersmith et al. developed a facile dip-coating procedure for the formation of multi-functional universal polydopamine (PDA) coatings (**Figure 19**).[21] This breakthrough led to the development of a wide variety of PDA-based systems, including antifouling,[21] hemocompatible,[243] and antibacterial surfaces.[244] PDA is widely described in current scientific literature, mainly because of its simplicity, low cost, and adaptability. The PDA coating is created by simply submerging a substrate in an aqueous alkaline solution of dopamine for an adjustable period of time. During the incubation, the PDA coating is spontaneously deposited. This primary coating can then be used as a primer for the immobilization of a secondary coating for the introduction of tailored surface properties.

The PDA coatings form through an oxidative polymerization of dopamine, starting from the oxidation of dopamine by dissolved oxygen at alkaline pH (**Figure 20**). The *o*-quinone product subsequently reacts through a nucleophilic cyclization, eventually leading to the formation of 5,6-dihydroxyindole.[245] In most of the currently proposed mechanisms, 5,6-dihydroxyindole and dopamine are considered the key building blocks of PDA. Besides, alternative mechanisms which propose PDA as a non-covalent assembly of dopamine, dopamine-quinone, and 5,6-dihydroxyindole have been proposed as well as a mechanism similar to the formation of eumelanin.[245] However, there is no general consensus on the exact mechanistic details of the PDA formation, and therefore it remains the topic of current investigations. Although PDA has proven itself as a useful tool for substrate-independent surface modification, it suffers from slow polymerization rates and limited coating thickness (i.e., a maximum coating thickness in nanometer range).[21] Furthermore, the PDA coating is non-transparent and has a dark-brown color, making it unsuitable for various optical applications.

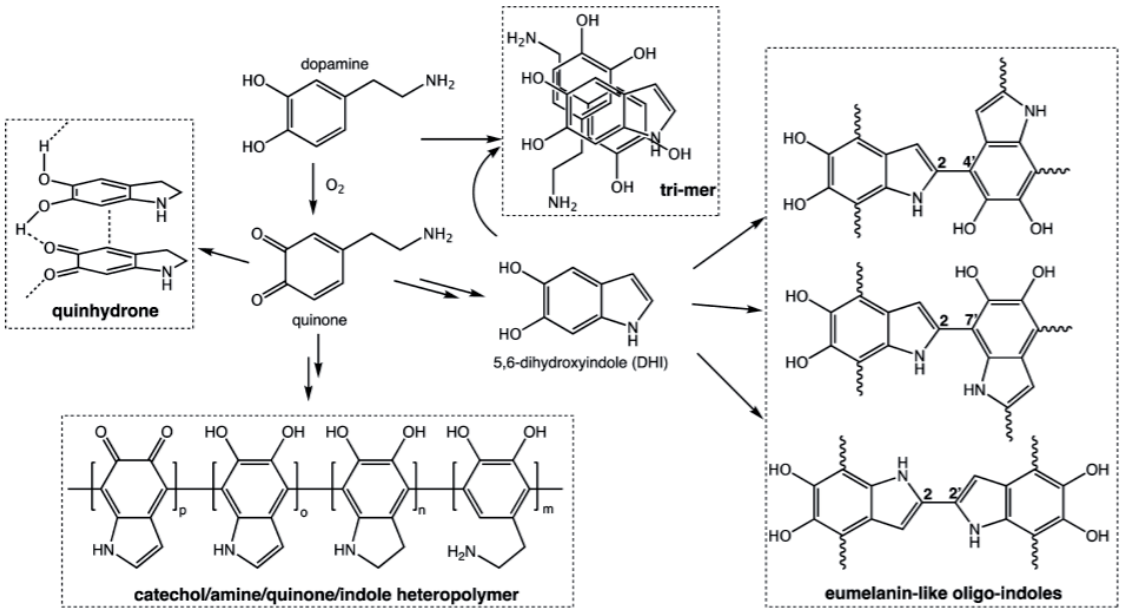

Figure 19. A schematic representation of the currently proposed mechanisms for the formation of the PDA coating. This figure was reproduced with permission from ref. 245 Copyright © 2018, American Chemical Society.

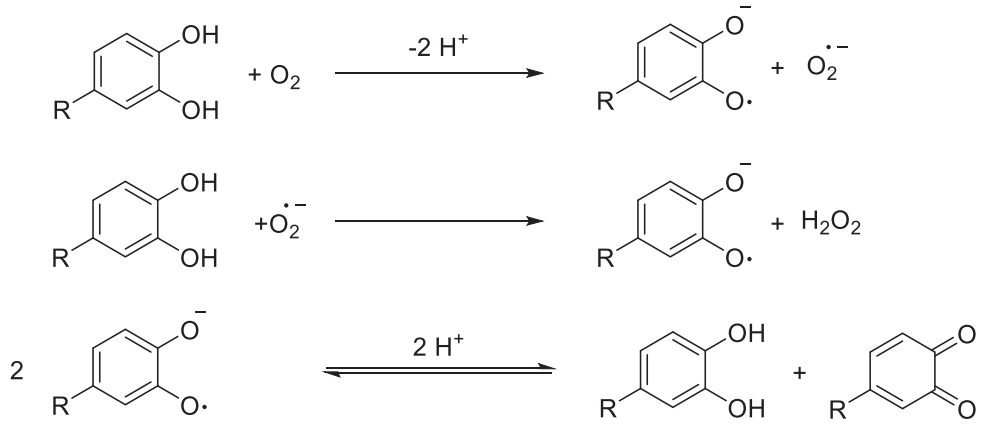

Figure 20. Oxidation of the catechol to its *o*-quinone form. This figure was reproduced with permission from ref. 246 Copyright © 2014, Royal Society of Chemistry.

2.6.3. Mussel-inspired Polymeric Coatings

In case of catechol-functionalized polymeric structures, the catechol moieties normally function as both crosslinking and substrate-binding groups. The required number of catechol moieties per macromolecule for stable surface functionalization is mainly dictated by the type

of the substrate to be coated. When the substance is bound to the surface via covalent bonds, a single catechol moiety might be sufficient for stable coating formation. In case of TiO_2 substrates, strong coordinative interactions bind catechol moieties to the surface. However, because of oxidative detachment, multiple catechol moieties are required to effectively immobilize the polymer on the surface in a long-term stable manner. In case of inert surfaces (e.g., PTFE surfaces), even higher catechol functionalization is required, resulting from the relatively weak binding of the polymer to the surface via hydrophobic interactions. Multivalent surface attachment via catechol groups has proven itself as a highly efficient strategy for the substrate-independent immobilization of polymeric coating materials, such as linear (block-co)polymers,[247] branched polymers,[248] and hyperbranched (i.e., dendritic) polymers.[195]

2.6.4. Mussel-inspired Dendritic Polyglycerol

The adhesion and solidification of the mussel byssus requires 30 seconds till 8 minutes in nature.[233] In contrast, the initial PDA coating procedure by Messersmith et al. required 24 hours to obtain up to 50 nm of PDA film.[21] Since then, the coating time has been addressed in several studies, leading to the development of various methods accelerating PDA formation, including methods applying chemical oxidizing agents (e.g., $NaIO_4$) and methods utilizing ultra violet (UV) irradiation.[249-250] However, the use of oxidizing agents is limited due to their potential toxicity, whereas the use of UV irradiation might be unpractical in some technical applications. Therefore, there is a need for new polymeric structures that polymerize at a similar speed as the mfps, while providing sufficient substrate adhesion. Although dopamine effectively mimics the chemical functionality of mfp-5, it lacks similarity in molecular structure and weight. Haag et al. have reported a hetero-multivalent catechol- and amine-functionalized dPG, which mimicked the functional groups, molecular weight, and structure of mfps (**Figure 21**).[251] The so-called mussel-inspired dPG (MI-dPG) was synthesized by first transforming all the peripheral hydroxyl moieties of dPG into amines, subsequently followed by catechol functionalization of 40% of the amine moieties. The excess of amine groups enhanced inter-layer interactions via crosslinking reactions and provided functional groups for secondary modification of the coatings.[252] Haag et al. showed in their later study that stable coatings on TiO_2 are already obtained after only 10 minutes of dip-coating.[180] Furthermore, it has been shown that the coating's roughness and thickness can be controlled by simple adjustments in the MI-dPG concentration and the pH of the polymerization reaction.[252] Besides, coatings with a thickness and roughness gradient have been fabricated by simply adjusting the immersion

depth of the substrate.[253] In their further studies, they have introduced a nanometer roughness and antimicrobial surface properties to the MI-dPG coating by using copper (Cu) or silver (Ag) nanoparticles.[244, 253]

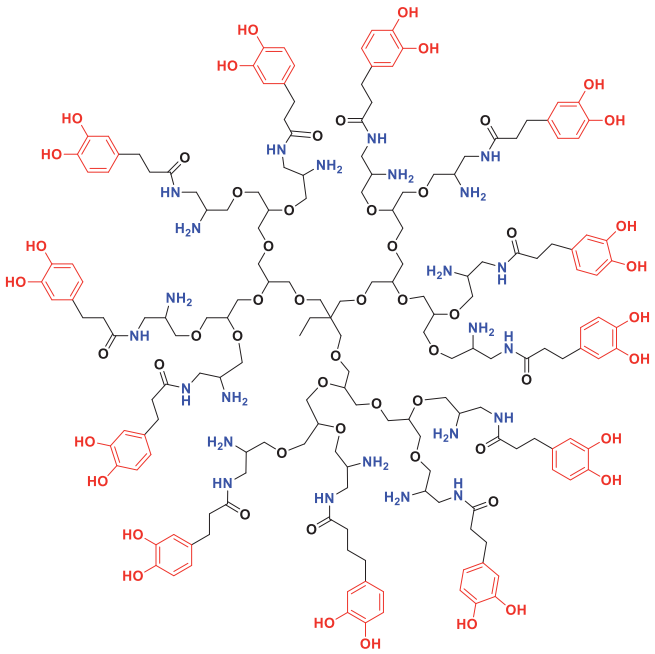

Figure 21. An idealized representation of the molecular structure of MI-dPG, containing similar amounts of catechol and amine functional groups as found in the native mfp-5. The amount of the glycerol monomers in the core (shown in black) varies with the size of the polymer, while the dPG-core shows 60% of branching.[190]

2.7. Functional Mussel-inspired Surface Coatings

Following the detailed description of the mussel adhesion and catechol chemistry in the previous sections of this thesis, the next section will give examples of applying functional mussel-inspired coatings for preventing biomaterial-associated, shear-induced platelet activation and thrombosis.

2.7.1. Mussel-inspired Antithrombogenic Surfaces

In 2009, Kim et al. created the first mussel-inspired anti-thrombogenic surface by immobilizing dopamine-conjugated heparin on negatively charged metal surfaces.[254] Since then, other studies have shown that dopamine-heparin conjugates are also suitable for the functionalization

of polymeric surfaces, such as polyurethane (PU) an polyethersulfone (PES).[144, 255] Using dopamine-heparin conjugates circumvents the need for chemical pretreatment of the surface, and the surface modification occurs in a single step. Therefore, employing dopamine-conjugated heparin is an interesting alternative to other universal coating methods, which commonly utilize complex machinery or require the substrate to have specific chemical or physical properties.

As an alternative approach to immobilize heparin on the surface of biomaterials, heparin has been covalently bound on a PDA coating in several blood-contacting applications, such as heparinized stents,[256] heparinized hemodialysis membranes,[257] heparinized bone implants,[258] nano-anticoagulant carriers,[259] and mesoporous heparin-releasing films.[260] Also catechol-functionalized, heparin-mimicking polymers have been introduced to solid substrates.[144] Other alternative approaches for the surface immobilization of heparin-mimicking structures include the formation of LbL assemblies and the binding of heparin-mimicking polymers to PDA films.[261-263]

2.7.2. Mussel-inspired Hydrophilic Antifouling Surfaces

Already in the fundamental work by Messersmith et al., a PDA film was used for immobilizing PEG as a hydrophilic antifouling agent on the surface.[21] Since then, other substrate-independent adhesive layers, such as coatings based on MI-dPG, tannic acid, and aminomalononitrile have been used to effectively immobilize functional polymers on the surface.[180, 264-267] Using bi-layer systems (i.e., systems consisting of an adhesive layer modified with a functional top layer) can provide additional control over the coatings' roughness and thickness, which can be beneficial, for instance, in controlled stem cell culturing and in the creation of wetting gradients for fog harvesting.[252, 268-269] Additionally, the use of an adhesive layer can introduce multiple simultaneous functionalities (e.g., the introduction of silver nanoparticles (AgNPs) to MI-dPG in combination with an antifouling hydrophilic polymeric top layer combines antimicrobial and antifouling surface chemistries).[264]

Mussel-inspired chemistry can also be used for the direct immobilization of functional monolayers. The use of monolayer coatings might be beneficial especially in polymeric filter membranes, as too thick coatings can obstruct the membrane's pores, thus hampering the membrane's technical applicability. In a study by Wei et al., dPG was functionalized with catechol moieties at various degrees and subsequently immobilized on a manifold of substrates

to introduce antifouling surface properties (**Figure 22**).[270] In their study, a certain amount of catechol moieties was required to immobilize dPG in a stable manner. However, when the catechol functionalization was too high (30 %) the antifouling properties of dPG were reduced, most likely because of the random distribution of the catechol-groups on the dPG's periphery: while some of the catechols were mediating surface binding, others were facing away from the surface, thus mediating protein binding.

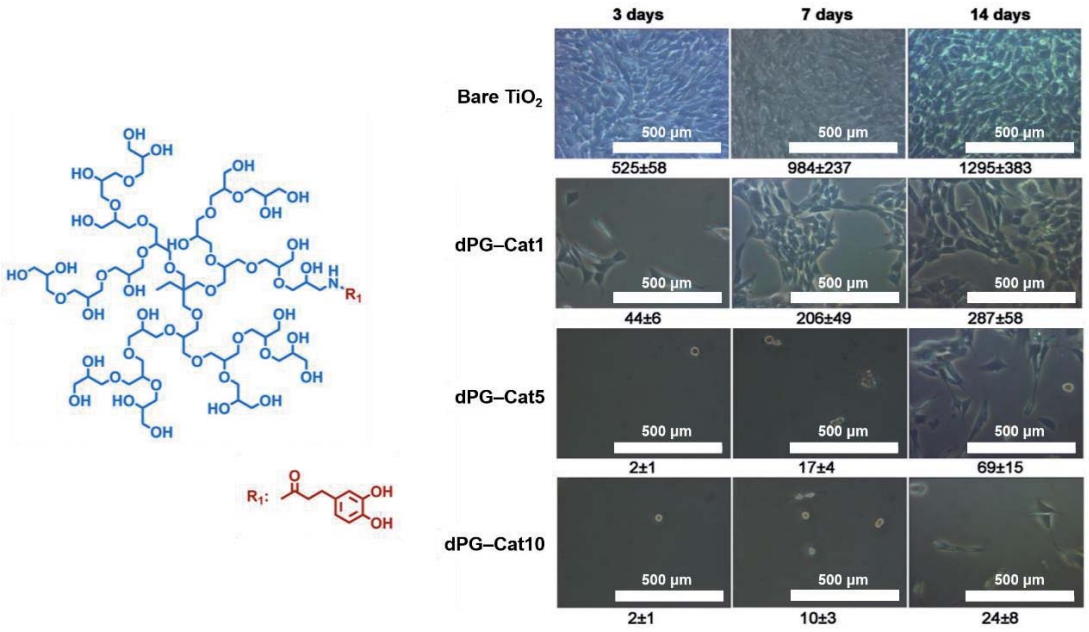

Figure 22. dPG-catechol monolayers with varying catechol functionalization. Wei et al. observed that the degree of catechol functionalization influenced the stability of catechol-functionalized dPG on the surface. Resulting from oxidation of the catechols, 1% catechol functionalized dPG (dPG-Cat1) detached from the surface over time, resulting in the loss of antifouling properties after 14 days of cell culturing. Higher degrees of catechol functionalization led to more stable dPG immobilization, resulting in prolonged antifouling properties. dPG–Cat5 = 5% catechol-functionalized dPG, dPG–Cat10 = 10% catechol functionalized-dPG. This figure was reproduced with permission from ref. 195 Copyright © 2014, Elsevier.

In a follow up work, Wei et al. introduced antifouling surface properties to biomedically relevant TiO_2 and polystyrene (PS) surfaces, via the use of crosslinked hierarchical polymer multilayers.[239] In case of the TiO_2 substrate, Wei first immobilized dPG–Cat10 on the substrate

as a stable base layer. Subsequently, the base-layer was post-functionalized with dPG–Cat1, via the use of a straightforward dip coating procedure (**Figure 23A**). By using this strategy, the antifouling dPG–Cat1 was immobilized on the surface in a stable manner, which was not possible via the direct immobilization of dPG–Cat1 on the TiO_2 surface. [239] The stable crosslinking between the dPG–Cat10 and dPG–Cat1 layers was proposed to occur through the formation of aryl-aryl bonds between the catechol moieties of the adjacent layers. Furthermore, it was proposed that the formation of these aryl-aryl bonds contributed to the intralayer stability of the system (**Figure 18B**).[239] For the functionalization of PS, the direct binding of the dPG–Cat10 layer was found to be insufficient, resulting from the weaker binding interactions between the catechol moieties and the substrate. Therefore, MI-dPG was first immobilized on the PS surface, as a reactive and stable base layer. Subsequently, dPG–Cat10 and dPG–Cat1 were immobilized on the MI-dPG coating, respectively (**Figure 23B**). In this way, stable and highly effective antifouling PS surfaces were obtained.[239]

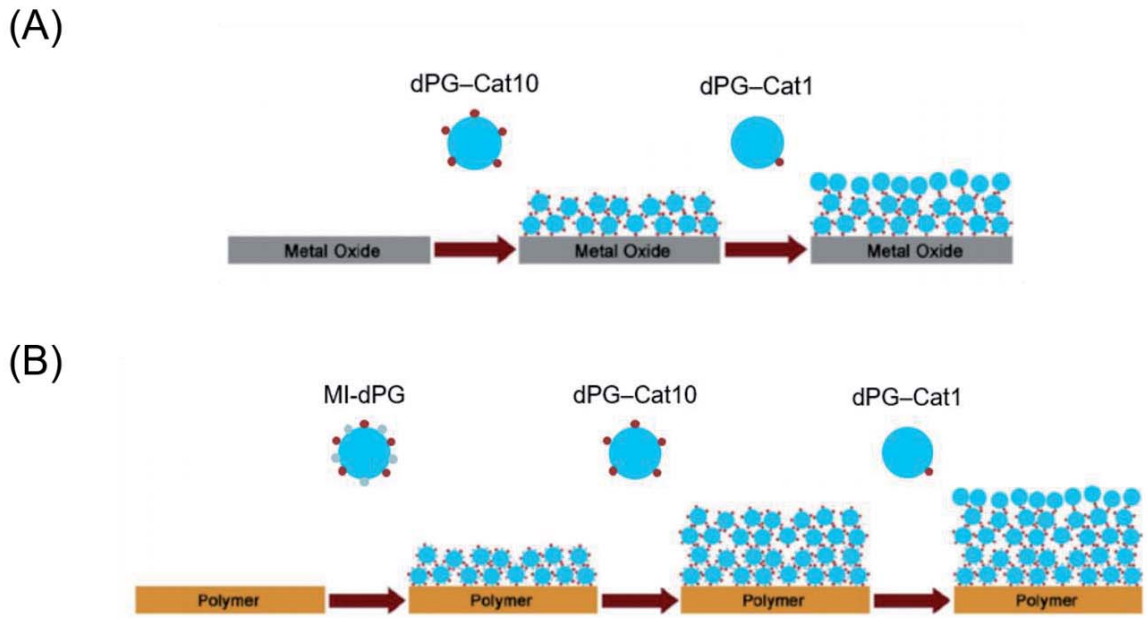

Figure 23. A graphical representation of the hierarchical coating method developed by Wei et al. (A) Immobilization of dPG–Cat10 and dPG–Cat1 on TiO_2 substrates. (B) Immobilization of MI-dPG, dPG–Cat10, and dPG–Cat1 on the PS surface. This figure was reproduced with permission from ref. 239 Copyright © 2014, Wiley-VCH.

An alternative mussel-inspired approach was developed by Yu et al. who created a lPG block-copolymer functionalized with a surface-binding block that carried amine, phenyl , and catechol moieties (**Figure 24**).[181] By applying the block-copolymer strategy, all surface tethering groups were pointing to the surface, while the hydrophilic domain of the block-copolymer was facing away from the substrate (i.e., effectively preventing protein adhesion). The stability of the coating was enhanced applying additional crosslinking via monolayer formation under slightly acidic conditions (i.e., keeping the catechol in its unoxidized form), followed by oxidation of the catechol, leading to crosslinking reactions between the amines and *o*-quinones of adjacent polymer chains.

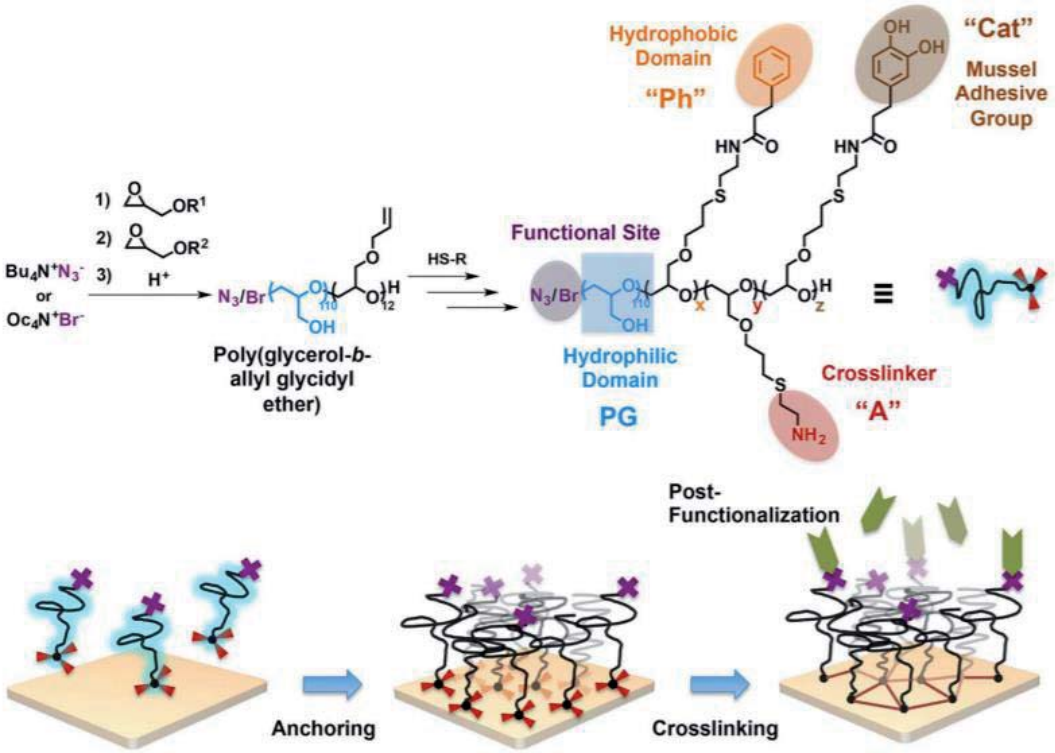

Figure 24. A schematic representation of the block-copolymer antifouling approach as performed by Yu et al. The block copolymer was functionalized with a surface-tethering block containing phenyl, catechol, and amine functional groups. This figure was reproduced with permission from ref. 181 Copyright © 2017, American Chemical Society.

2.7.3. Mussel-inspired Superhydrophobic/Superamphiphobic Surfaces

Superhydrophobic coatings show a high potential in the prevention of biomaterial-induced thrombosis. Various mussel-inspired superhydrophobic coatings have been developed, including silver nanoparticle-functionalized PDA coatings functionalized with perfluorodecanethiols,[271] superhydrophobic perfluorodecyl trichlorosilane-functionalized PDA-coated sand,[272] and n-octadecyl-functionalized PDA-coated superhydrophobic textiles.[273] Schlaich et al. created MI-dPG-based superamphiphobic surfaces (i.e., surfaces which are both superhydrophobic and superoleophobic) via hierarchical pH-controlled polymerization of micro- and nanostructures of MI-dPG.[252] Additional use of gold and silver nanoparticles introduced nanometer roughness to the micrometer roughed MI-dPG coating. The hierarchical structures were subsequently functionalized using heptadecafluoroundecanoyl chloride to introduce superamphiphobic surface properties (**Figure 25**).

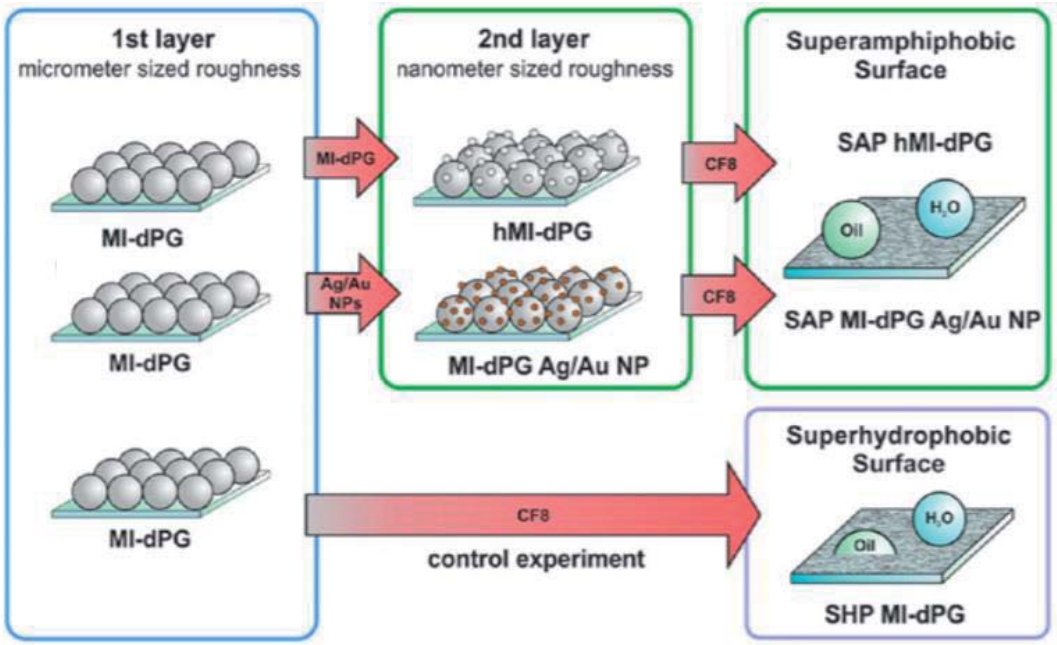

Figure 25. A schematic representation of the work performed by Schlaich et al., who carefully investigated the relation between surface roughness and the respective wetting properties. Superamphiphobicity was achieved by functionalizing a micro- and nanometer roughed MI-dPG coating with hydrophobic fluoroundecanoyl chloride (CF8). This figure was reproduced with permission from ref. 252 Copyright © 2016, American Chemical Society.

As highlighted in this thesis, the use of mussel-inspired coatings shows a great potential for the creation of surfaces with highly antifouling and hemocompatible surface properties. So far, mussel-inspired coatings with bioactive and antifouling properties have been developed. However, because of the various complex biological interactions between biomaterials, soluble blood components, and the blood cells, the rational design of coatings with long-term stability and *in vivo* efficiency remains challenging. Furthermore, the mechanism behind the antifouling properties of hydrophilic surface-bound polymers is not yet fully understood. Therefore, there is a great need for the further development of mussel-inspired antifouling and antithrombogenic surface coatings. Additionally, the development of these coatings would benefit from the application of flow experiments with whole blood under elevated shear conditions, as most of the current biomaterial-related research focuses on observing anti-platelet properties under clinically irrelevant static conditions.

3. SCIENTIFIC GOALS

The aim of the current doctoral thesis was to develop mussel-inspired PG-based coatings for the prevention of biomaterial-related fouling. The first project of this thesis aimed at the creation of a two-layer antifouling coating for medically relevant TiO_2. The developed coating consisted of MI-dPG as a substrate-independent adhesive layer, and oligo-amine-functionalized linear PG (lPG–b–OA_{11}, OA = oligo-amine) as an antifouling hydrophilic top-layer. The lPG–b–OA_{11}-functionalized coating was compared to a similar HO–PEG–NH_2-functionalized control coating. The first project covered the characterization and comparison of the various coatings in respect to their formation, chemical stability, and antifouling performance. It was hypothesized that the introduction of lPG–b–OA_{11} or HO–PEG–NH_2 to the MI-dPG coating would result in the formation of stable substrate-independent antifouling coatings. Furthermore, it was expected that the multivalent immobilization of lPG–b–OA_{11} would contribute to its stability on the MI-dPG coating.

The second project of this thesis aimed at the application of lPG–b–OA_{11} and HO–PEG–NH_2-functionalized MI-dPG coatings on TiO_2 in an *in vitro* blood platelet adhesion model. The hemo- and biocompatibility of the various coatings was evaluated by characterizing their cytotoxicity, complement activating properties, and platelet activating properties. Additionally, the adhesion of blood platelets was investigated under flow conditions, utilizing the stagnation point flow model developed by Affeld et al.[111-112, 274] It was expected that the

introduction of lPG–b–OA_{11} or HO–PEG–NH_2 to the MI-dPG coating would decrease the number of adherend platelets compared to the uncoated substrate. Furthermore, the lPG–b–OA_{11}-functionalized system was expected to be highly biocompatible.[275-276] A VAD prototype was coated with MI-dPG under industrially feasible conditions, and a method for the visualization of the coating was developed. It was hypothesized that the coating of complex 3D shapes (such as VADs) with MI-dPG would be feasible under flow conditions. However, parameters such as the flow rate, polymer concentration, and buffer pH were expected to heavily influence the coating process.

The aim of the last project of this thesis was to develop substrate-independent mussel-inspired antifouling surface coatings, via the direct grafting of glycidol monomers from MI-dPG-coated substrates (i.e., via the direct grafting of dPG from the MI-dPG coating). Hydrophilic TiO_2 and hydrophobic PDMS were coated with MI-dPG, and subsequently the surface-bound amines of the MI-dPG coating were utilized to initiate the grafting of dPG from the surface. Earlier studies have reported the direct covalent grafting of dPG from silica, steel, and aluminum.[277-279] However, these approaches all required specific physical or chemical substrate properties, surface activation prior to the grafting process, the use of organic solvents, or the use of the highly caustic base sodium methoxide. In contrast, the novel method developed in the last project of this thesis was performed in the absence of organic solvents or caustic bases, in a substrate-independent manner. It was hypothesized that the grafting procedure (i.e., coating thickness, surface wettability, and surface roughness) could be controlled by carefully adjusting the reaction time and temperature.

4. PUBLICATIONS

4.1. Mussel-inspired Multivalent Linear Polyglycerol Coatings Outperform Monovalent Polyethylene Glycol Coatings in Antifouling Surface Properties

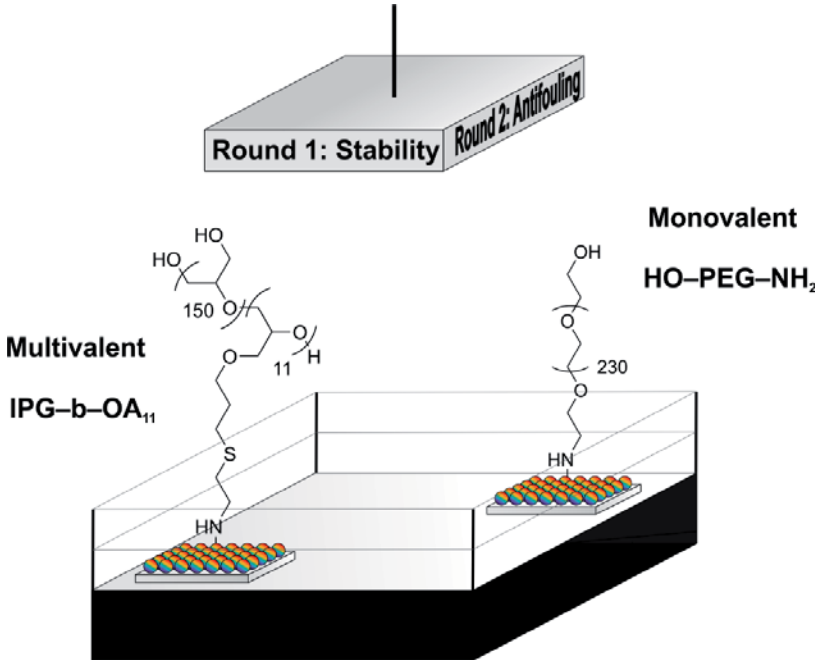

Figure 26. Graphical abstract. This figure was reproduced with permission from ref. 180 Copyright © 2019, American Chemical Society.

Michaël W. Kulka, Ievgen S. Donskyi, Nina Wurzler, Dirk Salz, Özlem Özcan, Wolfgang E.S. Unger, Rainer Haag, *ACS Appl. Bio Mater.* **2019***, 2,* 5749.

https://doi.org/10.1021/acsabm.9b00786

Contributions: **M.W.K.**: Planned and coordinated the project, conducted and interpreted all CA, AFM, SEM, and quartz crystal microbalance (with dissipation monitoring) (QCM-D) measurements, and summarized all results, discussions, and conclusions in the form of a scientific publication.

4.2. The Application of Dual-layer, Mussel-inspired, Antifouling Polyglycerol-based Coatings in Ventricular Assist Devices

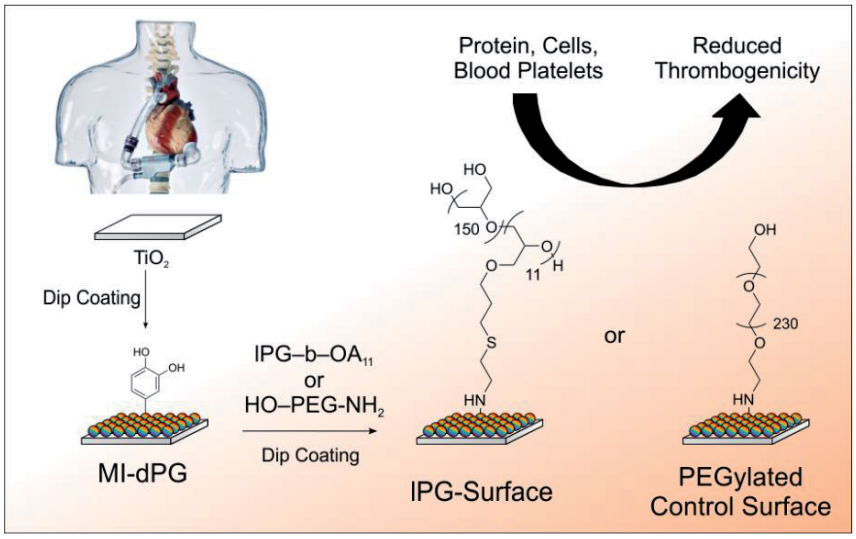

Figure 27. Graphical abstract. This figure was reproduced with permission from ref. 280 Copyright © 2020, Wiley-VCH.

Michaël W. Kulka, Sarah Smatty, Kim Silberreis, Felix Hehnen, Tim Bierewirtz, Yannic Kerkhoff, Chuanxiong Nie, Carsten Grötzinger, Sebastian Friedrich, Lars I. Dahms, Jens Dernedde, Ingo Grunwald, Ulrich Kertzscher, Klaus Affeld, Michael Schirner, Rainer Haag, *Wiley Adv. Mater. Interfaces* **2020**, *Accepted.*

Contributions: **M.W.K.:** Planned and coordinated the project, executed all synthesis and coating experiments, and performed all SEM measurements. Interpreted all data and summarized the results, discussions, and conclusions in the form of a scientific publication.

WILEY-VCH

The Application of Dual-Layer, Mussel-Inspired, Antifouling Polyglycerol-Based Coatings in Ventricular Assist Devices^

Michaël W. Kulka,[a] Sarah Smatty,[b] Felix Hehnen,[b] Tim Bierewirtz,[b] Kim Silberreis,[a,c] Chuanxiong Nie,[a] Yannic Kerkhoff,[a] Dr. Carsten Grötzinger,[d] Sebastian Friedrich,[e] Dr. Lars Ingemar Dahms,[f] Dr. Jens Dernedde,[c] Prof. Dr. Ingo Grunwald,[g] Prof. Dr. Michael Schirner,[a] PD Dr.-Ing. Ulrich Kertzscher,[b] Prof. Dr.-Ing. Klaus Affeld,[b] Prof. Dr. Rainer Haag [a,]*

[a] Institute for Chemistry and Biochemistry, Freie Universität Berlin, Takustraße 3, 14195 Berlin, Germany

[b] Biofluid Mechanics Lab, Charité-Universitätsmedizin Berlin, Augustenburger Platz 1, 13353 Berlin, Germany

[c] Institute for Laboratory Medicine, Clinical Chemistry and Pathobiochemistry, Charité - Universitätsmedizin Berlin, Augustenburger Platz 1, 13353 Berlin, Germany

[d] Department of Hepatology and Gastroenterology, Charité - Universitätsmedizin Berlin, Augustenburger Platz 1, 13353 Berlin, Germany

[e] Process Engineering Department, Berlin Heart GmbH, Wiesenweg 10, 12247 Berlin, Germany

[f] Quality Assurance and Regulatory Affairs, qtec group GmbH, Niels-Bohr-Ring 3-5, 23568 Lübeck, Germany

[g] Department of Industrial and Environmental Biology, Hochschule Bremen – City University of Applied Sciences, Neustadtswall 30, 28199 Bremen, Germany

KEYWORDS: *antifouling, polyglycerol, platelet adhesion, shear-induced thrombus formation, stagnation-point flow model, ventricular assist device*

Abstract

Continuous-flow ventricular assist devices (VADs) have established themselves as a lifesaving therapy option in patients with severe cardiovascular disease. Unfortunately, complications with VADs resulting from the shear-induced formation of surface blood clots are common. In the current work, an antifouling coating based on the combination of mussel-inspired dendritic polyglycerol (MI-dPG) and linear polyglycerol (lPG) was tested for its cell-repelling properties, biocompatibility, and complement activating properties. Furthermore, the adhesion and activation of blood platelets were tested under static and flow conditions. The adhesion and proliferation of two cell types were studied by means of LIVE/DEAD™ cell staining, and it was clearly observed that the lPG-functionalized MI-dPG coating prevented cell adhesion. Additionally, no cell mortality was observed on all substrates, indicating the biocompatibility of the tested coatings. All coatings showed lower (or equal) complement-activating properties than bare titanium, which is considered a highly biocompatible material.[1] Most importantly, the lPG-functionalized system prevented the adhesion and activation of blood platelets under static and flow conditions. Finally, a prototype VAD was successfully coated with MI-dPG under flow conditions. In the current study, we proved the efficient lPG-functionalization of the MI-dPG coating to obtain cell- and platelet-repelling surfaces. [2]

Introduction

Cardiovascular diseases (CVDs) account for 45% of all deaths, and are the main cause of death for men in all but 12 countries of Europe.[3] The treatment of patients suffering from CVDs includes lifestyle adaptations (such as quitting smoking and dietary changes), medication for the

reduction of low-density lipoprotein cholesterol, cardiac rehabilitation, and surgical interventions (e.g., coronary artery bypass grafting), percutaneous coronary intervention, and the placement of electronic pacemakers or ventricular assist devices (VADs).[4] VADs are electro-mechanical devices for cardiac circulation, which are used to partially or fully replace the function of a failing heart.[5] Over the last decades, VADs have established themselves as livesaving treatment option for patients with refractory heart failure, with a 2-year survival rate of 80%.[6] The Food and Drug Administrations has approved the use of continuous-flow VAD systems.[7] However, the use of these systems has its shortcommings: as a result of unspecific protein adhesion and high wall shear rates, the formation of surface blood clots in VADs is common (**Figure 1**).[8] The release of these blood clots into the bloodstream constitutes a major risk, as the clots might occlude arteries, effectively blocking the supply of nutrition and oxygen to the downstream tissue. Additionally, the formation of surface blood clots hinders the effectiveness of the VAD system, leading to repeated invasive surgical interventions to clean or fully replace the VAD (i.e., in case of intracorporeal systems). Therefore, the development of durable blood-contacting materials for the prevention of surface blood clots is of major interest for VAD-patients.

Commonly, titanium (Ti) (covered with a natural layer of titanium dioxide (TiO_2)) and its alloys are used for the production of VADs, resulting from the excellent biocompatibility and low costs of these materials.[9] However, the application of these materials is far from ideal with respect to their hemocompatibility. Additionally, it seems that the potential for alternative hemocompatible bulk biomaterials has been largely explored.[9] Consequently, scientists have shifted their attention towards surface coatings and surface engineering for the reduction of biomaterial-induced thrombosis. A wide variety of antithrombogenic coating materials has been developed, and the use of coatings has proven itself as a useful strategy for the reduction of

biomaterial-induced thrombosis in VADs. In general, VAD coatings can be divided into bioactive coatings and inorganic/organic bioinert coatings.[9, 10, 11] Alternatively, the use of endothelial cell linings for the reduction of biomaterial-induced thrombosis has also been investigated.[12]

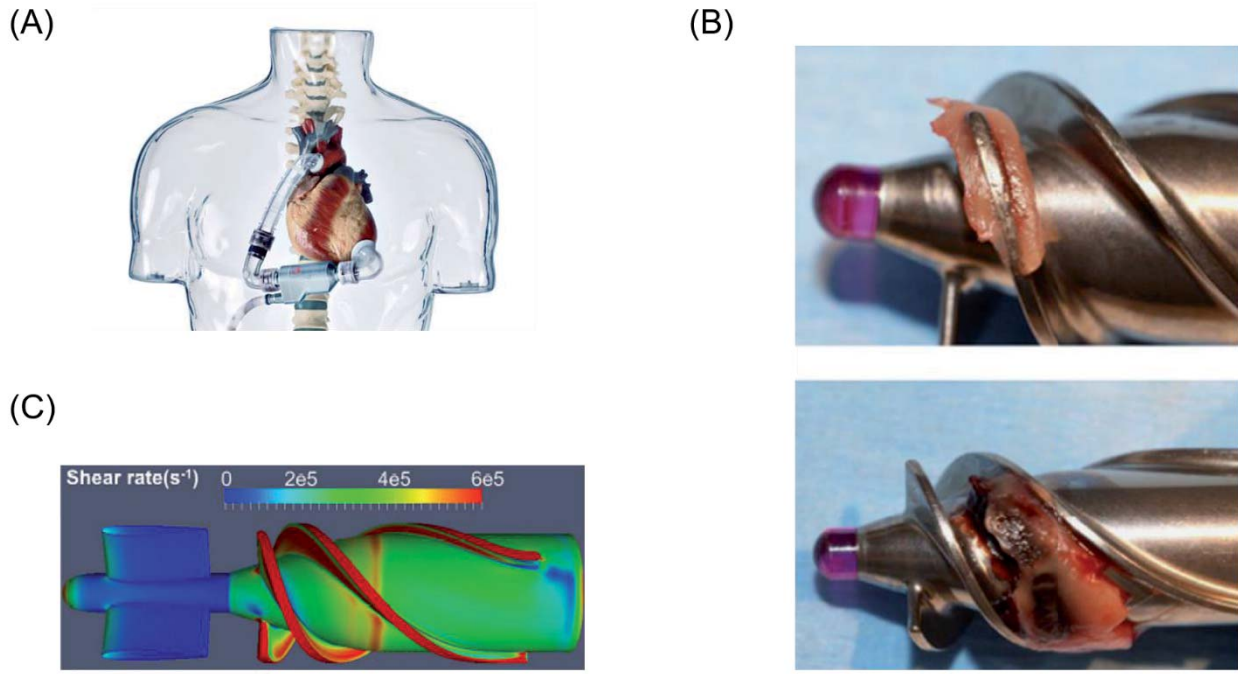

Figure 1. (A) The INCOR® continuous-flow VAD system by Berlin Heart GmbH, which reaches rotation numbers between 5,000-10,000 rotations/min (2-9 l/min), leading to shear strain rates up to maximum 200,000 1/s. The production of this specific model of VAD was terminated at the end of 2018. (B) Examples of thrombosis in the HeartMate II VAD system by Abbott Laboratories (Abbott Park, Illinois, USA). The top image shows a pure fibrin clot resulting from high shear. The bottom images shows a fibrin and blood clot (often observed at areas with lower wall shear stress).[13] This figure was reproduced with permission from ref. 13, Copyright © 2014, Elsevier. (C) An *in silico* modulation of the shear-rates within the HeartMate II VAD.[14] The red areas

represent the areas with high shear, whereas the yellow, green, and blue areas represent the areas with lower wall shear-stress. The blue part on the left of the image represents a flow straightener.[14] The image clearly illustrates the wide variety of shear rates in continuous-flow VAD systems. This figure was reproduced with permission from ref. 14, Copyright © 2016, Nature.

The immobilization of the bioactive anticoagulant heparin (i.e., an active biomolecule) has been widely reported in scientific literature,[15] and the use of this tactic has led to a variety of commercial systems, such as the CARMEDA BioActive Surface (W.L. Gore & Associates) and the Hepamed Heparin Coating (Medtronic plc).[16] When inorganic bioinert coatings are discussed, titanium nitride coatings and diamond like carbon coatings are often considered as the current standard.[10] An alternative to bioactive antithrombogenic coatings and inorganic bioinert coatings are polymeric antifouling surfaces,[17] which effectively prevent the initial adhesion of circulatory proteins and cells, thus lowering the inherent thrombogenicity of the surface. Polyethylene glycol (PEG) has classically been applied as antifouling polymer,[18] but suffers from issues considering instability upon heating in air, and immunological recognition upon repeated exposure.[19] Additionally, a publication by Kizhakkedathu showed that high molecular weight PEG may induce severe red blood cell aggregation, cell toxicity, and dose dependent activation of the blood coagulation, platelets, and complement system.[20] Therefore, there is a need for the development of novel polymeric materials which exhibit similar or superior antifouling properties as PEGylated surface, while showing higher thermal stability, oxidative stability, and biocompatibility under physiological conditions. Recently, polyglycerol has emerged as an alternative to PEG with higher oxidative stability and hemocompatibility.[20, 21]

Polymeric substances can be linked to the surface of blood contacting materials via a wide variety of methods. Traditionally, thiol and siloxane chemistries are applied to modify noble metals

and hydroxylated surfaces,[22] respectively. Alternatively, methods such as Langmuir-Blodgett deposition,[23] layer-by-layer assembly,[24] irradiation-mediated grafting,[25] and electrostatic or hydrophobic adsorption can be utilized for the effective immobilization of functional polymers on a surface.[26] However, most of these methods require specific chemical- and/or physical properties of the substrate or the use of complex machinery, thus limiting their application. Therefore, there is a need for novel facile coating methods that can extend the application of polymeric coatings to the blood-contacting materials that are hard to modify with the current methods.

An interesting alternative for the surface immobilization of polymeric substances is the use of mussel-inspired surface chemistry. Mussels can adhere to virtually every type of substrate, including substrates that are classically defined as non-adhesive (e.g., perfluorinated surfaces). Mussels tether themselves to the surface via so-called byssal threads. At the end of these byssal threads, a mixture of mussel foot proteins (mfps) is excreted in the form of an adhesive plaque (**Figure 2**).[27] This adhesive plaque effectively glues the byssal thread to the substrate, hereby fixating the mussel to the surface (even under wet conditions). A publication by Waite et al. showed the high prevalence of lysine- and 3,4-di-hydroxy-phenylalanine (DOPA) amino acids in the mfps that are excreted close to the plaque-substrate interface (i.e., mainly mfp-3 and mfp-5).[27] DOPA and lysine amino acids contain amine- and catechol-functional groups, respectively. Consequently, Waite et al. hypothesized the importance of the catechol functional group in the substrate-independent adhesion characteristics of mfp-3 and -5.[28] Later works showed the surface-binding of catechol functional groups via a broad range of reversible non-covalent interactions, including the formation of hydrogen bonds, π–π stacking, and the formation of strong but reversible complexes with metal oxides (**Figure 3**).[29] The tethering of catechols to metal oxides via the formation of complex structures was found to be exceptionally strong for Ti-

substrates (ca. 800 pN).[30] The oxidation of catechols leads to the formation of *o*-quinones, which readily react with nucleophiles such as amines and/or thiols to give the respective Michael adducts or Schiff bases. Therefore, the presence of surface-bound amines or thiols leads to the irreversible binding of catechols via the formation of covalent bonds.[29, 30]

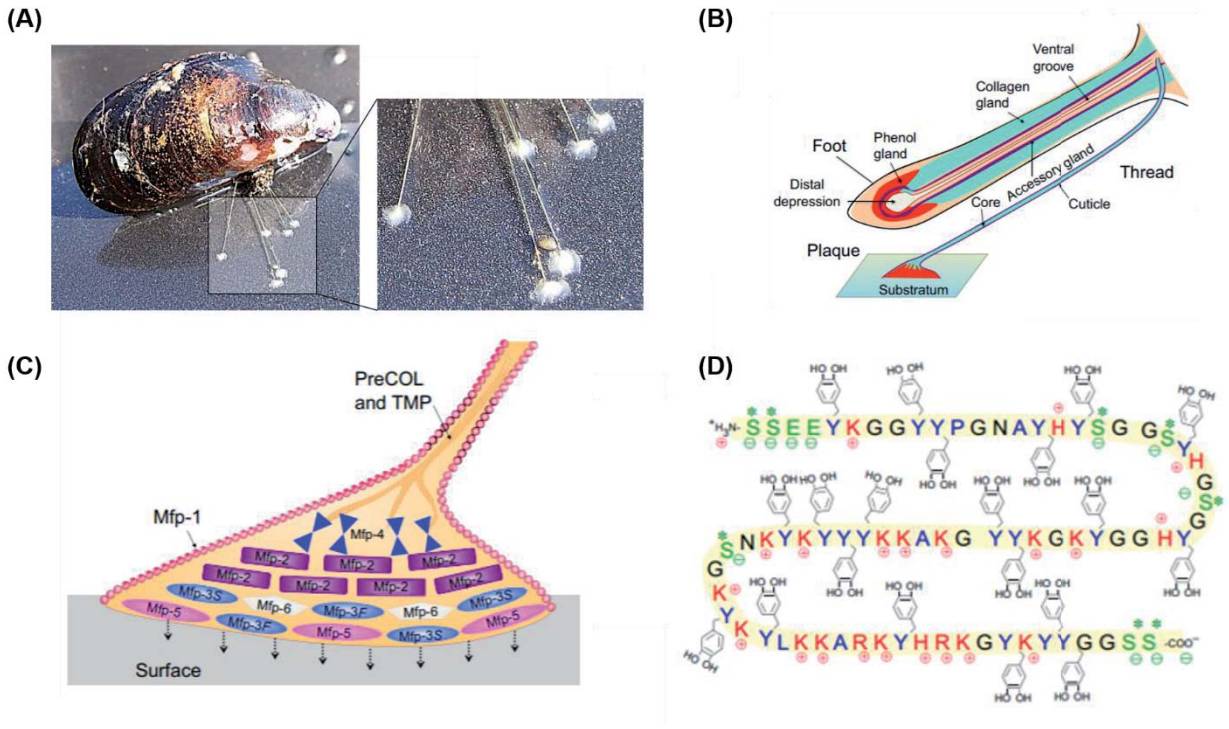

Figure 2. (A) Adhesion of *Mytilus edulis* via multiple byssal threads. The enlargement on the right shows the adhesive plaque (the white structure) in more detail. (B) Schematic representation of the mussel foot, which is responsible for the production and adhesion of the byssal threads to the surface. The foot extends from the protected interior of the mussel's shell upon the adhesion of the mussel to the surface.[27] (C) Graphical representation of the location of the various mfps in the adhesive plaque.[27] (D) Schematic representation of the protein sequence of adhesion-mediating mfp-5 of *Mytilus edulis* (Y = DOPA, K = Lysine, S = Serine, and G = Glycine).[27] Figures (B),

(C), and (D) were reproduced with permission from ref. 27 Copyright © 2017, The Company of Biologists LTD.

In 2007, Messersmith et al. hypothesized that the coexistence of the amine- and catechol-functional groups might contribute to the rapid adhesion of mussels to the substrate.[31] Therefore, they selected dopamine as a small molecule containing both functionalities. When dopamine-containing solutions were buffered to a slightly basic pH (as commonly found in marine environments) the spontaneous formation of polydopamine (PDA) coatings was observed (**Figure 3**).[31] The PDA coatings were found to form on a wide variety of substrates, independently from the physical- or chemical properties of the surfaces.[31] Furthermore, the covalent introduction of amine- or thiol-terminated methoxy-(polyethylene glycol) to these PDA coatings led to the creation of fouling-resistant surfaces.[31] Since Messersmith's initial work, the PDA coating has gained wide interest in the biomedical field (e.g., as a platform for bone and tissue engineering, drug delivery, antimicrobial activity, and patterned cell adhesion).[32] However, the initial method for the formation of PDA suffered from slow coating formation and limited coating thickness. Additionally, the PDA coating appears dark brown/black, making it unsuitable for various optical applications.[31]

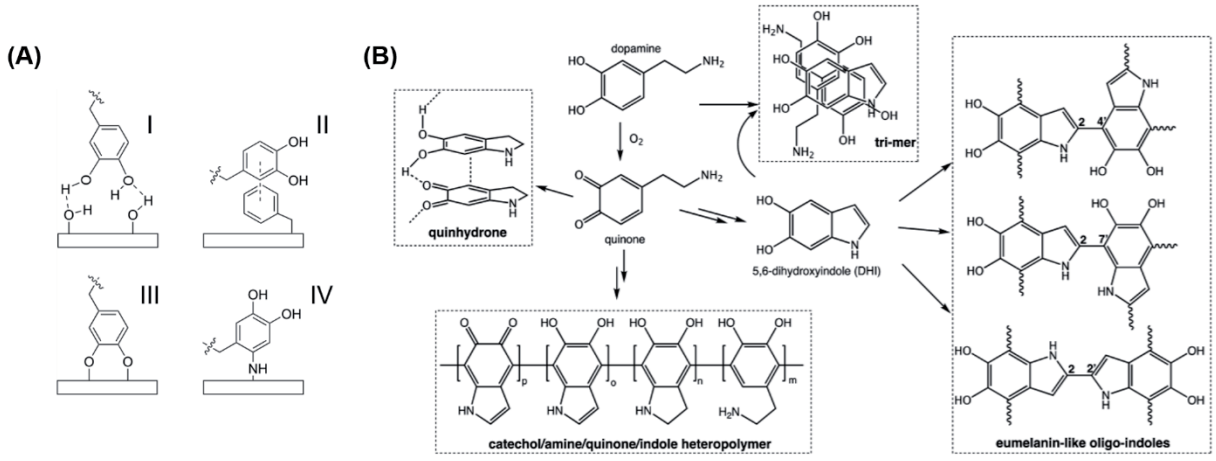

Figure 3. (A) Catechols can adhere to a wide variety of substrates via the formation of (I) hydrogen-bonds, (II) π–π stacking, (III) the formation of complex-structures, and (IV) the formation of Michael-adducts or Schiff bases.[29] (B) A summary of the proposed mechanisms for the formation of PDA. For a detailed review on the polymerization of dopamine, the reader is referred to the cited literature.[33] Figure (B) was adapted with permission from ref. 34 Copyright © 2013, American Chemical Society and ref. 35 Copyright © 2012, John Wiley & Sons.

In 2014, Wei and coworkers developed mussel-inspired dendritic polyglycerol (MI-dPG) (**Figure 4**), which did not only contain the functional groups that are commonly found in mfps, but also mimicked the size and molecular weight of the mfps.[36] Subsequent polymerization of MI-dPG under slightly alkalic oxidizing conditions led to the rapid formation of substrate-independent coatings with controllable coating thicknesses and roughness (thickness up to 4 μm after 4 hours of coating). Additionally, the coating appeared transparent to white, depending on the total thickness of the coating.[36] Earlier projects by our group showed the facile post-functionalization of the MI-dPG coating with nanoparticles and acyl chlorides, for the introduction of tailored surface properties.[37] In the current work, TiO_2 was especially of interest as it is commonly found as the blood contacting material in the interior of VADs.[9] We rescently demonstrated the succesfull formation of highly stable antifouling (i.e., protein and cell repelling) coatings via the introduction of an oligo amine-functionalized block-copolymer of linear polyglycerol (lPG–b–OA_{11}, OA= oligo amine) to MI-dPG-coated TiO_2 substrates (**Figure 4**).[2] It was hypothesized that the application of such an antifouling coating could prevent the primary adhesion of protein from the bloodstream to TiO_2. Consequently, the adhesion and subsequent activation of blood platelets could potentially be prevented. Therefore, the application of a lPG-

functionalized MI-dPG coating in VAD systems could potentially lower the risk of shear- and biomaterial-induced thrombosis.

The current study is a follow-up work of an earlier project by our group, which showed the facile formation, high stability, and antifouling properties of lPG–b–OA_{11}-functionalized MI-dPG on TiO_2 (**Figure 4**).[2] The aim of the current work was to investigate the applicability of this antifouling coating with respect to reduce shear- and biomaterial-induced thrombosis on medically relevant TiO_2. The lPG–b–OA_{11}-functionalized coating was compared to a control system, in which the MI-dPG coating was functionalized with an amine-terminated hydroxy-polyethylene glycol (HO–PEG–NH_2). Both linear polymers were of similar molecular weight (ca. 10 kDa), but varied in the amount of surface binding groups (i.e., multivalent surface binding via multiple amine groups for lPG–b–OA_{11} versus monovalent binding via a single amine group for HO–PEG–NH_2) (**Figure 4**).[2] Initially, the cytotoxicity of the relevant polymers was investigated towards two cell types. Subsequently, the proliferation, adhesion, and viability of these cells were investigated on bare TiO_2 substrate, the MI-dPG coating, and the MI-dPG coating post-functionalized with lPG–b–OA_{11} or HO–PEG–NH_2. Next, the complement activating properties of the various coatings were studied. Most importantly, the adhesion and activation of blood platelets were studied on the various substrates under static and flow conditions. Finally, the applicability of MI-dPG as a coating material for VADs was investigated. A prototype VAD systems was coated with MI-dPG under flow conditions, and subsequently the coating was visualized via the immobilization of a commercially available amine-functionalized fluorophore.

Results and Discussion

The investigated coatings consisted of MI-dPG (surface **1**) post-functionalized with either lPG–b–OA_{11} (surface **2**) or HO–PEG–NH_2 (surface **3**) (**Figure 4**). As substrate material, glass coated with a transparent TiO_2-layer (ca. 30 nm) was utilized (see **Section 1.2.** of the Electronic Supplementary Information (ESI)). The MI-dPG and lPG–b–OA_{11} polymers were synthesized according to methods that were published earlier by our group.[2] In brief, MI-dPG was synthesized in a four step synthesis, starting from dendritic polyglycerol (dPG). First, 100% of the hydroxyl functional groups of the dPG scaffold were transformed to amines via mesylation, azidation, and subsequent reduction of the azide groups. Next, 40% of these amines were functionalized with catechols (**Figure 4**).[37a] Under basic oxidizing conditions, the MI-dPG polymer can undergo crosslinking reactions via the formation of Michael-adducts or Schiff bases between the amine- and catechol-functional groups of adjacent MI-dPG polymers. A previous study by our group showed that the polymerization of MI-dPG leads to the formation of aggregates in solution, which form the MI-dPG coating via a precipitation and aggregation mechanism.[37a] The binding of the MI-dPG coating to the substrate occurs through the versatile binding properties of its catechol moieties (**Figure**s **3** and **4**). Another study of our group has shown the effective formation of MI-dPG coatings on a broad range of substrates.[36] The lPG–b–OA_{11} block-copolymer was synthesized in a three-step synthesis, starting with the synthesis of a block-copolymer of ethoxyethyl glycidyl ether (EEGE) and allyl glycidyl ether (AGE), utilizing a modified version of a method that was earlier published by Gervais et al.[2, 38] Subsequently, the EEGE–b–AGE block-copolymer was acetal deprotected, transforming the EEGE-block to lPG. Finally, the lPG–b–AGE polymer was functionalized with amine-functional groups, giving the lPG–b–OA_{11} block-copolymer (**Figure 4**).[2] lPG–b–OA_{11} was subsequently immobilized on the MI-dPG coating utilizing a straight-

forward dip-coating procedure under basic oxidizing conditions (i.e., lPG–b–OA_{11} was bound to the MI-dPG coating via the formation of Michael-adducts and Schiff bases).[2] In addition, a PEG-based control coating was established by incubating the MI-dPG coating with a solution of commercially available HO–PEG–NH_2 (**Figure 4**).[2] For a more detailed description of the synthesis of the lPG–b–OA_{11} and MI-dPG polymers, the formation/stability of the various coatings, and the antifouling characteristics of the lPG–b–OA_{11} functionalized MI-dPG coating, the reader is referred to the cited literature.[2]

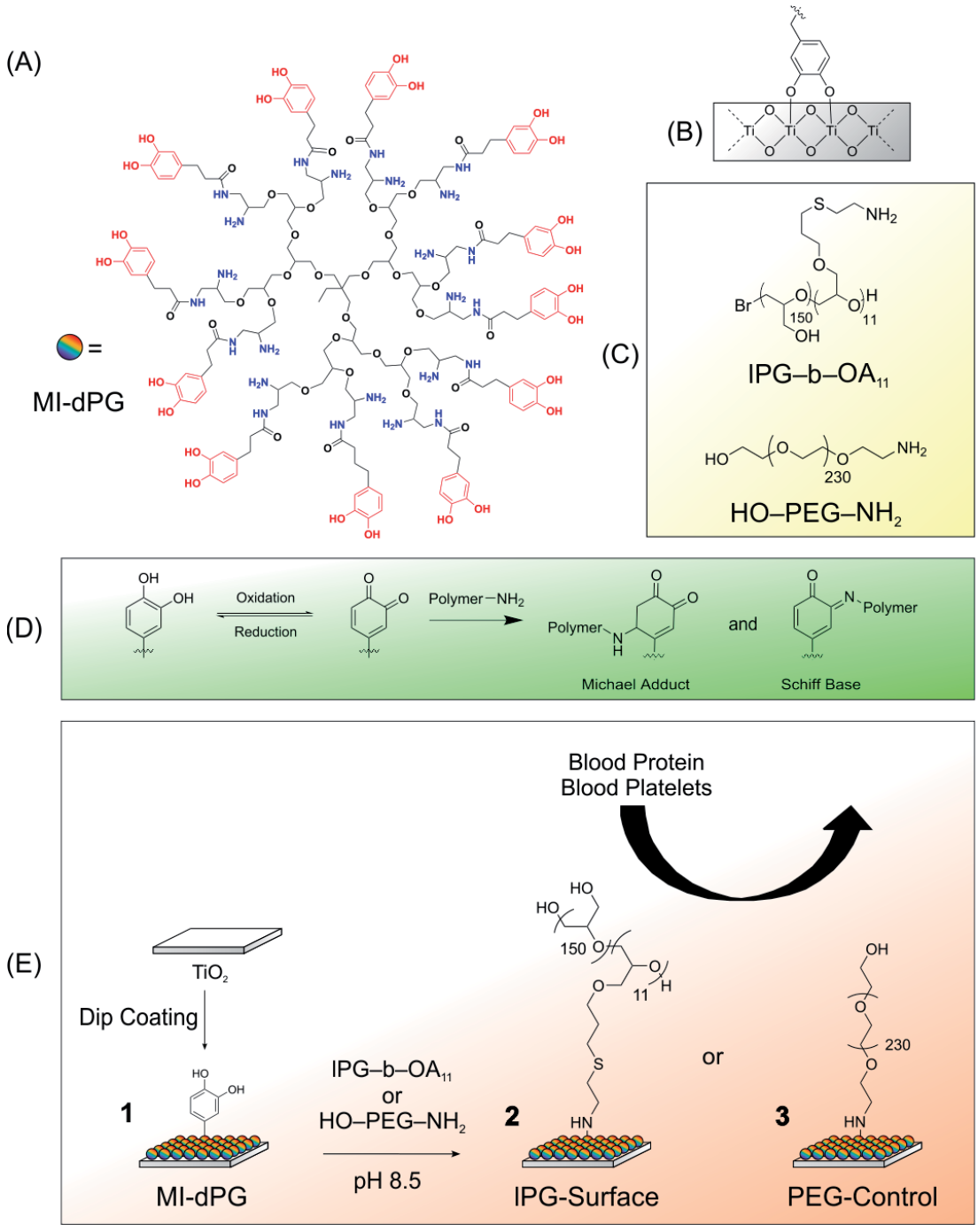

Figure 4. (A) The molecular structure of MI-dPG. The shown structure is an idealized molecular structure; the amount of the glycerol monomers in the core (in black) varies with the size of the polymer. The dPG-core size used in this work: M_n: 12 kDa and PDI: 1.3. Furthermore, the dPG-

core shows up to 60% of branching.[39] (B) The proposed coordination for the binding of the catechol moieties to the TiO_2 surface.[40] (C) The molecular structure of lPG–b–OA_{11} and HO–PEG–NH_2. (D) Catechols readily react with amine- (and/or thiol-) functionalized polymers, giving the Schiff base and Michael addition products. Via the depicted chemistry, the MI-dPG coating was crosslinked and post-functionalized with lPG–b–OA_{11} or HO–PEG–NH_2 to give surfaces **2** or **3**, respectively. (E) A schematic display of the functional surfaces **1**, **2**, and **3**.

Cell Adhesion and Proliferation Tests

The proliferation and adhesion of human alveolar basal epithelial carcinoma cells (A549) and chicken fibroblast cells (DF-1) was investigated on the various coatings, in order to assess the biocompatibility of the substrates to a broad range of cell types. The proliferation of (for the VAD-system more relevant) human umbilical vein endothelial cells (HUVEC) on bare TiO_2 and surfaces **1**, **2**, and **3** was studied in detail in an earlier project of our group.[2] It is important to notice that the coatings that were studied in this work were developed as blood-contacting materials, i.e., the coatings would not be exposed to any sort of tissue during their application in VAD systems. Nevertheless, it was important that the coatings showed antifouling and cell-repelling properties while not being toxic to (any type of) cells, as the adhesion (and subsequent proliferation) of cells from the bloodstream to the VAD's interior could potentially lead to major complications.

Cell adhesion and proliferation was assessed by directly seeding the cells onto the bare TiO_2 substrate and surfaces **1**, **2**, and **3**. After 24 h of culturing, the cells were stained with a commercial LIVE/DEAD™ cell staining kit. Analysis of the stained cells was achieved utilizing a fluorescence microscope and the Java-based, image-processing program "ImageJ" (the quantification process is described in **Figure S1** and **Section 1.8.** of the ESI). The adhesion and

proliferation of the cells were also studied in the presence of high concentrations of the dissolved lPG–b–OA_{11} and HO–PEG–NH_2 polymers. For this, the A549 and DF-1 cells were cultured on tissue culture polystyrene (TCPS) for 24 h. Subsequently, the cell medium was exchanged for medium containing dissolved lPG–b–OA_{11} or HO–PEG–NH_2 at 10 mg/ml. After another 24 h of cell culturing, the cells were stained and the cell number, cellular morphology, and overall cell viability were quantified. As a negative control, the cells were incubated with normal cell medium on TCPS. The morphology of the cells was reported as a normalized shape factor that describes the circularity of the adherent cells. Cell circularity is often used as a parameter describing the adhesion of cells: fully circular cells (i.e., cells with a shape factor of 1) do not adhere, whereas spread-out cells (i.e., cells with low shape factors) do adhere to the surface.

On the TCPS control, high cell numbers of both cell types were observed in comparison to the other tested substrates (**Figures 5** and **6** and **Table S1** of the ESI). Furthermore, the cells were mainly observed in their spread-out adherent state (**Figures 5** and **6** and **Table S1** of the ESI). When the cells were cultured on TPCS in the presence of dissolved lPG–b–OA_{11}, a significant reduction in the cell number was observed for both the A549 (59% reduction in respect to TCPS) and DF-1 cells (78% reduction in respect to TCPS) (**Figures 5** and **6** and **Table S1** of the ESI). Furthermore, the DF-1 cells showed an increased circularity in respect to the bare TCPS substrate, which indicated that the cells adhered less well to TCPS in the presence of lPG–b–OA_{11} (**Figures 5** and **6** and **Table S1** of the ESI). The A549 cells did only show a minor nonsignificant increase in their circularity, indicating that the adhesion of the cells was only slightly reduced by the presence of lPG–b–OA_{11} (**Figures 5** and **6** and **Table S1** of the ESI). When the cell numbers of the A549 and DF-1 cells were quantified on TCPS in the presence of dissolved HO–PEG–NH_2, strong reductions in the cell numbers of the A549 (59% reduction in respect to TCPS) and DF-1

cells (73% reduction in respect to TCPS) were observed. However, incubation with HO–PEG–NH_2 did not lead to significant changes in the cell circularities of both cell types, in respect to the bare TCPS substrate (**Figures 5** and **6** and **Table S1** of the ESI). The observed reductions in the cell adhesion were explained by the electrostatic binding of the positively charged amines of the lPG–b–OA_{11} and HO–PEG–NH_2 polymers to the negatively charged TCPS surface,[41] which led to the formation of a surface hydration layer that functioned as a physical barrier for the prevention of cell adhesion.[42] As a result, reduced cell numbers were observed for TCPS in the presence of dissolved lPG–b–OA_{11} or HO–PEG–NH_2. Furthermore, electrostatic immobilization of lPG–b–OA_{11} on the TCPS substrate led to increased cell circularity for both cell types (i.e., reduced cell adhesion), which was explained by the antifouling surface properties of the lPG–b–OA_{11} monolayer.[17b] The stability of the lPG–b–OA_{11} monolayer might have resulted from multivalent electrostatic interactions between the amine groups of the OA-block of lPG–b–OA_{11} and the TCPS surface. For the TiO_2 substrate, a significant reduction in the cell number was observed in respect to the bare TCPS substrate for both cell types (39% reduction for both cell types) (**Figures 5** and **6** and **Table S1** of the ESI). Additionally, the circularity of the DF-1 cells significantly increased in respect to the TCPS substrate. A minor nonsignificant increase in the circularity was observed for the A549 cells on TiO_2 when compared to the TCPS substrate (**Figures 5** and **6** and **Table S1** of the ESI). For surface **1**, a significant increase in the cell number of both cell types was observed in respect to TiO_2 (58% increase for the A549 cells and 71% increase for the DF-1 cells) (**Figures 5** and **6** and **Table S1** of the ESI). Additionally, the circularity of both cell types clearly increased on surface **1** in respect to the bare TiO_2 substrate (**Figures 5** and **6** and **Table S1** of the ESI). Although higher cell numbers were observed, analysis of the cell morphology indicated that the cells adhered less well on surface **1** than on the bare TiO_2 substrate, which was explained by the

increased hydrophilic character of surface **1** in comparison to bare TiO_2. For surface **2**, a significant decrease in the cell number of both cell types was observed in respect to surface **1** (43% reduction for the A549 cells and 53% reduction for the DF-1 cells) (**Figures 5** and **6** and **Table S1** of the ESI). Furthermore, the circularity of both cell types increased on surface **2** in respect to surface **1** (**Figures 5** and **6** and **Table S1** of the ESI). The circularity observed for surface **2** was the highest of all investigated substrates, indicating that surface **2** was the most effective coating for the prevention of cell adhesion. The non-adhesion of the cells to surface **2** was in line with an earlier work by our group, which showed the antifouling properties of surface **2**.[2] The non-adherent behavior of the cells was explained by the formation of a surface hydration layer, which formed a physical barrier that effectively prevented the adhesion of the A549 and DF-1 cells.[42] For surface **3**, a slight but nonsignificant decrease in the cell number of both cell types was observed in respect to surface **1** (10% reduction for the A549 cells and 7% reduction for the DF-1 cells) (**Figures 5** and **6** and **Table S1** of the ESI). Furthermore, the circularity of both cell types clearly decreased on surface **3** in respect to surface **1**, indicating improved adhesion of the cells to the surface (**Figures 5** and **6** and **Table S1** of the ESI). These results were unexpected, as the introduction of HO–PEG–NH_2 was supposed to introduce antifouling properties to the surface.[18] These findings were explained by suboptimal grafting of the HO–PEG–NH_2 polymer to surface **1**, as a result from the use of high molecular weight PEG with a single anchoring amine-group.[2, 43] As a result, the sufficient formation of a stable surface hydration layer might have not occurred, resulting in the adhesion of the A549 and DF-1 cells.[42] Further optimization of surface **3** (e.g., optimization of the chain length and surface density of HO–PEG–NH_2) might lead to coatings with antifouling properties that are superior to those of surface **3**. However, optimization of the PEG-based system was beyond the scope of the current investigation.

Next, the cell viability at the surface was investigated via LIVE/DEAD™ cell staining. The total viability of the adherent cells was determined by dividing the amount of living cells by the total amount of cells that were observed on the surface (**Figures 5** and **6** and **Table S1** of the ESI). High cell viability (> 95%) was observed in all cases. Only for the DF-1 cells on TCPS in the presence of dissolved lPG–b–OA_{11} (10 mg/ml) a slightly reduced cell viability (74.1 ± 11.3%) was observed (**Figure S4** of the ESI). This observation was explained by the presence of free amines in the OA-block of lPG–b–OA_{11}. Similar cytotoxic effects have also been observed for other amine-containing polymeric structures.[44] However, it has to be noticed that lPG–b–OA_{11} in its bound form (i.e., surface **2**) did not reduce cell viabilities at the surface for the both cell types (**Figure S4** and **Table S1** of the ESI). Besides, no reduced cell viability was observed for the A549 cells on TPCS in the presence of dissolved lPG–b–OA_{11} (10 mg/ml), indicating that the different cell types were not equally sensitive to lPG–b–OA_{11}.

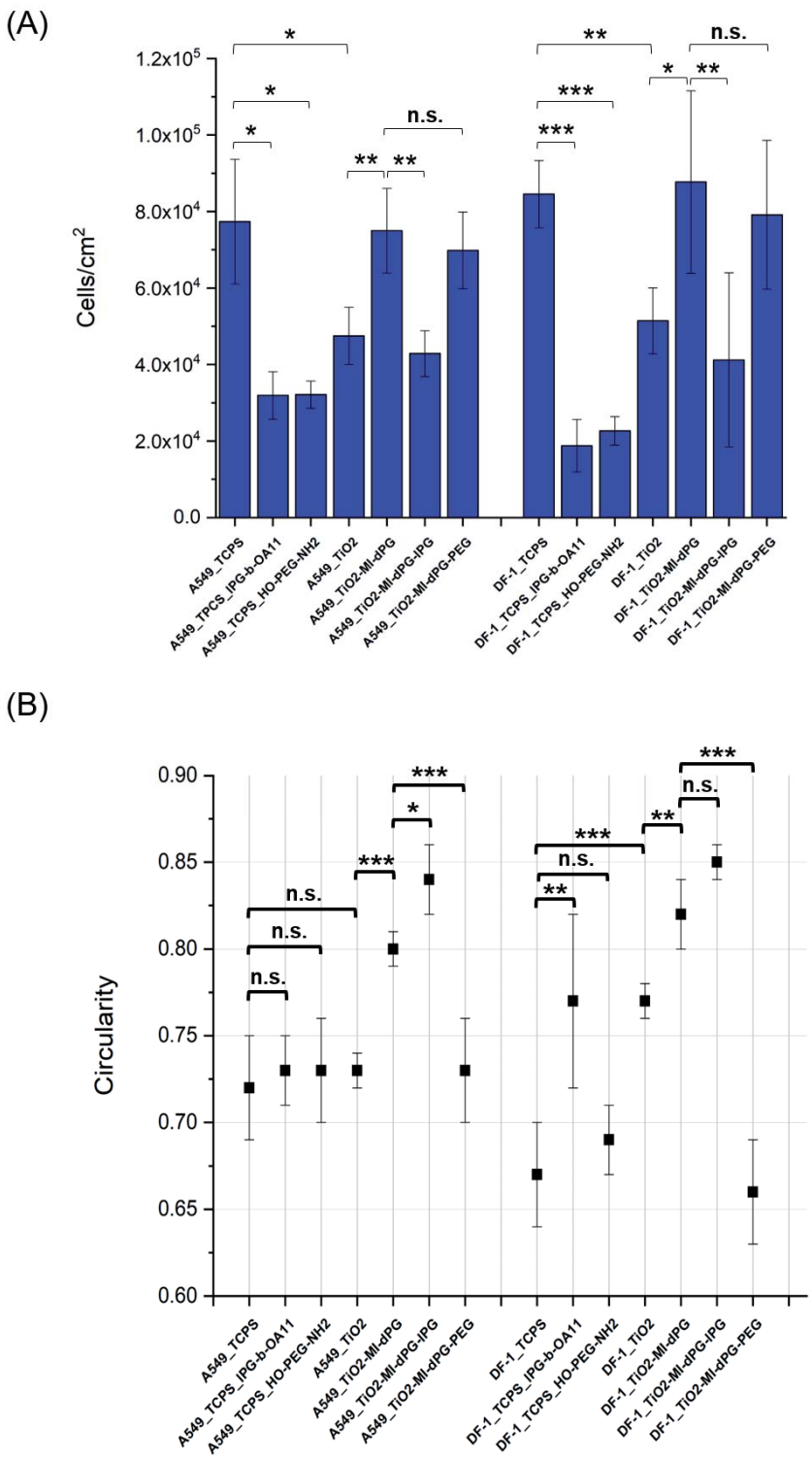

Figure 5. (A) A graphical representation of the cell numbers on the various coatings. The error bars represent the standard deviation from the mean. The amount of cells was determined from 3

images per coating type. (B) A graphical representation of the circularity of the cells on the various coatings. The circularity was determined from minimal 3 images per coating type, while analyzing minimal 20 cells per image. For the morphology analysis of the A549 and DF-1 cells on surface **2** and on TCPS incubated with lPG–b–OA_{11} a minimum of 5 cells per image was analyzed. The error bars represents the standard deviation from the mean, n.s. = not significant. * $p \leq 0.05$, ** $p \leq 0.01$, *** $p \leq 0.001$. The p-values were calculated utilizing a 2-tailed T-test under the assumption of equal variance.

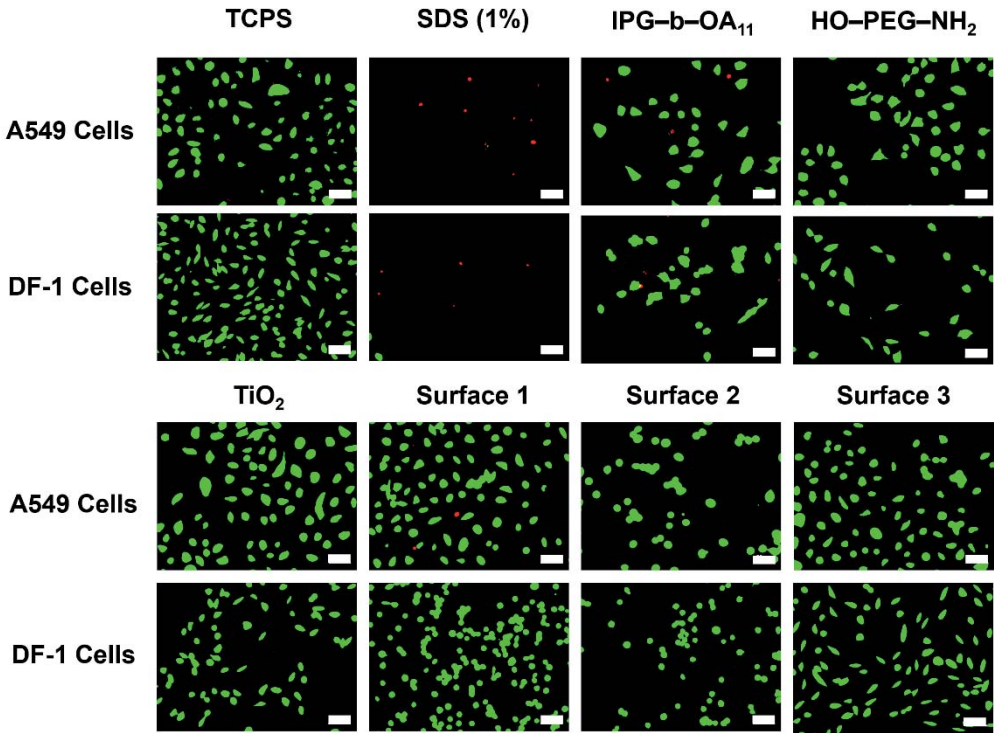

Figure 6. LIVE/DEAD™ Staining of A549 and DF-1 cells on the various substrates. Alive cells appear in green whereas dead cells appear in red. The scale bars represent 50 µm. Incubation of the cells on TCPS showed the normal growth and spreading of live cells, whereas dead cells were observed on TCPS that was incubated with medium that contained 1 wt% sodium dodecyl sulfate

(SDS). Incubation with lPG–b–OA_{11} (10 mg/ml) led to reduced cell viability for the DF-1 cells, whereas incubation with the HO–PEG–NH_2 (10 mg/ml) did not affect the cell viability on the TCPS surface. Furthermore, no reduced cell viability was observed for the A549 and DF-1 cells on the TiO_2 substrate and surfaces **1**, **2**, and **3**.

Cytotoxicity Testing

LIVE/DEAD™ staining can only quantify toxic effects directly at the surface. Therefore, the concentration-dependent cytotoxicity of dissolved lPG–b–OA_{11} and HO–PEG–NH_2 was assessed using a commercially available cell counting kit-8 (CCK-8), which is a sensitive colorimetric assay for the quantification of viable cells. The tests were performed by culturing A549 and DF-1 cells for 24 h on TCPS in cell medium that contained the respective polymers at various concentrations (0.08 - 10 mg/ml). Subsequently, the cell viability in the medium was quantified (**Figure S5** of the ESI). No cytotoxicity (i.e., a cell viability of > 80%) was observed in case of the A549 cells for lPG–b–OA_{11} concentrations up till 5 mg/ml (**Figure S5** of the ESI). However, clearly reduced cell viability (44.2 ± 3.2%) was observed for high lPG–b–OA_{11} concentrations (10 mg/ml) (**Figure S5** of the ESI). In case of the DF-1 cells, no cytotoxicity was observed up till lPG–b–OA_{11} concentrations of 2.5 mg/ml (**Figure S5** of the ESI). However, a slightly decreased cell viability was observed for the DF-1 cells at a lPG–b–OA_{11} concentration of 5 mg/ml (63.0 ± 3.4% viability), and for higher concentrations a further reduction of the cell viability was observed (41.4 ± 5.8% viability for lPG–b–OA_{11} at 10 mg/ml) (**Figure S5** of the ESI). Again, the reduced cell viability was explained by the presence of free amines in the OA-block of lPG–b–OA_{11}.[44] In contrast, HO–PEG–NH_2 did not show any cytotoxicity in both cell types up to concentrations of 10 mg/ml, which

was explained by the biocompatible character of PEG and the low prevalence of free amines in the polymer chains.

An earlier work of our group showed the high stability of surface **2** in both phosphate-buffered saline (PBS) (10 mM, pH 7.4) and aqueous SDS (1 wt%) for at least one month at room temperature.[2] Besides, only relatively low concentrations of lPG–b–OA_{11} are required (i.e., 1 mg/ml) for the creation of surface **2** from surface **1**. Therefore, it is highly unlikely that surface **2** would release sufficient (if any) lPG–b–OA_{11} to elevate local concentrations of the unbound polymer until a point of cytotoxicity. Additionally, after 24 h of cell culturing no cytotoxicity was observed via LIVE/DEAD™ cell staining in case of surface **2** for both cell lines, furthermore indicating the biocompatibility of the lPG–b–OA_{11}-functionalized MI-dPG coating. The combined cytotoxicity and cell proliferation/adhesion data showed the biocompatibility of surfaces **1**, **2**, and **3** and their constituents to the A549 and DF-1 cells. Furthermore, the cell repelling properties of surface **2** were clearly displayed.

Substrate-Induced Complement Activation

Besides thrombogenicity, blood-related complement activation constitutes another important aspect in blood compatibility.[15, 45] Therefore, the complement activation was assessed by measuring the level of anaphylatoxin C5a in platelet rich plasma (PRP) that was exposed to the TiO_2-substrate or surfaces **1**, **2**, or **3**, using a commercially available enzyme-linked immunosorbent assay (ELISA). The tests were performed with full Ti-substrates (covered with a natural TiO_2-layer), as glass is known to trigger the activation of the complement system.[46] Observations showed slightly lower C5a levels in the PRP-supernatant of surface **3** when compared to surface **2**, after 2, 3, 4, and 5 h of incubation. Nevertheless, the C5a levels observed for the PRP on surface **2** were similar (or lower) to the levels observed for the PRP on TiO_2, at t =

3 h (1.50 ± 0.06 ng/ml for TiO_2 and 1.45 ± 0.08 ng/ml for surface **2**), t = 4 h (1.67 ± 0.05 ng/ml for TiO_2 and 1.40 ± 0.06 ng/ml for surface **2**), and t = 5 h (1.61 ± 0.08 ng/ml for TiO_2 and 1.53 ± 0.09 ng/ml for surface **2**) (**Table S2** and **Figure S6** of the ESI). When the C5a levels at t = 5 h of the PRP-supernatant of TiO_2 and surfaces **1**, **2**, and **3** were compared to PRP in which complement activation was triggered by adding zymosan from *Saccharomyces cerevisiae* (positive control), lower C5a-levels were clearly observed for all substrates (**Table S2** and **Figure S6** of the ESI). However, compared to non-activated PRP (negative control), all substrates showed a slight elevation of the C5a levels (**Table S2** and **Figure S6** of the ESI). Still, the results showed only minor variation between the C5a levels in the PRP-supernatant of TiO_2 and surfaces **1**, **2**, and **3**, even after 5 h of incubation, indicating that the coatings showed similar (or even slightly better) complement compatibility as the full Ti substrates (**Table S2** and **Figure S6** of the ESI).

Substrate-Induced Platelet Activation

The thrombogenicity of the biomaterials was assessed by investigating the degree of the platelet deposition on the various substrates and by assessing the morphology of the adherent blood platelets by means of scanning electron microscopy (SEM). As whole blood contains many other types of blood cells, the tests were performed with PRP, which only contains blood platelets and the soluble blood factors. Platelets change their shape from spherical to stellate appearance upon activation (finally resulting in the formation of platelet aggregates), which can be monitored by means of SEM.[47] Many investigations have been focused on biomaterial-induced activation of blood platelets. However, most of these studies did not consider the time-dependent accumulation of pro-thrombogenic protein on the surface of the biomaterial, prior to platelet adhesion and activation. As the long-term fate of the development such a protein corona is hard to determine *in*

vitro, the TiO_2-substrate and surfaces **1**, **2**, and **3** were incubated with fibrinogen from human plasma (Fib) as a pro-thrombogenic agent, prior to the platelet adhesion experiments. Fib is considered the main protein promoting the adhesion of platelets to biomaterials under low shear conditions.[48] In this way, the long-term aggregation of pro-thrombogenic protein on the various substrates was simulated. From now on, the Fib-incubated substrates will be referred to as "surface **X (Fib)**", whereas the non-Fib-incubated substrates will be denoted as "surface **X**" (with **X** = the TiO_2 substrate or surface **1**, **2**, or **3**). Analysis of TiO_2 **(Fib)** and surface **1 (Fib)** clearly showed the formation of large aggregates of activated platelets after 3 h incubation with PRP at 37 °C (**Figure 7**). In contrast, on surface **2 (Fib)** the platelets were mainly found in their inactivated spherical shape, which was explained by the reduced degradation of Fib as a result of the high presence of –OH moieties at the surface.[48] Furthermore, the overall number of platelets appeared to be lower on surface **2 (Fib)** than on the other surfaces. For surface **3 (Fib)**, the results varied, and the platelets were found in both activated and inactivated form. Nevertheless, fewer platelets seemed to appear on surface **3 (Fib)** than on the TiO_2-substrate and surface **1 (Fib)**. The overall number of platelets on the surface is often used to indicate the thrombogenicity of the surface.[49] However, in this work the platelets merged in their final stage of activation. Therefore, exact platelet quantification was challenging (and therefore considered inaccurate) when performed by SEM.

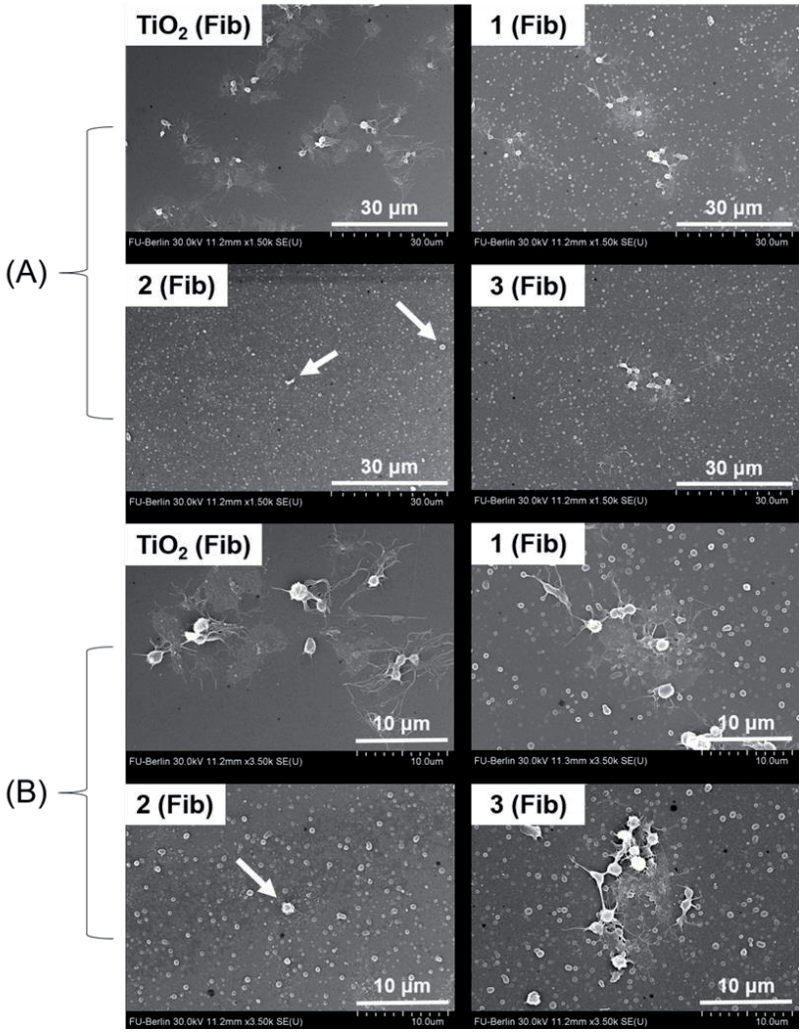

Figure 7. (A) SEM images of the TiO_2-substrate **(Fib)**, and surfaces **1 (Fib)**, **2 (Fib)**, and **3 (Fib)** after incubation with PRP, at an enlargement of 1,500x. (B) SEM images of the same surfaces at an enlargement of 3,500x. Strong activation and platelet spreading was observed on the TiO_2-substrate **(Fib)** and surface **1 (Fib)**. Surface **2 (Fib)** showed almost no adhesion of platelets. Additionally, the settled platelets were mainly found in their inactive, spherical state. On surface **3 (Fib)**, fewer platelets were observed than on the TiO_2-substrate **(Fib)** and surface **1 (Fib)**. Nevertheless, the number of platelets seemed higher for surface **3 (Fib)** than for surface **2 (Fib)**.

Furthermore, many of the platelets observed on surface **3 (Fib)** appeared in their activated morphology.

Platelet Adhesion in the Stagnation-Point Flow Model

In order to perform *in vitro* quantitative monitoring of platelet adhesion under variable wall shear conditions, Affeld and coworkers developed the stagnation-point flow model (**Figure S2** of the ESI).[8b, 50] The stagnation-point flow model was developed to mimic the blood flow at the bifurcations of larger blood vessels, and therefore it assesses the adhesion of platelets under clinically relevant wall shear rates. The stagnation-point flow model enables visualization of platelet adhesion at wall shear stresses from 0-180 1/s in a single measurement, by using a custom-made flow chamber, a fluorescence-inverted microscope, and blood containing fluorescently labeled platelets (**Figure 8**). To investigate platelet adhesion to the TiO_2-substrate and surfaces **1**, **2**, and **3** in the stagnation-point flow model, glass cover slips were coated with a transparent TiO_2 layer by means of PVD (see **Section 1.2.** of the ESI). Subsequently, these cover slips were functionalized to give surfaces **1**, **2**, and **3**, respectively. Collagen-coated glass substrates were used as positive control to confirm the clotting ability of the blood. Besides, coverslips that were spin-coated with polyurethane (PU) or polydimethylsiloxane (PDMS) were tested as medically relevant reference materials.[51] Substrates within one sequence, (i.e., TiO_2, PU, PDMS, collagen, and surfaces **1**, **2**, and **3**), were always performed with blood originating from the same donor, ensuring that the observations resulted from the different coating types, rather than from donor-related blood variations. In total, 9 sequences were performed, i.e., every substrate was tested with blood from 9 different donors. Furthermore, the order in which the substrates were measured was varied in such a manner, that it was ensured that the observations resulted from the coating's

surface properties, rather than from time-dependent alterations of the blood. Although large variations are common in platelet adhesion experiments,[8b] a clear reduction in platelet adhesion was observed from collagen (the adhesion to collagen was set to 100%) > PDMS (93.4 ± 11.0% adhesion respective to collagen) > PU (80.9 ± 17.2% adhesion respective to collagen) > surface **3** (71.3 ± 22.7% adhesion respective to collagen) > TiO_2 (60.0 ± 27.0% adhesion respective to collagen) > surface **1** (34.7 ± 16.7% adhesion respective to collagen) > surface **2** (13.6 ± 8.2% adhesion respective to collagen) (**Figure 8** and **Table S3** of the ESI). The highest surface coverage was observed for collagen, which was explained by the high affinity of the platelets' collagen receptors to the collagen substrate.[52] High platelet adsorption was also observed for the PDMS spin-coated substrate, which was explained by the hydrophobic character of this surface.[48, 53] Interestingly, TiO_2-substrate seemed to perform well at first sight. However, single-dispersed platelets were always observed at t = 240 sec (**Figure 8**). When compared to the TiO_2 substrate, higher surface coverage was observed for the PU substrate, which was explained by the more hydrophobic character of PU when compared to the TiO_2 substrate.[48, 53] Surface **1** showed a significant reduction of platelet adhesion in comparison to TiO_2, which was in line with the increased hydrophilic character of the surface.[48, 53] Surface **2** clearly showed the best platelet-repelling properties of all tested substrates, which was explained by the formation of a tightly bound surface water layer that prevented the adhesion of pro-coagulant protein (i.e., Fib and/or von Willebrand factor).[42] Surprisingly, surface **3** showed a relatively high surface coverage with platelets, which potentially resulted from a suboptimal PEG grafting density as a consequence of monovalent grafting of the PEG chains and the use of high molecular weight PEG (**Figure 8**). However, it is expected that optimization of the PEG-chain density on the MI-dPG coating will lead to surfaces that show better antifouling properties than surface **3**.[2, 20, 43]

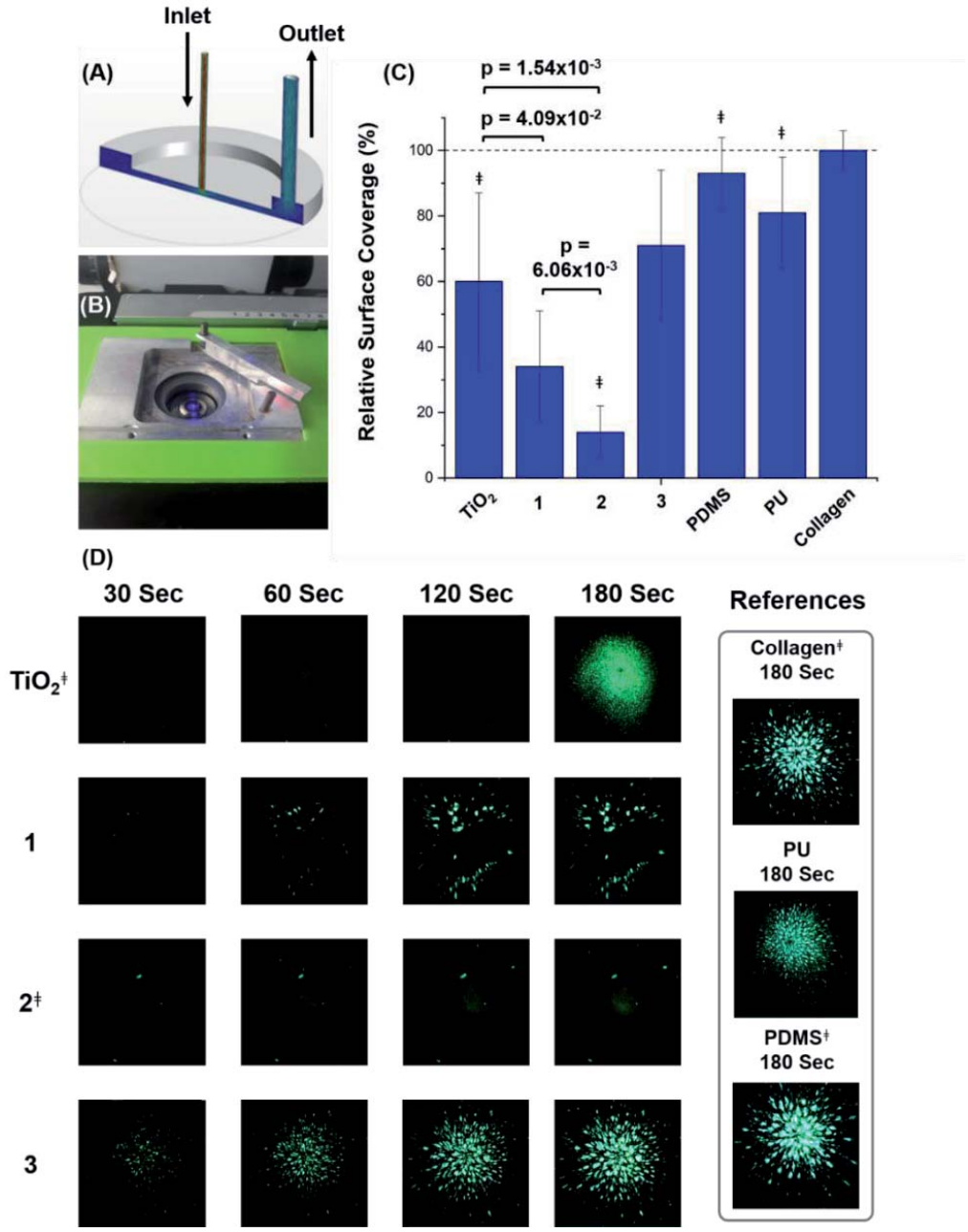

Figure 8. (A) A computational fluid dynamics simulation of the flow within the stagnation-point flow model's flow module. Whole blood is led over the surface via the inlet at the center of the flow module. The blood leaves the system via the outlet at the edge of the flow module. For a more elaborate explanation of the flow module the reader is referred to **Figure S2** of the ESI. (B) The

holder for the flow module on top of the fluorescence microscope. The flow module is placed in the circle-structure. (C) Graphical representation of the relative platelet adhesion in the stagnation-point flow model at t = 180 s. All values shown are relative to the adhesion observed for the collagen positive control (i.e., the adhesion to collagen was set to 100%). The results showed that surface **2** clearly suppressed the adhesion of blood platelets. The error bars represent the standard deviation from the mean. All measurements were performed with n = 9, ǂn = 8. The p-values were calculated using a two-tailed T-test while assuming unequal variance. (D) The fluorescence images obtained from the stagnation-point flow model for the TiO_2-substrate and surfaces **1**, **2**, and **3** at various time points. Additionally, PU and PDMS were also included in the measurements.

Coating Applicability in VADs

To study the applicability of surface **1** on complex 3-dimensional substrates such as VADs, fluorescence studies of surface **1** post-functionalized with a commercially available amine-functionalized fluorophore (tetramethylrhodamine (TAMRA)-amine (5-isomer)) were performed on a prototype VAD that was provided by Berlin Heart GmbH (Berlin, Germany) (**Figure 9**). Optimization of the TAMRA-amine post-functionalization was performed prior to the coating procedure (**Figure S3** of the ESI), in order to prevent false positives in the absence of the MI-dPG coating.

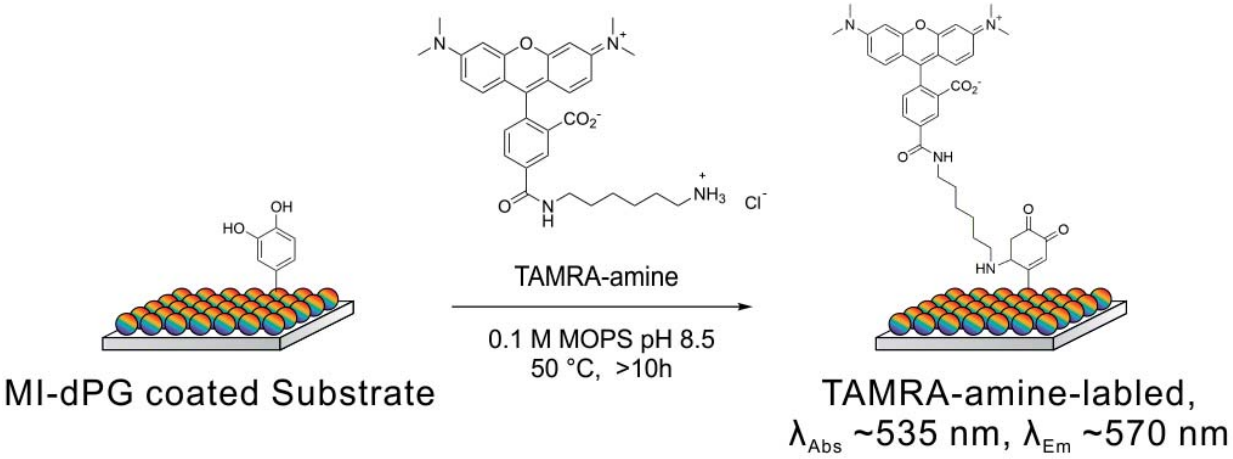

Figure 9. Schematic representation of the functionalization of surface **1** with TAMRA-amine.

Fluorescence studies showed that the VAD prototype was successfully coated under low rotational speed (90 rotations/min) (**Figure 10**). However, the fluorescence seemed more apparent at the edges of the rotor blade. These results were explained by the rotation of the rotor blade during the coating process, which might have led to a locally enhanced transport of MI-dPG and TAMRA-amine to the surface. To obtain a more homogenous distribution of the coating, the functionalization of the rotor blade was performed again under static conditions (i.e., dip coating). However, the fluorescence measurements showed similar results after introduction of the fluorophore to the MI-dPG coating. This observation was explained by the scattering of the incident light by the rounded shapes of the rotor blade. The results illustrated the limitations of fluorescence spectroscopy as a method for the control of the coating's quality. However, the combined results showed the suitability of surface **1** in the on-line coating of VADs, i.e., the complete blood-contacting surface of a VAD was coated with MI-dPG under flow conditions, despite the aggregation and precipitation mechanism that underlies the formation of the MI-dPG coating.[37a] Based on an earlier study by our group, the further functionalization of surface **1** with

lPG–b–OA_{11} will lead to the formation of a highly stable protein- and cell-repelling surface within the VAD system.[2] Furthermore, the current study clearly showed the *in vitro* effectiveness of surface **2** in the reduction of platelet activation and adhesion under static and flow conditions. Therefore, surface **2** shows the potential to reduce biomaterial- and shear-induced thrombosis in VAD systems and other blood-contacting materials.

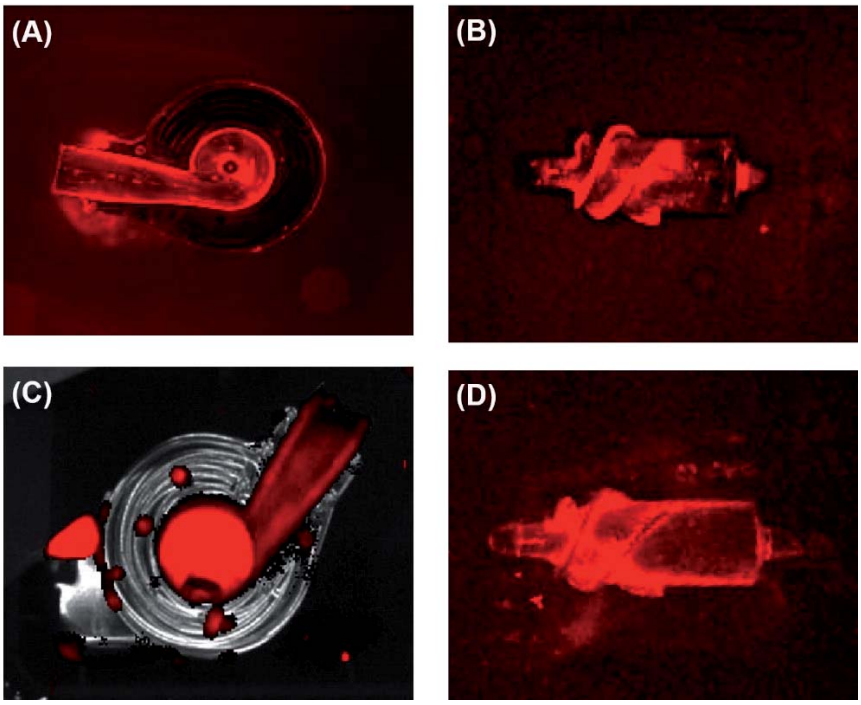

Figure 10. The VAD was MI-dPG coated under flow conditions and subsequently functionalized with TAMRA-amine at 10 µg/ml. (A) The picture shows the top plate of the coated VAD prototype. The illuminated channel represents the blood outlet of the VAD. (B) The rotor blade of the dynamically coated VAD, showing local variations in the fluorescence intensity. (C) The body of the VAD. The top plate shown in (A) is placed on top of this body to close the VAD, whereas

the rotor blade shown in (B) is placed in the illuminated channel shown in (C). It was clearly observed that the blood outlet was successfully coated (right top of (C)). The VAD chamber showed bright fluorescence, which resulted from the TAMRA-amine functionalization of the MI-dPG coating in the VAD. (D) The dip-coated rotor blade after TAMRA-amine functionalization. The fluorescence appeared almost equal to the fluorescence that was observed for the rotor blade that was coated with MI-dPG under flow conditions.

Conclusions

In the current work, the cell and platelet repelling properties of MI-dPG and MI-dPG post-functionalized with lPG–b–OA_{11} or HO–PEG–NH_2 were investigated, in order to prove the applicability of the various coatings in the prevention of biomaterial- and shear-induced thrombosis in continuous-flow ventricular assist devices. When the adhesion and proliferation of adenocarcinomic human alveolar basal epithelial cells and chicken fibroblast cells were studied on the various substrates by fluorescent staining of the live and dead cells, it was clearly observed that the MI-dPG coating post-functionalized with lPG–b–OA_{11} outperformed all other systems considering the rejection of cellular adhesion. These findings were in line with an earlier work by our group, which showed the protein and cell-repelling properties of the lPG–b–OA_{11}-functionalized MI-dPG coating. High viabilities (> 95%) were observed for all coating types. Subsequently, the cytotoxicity of the dissolved lPG–b–OA_{11} and HO–PEG–NH_2 polymers towards adenocarcinomic human alveolar basal epithelial cells and chicken fibroblast cells was investigated in cell culture based experiments, in order to simulate leaching-induced cytotoxicity of these (water soluble) polymers. For the lPG–b–OA_{11} polymer no cytotoxicity was observed until 5 mg/ml and 2.5 mg/ml for the A549 and the DF-1 cells, respectively. For HO–PEG–NH_2, no cytotoxicity was observed until 10 mg/ml for both cell lines. It is important to notice that

leaching of HO–PEG–NH_2 and lPG–b–OA_{11} was not expected, based on the stability data presented in an earlier work of our group.[2] Adenocarcinomic human alveolar basal epithelial cells and chicken fibroblast cells were used in the current study, in order to show the biocompatibility of the tested coatings and their respective constituents to a broad range of cell types. Furthermore, the proliferation and adhesion of medically more relevant human umbilical vein endothelial cells on the various coatings were already investigated in an earlier study by our group.[2] It is important to notice, that in their aimed application, the coatings would not get into contact with any type of tissue (i.e., the coatings were developed as blood-contacting materials for the interior of VADs). Nevertheless, it was important that the coatings would reject cellular adhesion without being toxic to cells, as the adhesion and subsequent proliferation of cells from the bloodstream to the blood-contacting surface of the VAD could potentially lead to major complications.

When the substrate-induced activation of the complement system was analyzed by measuring the C5a levels in platelet rich plasma that had been incubated with the various coatings, no clear increase of C5a was observed in comparison to the bare TiO_2-substrate. Platelet activation tests at near static conditions showed a strong activation of platelets on the fibrinogen-incubated TiO_2 and MI-dPG surfaces. Less platelet activation was observed on (fibrinogen-incubated) MI-dPG post-functionalized with monovalent PEG, and almost no activation was seen on (fibrinogen-incubated) MI-dPG that was post-functionalized lPG–b–OA_{11}. When platelet adhesion from whole blood was investigated in the stagnation-point flow model under defined low shear-rates (0-180 1/s), high platelet adhesion was observed for the collagen-, PDMS-, PU-, and the TiO_2 substrates. The introduction of the MI-dPG coating significantly reduced the number of adherent platelets. The lowest number of platelets was clearly observed on MI-dPG post-functionalized with lPG–b–

OA_{11}. The low adhesion to the lPG–b–OA_{11} post-functionalized MI-dPG coating was explained by the formation of a surface hydration layer that effectively formed a barrier layer that prevented platelet adhesion.[15] Strong adhesion of blood platelets was observed for MI-dPG post-functionalized with HO–PEG–NH_2, which most likely resulted from the use of a high molecular weight PEG and a suboptimal monovalent grafting of the linear polymer.[2, 20, 43] Finally, a VAD was coated with MI-dPG using a circulation system that allowed for the adhesion of MI-dPG while the pump was running at lower rotational speed. Subsequent visualization of the coating was achieved by the post-functionalization of the MI-dPG coating with a commercially available fluorophore. The fluorescence data showed the successful coating of the whole interior of the VAD.

To summarize: the combined results clearly indicated that the MI-dPG coating post-functionalized with lPG–b–OA_{11} showed better antifouling surface properties than TiO_2, MI-dPG, and the MI-dPG coating that was post-functionalized with HO–PEG–NH_2. Furthermore, no cytotoxicity and obvious complement activation were observed for any of the coatings that were topic of the current study. The lPG–b–OA_{11} functionalized MI-dPG coating successfully prevented the activation of blood platelets under static conditions, and furthermore prevented the adhesion of activated blood platelets under medically relevant flow conditions. Additionally, MI-dPG was used to successfully coat a VAD under flow conditions. The combined results identify the lPG–b–OA_{11} functionalized MI-dPG coating as a promising material for the effective reduction of surface blood clots in 3-dimensional, blood-contacting implant devices such as continuous-flow VADs.

Experimental Section

All materials and methods can be found in the ESI.

Acknowledgements

We would kindly like to thank Dr. D. Salz (Fraunhofer IFAM, Bremen) for providing us with the TiO_2-coated glass substrates. Furthermore, we would like to thank the physicians Dr. N. Al Besher and Dr. M. Buhlaiga (Institute for Transfusion medicine, Charité-Universitätsmedizin Berlin, Berlin), for their support considering the blood samples. Besides, we would like to thank Dr. C. Schlaich (Freie Universität Berlin, Berlin) for synthesizing the used MI-dPG. Additionally, we would like to thank S. Zürner, Dr. L. Kaufmann, and Dr. V. Kunz (Berlin Heart GmbH, Berlin) for their technical support considering the VAD prototype. We would also like to thank Dr. P. Winchester and Dr. R. Randriantsilefisoa for proofreading the manuscript. Finally, we would like to acknowledge the assistance of the BioSupraMol core facility (located at the Freie Universität Berlin and supported by the Deutsche Forschungsgemeinschaft) in the characterization of the used polymeric materials.

Received: ((will be filled in by the editorial staff))

Revised: ((will be filled in by the editorial staff))

Published online: ((will be filled in by the editorial staff))

References

[1] M. Saini, Y. Singh, P. Arora, V. Arora, K. Jain, *World Journal of Clinical Cases: WJCC* **2015**, *3*, 52.

[2] M. W. Kulka, I. S. Donskyi, N. Wurzler, D. Salz, Ö. Ozcan, W. E. S. Unger, R. Haag, *ACS Applied Bio Materials* **2019**, *2*, 5749.

[3] E. Wilkins, L. Wilson, K. Wickramasinghe, P. Bhatnagar, J. Leal, R. Luengo-Fernandez, R. Burns, M. Rayner, N. Townsend, *European Cardiovascular Disease Statistics 2017* **2017**.

[4] J. A. Ambrose, R. S. Barua, *Journal of the American College of Cardiology* **2004**, *43*, 1731; b) J. Kochar, J. M. Gaziano, L. Djoussé, *Aging and Disease* **2011**, *2*, 149; c) B. A. Ference, H. N. Ginsberg, I. Graham, K. K. Ray, C. J. Packard, E. Bruckert, R. A. Hegele, R. M. Krauss, F. J. Raal, H. Schunkert, G. F. Watts, J. Borén, S. Fazio, J. D. Horton, L. Masana, S. J. Nicholls, B. G. Nordestgaard, B. van de Sluis, M.-R. Taskinen, L. Tokgözoğlu, U. Landmesser, U. Laufs, O. Wiklund, J. K. Stock, M. J. Chapman, A. L. Catapano, *European Heart Journal* **2017**, *38*, 2459; d) L. Anderson, N. Oldridge, D. R. Thompson, A.-D. Zwisler, K. Rees, N. Martin, R. S. Taylor, *Journal of the American College of Cardiology* **2016**, *67*, 1; e) P. W. Serruys, M.-C. Morice, A. P. Kappetein, A. Colombo, D. R. Holmes, M. J. Mack, E. Ståhle, T. E. Feldman, M. van den Brand, E. J. Bass, N. Van Dyck, K. Leadley, K. D. Dawkins, F. W. Mohr, *New England Journal of Medicine* **2009**, *360*, 961; f) S. K. Mulpuru, M. Madhavan, C. J. McLeod, Y.-M. Cha, P. A. Friedman, *Journal of the American College of Cardiology* **2017**, *69*, 189.

[5] M. M. Givertz, *Circulation* **2011**, *124*, e305.

[6] A. R. de Biasi, K. B. Manning, A. Salemi, *The Journal of Thoracic and Cardiovascular Surgery* **2015**, *149*, 667.

[7] K. Kirklin, D. C. Naftel, F. D. Pagani, R. L. Kormos, L. W. Stevenson, E. D. Blume, M. A. Miller, J. T. Baldwin, J. B. Young, *The Journal of Heart and Lung Transplantation* **2014**, *33*, 555.

[8] a) M. Weber, H. Steinle, S. Golombek, L. Hann, C. Schlensak, H. P. Wendel, M. Avci-Adali, *Frontiers in Bioengineering and Biotechnology* **2018**, *6*, 1; b) K. Affeld, J. Schaller, T. Wölken, T. Krabatsch, U. Kertzscher, *Biointerphases* **2016**, *11*, 029804.

[9] a) T. G. Kim, H. Lee, Y. Jang, T. G. Park, *Biomacromolecules* **2009**, *10*, 1532; b) S. Alibeik, S. Zhu, J. W. Yau, J. I. Weitz, J. L. Brash, *Acta Biomaterialia* **2011**, *7*, 4177; c) J. Lahann, D. Klee, W. Pluester, H. Hoecker, *Biomaterials* **2001**, *22*, 817.

[10] D.-C. Sin, H.-L. Kei, X. Miao, *Expert Review of Medical Devices* **2009**, *6*, 51.

[11] K. Yamazaki, S. Kihara, T. Akimoto, O. Tagusari, A. Kawai, M. Umezu, J. Tomioka, R. L. Kormos, B. P. Griffith, H. Kurosawa, *The Japanese Journal of Thoracic and Cardiovascular Surgery* **2002**, *50*, 461.

[12] a) V. V. Nikolaychik, D. M. Wankowski, M. M. Samet, P. I. Lelkes, *American Society for Artificial Internal Organs Journal* **1996**, *42*, 487; b) T. Scott-Burden, C. L. Tock, J. P. Bosely, F. J. Clubb, S. M. Parnis, J. J. Schwarz, D. A. Engler, O. H. Frazier, S. W. Casscells, *Circulation* **1998**, *10*, 11339.

[13] N. Uriel, J. Han, K. A. Morrison, N. Nahumi, M. Yuzefpolskaya, A. R. Garan, J. Duong, P. C. Colombo, H. Takayama, S. Thomas, Y. Naka, U. P. Jorde, *Journal of Heart and Lung Transplantation* **2014**, *33*, 51.

[14] W. Wu, F. Yang, J. Wu, N. Aubry, M. Massoudi, J. F. Antaki, *Scientific Reports* **2016**, *6*.

[15] C. Cheng, S. Sun, C. Zhao, *Journal of Materials Chemistry B* **2014**, *2*, 7649.

[16] R. Biran, D. Pond, *Advanced Drug Delivery Reviews* **2017**, *112*, 12.

[17] a) M. Amiji, K. Park, *Journal of Biomaterials Science, Polymer Edition* **1993**, *4*, 217; b) M. Weinhart, T. Becherer, N. Schnurbusch, K. Schwibbert, H.-J Kunte, R. Haag, *Advanced Engineering Materials* **2011**, *13*, B501; c) M. Wyszogrodzka, R. Haag, *Biomacromolecules* **2009**, *10*, 1043; d) T. Becher, Q. Wei, P.-L. M. Noeske, I. Grunwald, R. Haag, *Advanced Materials* **2014**, *26*, 2688; e) L. Liu, Q. Liu, A. Singh, *Proteins at Interfaces III State of the Art*, **2012,** *1120*, 661; f) T. Mohan, R. Kargl, K. E. Tradt, M. R. Kulterer, M. Braćić, S. Hribernik, K. Stana-Kleinschek, V. Ribitsch, *Carbohydrate Polymers* **2015**, *116*, 149; g) X. Jin, J. Yuan, J. Shen, *Colloids and Surfaces* **2016**, *145*, 275; h) S. Jiang, Z. Cao, *Advanced Materials* **2010**, *22*, 920; i) A. K. Epstein, T.-S. Wong, R. A. Belisle, E. M. Boggs, J. Aizenberg, *Proceedings of the National Academy of Sciences of the United States of America* **2012**, *109*, 13182.

[18] a) W. R. Gombotz, W. Guanghui, T. A. Horbett, A. S. Hoffman, *Journal of Biomedical Materials Research* **1991**, *25*, 1547; b) L. D. Unsworth, H. Sheardown, J. L. Brash, *Langmuir* **2005**, *21*, 1036; c) K. Prime, G. Whitesides, *Science* **1991**, *252*, 1164; d) L. J. Ho, K. Jindrich, A. J. D., *Journal of Biomedical Materials Research* **1989**, *23*, 351; e) K. L. Prime, G. M. Whitesides, *Journal of the American Chemical Society* **1993**, *115*, 10714.

[19] a) S. Han, C. Kim, D. Kwon, *Polymer* **1997**, *38*, 317; b) A. Judge, K. McClintock, J. R. Phelps, I. MacLachlan, *Molecular Therapy* **2006**, *13*, 328.

[20] M. Imran ul-haq, B.F. Lai, J.N. Kizhakkedathu, *Biomaterials* **2012**, *33*, 9135.

[21] C. Siegers, M. Biesalski, R. Haag, *Chemistry* **2004**, *10*, 2831**.**

[22] a) C. D. Bain, E. B. Troughton, Y. T. Tao, J. Evall, G. M. Whitesides, R. G. Nuzzo, *Journal of the American Chemical Society* **1989,** *111*, 321; b) A. Y. Fadeev, Y. V. Kazakevich, *Langmuir* **2002**, *18*, 2665.

[23] D. Kubies, L. Machová, E. Brynda, J. Lukáš, F. Rypáček, *Journal of Materials Science: Materials in Medicine* **2003**, *14*, 143.

[24] C. Boura, P. Menu, E. Payan, C. Picart, J. C. Voegel, S. Muller, J. F. Stoltz, *Biomaterials* **2003**, *24*, 3521.

[25] P. Petrov, G. Georgiev D. Momekova G. Momekov, C. B. Tsvetanov, *Polymer* **2010**, *51*, 2465.

[26] a) P. Bertrand, A. Jonas, A. Laschewsky, R. Legras, *Macomolecular Rapid Communications* **2000**, *21*, 319; b) C. Freij-Larsson, T. Nylander, P. Jannasch, B. Wesslén, **1996**, *Biomaterials*, *17*, 2199.

[27] J. H. Waite, *The Journal of Experimental Biology* **2017**, *220*, 517.

[28] J. H. Waite, M. L. Tanzer, *Science* **1981**, *212*, 1038.

[29] J. Saiz-Poseu, J. Macebo-Aracil, F. Nador, F. Busqué, D. Ruiz-Molina, *Angewandte Chemie International Edition* **2019**, *58*, 696.

[30] H. Lee, N. F. Scherer, P. B. Messersmith, *PNAS* **2006**, *103*, 12999.

[31] H. Lee, S. M. Dellatore, W. M. Miller, P. B. Messersmith, *Science* **2007**, *318*, 426.

[32] R. Batul, T. Tamanna, A. Khaliq, A. Yu, *Biomaterials Science* **2017**, *5*, 1204.

[33] J. H. Ryu, P. B. Messersmith, H. Lee, *ACS Applied Materials Interfaces* **2018**, *10*, 7523.

[34] J. Liebscher, R. Mrówczyński, H. A. Scheidt, C. Filip, N. D. Hădade, R. Turcu, A. Bende, S. Beck, *Langmuir* **2013**, *29*, 10539.

[35] S. Hong, Y. S. Na, S. Choi, I. T. Song, W. Y. Kim, H. Lee, *Advanced Functional Materials* **2012**, *22*, 4711.

[36] Q. Wei, K. Achazi, H. Liebe, A. Schulz, P.-L. M. Noeske, I. Grunwald, R. Haag, *Angewandte Chemie International Edition* **2014**, *53*, 11650.

[37] a) C. Schlaich, L. Cuellar Camacho, L. Yu, K. Achazi, Q. Wei, R. Haag, *ACS Applied Materials & Interfaces* **2016**, *8*, 29117; b) M. Li, C. Schlaich, M. W. Kulka, I. S. Donskyi, T. Schwerdtle, W. E. Unger, R. Haag, *Journal of Materials Chemistry B* **2019**, *7*, 3438.

[38] M. Gervais, A.-L. Brocas, G. Cendejas, A. Deffieux, S. Carlotti, *Macromolecules* **2010,** *43*, 1778.

[39] A. Sunder, R. Hanselmann, H. Frey, R. Mülhaupt, *Macromolecules* **1999**, *32*, 4240.

[40] S. P. Pujari, L. Scheres, A. T. M. Marcelis, H. Zuilhof, *Angewandte Chemie International Edition* **2014**, *53*, 6322.

[41] I. F. Amarai, A. L. Cordeiro, P. Sampaio, M. A. Barbosa, *Journal of Biomaterials Science, Polymer Edition* **2007**, *18*, 469.

[42] S. Chen, L. Li, C. Zhao, J. Zheng, *Polymer* **2010**, *51*, 5283.

[43] S. J. Sofia, V. Premnath, E. W. Merrill, *Macromolecules* **1998**, *31*, 5059.

[44] D. Fisher, Y. Li, B. Ahlemeyer, J. Krieglstein, T. Kissel, *Biomaterials* **2003**, *24*, 1121.

[45] T. E. Mollnes, *Vox Sanguinis* **1998**, *74*, 303.

[46] J. Hed, M. Johansson, M. Lindroth, *Immunology Letters* **1984**, *8*, 295.

[47] M. I. Jones, I. R. McColl, D. M. Grant, K. G. Parker, T. L. Parker, *Journal of Biomedical Materials Research* **2000**, *52*, 413

[48] B. Sivaraman, R. A. Latour, *Biomaterials* **2010**, *31*, 832.

[49] W. Wang, Z. Zheng, X. Huang, W. Fan, W. Yu, Z. Zhang, L. Li, C. Mao, *Journal of Biomedical Materials Research Part B: Applied Biomaterials* **2017**, *105*, 1737.

[50] K. Affeld, S. Stefansdottir, J. Schaller, U. Kertzscher, *Biomed Tech* **2014**, *59*, 11

[51] a) M. Kütting, J. Roggenkamp, U. Urban, T. Schmitz-Rode, U. Steinseifer, *Expert Review of Medical Devices* **2011**, *8*, 227; b) B. H. Shin, B. H. Kim, S. Kim, K. Lee, Y. B. Choy, C. Y. Heo, *Biomaterials Research* **2018**, *22*, 37.

[52] D. E. Roberts, A. McNicol, R. Bose, *Journal of Biological Chemistry* **2004**, *279*, 19421.

[53] W. Norde, *Macromolecular Symposia* **1996**, *103*, 5.

Supporting Information To: The Application of Dual-Layer, Mussel-Inspired, Antifouling Polyglycerol-Based Coatings in Ventricular Assist Devices

Michaël W. Kulka,[a] Sarah Smatty,[b] Felix Hehnen,[b] Tim Bierewirtz,[b] Kim Silberreis,[a,c] Chuanxiong Nie,[a] Yannic Kerkhoff,[a] Dr. Carsten Grötzinger,[d] Sebastian Friedrich,[e] Dr. Lars Ingemar Dahms,[f] Dr. Jens Dernedde,[c] Prof. Dr. Ingo Grunwald,[g] Prof. Dr. Michael Schirner,[a] PD Dr.-Ing. Ulrich Kertzscher,[b] Prof. Dr.-Ing. Klaus Affeld,[b] Prof. Dr. Rainer Haag [a,]*

[a] Institute for Chemistry and Biochemistry, Freie Universität Berlin, Takustraße 3, Berlin 14195, Germany

[b] Biofluid Mechanics Lab, Charité-Universitätsmedizin Berlin, Augustenburger Platz 1, Berlin 13353, Germany

[c] Institute for Laboratory Medicine, Clinical Chemistry and Pathobiochemistry, Charité - Universitätsmedizin Berlin, Augustenburger Platz 1, Berlin 13353, Germany

[d] Department of Hepatology and Gastroenterology, Charité - Universitätsmedizin Berlin, Augustenburger Platz 1, Berlin 13353, Germany

[e] Process Engineering Department, Berlin Heart GmbH, Wiesenweg 10, 12247 Berlin

[f] Quality Assurance and Regulatory Affairs, qtec group GmbH, Niels-Bohr-Ring 3-5, 23568 Lübeck

[g] Department of Industrial and Environmental Biology, Hochschule Bremen – City University of Applied Sciences, Neustadtswall 30, 28199 Bremen, Germany

1. EXPERIMENTAL SECTION

The chemicals were purchased from Merck (Darmstadt, Germany) and Rapp Polymere GmbH (Tübingen, Germany). The TAMRA-amine (5-isomer) dye was purchased from Lumiprobe (Hannover, Germany). All chemicals were used as received without further purification, unless mentioned otherwise.

1.1. Scanning Electron Microscopy

Platelet morphology was investigated using a SU8030 field-emission scanning electron microscope (FE-SEM) by Hitachi (Tokyo, Japan), at an accelerating voltage (V_{ac}) of 20 kV, a current of 20 µA, and a working distance of 21.6 cm. Prior to the measurements the substrates were sputtered with a 5 nm conductive gold layer, using a compact coating unit CCU-010 by Safematic GmbH (Bad Ragaz, Switzerland).

1.2. Titan Coating via Physical Vapor Deposition

Borosilicate glass cover slips (ø 25 mm, thickness No. 1) were purchased from VWR International (Radnor, Pennsylvania, USA), and coated with a transparent titanium dioxide layer (ca. 30 nm) via physical vapor deposition (PVD). The TiO_2 coatings were produced using radio frequency (13.56 MHz) reactive sputtering. Oxygen 5.0 and Argon 4.6 were purchased from Linde plc (Munich, Germany), and a titanium target (99.9% purity) was purchased from Sindlhauser Materials GmbH (Kempten, Germany). First, the sputtering chamber (50 cm x 50 cm x 50 cm) was evacuated to a base pressure of 1 x 10^{-5} mbar. Next, the substrates were cleaned via an oxygen

plasma treatment (60 standard cubic centimeter per minute (sccm)) and argon (60 sccm) for 5 min each (sputtering power: 2380 W). Without venting the chamber, the target was sputtered using an Ar-flux (120 sscm, sputter power: 2380 W). After the sputter plasma showed a blue color, an additional 9 sccm of oxygen was added to the chamber. The blue color indicated that metallic titanium was on the surface of the target, i.e., the absence of a TiO_2-layer. After a reactive sputtering time of 10 min, a 25 nm thick TiO_2-coating was obtained on the substrates. To obtain fully oxidized TiO_2, the distance between target and substrate was maximized (58 cm).

1.3. Coating Formation and Post-Functionalization

Organic residues were removed from the TiO_2-coated glass substrates by ultrasonic treatment of the surface in Milli-Q (15 min). Next, the substrates were immerged in a solution of MI-dPG (4 mg, $1.33x10^{-4}$ mmol) in MeOH (4 ml) to which an aqueous solution of 3-(*N*-morpholino)propane sulfonic acid (MOPS) buffer (1.33 ml, 0.1 M, pH 8.5) was added, which initiated the polymerization of MI-dPG. The surfaces were left in the polymerizing solution for 10 min (immersion depth ca 1 cm). Subsequently, the surfaces were taken from the solution, thoroughly rinsed with deionized H_2O (3x) and EtOH (3x), and finally dried under a N_2-flow. Post-functionalization of the MI-dPG-coated substrates with lPG–b–OA_{11} was performed by placing the substrates overnight into a solution of lPG–b–OA_{11} (4 mg, $3.77x10^{-4}$ mmol) in MOPS-buffer (4 ml, 0.1 M, pH 8.5) at 50 ^{o}C. Subsequently, the substrates were thoroughly rinsed with deionized H_2O (3x) and EtOH (3x). Post-functionalization of the surface with HO–PEG–NH_2 was performed by placing the MI-dPG coated surface overnight into a solution of the HO–PEG–NH_2 (4 mg, $4x10^{-4}$ mmol) in MOPS-buffer (4 ml, 0.1 M, pH 8.5) at 50 ^{o}C. Subsequently, the surfaces were thoroughly rinsed with deionized H_2O (3x) and EtOH (3x). For the MI-dPG coating of the

ventricular assist device (VAD) prototype, the rotational speed of the VAD was set to 90 rotations/min, using custom software by Berlin Heart GmbH. The VAD was connected to a circulatory system (internal volume of ca 25 ml), which possessed two inlets/outlets that allowed for the full removal of air bubbles from the system. The system was filled with a solution of MI-dPG in MeOH (20 ml, 0.5 mg/ml), and subsequently MOPS-buffer (5 ml, 0.1 M, pH 7.5) was added to initiate the polymerization reaction. The pump was then started and left running overnight (ca. 10 h) at room temperature. Next, the system was emptied and rinsed with deionized H_2O (3x) and EtOH (3x). For dip-coating, the rotor blade was immersed in a solution of MI-dPG in MeOH (20 ml, 1 mg/ml), and subsequently MOPS-buffer (5 ml, 0.1 M, pH 8.5) was added to initiate the polymerization of MI-dPG. The rotor was left in the polymerizing solution for 5 min. Next the rotor was turned 180 degrees and incubated for another 5 min so that a homogenous MI-dPG coating was obtained on both sides of the rotor. After the coating procedure, the rotor was thoroughly rinsed with deionized H_2O (3x) and EtOH (3x). For an elaborate report on the synthesis, chemical composition, stability, and surface fouling properties of the TiO_2-substrate, the MI-dPG coating, and the MI-dPG coating functionalized with lPG–b–OA or HO–PEG–NH_2, the reader is referred to an earlier work by our group.[1]

1.4. Polyurethane (PU) and Polydimethylsiloxane (PDMS) Spin-Coating

Glass cover slips were cleaned by ozone/UV-treatment for 15 min and subsequently immerged in EtOH under ultrasonic treatment. The cleaned cover slips were then spin coated (1 min at 12,000 rounds per minute (rpm)) for 40 seconds, using a WS-650Mz-23NPPB spin coater by Laurell Technologies corporation (North Wales, Pennsylvania, USA) and a 1 wt% solution of PU in DMF or a 1 wt% of PDMS in xylol, respectively. The spin coated cover slips were used as reference

materials in the assessment of the platelet adhesion in the stagnation point flow model. The stagnation point flow model is described in more detail in **Section 1.11.** of this document.

1.5. Platelet-Rich Plasma Preparation

For the tests that required platelet rich plasma (PRP), the following procedure for the preparation of PRP was applied: whole-blood was drawn from a healthy male donor after informed content, and collected into a vacutainer tube which contained citrate as anticoagulant agent. Subsequently, the vacutainer tube was centrifuged at 1,000 rpm for 10 min, after which a two-layer system was obtained. Next, the top layer (i.e., PRP) was gently removed by using a micropipette. Disturbance of the layers led to the observation of leukocytes and erythrocytes in SEM investigations, and was therefore prevented.

1.6. Cell Viability Testing

Adenocarcinomic human alveolar basal epithelial cells (A549 cells) and chicken fibroblast cells (DF-1 cells) were maintained as a monolayer culture in tissue culture polystyrene (TCPS) petri dishes containing Dulbecco's Modified Eagle Medium (DMEM) supplemented with fetal bovine serum (FBS) (10 v%), L-glutamate (0.3 mg/ml)), streptomycin (100 mg/ml), and penicillin (100 units/ml). The cell lines were cultured at 37 °C and 5% CO_2, using a laboratory CO_2 incubator by Heraeus Holding GmbH (Hanau, Germany). One day prior to the introduction of lPG–b–OA_{11}, the cells were seeded into a 96-well plate at a density of $1x10^5$ cells/ml. After 24 h of cell culturing, the cells were washed with phosphate-buffered saline (PBS) and subsequently covered with DMEM containing lPG–b–OA_{11} at various concentrations (0-10 mg/ml). The solutions were

filtered prior to the experiment, utilizing regenerated cellulose syringe filters (pore size: 0.2 μm) by the Sartorius group (Göttingen, Germany). After another 24 h of cell culturing, the cell viability was investigated using a commercially available cell counting kit (WST-8/CCK8, Order No: ab228554) by Abcam plc. (Cambridge, United Kingdom). The absorbance was measured at 450 nm using an Infinite 200 pro plate reader by the Tecan Austria GmbH (Groedig, Austria). The absorbance of the sample was compared to an untreated control, to obtain a relative measure for the viability of the cells.

1.7. LIVE/DEAD™ Staining

A549 cells and DF-1 cells were maintained as a monolayer culture in TCPS petri dishes containing DMEM supplemented with FBS (10 v%), L-glutamate (2 mM), streptomycin (100 mg/ml), and penicillin (100 units/ml). The cell lines were cultured at 37 °C and 5% CO_2, using a laboratory CO_2 incubator by Heraeus Holding GmbH (Hanau, Germany). MI-dPG-coated substrates were prepared according to the procedure described in **Section 1.3**. Subsequently, the MI-dPG coated TiO_2 substrates were sterilized with EtOH (70 v% in Milli-Q), and the cells were seeded on the MI-dPG coating at a concentration of 1 x 10^5 cells/ml. After 24 h of cell culturing, the cells were stained utilizing a commercially available LIVE/DEAD™ Viability/Cytotoxicity Kit (Order No: L3224) by Thermo Fisher Scientific Inc. (Waltham, Massachusetts, USA). To access the cytotoxicity of lPG–b–OA_{11}, the cells were first cultured for 24 h in a DMEM-containing a 96-well plate. Next, the cells were washed with PBS, and subsequently DMEM containing lPG–b–OA_{11} (10 mg/ml) was placed on the cells. The lPG–b–OA_{11} solution was filtered prior to the experiment, utilizing regenerated cellulose syringe filters (pore size: 0.2 μm) by the Sartorius group (Göttingen, Germany). After another 24 h of cell culturing, the cytotoxicity was assessed

by staining the cells with same LIVE/DEAD™ kit as used for the cells on the MI-dPG-coated substrates. The cells were visualized using AxioObserver Z.1 microscope by the Carl Zeiss AG (Oberkochen, Germany). Zen blue software (also provided by the Carl Zeiss AG) was applied for image editing.

1.8. Automated LIVE/DEAD™ and Cell Morphology Quantification

Automatic image analysis was performed with the Java-based image-processing program "ImageJ" developed by the Laboratory for Optical and Computational Instrumentation of the University of Wisconsin (Madison, Wisconsin, USA).[2] First, cell recognition was achieved via distinctive assessment of fluorescence signals from live and dead cells. Next, the cells were separated from the background utilizing a fluorescence thresholding value (threshold $_{Live}$: 1731, threshold $_{Dead}$: 889, 16 bit images). After binarization, cell clusters were segmented utilizing a classical watershed algorithm for the separation of different objects in an image (coefficient: 0.6). Subsequently, the particle analyzer function from ImageJ was utilized for cell quantification and morphology analysis (cell size and circularity). To avoid counting single pixels or cell fragments, only objects above a specific size were analyzed (i.e., > 100 μm for live and > 15 μm for dead cells). Finally, the results were manually evaluated by comparing the outlines of the analyzed particles with the original fluorescence images.

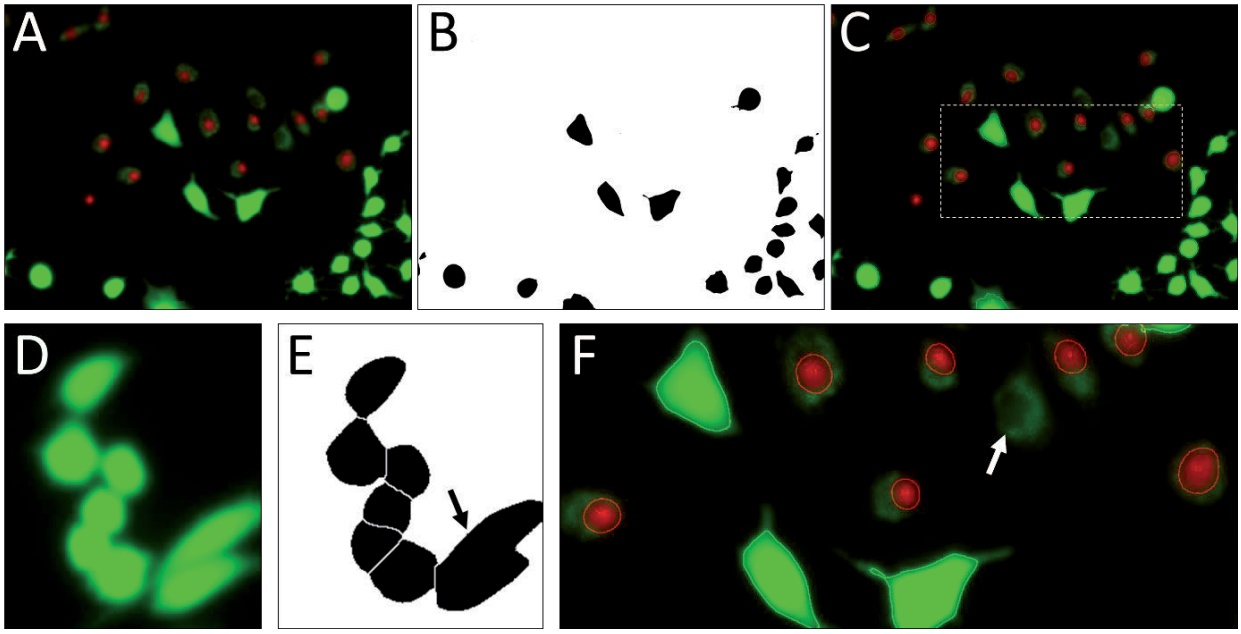

Figure S1. (A) Overlay of the fluorescence channels (green: live cells, red: dead cells). (B) Binary image after thresholding the green channel at 1731. (C) Overlay of the green and red fluorescence channel, with the particles recognized as cells outlined. (D) Crop of a cell cluster. (E) Binary image after watershed segmentation of the cell cluster. Six successful segmentations and two cells unsegmented (black arrow). (F) Zoom of the white box from image (C); one dead cell was not successfully stained and thus not analyzed (white arrow). However, most cells were successfully quantified.

1.9. Complement Activation Testing

Assessment of the complement-activating properties was performed on full Ti-substrates, as glass is known to activate the complement system.[3] A commercial ELISA kit (C5a DuoSet) by Bio-Techne GmbH (Wiesbaden, Germany) was applied to detect human C5a, a protein fragment released from the complement component C5 upon activation. The colorimetric assay was performed in a 96-well format and each individual condition was analyzed as triplicate, according to the provided description. The TiO_2-substrate and surfaces **1**, **2**, and **3** were then incubated with PRP for 0 – 5 h, and samples were taken from the PRP at t = 0, 30 min, and at 1, 2, 3, 4, and 5 h. As a negative control, PRP was incubated in petri dishes without further substrates. As a positive control, PRP with zymosan from *Saccharomyces cerevisiae* purchased from Sigma Aldrich (Darmstadt, Germany) was incubated in a petri dish. For analysis, the samples were diluted 50-fold with the provided reagent diluent (1% bovine serum albumin (BSA) in PBS), and subsequently the absorbance of the diluted samples was measured at 450 nm and 570 nm, using a microplate reader by Tecan Group Ltd. (Männedorf, Switzerland). The C5a levels were determined in comparison to an evaluated linear regression of the standardized values.

1.10. Platelet Activation Testing

Petri dishes containing the TiO_2-substrate or surface **1**, **2**, or **3** were incubated with PRP at 37 °C for 3 h, while shaking on a laboratory shaker (at 50 rpm) to prevent sedimentation. Next, the substrates were gently washed with PBS (3x) and immerged in a glutaraldehyde solution (2.5% in Milli-Q) for 1 h at room temperature. Subsequently, the substrates were gradually dehydrated by submerging the substrates in EtOH/H_2O mixtures of v/v= 50/50, 70/30, and 100/0, for 15 min per

solution. The substrates were then gold sputtered prior to SEM analysis. In subsequent SEM analysis, the activated platelets were observed as irregularly spread out structures on the surfaces, whereas inactivated platelets remained in their spherical shape.

1.11. The Stagnation-Point Flow Model

Whole blood was drawn from a healthy male donor and collected into a citrate vacutainer tube. A solution of quinacrine dihydrochloride (25 µmol, 1.25 mM) (i.e., a fluorescent dye) in PBS (20 ml, 10 mM, pH 7.4) was prepared, and subsequently gently mixed with the drawn blood (50 µl per ml blood). Prior to every measurement, the flow chamber and tubing were filled with PBS-solution, and all air bubbles were removed from the system. Subsequently, blood was infused into the system at 40 ml/h, by means of a PHD ULTRA syringe pump by Harvard Apparatus (Holliston, Massachusetts, USA). Upon entering the system, the blood was mixed (in a custom-made mixing chamber for laminar flow systems) with a solution of adenosine diphosphate (ADP) in PBS-solution (200 µmol/l), which reactivated the previously anticoagulated blood and stimulated the platelets to accumulate. Next, the whole blood entered the flow chamber, which consisted of (1) a top plate with an inflow tube (diameter 600 µm) made of stainless steel, (2) and a lower ring of stainless steel, and (3) holding a transparent TiO_2-coated glass cover slip on which the platelets accumulated. The lower ring and the cover glass were sealed with a (4) silicone-sealing ring (**Figure S2**). PU and PDMS spin-coated glass cover slips were utilized as reference materials. The blood entered the flow chamber in the center of the top plate, resulting in a stagnation point laminar flow over the coated cover slip. The flow chamber was irradiated with a 50 W mercury vapor lamp equipped with a filter block, both purchased from Leica (Wetzlar, Germany). The filter block permitted wavelengths of 355-425 nm to pass, resulting in visualization of the dyed platelets by

fluorescence. Platelet adhesion onto the bottom plate of the flow chamber was observed with a Fluovert FU-inverted microscope also purchased from Leica. A DFK 33U X 250 camera by Imaging Source (Bremen, Germany) was attached to the microscope for the visual recording of the adhesion process. The camera recorded with a resolution of 2048 x 2048, a frame rate of 1/s and a 925 ms exposure time.

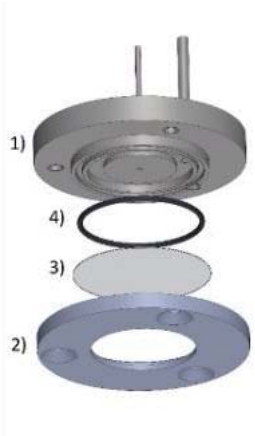

Figure S2. Schematic representation of the stagnation point flow model. (1) The top plate with inlet and outlet. (2) The stainless steel bottom plate. (3) The transparent (coated) cover slip on which the platelet adhesion was visualized. (4) A silicon ring to seal the system.

1.12. TAMRA-Amine Post-Functionalization

Special Ti-substrates (covered with a natural TiO_2-layer) provided by Berlin Heart GmbH were MI-dPG coated according to the method described in **Section 1.3**. Subsequently, a TAMRA-amine solution (0.01 mg/ml) in MOPS (0.1 M, pH 8.5) was suspended on the MI-dPG-coated substrates, and the surfaces were incubated overnight at 50 ^{o}C. Next, the substrates were incubated with deionized H_2O for 48 h to remove all non-bound TAMRA-amine. Finally, the surfaces were washed thoroughly with deionized H_2O (3x) and EtOH (3x) and dried by means of a N_2 flow. As

negative control, the experiments were repeated with the bare (uncoated) substrates. No fluorescence was observed for the TAMRA-amine-incubated Ti-substrate after incubation of the surface with deionized water. For coating visualization, the TAMRA-amine-incubated substrates were immerged in PBS, to enhance the photo-active properties of the coating. Additionally, immerging the samples in PBS reduced reflection artifacts. The uniformity of the coating was evaluated by imaging the components in a Lumina II fluorescence imager by Perkin Elmer (Waltham, Massachusetts, USA) using Living Image 3.1 acquisition software. The excitation light was generated using a xenon lamp with a 500-550 nm excitation filter. Additionally, a 575-650 nm emission filter was used.

Figure S3. A fluorescence image of bare Ti-substrates and MI-dPG-coated Ti-substrates, incubated with TAMRA-amine at various concentrations. The white circles represent the

substrates. For sample VI the fluorescence intensity was so high that the substrate could not be observed. The samples were placed in small petri dishes filled with distilled water (seen as circles around the substrates), which amplified the fluorescent signal from the substrates. For I till IV: Ti functionalized with TAMRA-amine in MOPS-buffer at 100 µg/ml, 10 µg/ml, 1 µg/ml, and 0.1 µg/ml, respectively. For V: the bare Ti-substrate. For VI till IX: MI-dPG-coated Ti functionalized with TAMRA-amine in MOPS at 100 µg/ml, 10 µg/ml, 1 µg/ml, and 0.1 µg/ml. It was clearly observed that a TAMRA-amine concentration of 10 µg/ml led to fluorescence on the MI-dPG-coated Ti-substrate, whereas no fluorescence was observed on the bare Ti-substrate.

1.13. VAD Coating Visualization

After coating of the VAD prototype with MI-dPG, as described in **Section 1.3**. The circulatory system was filled with a TAMRA-amine solution (0.26 mg, 4.91×10^{-4} mmol) in MOPS-buffer (26 ml, 0.1 M, pH 8.5) and the VAD prototype was started at a rotational speed of 90 rpm. The whole circuit (including the VAD) was then placed in an oven at 50 ^{o}C, and the system was left running for 10 h. Next, the system was removed from the oven, the VAD was stopped, the TAMRA-amine solution was removed from the system, and the system was rinsed with deionized H_2O (3x) and EtOH (3x). After that, the system was filled with deionized H_2O, and the VAD was started at a rotational speed of 90 rpm. The system was left running for 48 h at room temperature to remove all non-bound TAMRA-amine. Finally, the VAD was stopped, the deionized H_2O was removed from the circuit, the VAD was additionally dried under N_2-flow, and the VAD was removed from the circulatory system. The VAD prototype was then dismounted, and its parts were analyzed by means of fluorescence spectroscopy, as described in **Section 1.12.**

For comparison, one VAD rotor was dip-coated (i.e., static conditions), as described in **Section 1.3.** After the MI-dPG coating, the rotor blade was immersed in a TAMRA-amine solution (0.01 mg/ml) in MOPS (0.1 M, pH 8.5), and the rotor was incubated overnight (ca. 10 h at 50 ºC). Next, the rotor was incubated with deionized H_2O for 48 h at room temperature to remove all non-bound TAMRA-amine. Subsequently, the rotor was washed with deionized H_2O (3x) and EtOH (3x), and dried using a N_2-flow.

2. SUPPORTING DATA

Table S1. LIVE/DEAD™ Quantification and Morphology assessment of A549 and DF-1 Cells on the Various Substrates.

Cell Type	*Substrate*	*#Images*[A]	*Live*[B]	*Dead*[B]	*Total*[B]	*Viability*[C]	*Cells / Image*[D]	*Shape Factor*
A549								
	TCPS	3	85 136 94	2 4 4	87 140 98	96.9 ± 0.9 %	108.3 ± 22.8	0.72 ± 0.03
	lPG–b–OA_{11}[E]	3	45 53 30	2 1 3	47 54 33	94.9 ± 3.7 %	44.7 ± 8.7	0.73 ± 0.02
	HO–PEG–NH_2[E]	3	47 37 49	1 1 0	48 38 49	98.4 ± 1.4 %	45 ± 5.0	0.73 ± 0.03
	TiO_2	4	53 58 71 80	1 1 2 0	54 59 73 80	98.4 ± 1.1 %	66.5 ± 10.5	0.73 ± 0.01

	MI-dPG	4	89 93 129 98	1 7 2 1	90 100 131 99	97.33 ± 2.9 %	105 ± 15.5	0.80 ± 0.01
	MI-dPG–lPG	4	50 52 56 71	4 1 3 3	54 53 59 74	95.4 ± 2.3 %	60 ± 8.4	0.84 ± 0.02
	MI-dPG–PEG	4	104 82 112 82	4 1 3 3	108 83 115 85	98.5 ± 0.9 %	97.8 ± 14.0	0.73 ± 0.03
DF-1								
	TCPS	3	98 133 115	6 1 2	104 134 117	97.3 ± 2.7 %	118.3 ± 12.3	0.67 ± 0.03
	lPG–b–OA_{11}[E]	3	31 18 11	8 4 7	39 22 18	74.1 ± 11.3 %	26.3 ± 9.1	0.77 ± 0.05
	HO–PEG–NH_2[E]	3	38 28 25	1 0 3	39 28 28	95.6 ± 5.6 %	31.7 ± 5.2	0.69 ± 0.02

TiO_2	4	63	0	63	97.5 ± 2.0 %	72 ± 12.1	0.77 ± 0.01
		59	3	62			
		68	2	71			
		90	2	92			
MI-dPG	4	118	3	121	98.2 ± 1.0 %	122.8 ± 33.4	0.82 ± 0.02
		153	1	154			
		145	2	147			
		67	2	69			
MI-dPG–lPG	6	44	2	46	96.1 ± 4.7 %	57.7 ± 31.9	0.85 ± 0.01
		6	0	6			
		64	0	64			
		51	1	52			
		56	8	64			
		109	5	114			
MI-dPG–PEG	4	153	1	154	99.3 ± 0.5 %	110.8 ± 27.2	0.66 ± 0.03
		113	0	113			
		82	1	83			
		92	1	93			

(A) The total amount of images taken on the substrate. (B) The amount of live/dead/total cells observed on a 1.4 x 10^{-3} cm^2 portion of the respective substrate. (C) The cell viability calculated as an average from the various images per substrate-type. (D) The amount of cells observed on a 440 µm x 330 µm fraction of the respective surface. (E) The data observed for TCPS after 24 h of culturing in the presence of 10 mg/ml lPG–b–OA_{11} or HO–PEG–NH_2.

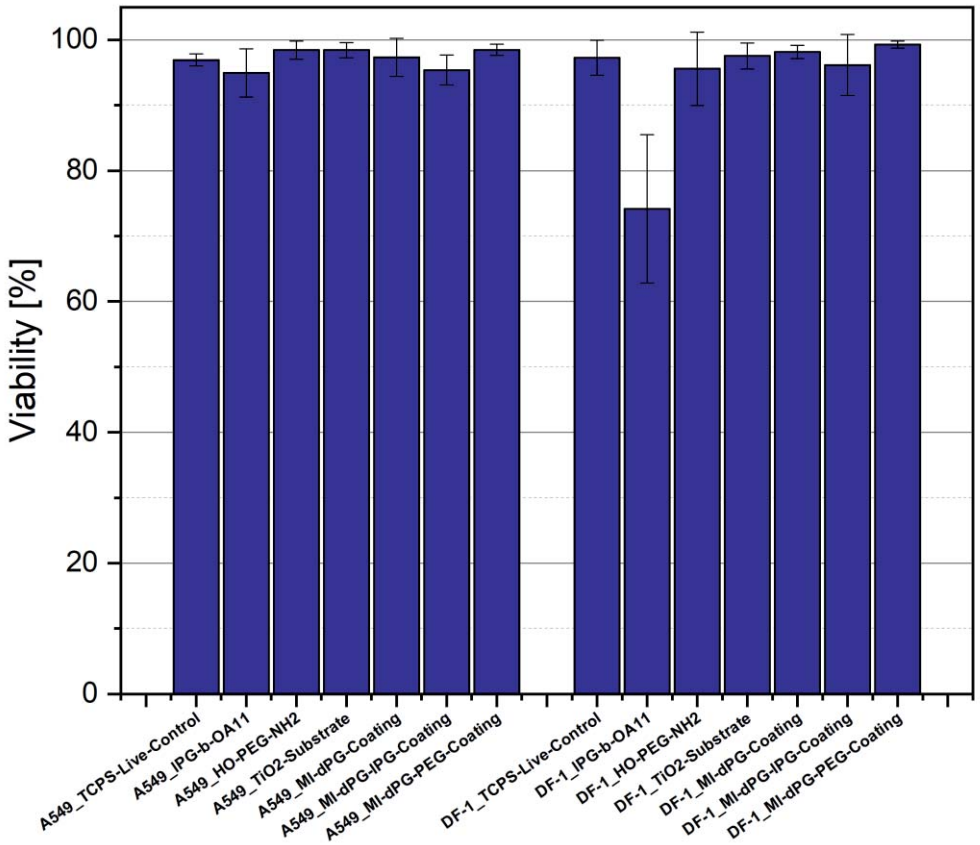

Figure S4. A graphical representation of the quantification cell viability at the surface as obtained by LIVE/DEAD™ staining. Quantification was performed by growing the cells on one substrate per substrate type. Subsequently, averages and deviation were calculated by taking a minimum of 3 images at random locations on the surface. The total amount of images taken per substrate type, and the total amount of live and dead cells observed on these images can be found in **Table S1**. The error bars represent the standard deviation from the mean.

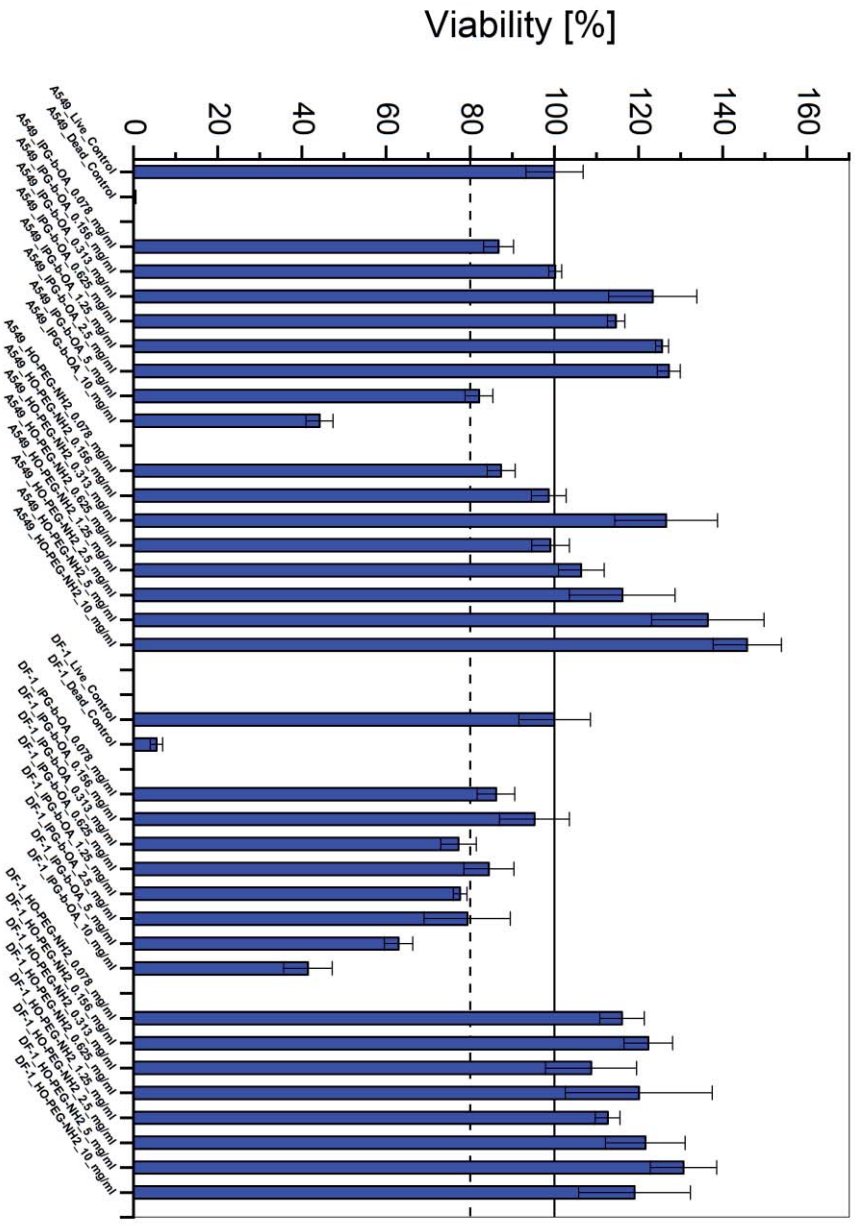

Figure S5. CCK-8 cell viability obtained for A549 and DF-1 cells at various concentrations of lPG–b–OA_{11} and HO–PEG–NH_2. As positive control (i.e., Live_Control) the cells were incubated on TCPS, as negative control the cells were incubated with medium containing 1 wt% SDS (i.e., Dead_Control).

Table S2. Time-Dependent C5a-Concentration in the PRP-Supernatant of Various Substrates.

Time (h)	*Substrate*	*C5a Concentration (ng/ml)*	*STDEV (ng/ml)*
0	Prp	1.13	0.06
	Zym	1.61	0.10
	TiO_2	1.73	0.08
	1	1.38	0.04
	2	0.83	0.08
	3	1.20	0.10
0.5 h	Prp	0.85	0.03
	Zym	2.68	0.34
	TiO_2	1.84	0.13
	1	2.06	0.08
	2	1.44	0.10
	3	1.62	0.07
1 h	Prp	0.78	0.02
	Zym	3.12	0.13
	TiO_2	1.53	0.05
	1	1.26	0.02
	2	1.77	0.06
	3	1.49	0.07

2 h	Prp	0.57	0.03
	Zym	3.05	0.22
	TiO_2	1.38	0.04
	1	1.05	0.03
	2	1.61	0.13
	3	1.29	0.08
3 h	Prp	0.96	0.05
	Zym	2.82	0.12
	TiO_2	1.50	0.06
	1	1.21	0.03
	2	1.45	0.08
	3	1.19	0.06
4 h	Prp	1.07	0.05
	Zym	3.10	0.13
	TiO_2	1.67	0.05
	1	1.28	0.06
	2	1.40	0.06
	3	1.24	0.04

	Prp	0.99	0.06
	Zym	3.08	0.12
5	TiO_2	1.61	0.08
	1	1.27	0.05
	2	1.53	0.09
	3	1.23	0.06

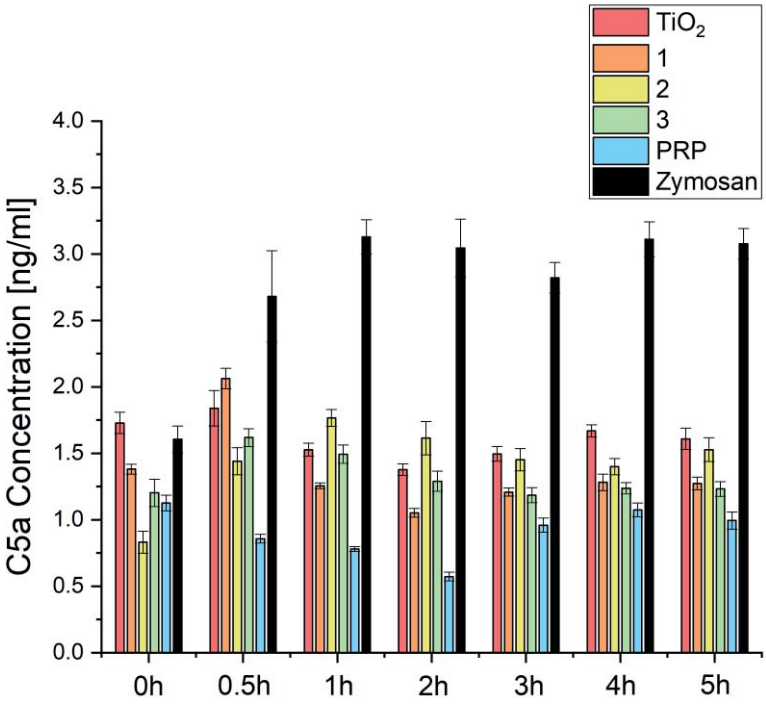

Figure S6. Graphical display of the C5a levels in the PRP-supernatant of TiO_2 (red) and surfaces **1** (orange), **2** (yellow), and **3** (green). The samples were compared to PRP (light blue) and PRP in which the complement activation was triggered by adding zymosan from *Saccharomyces cerevisiae* (black). The error bars represent the standard deviation from the mean. All measurements were performed with n = 3.

Table S3. Time-Dependent Surface Coverage (in % of the Total Measured Area) of the Stagnation Point Flow Model for the TiO_2-Substrate and Surfaces 1, 2, and 3.

	Time (s)					
	0	*30*	*60*	*120*	*180*	*240*
TiO_2	0.73%	2.82%	3.25%	3.59%	3.60%	3.72%
	0.78%	1.58%	2.16%	2.84%	-	4.82%
	-	3.88%	4.77%	5.48%	5.71%	6.00%
	1.30%	3.95%	5.11%	6.80%	7.70%	7.81%
	0.92%	2.61%	3.46%	4.41%	5.11%	5.80%
	1.03%	0.76%	0.94%	4.20%	5.60%	6.45%
	1.21%	2.00%	2.16%	2.23%	4.43%	6.08%
	0.90%	1.44%	1.49%	1.09%	-	-
1	0.70%	-	-	4.04%	3.94%	3.29%
	0.95%	1.35%	1.37%	1.30%	1.89%	3.65%
	0.79%	1.00%	1.07%	1.07%	2.32%	2.36%
	0.96%	-	-	4.27%	4.89%	5.28%
	0.81%	1.13%	0.98%	1.48%	2.15%	2.46%
	1.02%	0.77%	1.06%	1.06%	1.25%	3.62%
	1.32%	1.31%	1.70%	3.08%	3.67%	4.38%
	0.61%	0.94%	1.21%	1.73%	1.82%	2.01%
	-	1.54%	1.53%	1.49%	1.48%	1.47%

	0.84%	0.86%	0.82%	0.82%	0.91%	0.81%
	1.01%	0.85%	0.77%	0.88%	0.79%	0.93%
	0.43%	0.43%	0.50%	0.50%	0.43%	0.44%
	0.53%	0.61%	0.66%	0.70%	0.81%	0.75%
2	-	-	-	-	-	-
	0.53%	1.15%	-	1.82%	2.15%	2.39%
	0.62%	0.55%	0.57%	0.58%	0.58%	0.54%
	0.63%	0.69%	0.62%	0.63%	0.74%	0.64%
	0.50%	0.54%	0.52%	1.18%	1.82%	1.88%
	1.37%	0.79%	1.16%	1.25%	2.19%	4.65%
	0.77%	2.77%	4.08%	5.27%	6.57%	6.91%
	-	4.17%	5.09%	5.72%	6.29%	6.73%
	0.69%	1.03%	1.40%	3.13%	4.45%	5.21%
3	0.71%	2.44%	3.52%	4.77%	5.54%	6.36%
	0.89%	2.67%	4.22%	6.22%	6.71%	7.16%
	0.75%	2.90%	4.16%	5.51%	6.46%	7.07%
	0.62%	0.71%	0.69%	0.83%	3.24%	4.55%
	1.13%	2.98%	4.24%	5.99%	6.96%	7.65%

	1.10%	3.47%	4.51%	5.15%	-	-
	1.42%	3.46%	4.57%	6.10%	7.24%	-
	1.00%	3.45%	5.11%	7.09%	7.17%	6.87%
	0.53%	-	3.05%	4.60%	5.20%	-
PDMS	1.29%	4.27%	5.70%	7.22%	7.51%	6.93%
	1.76%	2.46%	4.21%	6.21%	6.67%	6.49%
	-	4.64%	5.86%	7.50%	7.79%	6.90%
	1.40%	4.40%	6.02%	7.60%	7.22%	6.44%
	-	4.59%	6.84%	8.27%	7.73%	6.42%
	0.72%	3.85%	4.44%	5.01%	5.63%	6.37%
	1.04%	2.30%	4.25%	5.10%	5.62%	5.56%
	1.82%	2.60%	3.22%	4.03%	3.95%	5.27%
	3.03%	4.25%	4.93%	6.52%	7.23%	7.30%
PU	1.05%	2.58%	3.72%	5.36%	5.87%	6.80%
	0.84%	2.51%	3.24%	4.26%	4.85%	5.37%
	1.17%	4.16%	5.06%	6.31%	7.07%	6.97%
	7.54%	-	-	8.16%	8.19%	7.52%
	3.72%	3.95%	5.16%	6.19%	6.62%	6.60%

Collagen	1.27%	4.32%	5.91%	6.95%	7.05%	6.95%
	0.67%	3.23%	5.30%	7.11%	7.61%	7.43%
	1.35%	4.44%	5.99%	6.98%	7.08%	6.91%
	1.34%	3.65%	5.54%	7.42%	7.83%	-
	0.84%	3.96%	6.10%	8.29%	7.70%	6.64%
	1.35%	3.95%	6.29%	8.35%	7.03%	6.37%
	-	4.71%	6.19%	7.34%	7.65%	7.84%
	0.92%	2.83%	-	6.42%	8.45%	-

All outliers have been removed from this table. The averages and standard deviations shown in the publication were calculated from the values at t = 180 s.

3. LITERATURE

[1] M. W. Kulka, I. S. Donskyi, N. Wurzler, D. Salz, Ö. Özcan, W. E. S. Unger, R. Haag, *ACS Applied Bio Materials* **2019**, *2*, 5749.

[2] M. D. Abràmoff, P. J. Magalhães, S. J. Ram, *Biophotonics international* **2004**, *11*, 36.

[3] J. Hed, M. Johansson, M. Lindroth, *Immunology Letters* **1984**, *8*, 295.

4.3. Surface-initiated Grafting of Dendritic Polyglycerol from Mussel-inspired Adhesion Layers for the Creation of Biocompatible Cell-repelling Coatings

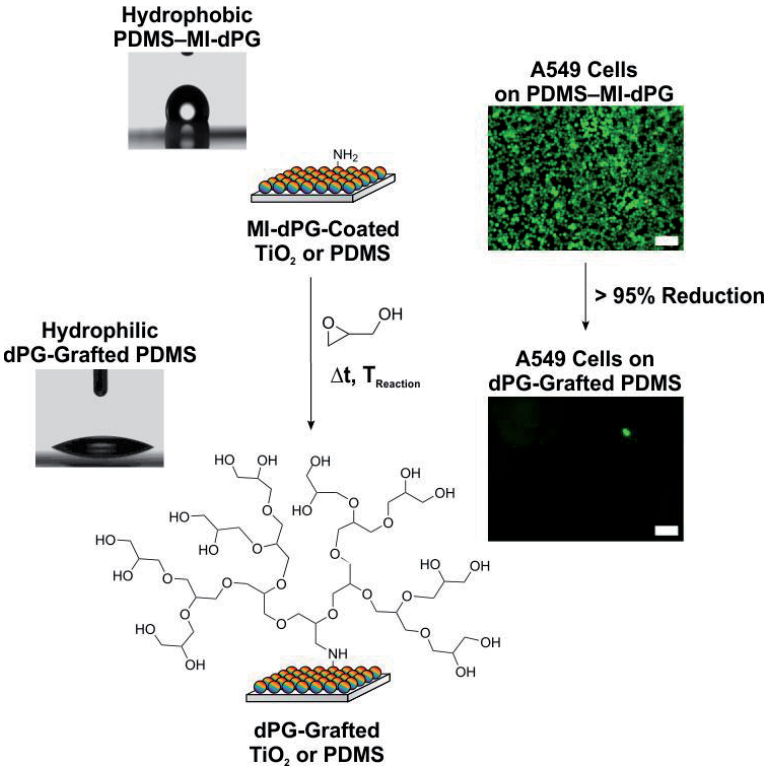

Figure 28. Graphical abstract. This figure was reproduced with permission from ref. 281 Copyright © 2020, Wiley-VCH.

Michaël W. Kulka, * Chuanxiong Nie, Philip Nickl, Yannic Kerkhoff, Arushi Garg, Dirk Salz, Jörg Radnik, Ingo Grunwald, Rainer Haag, * Wiley Adv. Mater. Interfaces **2020**, *Submitted*.

*Corresponding Author

Contributions: **M.W.K.**: Conceived, planned, and coordinated the project, executed all synthesis and coating experiments, and performed all CA and SEM measurements. Interpreted all data and summarized the results, discussions, and conclusions in the form of a scientific publication.

Surface-Initiated Grafting of Dendritic Polyglycerol from Mussel-Inspired Adhesion-Layers for the Creation of Biocompatible Cell-Repelling Coatings

Michaël W. Kulka,[a] Chuanxiong Nie,[a] Philip Nickl,[a,b] Yannic Kerkhoff,[a] Arushi Garg,[a] Dirk Salz,[c] Jörg Radnik,[b] Ingo Grunwald,[c,d] Rainer Haag*,[a]

[a] Institute for Chemistry and Biochemistry, Freie Universität Berlin, Takustraße 3, 14195 Berlin, Germany

[b] BAM – Federal Institute for Material Research and Testing, Division of Surface Analysis and Interfacial Chemistry, Unter den Eichen 44-46, 12205 Berlin, Germany

[c] Fraunhofer Institute for Manufacturing Technology and Advanced Materials IFAM, Wiener Straße12, 28359 Bremen, Germany

[d] Hochschule Bremen – City University of Applied Sciences, Department of Industrial and Environmental Biology, Neustadtswall 30, 28199 Bremen, Germany

KEYWORDS: *cell-repelling surface coatings, surface-initiated grafting, mussel-inspired adhesives, dendritic polyglycerol*

ABSTRACT

Biofouling is a major challenge in the application of textiles, biosensors, and biomedical implants.[1] In the current work, a straightforward method for the solvent-free polymerization of antifouling dendritic polyglycerol (dPG) from mussel-inspired dendritic polyglycerol (MI-dPG) coatings on hydrophilic titanium dioxide (TiO_2) and hydrophobic polydimethylsiloxane (PDMS) is reported. Surface characterization was performed by static water contact angle (CA) measurements, X-ray photoelectron spectroscopy (XPS), and scanning electron microscopy (SEM). Significant lower CA values were obtained after dPG grafting from MI-dPG-coated TiO_2 and MI-dPG coated PDMS. Furthermore, XPS showed a time-dependent increase of the C–O bond content upon dPG grafting from MI-dPG-coated TiO_2 and MI-dPG-coated PDMS. Analysis of the surface morphology by SEM showed a clear time-dependent increase in the surface roughness upon dPG grafting from MI-dPG-coated TiO_2 and MI-dPG-coated PDMS. When the proliferation and viability of two adhesive cell types were studied via LIVE/DEAD™ staining, a strong reduction in the cell density was observed after the dPG grafting from MI-dPG-coated TiO_2 and MI-dPG-coated PDMS (a decrease of > 95% in all cases). Additionally, the cell viability was found to be high (> 88%). The combined results showed the biocompatibility and highly cell-repelling surfaces of dPG from MI-dPG-coated TiO_2 and MI-dPG-coated PDMS.

INTRODUCTION

Unspecific biofouling is a considerable challenge in the application of medical implants, biosensors, and other surgical and protective equipment in hospitals. For example, biofouling can lead to deterioration of the surface, and increases the risk of infectious contamination and thrombosis (e.g., in case of joint prosthesis, urinary catheters, and intravenous stents).[2]

Furthermore, biofouling is encountered in marine applications, where it is the cause of high expenses resulting from fouling-related decreased fuel efficiency.[3] Additionally, the metabolic activity of the attached organisms can cause local corrosion, thus creating further costs.[4] Many projects have focused on the development of long-term stable non-fouling surface coatings for industrial-, marine-, and biomedical-applications. The immobilization of hydrophilic polymeric substances has proven itself as an effective strategy for the introduction of antifouling surface properties.[5] The mechanism underlaying the fouling-resistance of hydrophilic polymer coatings is based on the formation of a surface hydration layer in the absence of net charge. This hydration layer acts as a physical barrier for the prevention of unspecific protein-fouling, and furthermore prevents cellular- and bacterial- adhesion.

Many methods for the surface-immobilization of polymeric substances have been developed, including but not limited to: the use of polymeric layer-by-layer assemblies,[6] irradiation-mediated grafting,[7] Langmuir-Blodgett deposition,[8] and the use of electrostatic or hydrophobic adsorption.[9] Additionally, thiol- and silane-chemistry are classically used for the functionalization of noble metals and hydroxylated surfaces, respectively.[10] Although these methods can be applied to a wide variety of substrates, most of these processes require complex machinery and/or specific chemical or physical properties of the support material, thus limiting their application. Therefore, there is a need for the development of straight-forward surface-functionalization procedures, for the facile functionalization of a wide range of substrate-types. An interesting alternative for the immobilization of polymeric substances is the use of mussel-inspired surface chemistry. Mussels can rapidly adhere to virtually every type of organic or inorganic surface under wet conditions, even to substrates that are classically categorized as adhesion resistant (e.g., polytetrafluoroethylene (PTFE)).[11] Mussels adhere themselves to the

surface via an adhesive plaque that is excreted by the mussels' foot at the end of the byssal threads.[12] Earlier works showed the high prevalence of the catechol-containing amino acid L-DOPA and the amine-containing amino acid L-lysine in the mussel foot proteins (Mfps) that are excreted close to the substrate (i.e., mainly Mfp-5).[12] Based on these findings, Waite et al. hypothesized the essence of the catechol moieties in the substrate-independent binding character of some of the Mfps.[13] Later works confirmed the adhesion of catechols to a broad range of substrates via the formation of hydrogen-bonds, via π–π stacking, via the formation of coordination complex structures, and via the formation of Michael adducts and Schiff bases under oxidizing conditions.[14] The reversible surface binding of the catechols via the formation of complex structures was found to be especially strong in case of titanium dioxide (TiO_2) substrates, with a single molecule interaction force of ca. 800 pN.[15]

In 2007, Messersmith et al. hypothesized that the high prevalence of amine and catechol functional groups in the Mfps could contribute to the rapid adhesion of mussels.[16] Therefore, dopamine was selected as a small molecule containing both amine and catechol functionalities. When dopamine-containing solutions were buffered to a basic pH, auto-oxidation of the catechol moieties to their respective *o*-quinone forms occurred. Subsequently, a series of polymerizing reactions occurred, which finally led to the formation of polydopamine (PDA) coatings on a wide variety of substrates. The PDA coating was easily post-functionalized with amine- or thiol-containing secondary reagents via straightforward dip coating procedures, introducing specific surface properties. As a result of its substrate-independent applicability and facile post-functionalization, the PDA coating has gained a lot of interest in the field of biomaterials, e.g., PDA has been applied in bone and tissue engineering, for the introduction of antimicrobial activity to the surface, in the creation of surfaces with patterned cell adhesion, and for the

introduction of anticoagulant surface properties.[17] Although PDA has proven itself as a useful tool for surface functionalization, the initial coating procedure suffered from slow polymerization rates and a limited coating thickness.[16] Additionally, resulting from its dark-brown to black color, the PDA coatings is unsuitable for various optical applications.[16] Various methods for the acceleration of the polymerization reaction of PDA have been developed, but most of these methods utilize toxic agents to enhance the polymerization rate.[18] Therefore, there is a further need for the development of substrate-independent coating materials for the introduction of tailored surface properties.

In 2014, Wei et al. developed mussel-inspired polyglycerol (MI-dPG), which did not only contain the functional groups that are commonly found in Mfps, but also mimicked the molecular structure and weight of Mfps (**Figure 1**).[19] Polymerization of MI-dPG under slightly basic conditions led to the rapid formation of substrate-independent coatings with a controllable coating roughness and thickness (up till 4 μm after 4 hours of coating).[19] Furthermore, the coatings appeared transparent at low coating thickness. Earlier works by our group have shown the facile post-functionalization of the MI-dPG coating with nanoparticles and amine-containing secondary reagents, for the introduction of antifouling and antibacterial surface properties.[20] Furthermore, the amine moieties of the MI-dPG coating have been utilized for the immobilization of acyl chloride-containing secondary reagents.[21]

In the current scientific literature, the immobilization of poly(ethylene glycol) (PEG) is often considered as the gold standard for the creation of antifouling surface coatings.[22] For instance, in Messersmith's initial work on PDA, cell-repelling surface properties were introduced to the surface via the covalent grafting of thiol- or amine-terminated methoxy-PEG (mPEG) onto PDA coatings.[16] Unfortunately, PEG suffers from issues considering instability upon heating in

air,[23] and immunological recognition upon repeated exposure.[24] Therefore, there is a need for the development of hydrophilic antifouling surface coatings that show similar or better antifouling properties than PEG, while showing higher biocompatibility and oxidative/thermal stability than PEG under physiological conditions. The use of dendritic polyglycerol (dPG) offers an interesting alternative for the creation of antifouling coatings. An earlier work by Siegers and coworkers showed the higher oxidative stability of bulk dPG in comparison to PEG.[25] Additionally, multiple projects showed that the immobilization of dPG on the substrate leads to the creation of antifouling surfaces.[25-26] Although these approaches clearly illustrated the antifouling potency of dPG, most of them required multistep functionalization of the dPG-core prior to surface functionalization, thus leading to high production costs. Khan et al. and Moore et al. gave alternative approaches that both grafted dPG directly from silica (Si)-based substrates.[27] However, both approaches required the use of the highly reactive caustic base sodium methoxide.[27] A method reported by Weber et al. showed the grafting of dPG from aluminum, steel, and silicon surfaces without the use of a base. However, the grafting reactions were performed in an organic solvent, and the substrates required the introduction of –OH moieties to the surface prior to the grafting process.[28] In the current work, the surface-bound amines of the MI-dPG coating were utilized to initiate ring-opening polymerization of bulk glycidol (i.e., in a solvent-free procedure) under elevated temperatures (i.e., to graft dPG from the MI-dPG coating) (**Figure 1**). By following this strategy, the direct grafting of antifouling dPG from the surface was extended to a wide variety of substrates, resulting from the substrate-independent adhesion character of the MI-dPG coating. In the presented work, hydrophilic titanium dioxide and hydrophobic PDMS were used as substrate materials. These materials were selected because of their relevance in biomedical applications. Furthermore, these

materials showed large variations in their chemical and physical surface properties. Therefore, the functionalization of these materials provided a proof-of-concept for the substrate-independent applicability of the novel method presented in this work. It was hypothesized that the thickness and morphology of the grafted dPG-layer would vary as a function of the reaction time and temperature. Furthermore, it was foreseen that the introduction of the dPG-layer would lead to the formation of a tightly bound surface hydration layer that would function as a physical barrier for the prevention of cell-adhesion.[27-28]

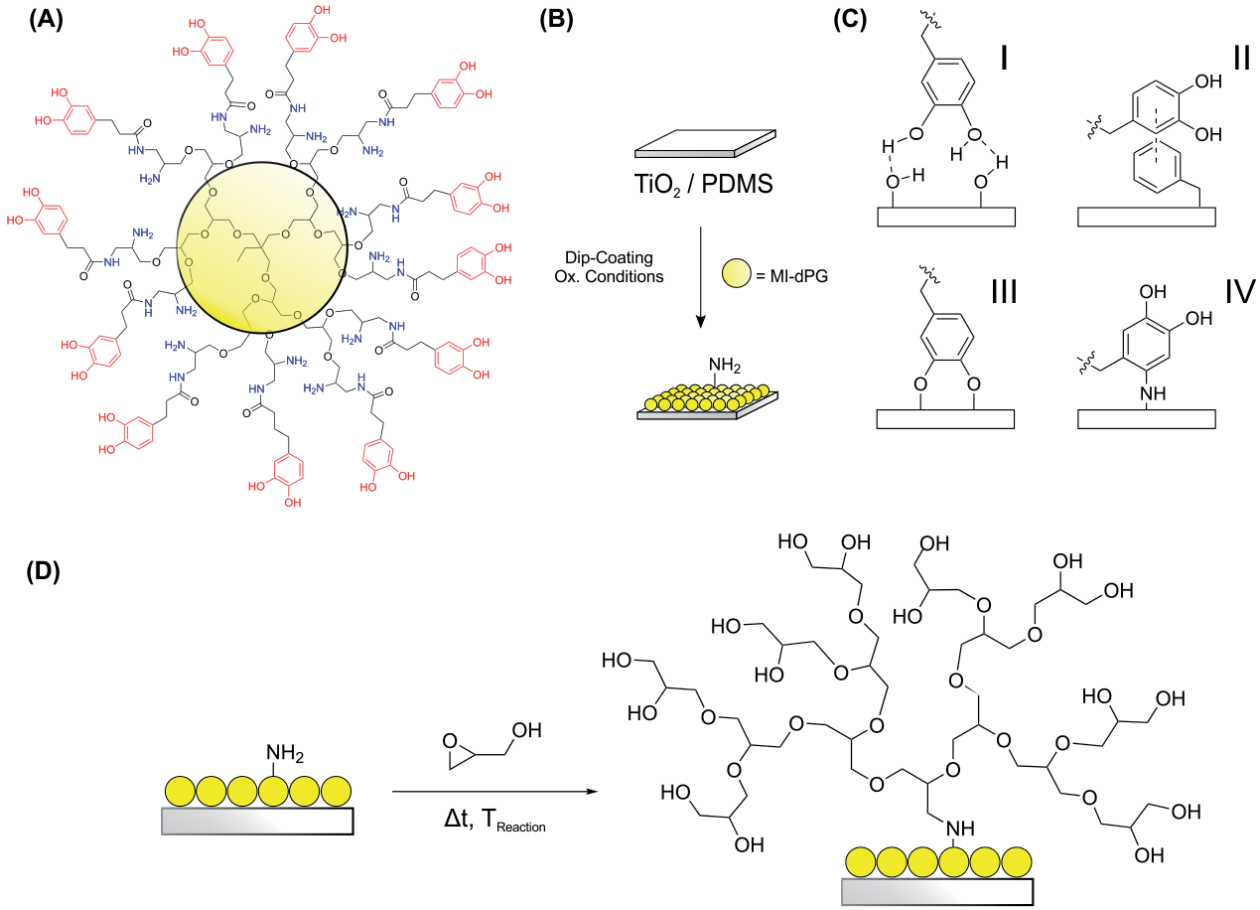

Figure 1. (A) A schematic representation of the molecular structure of MI-dPG. The shown structure is an idealized molecular structure; the number of glycerol monomer (shown within the yellow sphere) varies with the size of the polymer. The dPG-core shows ~55% branching.[29] The catechol moieties are depicted in red. The amine moieties are depicted in blue. (B) A schematic representation of the dip coating of TiO_2 and PDMS substrates with MI-dPG. (C) The various ways in which catechols can adhere to the surface. (I) On surfaces that contain hydrogen bond donors/acceptors, catechols can adhere via hydrogen bond formation, (II) on surfaces that contain aromatic systems, catechols can bind via π–π interactions, (III) catechols can tether to certain metal oxide surfaces (especially TiO_2) via the formation of strong but reversible metal complexes, (IV) finally, catechols can irreversibly bind to amine (and thiol) functionalized surfaces via the formation of Michael adducts and Schiff bases.[14] (D) A schematic representation of the grafting process performed in this work. After the coating of TiO_2 and PDMS with MI-dPG, the MI-dPG coating was utilized as a macro-initiator for the thermally induced ring-opening polymerization of glycidol from the surface (i.e., the grafting of dPG).

RESULTS AND DISCUSSION

First, transparent TiO_2-coated substrates were produced according to **Section 1.2.1.** of the Electronic Supplementary Information (ESI) (i.e., a transparent model coating with the surface properties of bulk titanium). Subsequently, these substrates were functionalized with MI-dPG, according to a modified version of the dip coating method that was earlier described by Wei and coworkers (**Sections 1.1.4.** and **1.2.3.** of the ESI).[19] After dip coating, the MI-dPG-coated surfaces were put in a substrate holder in a custom made flask at 110 °C under high vacuum for > 10 h (from now on referred to as TiO_2–MI-$dPG_{110\ °C,\ HV}$) (**Figure S1** of the ESI), ensuring that

all solvent was removed from the coatings prior to the grafting process. Interestingly, this drying process led to an increase in the CA, when the coatings were compared to MI-dPG coatings that were dried under atmospheric pressure for one hour at 50 °C (from now on referred to as TiO_2–MI-dPG$_{50\ °C,\ ATM}$) (**Figure S3** and **Table S1** of the ESI). This observation was explained by further intra-layer crosslinking of the MI-dPG coating under elevated temperatures and high vacuum, effectively leading to the loss of free amines, therefore effectively making the coating less hydrophilic. Analysis of TiO_2–MI-dPG$_{50\ °C,\ ATM}$ by X-ray photoelectron spectroscopy (XPS) showed a 1.35 : 1 ratio of C–O to C–C bonds (**Figure 3A** and **Tables S3** and **S4** of the ESI), which was roughly in line with an earlier work of our group.[20a] For TiO_2–MI-dPG$_{110\ °C,\ HV}$ the C–O bond content of the MI-dPG coating slightly decreased to a 1.09 : 1 ratio of C–O to C–C bonds. Additionally, the N1s' elemental content observed for TiO_2–MI-dPG$_{50\ °C,\ ATM}$ was clearly higher than the N1s' elemental content observed for TiO_2–MI-dPG$_{110\ °C,\ HV}$ (7.3 atomic percent (at.%) and 5.8 at.%, respectively) (**Figure 3C** and **Figure S5** and **Table S5** of the ESI). This observation was explained by the occurrence of additional Michael-type addition reactions and the formation of Schiff bases between the *o*-quinones and free amines present in the MI-dPG coating under vacuum at elevated temperatures. A slightly higher Ti2p content was observed for TiO_2–MI-dPG$_{110\ °C,\ HV}$ than for TiO_2–MI-dPG$_{50\ °C,\ ATM}$ (0.8 at.% and 0.6 at.%, respectively), indicating that the coating decreased its thickness as a result of the drying process at elevated temperatures under reduced pressure (**Figure 3C** and **Figure S5** and **Table S5** of the ESI). The combined results suggest the additional crosslinking and shrinkage of the coating upon heating at elevated temperatures under vacuum conditions. This additional crosslinking might contribute positively to the stability of the MI-dPG coating on the surface. All coatings further discussed in

this work were polymerized from MI-dPG coatings that were previously dried at 110 °C under high vacuum conditions.

To determine the optimal dPG grafting time and temperature (i.e., the time and temperature that would result in the lowest CA), glycidol was grafted from TiO_2–MI-dPG for t = 30 min, 1 h, 3 h, and 24 h at 80 °C, 100 °C, and 120 °C (from now on referred to as TiO_2–MI-dPG@$dPG_{\Delta t,\ T}$, with Δt = reaction time and T = reaction temperature) (**Section 1.2.4.** of the ESI). A time- and temperature-dependent decrease of the CA was clearly observed after the grafting of dPG from the MI-dPG-coated substrates (**Figure 2A**, **2B**, and **Figure S4** and **Table S2** of the ESI). CA measurements showed surface wetting for TiO_2–MI-dPG@$dPG_{3\ h,\ 100\ °C}$ and TiO_2–MI-dPG@$dPG_{24\ h,\ 80\ °C}$ (**Figure 2A**, **2B**, and **Figure S4** and **Table S2** of the ESI). Interestingly, when the grafting process was performed at 120 °C the CA reached ca. 25°, i.e., no surface wetting was observed. This observation was explained by a synergetic effect between the surface roughness and the hydrophilic surface chemistry in case of TiO_2–MI-dPG@$dPG_{3\ h,\ 100\ °C}$ and TiO_2–MI-dPG@$dPG_{24\ h,\ 80\ °C}$, significantly lowering the CA obtained for these substrates. When the grafting process was performed at higher reaction temperatures or with longer reaction times, the (nanometer-sized) surface roughness was potentially lost as a result of excessive dPG grafting. Consequently, CA values that are common for polyglycerol monolayer coatings were observed in case of longer grafting times with high reaction temperatures.[25] The combined results showed the successful grafting of dPG from the MI-dPG coated TiO_2 substrate.

As a control, bare TiO_2 substrates were incubated with glycidol for t = 30 min, 1 h, 3 h, and 24 h at 100 °C (from now on referred to as TiO_2@$dPG_{\Delta t,\ 100\ °C}$) (**Section 1.2.4.** of the ESI). CA measurements of TiO_2@$dPG_{\Delta t,\ 100\ °C}$ showed a time-dependent decrease in the CA, which was explained by the grafting of dPG from hydroxyl moieties present on the TiO_2 substrates

(**Figure 2A**, **2B**, and **Figure S4** and **Table S2** of the ESI). The results observed for the bare TiO_2 were in line with an earlier work by Weber and coworkers.[28] Nevertheless, surface wetting was not observed for TiO_2@$dPG_{\Delta t,\ 100\ °C}$. Furthermore, the CA value obtained for TiO_2@$dPG_{3\ h,\ 100\ °C}$ clearly exceeded the CA-value obtained for TiO_2–MI-dPG@$dPG_{3\ h,\ 100\ °C}$ (51° ± 4° and surface wetting, respectively), indicating that the grafting process was insufficient in absence of the MI-dPG coating (**Figure 2A**, **2B**, and **Figure S4** and **Table S2** of the ESI).

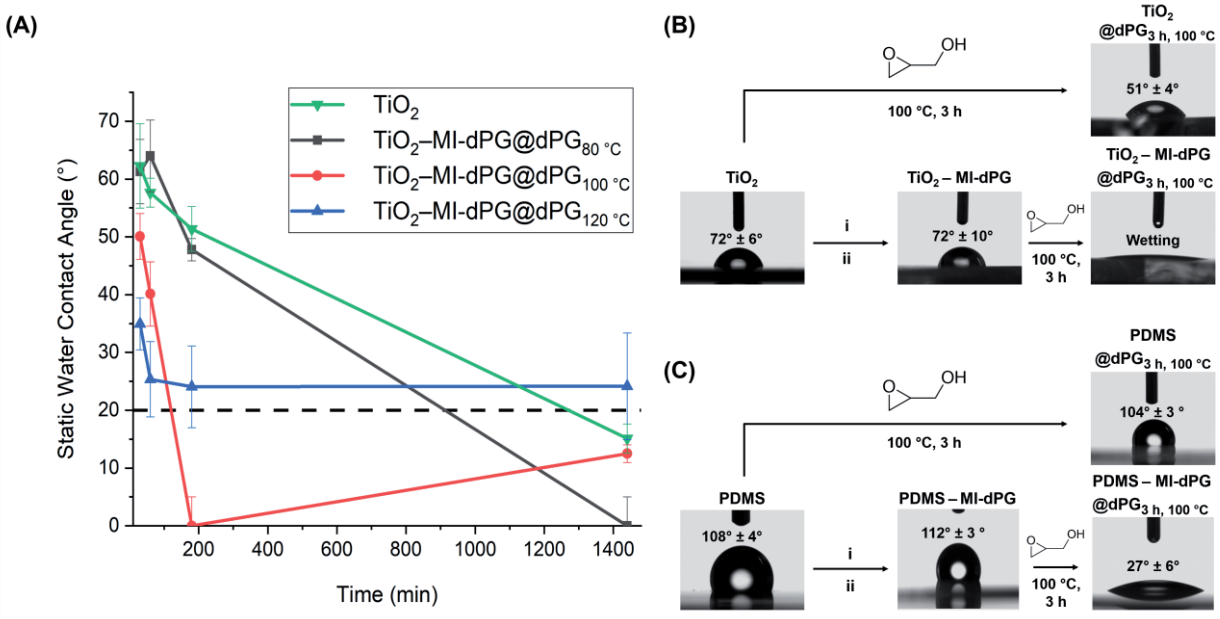

Figure 2. (A) A graphical representation of the CA obtained for TiO_2 (Green), TiO_2–MI-dPG@$dPG_{\Delta t,\ 80\ °C}$ (Black), TiO_2–MI-dPG@$dPG_{\Delta t,\ 100\ °C}$ (Red), and TiO_2–MI-dPG@$dPG_{\Delta t,\ 120\ °C}$ (Blue) as a function of the time (in minutes). The dotted black line represents the CA obtained for a polyglycerol monolayer on gold.[25] All measurements were performed as triplicates; the error bars represent the standard deviation from the mean. (B) The CA images obtained for TiO_2, TiO_2@$dPG_{3\ h,\ 100\ °C}$, TiO_2–MI-dPG, and TiO_2–MI-dPG@$dPG_{3\ h,\ 100\ °C}$. The shown CA values were obtained from measurements that were

performed in triplicate. The shown error reflects the standard deviation from the mean. (i): coating with MI-dPG, (ii): drying under high vacuum at 110 °C.

When the grafting process was characterized by means of XPS, a time-dependent increase of the C–O bond content was observed for TiO_2–MI-dPG@$dPG_{\Delta t,\ T}$ with T = 80 °C, 100 °C, or 120 °C and TiO_2@$dPG_{\Delta t,\ 100\ °C}$. However, for TiO_2@$dPG_{\Delta t,\ 100\ °C}$ the C–O bond content increased only slowly, whereas high C–O contents were already observed after 30 min of dPG grafting for all MI-dPG-coated systems at all tested temperatures (**Figure 3B**, and **Tables S6** and **S7** of the ESI). These observations further confirmed that the MI-dPG coating accelerated the dPG grafting process. Additionally, for TiO_2–MI-dPG@$dPG_{\Delta t,\ T}$, it was observed that the C–O content (and thus the dPG-layer) increased quicker when the dPG grafting was performed at higher temperatures (**Figure 3B** and **Tables S6** and **S7** of the ESI). When the elemental contents of titanium (i.e., the Ti2p elemental content) and nitrogen (i.e., the N1s elemental content) were investigated by means of XPS, a time-dependent decrease in the Ti2p content was observed for TiO_2@$dPG_{\Delta t,\ 100\ °C}$, which indicated the successful grafting of dPG from the surface (**Figure S5** and **Table S8** of the ESI). However, the Ti2p content remained high for TiO_2@$dPG_{30\ min,\ 100\ °C}$, TiO_2@$dPG_{1\ h,\ 100\ °C}$, and TiO_2@$dPG_{3\ h,\ 100\ °C}$, showing that the dPG grafting process occurred only slowly on the bare TiO_2 control (**Figure S5** and **Table S8** of the ESI). Only after 24 hours of dPG grafting, the Ti2p elemental content was clearly reduced on the bare TiO_2-substrate (**Figure S5** and **Table S8** of the ESI). When the elemental compositions of TiO_2–MI-dPG@$dPG_{\Delta t,\ T}$ were assessed by means of XPS, low but measurable Ti2p elemental contents were observed for TiO_2–MI-dPG and for TiO_2–MI-dPG@$dPG_{\Delta t,\ 80\ °C}$ with Δt = 30 min, 1 h, or 3 h (**Figure S5** and **Table S8** of the ESI). Only after 24 h of dPG grafting no Ti2p content

was observed for TiO_2–MI-dPG@$dPG_{24\ h,\ 80\ °C}$. In case of TiO_2–MI-dPG@$dPG_{\Delta t,\ T}$ with T = 100 °C or 120 °C, the Ti2p signal was already non-observable after 1 h of dPG grafting, indicating that the dPG-layer was already thick enough (i.e., > 10 nm) to completely suppress the Ti2p signal (**Figure 3C**, and **Figure S5** and **Table S8** of the ESI), i.e., showing that the grafting process occurred quicker at higher temperatures.

The speed of the dPG grafting process from the MI-dPG-coated TiO_2 substrates could also be followed by monitoring the N1s elemental content (the N1s signal originated from the amines present in the MI-dPG coating): a time-dependent decrease of the N1s content was clearly observed as a function of the reaction time, which indicated the grafting of the dPG-layer from the MI-dPG coating (**Figure 3C**, and **Figure S5** and **Table S8** of the ESI). Furthermore, it was observed that at higher temperatures the N1s signal decreased faster than at lower temperatures, which showed that the dPG grafting process occurred the fastest at 120 °C (**Figure S5** and **Table S8** of the ESI).

Many works have shown the relation between surface wettability and antifouling surface properties (i.e., protein and cell-repelling properties) for hydrophilic non-charged polymeric coatings.[5] In the present work, the combined results showed the successful grafting of hydrophilic antifouling dPG from MI-dPG-coated TiO_2 at all tested temperatures, and the lowest CA values were obtained for TiO_2–MI-dPG@$dPG_{3\ h,\ 100\ °C}$ and TiO_2–MI-dPG@$dPG_{24\ h,\ 80\ °C}$.

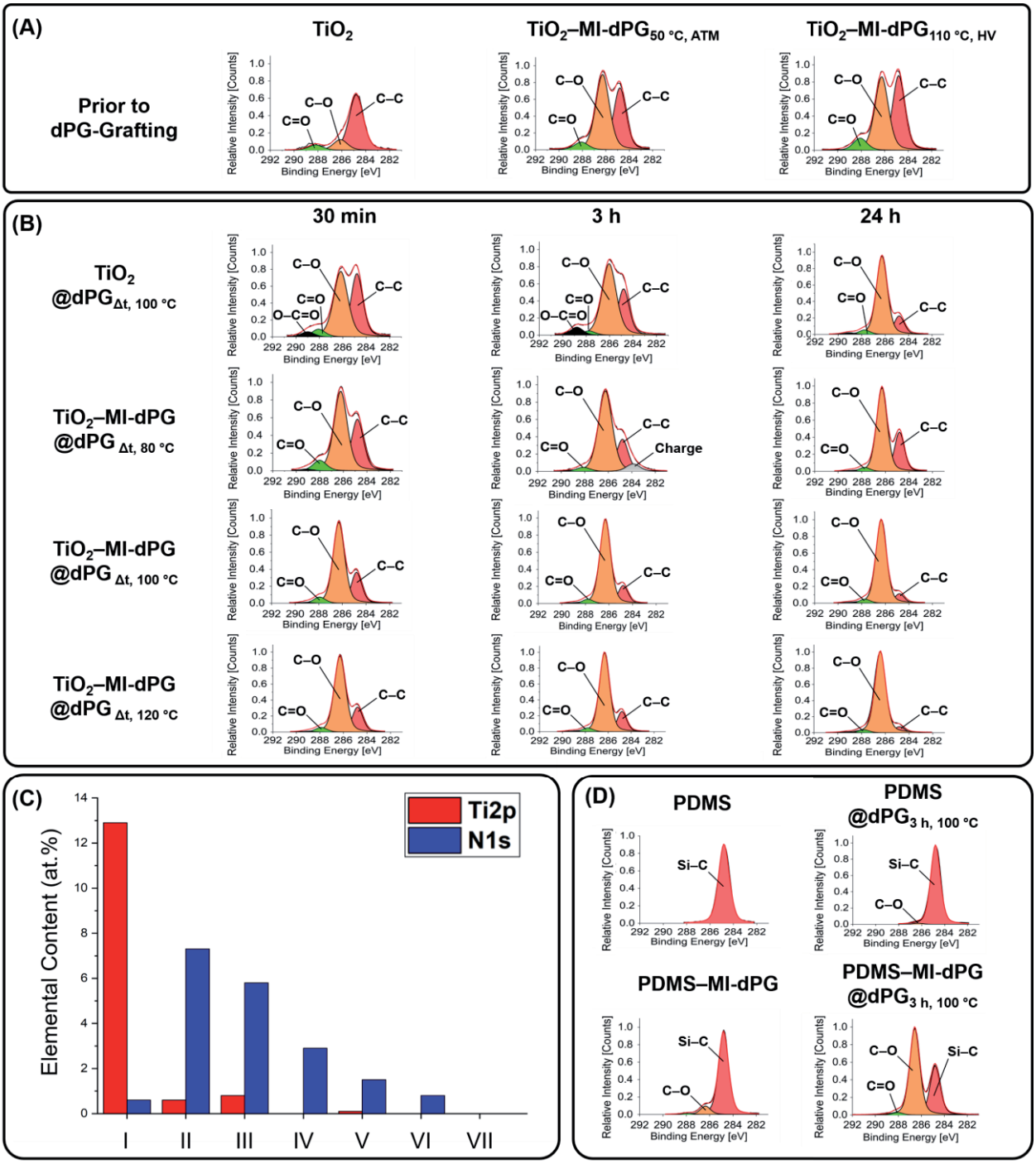

Figure 3. (A) Highly resolved C1s spectra of TiO_2, TiO_2–MI-$dPG_{50\ °C,\ ATM}$, and TiO_2–MI-$dPG_{110\ °C,\ HV}$. (B) Highly resolved C1s spectra of $TiO_2@dPG_{\Delta t,\ 100\ °C}$, TiO_2–MI-dPG@$dPG_{\Delta t,\ 80\ °C}$, TiO_2–MI-dPG@$dPG_{\Delta t,\ 100\ °C}$, and TiO_2–MI-dPG@$dPG_{\Delta t,\ 120\ °C}$. (C) The Ti2p (red) and N1s (blue) content of (I) the bare TiO_2-substrate, (II) TiO_2–MI-$dPG_{50\ °C,\ ATM}$,

(III) TiO_2–MI-dPG$_{110\ °C,\ HV}$ (IV) TiO_2–MI-dPG@dPG$_{30\ min,\ 100\ °C}$, (V) TiO_2–MI-dPG@dPG$_{1\ h,\ 100\ °C}$, (VI) TiO_2–MI-dPG@dPG$_{3\ h,\ 100\ °C}$, (VII) TiO_2–MI-dPG@dPG$_{24\ h,\ 100\ °C}$. (D) the XPS spectra obtained for PDMS, PDMS@dPG$_{3\ h,\ 100\ °C}$, PDMS–MI-dPG, and PDMS–MI-dPG@dPG$_{3\ h,\ 100\ °C}$.

To show the wider applicability of the developed dPG grafting process, hydrophobic polydimethylsiloxane (PDMS) was coated with MI-dPG (from now on referred to as PDMS–MI-dPG) and subsequently incubated with glycidol (**Sections 1.2.2.**, **1.2.3.**, and **1.2.4.** of the ESI). As industrial applications favor solvent-free reactions with short reactions times (i.e., enhancing productivity while lowering production costs), PDMS–MI-dPG was only incubated with glycidol under the optimized reaction conditions which were obtained from the dPG grafting from TiO_2–MI-dPG (i.e., 3 h at 100 °C). As a control, bare PDMS was incubated with glycidol under identical conditions. Analysis of PDMS@dPG$_{3\ h,\ 100\ °C}$ by means of CA measurements showed no significant change in the wetting characteristics of the PDMS surface after the dPG grafting process, which indicated that dPG was insufficiently grafted from the bare PDMS surface (**Figure 2C**). The CA obtained for the PDMS–MI-dPG surface showed a slightly decreased wetting character in comparison to the bare PDMS substrate, which was explained by the combination of the intrinsic hydrophobic character of PDMS (initial CA: 108° ± 4°) and the roughness introduced to the PDMS surface by the MI-dPG coating (**Figure 2C**). When PDMS–MI-dPG was subsequently incubated with glycidol, a clear decrease in the CA was observed (CA for PDMS–MI-dPG@dPG$_{3\ h,\ 100\ °C}$: 27° ± 6°), which was explained by the successful grafting of dPG from the MI-dPG coating (**Figure 2C**). Analysis of the bare PDMS substrate by means of XPS showed the high prevalence of a Si–C bond content and the absence

of C–O bonds (**Figure 3D** and **Tables S9** and **S10** of the ESI).[30] When PDMS was incubated with glycidol at 100 °C for 3 h, only a slight increase in the C–O content was observed, which further indicated the insufficient grafting of dPG from the bare PDMS substrate (**Figure 3D**, and **Tables S9** and **S10** of the ESI). When PDMS–MI-dPG was assessed by means of XPS, the highly resolved C1s spectrum showed the slight presence of C–O content (**Figure 3D**, and **Tables S9** and **S10** of the ESI), which was explained by the formation of the MI-dPG coating on PDMS. Analysis of PDMS–MI-dPG@dPG$_{3\ h,\ 100\ °C}$ showed a clear increase in the C–O content in respect to the PDMS–MI-dPG substrate (**Figure 3D**, and **Tables S9** and **S10** of the ESI), indicating the successful grafting of dPG from the MI-dPG coating on PDMS. When the elemental contents of silicon (i.e., the Si2p elemental content) and nitrogen (i.e., the N1s elemental content) were assessed for the various PDMS-based systems by means of XPS, a high Si2p signal was observed for the bare PDMS substrate (23.1 at.%) (**Figure S6** and **Table S11** of the ESI). After incubation with glycidol at 100 °C for 3 h, the Si2p signal did only show a minor change (Si2p content for PDMS@dPG$_{3\ h,\ 100\ °C}$: 22.7 at.%), which indicated that dPG was insufficiently grafted from the bare PDMS substrate (**Figure S6** and **Table S11** of the ESI). Analysis of the elemental content of the PDMS–MI-dPG substrate showed a clear reduction in the Si2p content (13.5 at.%) (**Figure S6** and **Table S11** of the ESI). Additionally, the N1s content increased from 0.1 at.% for bare PDMS to 1.4% for PDMS–MI-dPG (**Figure S6** and **Table S11** of the ESI). The combined results indicated the successful formation of the MI-dPG coating on PDMS. After the grafting of dPG from the PDMS–MI-dPG substrate, the Si2p content further decreased (to 7.5 at.% for PDMS–MI-dPG@dPG$_{3\ h,\ 100\ °C}$), indicating the successful formation of the dPG layer on top of the MI-dPG layer (**Figure S6** and **Table S11** of the ESI). Additionally, the N1s content decreased when compared to the PDMS–MI-dPG (to 0.3

at.% for PDMS–MI-dPG@dPG$_{3\ h,\ 100\ °C}$), further confirming the successful grafting of dPG (**Figure S6** and **Table S11** of the ESI).

When the surface morphology of the dPG grafting process was investigated by means of scattering electron microscopy (SEM), it was clearly observed that the MI-dPG coating introduced roughness in the micrometer range to the bare TiO_2 and PDMS substrates (**Figures 4A**, **4C**, **4E** and **4G**). This observation was in line with earlier works of our group.[19-20, 31] When the MI-dPG-coated substrates were subsequently incubated with glycidol at 100 °C for 3 h, a further increase in the surface roughness was clearly observed (**Figures 4F** and **4H**). In the case of TiO_2–MI-dPG@dPG$_{3\ h,\ 100\ °C}$, the grafted dPG appeared as merging smeared out micrometer-sized particles. For PDMS–MI-dPG@dPG$_{3\ h,\ 100\ °C}$, the grafted particles appeared less smeared out, indicating that the dPG grafting process from PDMS–MI-dPG might have occurred slower than from the TiO_2–MI-dPG substrate. Nevertheless, in both cases the SEM images clearly showed the successful grafting of dPG from the MI-dPG adhesive layer. When the bare TiO_2 substrate was incubated with glycidol at 100 °C for 3 h, some particles were observed on the surface (**Figure 4B**). However, the obtained SEM images clearly showed the enhanced grafting of dPG in the presence of the MI-dPG coating. When bare PDMS was incubated with glycidol under elevated temperatures, no clear changes in the surface morphology were observed (**Figure 4D**). For additional images of the dPG grafting process from TiO_2, TiO_2–MI-dPG, PDMS, and PDMS–MI-dPG (showing additional grafting times and temperatures), the reader is referred to **Figures S7** and **S8** of the ESI.

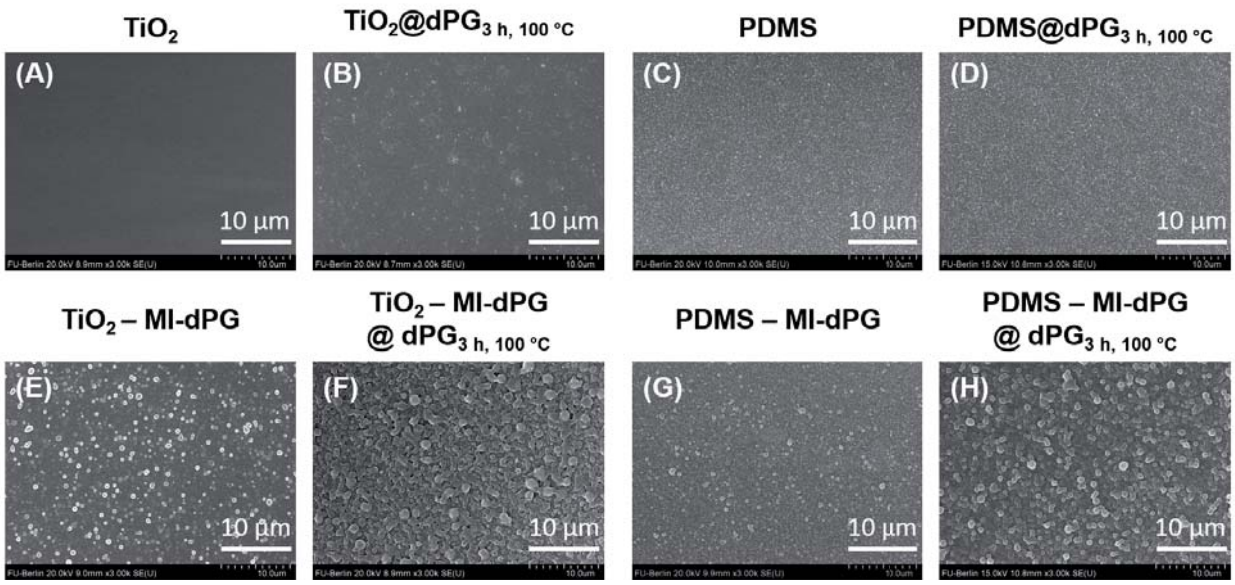

Figure 4. SEM images of the (A) bare TiO_2-substrate, (B) the TiO_2@$dPG_{3\ h,\ 100\ °C}$, (C) PDMS, (D) PDMS@$dPG_{3\ h,\ 100\ °C}$, (E) TiO_2–MI-dPG, (F) TiO_2–MI-dPG@$dPG_{3\ h,\ 100\ °C}$, (G) PDMS–MI-dPG, and (H) PDMS–MI-dPG@$dPG_{3\ h,\ 100\ °C}$. The shown images are a 3,000x enlargement of the measured surface.

The proliferation and viability of adhesive human adenocarcinoma cells (A549 cells) and chicken fibroblast cells (DF-1 cells) were investigated on the various substrates by means of LIVE/DEAD™ staining (**Sections 1.3.1.** and **1.3.2.** of the ESI). Abundant cell proliferation was observed for both the A549 and DF-1 cells on tissue culture polystyrene (TCPS) control. However, the A549 cells showed higher proliferation than the DF-1 cells under the set incubation conditions (**Figures 5A**, **6A**, and **6B**, and **Table S12** of the ESI)**.** Nevertheless, both cell types showed high viability on TCPS (**Figure 5A**, and **Figures 6C**, **6D**, and **Table S12** of the ESI). Abundant cell proliferation was also observed for both the A549 and DF-1 cells on the bare TiO_2 and PDMS substrates with high cell viabilities (**Figures 5B**, 5**C**, **6A**, **6B**, **6C**, and **6D**,

and **Table S12** of the ESI). As a control, the proliferation of A549 and DF-1 cells was also investigated on TiO_2@dPG$_{3\ h,\ 100\ °C}$ and PDMS@dPG$_{3\ h,\ 100\ °C}$ (**Figures 5B**, **5C**, **6A**, **6B**, **6C**, and **6D**, and **Table S12** of the ESI). For the A549 cells, no significant change in the cell number was observed for TiO_2@dPG$_{3\ h,\ 100\ °C}$, when the substrate was compared to bare TiO_2 (**Figures 5B** and **6A**, and **Table S12** of the ESI). In contrast, for the DF-1 cells a significant increase in the cell number was observed on TiO_2@dPG$_{3\ h,\ 100\ °C}$ (**Figures 5C** and **6B**, and **Table S12** of the ESI). For PDMS@dPG$_{3\ h,\ 100\ °C}$ no significant change in the A549 cell number was observed, when compared to the bare PDMS substrate (**Figure 5B** and **6A**, and **Table S12** of the ESI). In contrast, a significant increase in the DF-1 cell number was observed for PDMS@dPG$_{3\ h,\ 100\ °C}$, in respect to the bare PDMS substrate (**Figures 5C** and **6B**, and **Table S12** of the ESI). Furthermore, the cells observed on TiO_2@dPG$_{3\ h,\ 100\ °C}$ and PDMS@dPG$_{3\ h,\ 100\ °C}$ showed high viability (**Figures** 5**B**, **5C**, **6C**, and **6D**, and **Table S12** of the ESI). The results were explained by the insufficient grafting of a dPG-layer from the TiO_2 surface after 3 h of dPG grafting at 100 °C (as earlier confirmed by CA measurements, XPS, and SEM), which might have turned the surface slightly more hydrophilic and more favorable for the adhesion of the DF-1 cells. As a result, the cells could proliferate on the surface in a similar fashion as on the bare TiO_2 and PDMS substrates. On TiO_2–MI-dPG, no significant change in the A549 cell number was observed, when the substrate was compared to the bare TiO_2 substrate (**Figures 5B** and **6A**, and **Table S12** of the ESI). However, the number of DF-1 cells on TiO_2–MI-dPG was found to be significantly higher than for the bare TiO_2 substrate (**Figures 5C** and **6B**, and **Table S12** of the ESI). For the PDMS–MI-dPG substrate, similar results were obtained (**Figures 5C** and **6B**, and **Table S12** of the ESI). Besides, the cell viabilities of both cell types were found to be high on the TiO_2–MI-dPG and PDMS–MI-dPG substrates (**Figures 5B**, **5C**, **6C**, and **6D**, and

Table S12 of the ESI). Quantification of the A549 and DF-1 cells showed a dramatic decrease in the cell numbers of both cell types after the grafting of dPG from TiO_2–MI-dPG and PDMS–MI-dPG. In case of TiO_2–MI-dPG@dPG$_{3\ h,\ 100\ °C}$, a > 96% reduction of the cell density was observed for both cell types, when compared to the bare TiO_2 substrate (**Figures 5B**, **6A**, **6B**, and **Table S12** of the ESI). Similar results were obtained for PDMS–MI-dPG@dPG$_{3\ h,\ 100\ °C}$ (**Figures 5C**, **6A**, **6B**, and **Table S12** of the ESI). The remaining cells on TiO_2–MI-dPG@dPG$_{3\ h,\ 100\ °C}$ and PDMS–MI-dPG@dPG$_{3\ h,\ 100\ °C}$ appeared mainly alive (**Figures 5B**, **5C**, **6C**, and **6D**, and **Table S12** of the ESI), indicating the biocompatibility of the substrate. The dramatic reduction in the cell numbers of both cell types after the grafting of dPG from the MI-dPG-coated substrates was explained by the effective formation of a surface hydration layer, which formed a physical barrier that prevented cell adhesion.[5]

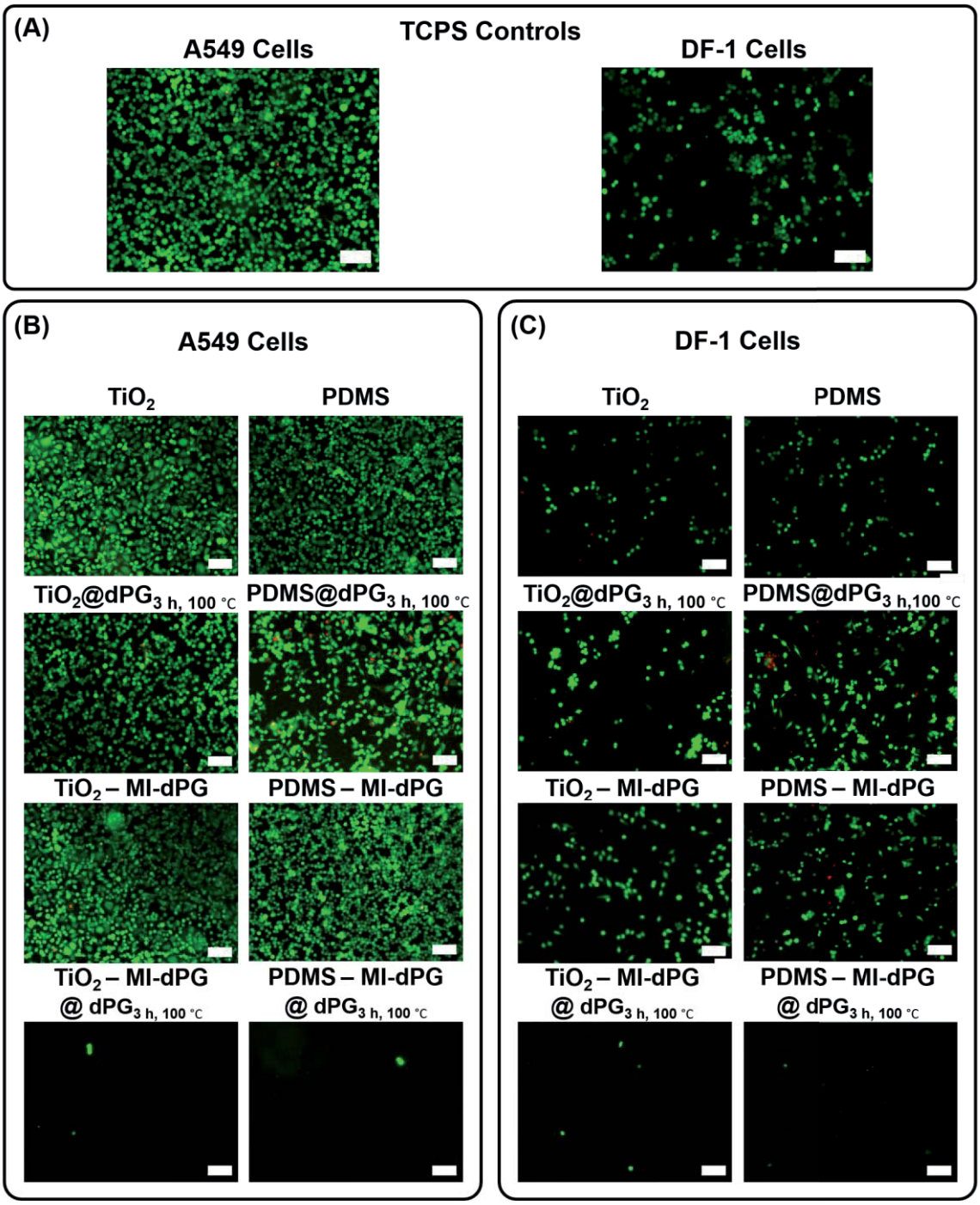

Figure 5. The images obtained after LIVE/DEAD™ staining (A) live cells appear in green, whereas dead cells appear in red. The white bar represents 100 μm. (B) The images obtained for the A549 cells on the various coating types. (C) The images obtained for the DF-1 cells for the various coating conditions.

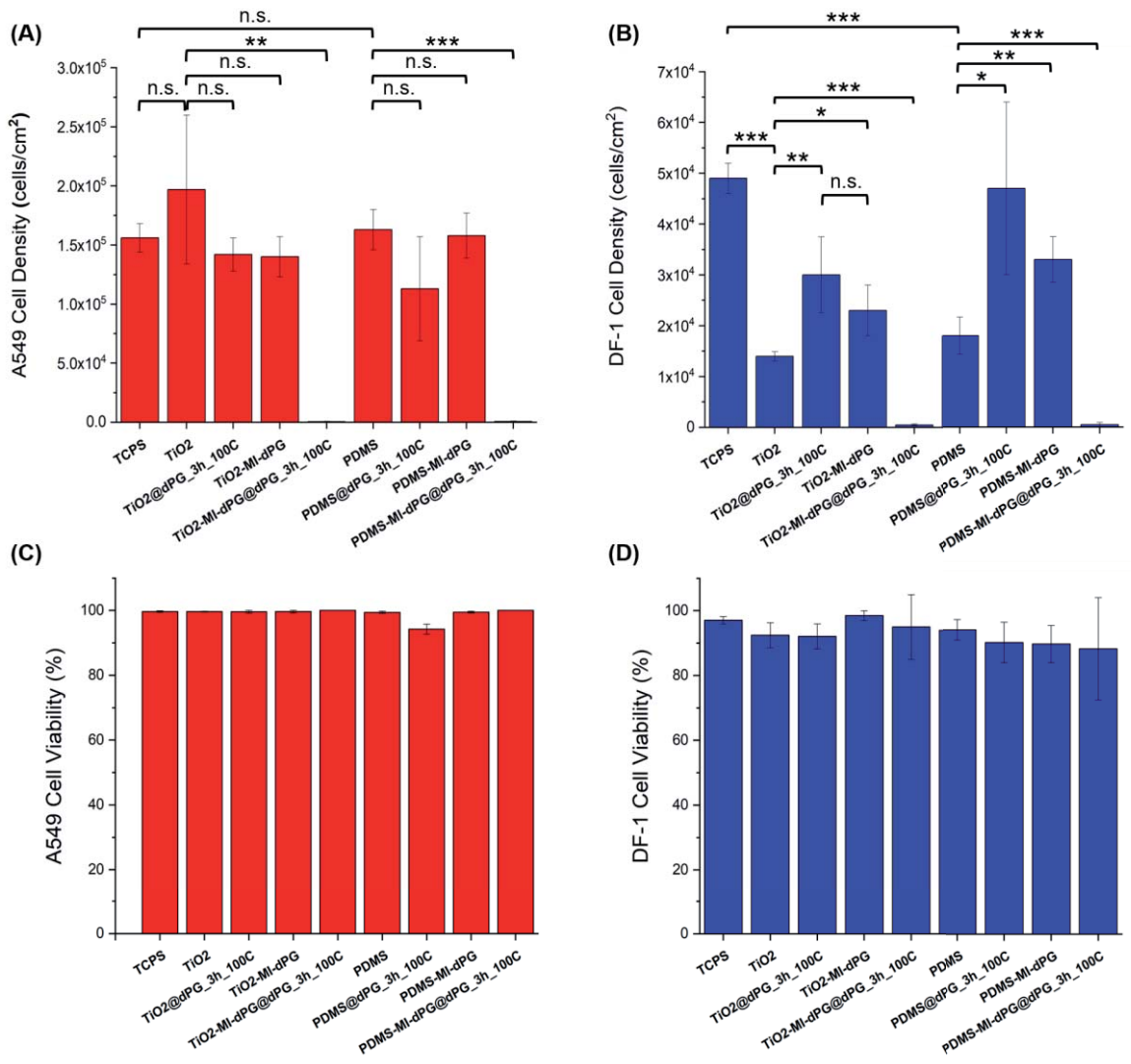

Figure 6. (A) A graph showing the A549 cell density on the various substrates. (B) A graph showing the DF-1 cell density on the various substrates. (C) The cell viability of the A549 cells on the various substrates as obtained via LIVE/DEAD™ cell staining. (D) The cell viability of the DF-1 cells on the various substrates as obtained via LIVE/DEAD™ cell staining. The shown error bars show the standard deviation from the mean. The cell numbers were quantified using at a minimum of 4 images per substrate type. To determine the cell viability, at least 3500 A549 cells or 350 DF-1 cells were analyzed in total per substrate type. In case of antifouling

TiO_2–MI-dPG@dPG$_{3\ h,\ 100\ °C}$ and PDMS–MI-dPG@dPG$_{3\ h,\ 100\ °C}$ a minimum of 10 cells per cell type was analyzed for quantification of the viability. * p = 0.05. ** p = 0.01. *** p = 0.001. The p values were calculated utilizing a two-tailed T-test under the assumption of equal variance.

CONCLUSIONS

In the current work, a novel universal method for the grafting of dendritic polyglycerol (dPG) from mussel-inspired adhesion layers was achieved. The successful grafting of dPG from TiO_2–MI-dPG and PDMS–MI-dPG was confirmed by means of CA measurements, XPS, and SEM. Additionally, it was shown that the dPG grafting process occurred insufficiently in the absence of the MI-dPG coating on both substrate types. When the proliferation and viability of A549 and DF-1 cells on the various coatings was investigated, high numbers of viable cells were observed on the tissue culture polystyrene control, on the bare TiO_2, and on the PDMS substrate. Introduction of the MI-dPG coating to the TiO_2 and PDMS substrates did not influence the A549 cell numbers, whereas the DF-1 cell numbers slightly increased. Subsequent dPG grafting from the MI-dPG coatings led to a dramatic decrease in the cell numbers of both cell types for both substrate types. However, no decrease in the cell viability was observed at the surface (> 88% viability in all cases). The reduced cell numbers were explained by the successful formation of a surface hydration layer on the dPG-grafted coating, which prevented the adhesion and proliferation of cells. The combined results showed that the grafting of dPG from MI-dPG-coated substrates provides a successful strategy for the creation of cell-repelling but highly biocompatible surfaces.

The method developed in the current work gives exact control over the wettability of the substrate (i.e., CA values from 60° till < 10° were easily achieved by adjusting the reaction time and temperature) while maintaining the chemical characteristics of the surface (i.e., effectively a dPG surface with tunable CA was developed). Resulting from the substrate-independent adhesion character of the MI-dPG polymer,[19] the method presented in the current work could be utilized to graft dPG from a broad spectrum of substrates, independent from the chemical or physical characteristics of the substrate materials. Therefore, the direct grafting of antifouling dPG as developed in earlier works,[27-28] can now be extended to a broad range of (medically relevant) hydrophilic and hydrophobic substrates (e.g. prosthetic materials, cardiovascular implant materials, and materials for implantable biosensors). Additionally, the dPG grafting process was performed in bulk (i.e., solvent-free), in the absence of caustic bases, and without activation of the substrate material prior to the grafting process, following a simple two-step procedure (i.e., MI-dPG coating of the substrate and dPG grafting).

EXPERIMENTAL SECTION

All materials and (analytical) methods are described in **Sections 1.1.**, **1.2.**, and **1.3.** of the ESI.

ASSOCIATED CONTENT

The ESI is available free of charge on the **XXXXX** website at DOI: **XXXXX.**

AUTHOR INFORMATION

Contact Corresponding Author:

E-Mail: michaelkulka91@gmail.com (M.W.K.), haag@chemie.fu-berlin.de (R.H.).

Author Contributions:

Michaël W. Kulka (main author): conceived the project and conducted all grafting experiments. Furthermore, he performed and interpreted all CA and SEM measurements. Arushi Garg performed a significant part of the grafting reactions under supervision of the main author during an internship. Philip Nickl fitted and interpreted all XPS data. Furthermore, he proofread the manuscript. Dirk Salz fabricated all titanium dioxide coated glass surfaces using special PVD techniques. Ingo Grunwald (PI) facilitated the machinery required for the titanium dioxide coating process and contributed to the interpretation of results that were discussed in the current work. Jörg Radnik (PI) facilitated the machinery required for the XPS measurements, and contributed to the discussion of the results of the current project. Rainer Haag (PI) facilitated the required pre-knowledge, work space, analytical support, and financial support that were required for this work.

Funding Sources

This work was funded by the German Ministry of Science and Education (BMBF) via the KMU-Innovativ program (under the project name "GlycoVAD").

ACKNOWLEDGEMENTS

First, we would like to thank the BMBF for the financial support of the "GlycoVAD" project via the KMU-Innovativ program. Additionally, we would like to thank M. Eng. J. Stockmann (Bundesanstalt für Materialforschung und -prüfung, Berlin, Germany) for performing the XPS measurements. We would also like to acknowledge the assistance of the core facility BioSupraMol (located at the Freie Universität Berlin and supported by the Deutsche Forschungsgemeinschaft (DFG)) in the chemical characterizations methods that were performed in this work. Finally, we would like to thank Dr. P. Winchester, and Dr. R. Randriantsilefisoa for proofreading the manuscript, and E. Ziegler and Dr. W. Fischer for taking care of all legal matters considering this work.

LITERATURE

[1] a) R. M. Donlan, *Clinical Infectious Diseases* **2001**, 33, 1387; b) D. Pavithra, M. Doble, *Biomedical Materials* **2008**, 3, 034003; c) N. Cole, E. B. H. Hume, A. K. Vijay, P. Sankaridurg, N. Kumar, M. D. P. Willcox, *Investigative Ophthalmology & Visual Science* **2010**, 51, 390; d) Y. Ohko, Y. Utsumi, C. Niwa, T. Tatsuma, K. Kobayakawa, Y. Satoh, Y. Kubota, A. Fujishima, *Journal of Biomedical Materials Research: An Official Journal of The Society for Biomaterials, The Japanese Society for Biomaterials, and The Australian Society for Biomaterials and the Korean Society for Biomaterials* **2001**, 58, 97; e) K. Vasilev, J. Cook, H. J. Griesser, *Expert Review of Medical Devices* **2009**, 6, 553; f) M. D. P. Willcox, E. B. H. Hume, Y. Aliwarga, N. Kumar, N. Cole, *Journal of Applied Microbiology* **2008**, 105, 1817; g) N. Wisniewski, M. Reichert, *Colloids and Surfaces B: Biointerfaces* **2000**, 18, 197; h) C. Yang, G. L. Liang, K. M. Xu, P. Gao, B. Xu, *Journal of Materials Science* **2009**, 44, 1894; i) K. T. Meilert, D. Laub, J. Kiwi, *Journal of Molecular Catalysis A: Chemical* **2005**, 237, 101; j) J. Bozja, J. Sherrill, S. Michielsen, I. Stojiljkovic, *Journal of Polymer Science Part A: Polymer Chemistry* **2003**, 41, 2297; k) B. Meyer, *International Biodeterioration & Biodegradation* **2003**, 51, 249; l) X. Li, Y. Xing, Y. Jiang, Y. Ding, W. Li, *International Journal of Food Science & Technology* **2009**, 44, 2161; m) A. CONTE, G. G. BUONOCORE, A. BEVILACQUA, M. SINIGAGLIA, M. A. D. NOBILE, *Journal of Food Protection* **2006**, 69, 866; n) E.-R. Kenawy, S. D. Worley, R. Broughton, *Biomacromolecules* **2007**, 8, 1359; o) P. Asuri, S. S. Karajanagi, R. S. Kane, J. S. Dordick, *Small* **2007**, 3, 50; p) D. M. Yebra, S. Kiil, K. Dam-Johansen, *Progress in Organic Coatings* **2004**, 50, 75; q) L. D. Chambers, K. R. Stokes, F. C. Walsh, R. J. K. Wood, *Surface and Coatings Technology* **2006**, 201, 3642; r) H.-C. Flemming, *Applied Microbiology and Biotechnology* **2002**, 59, 629.

[2] a) R. O. Darouiche, *New England Journal of Medicine* **2004**, 350, 1422; b) B. W. Trautner, R. O. Darouiche, *Am J Infect Control*

2004, 32, 177; c) I. H. Jaffer, J. C. Fredenburgh, J. Hirsh, J. I. Weitz, *Journal of Thrombosis and Haemostasis* **2015**, 13, S72.
[3] M. Hakim, I. Utama, B. Nugroho, A. Yusim, M. Baithal, I. Suastika, presented at Proceeding of SENTA: 17th Conference on Marine Technology **2017**.
[4] I. B. Beech, J. Sunner, *Current Opinion in Biotechnology* **2004**, 15, 181.
[5] S. Chen, L. Li, C. Zhao, J. Zheng, *Polymer* **2010**, 51, 5283.
[6] L. Q. Xu, D. Pranantyo, J. B. Liu, K.-G. Neoh, E.-T. Kang, Y. X. Ng, S. L.-M. Teo, G. D. Fu, *Rsc Advances* **2014**, 4, 32335.
[7] P. Petrov, G. Georgiev, D. Momekova, G. Momekov, C. B. Tsvetanov, *Polymer* **2010**, 51, 2465.
[8] J. Telegdi, T. Rigó, J. Beczner, E. Kálmán, *Surface Engineering* **2005**, 21, 107.
[9] a) P. Bertrand, A. Jonas, A. Laschewsky, R. Legras, *Macromolecular Rapid Communications* **2000**, 21, 319; b) C. Freij-Larsson, T. Nylander, P. Jannasch, B. Wesslén, *Biomaterials* **1996**, 17, 2199.
[10] a) C. D. Bain, E. B. Troughton, Y. T. Tao, J. Evall, G. M. Whitesides, R. G. Nuzzo, *Journal of the American Chemical Society* **1989**, 111, 321; b) S. P. Pujari, L. Scheres, A. T. M. Marcelis, H. Zuilhof, *Angewandte Chemie International Edition* **2014**, 53, 6322.
[11] H. Lee, S. M. Dellatore, W. M. Miller, P. B. Messersmith, *Science* **2007**, 318, 426.
[12] J. H. Waite, *The Journal of Experimental Biology* **2017**, 220, 517.
[13] J. H. Waite, M. L. Tanzer, *Science* **1981**, 212, 1038.
[14] J. Saiz-Poseu, J. Mancebo-Aracil, F. Nador, F. Busqué, D. Ruiz-Molina, *Angewandte Chemie International Edition* **2019**, 58, 696.
[15] H. Lee, N. F. Scherer, P. B. Messersmith, *Proc Natl Acad Sci U S A* **2006**, 103, 12999.
[16] S. M. D. Haeshin Lee, William M. Miller, Phillip B. Messersmith, *Science* **2007**, 318, 426.

[17] a) R. Batul, T. Tamanna, A. Khaliq, A. Yu, *Biomaterials science* **2017**, 5, 1204; b) T. G. Kim, H. Lee, Y. Jang, T. G. Park, *Biomacromolecules* **2009**, 10, 1532.
[18] Q. Wei, F. Zhang, J. Li, B. Li, C. Zhao, *Polymer Chemistry* **2010**, 1, 1430.
[19] Q. Wei, K. Achazi, H. Liebe, A. Schulz, P.-L. M. Noeske, I. Grunwald, R. Haag, *Angewandte Chemie International Edition* **2014**, 53, 11650.
[20] a) M. W. Kulka, I. S. Donskyi, N. Wurzler, D. Salz, Ö. Özcan, W. E. S. Unger, R. Haag, *ACS Applied Bio Materials* **2019**, 2, 5749; b) M. Li, C. Schlaich, M. W. Kulka, I. S. Donskyi, T. Schwerdtle, W. E. Unger, R. Haag, *Journal of Materials Chemistry B* **2019**.
[21] C. Schlaich, L. Yu, L. C. Camacho, Q. Wei, R. Haag, *Polymer Chemistry* **2016**, 7, 7446.
[22] a) K. Prime, G. Whitesides, *Science* **1991**, 252, 1164; b) J. H. Lee, J. Kopecek, J. D. Andrade, *Journal of Biomedical Materials Research* **1989**, 23, 351.
[23] S. Han, C. Kim, D. Kwon, *Polymer* **1997**, 38, 317.
[24] A. Judge, K. McClintock, J. R. Phelps, I. MacLachlan, *Molecular Therapy* **2006**, 13, 328.
[25] C. Siegers, M. Biesalski, R. Haag, *Chemistry – A European Journal* **2004**, 10, 2831.
[26] a) Q. Wei, S. Krysiak, K. Achazi, T. Becherer, P.-L. M. Noeske, F. Paulus, H. Liebe, I. Grunwald, J. Dernedde, A. Hartwig, T. Hugel, R. Haag, *Colloids and Surfaces B: Biointerfaces* **2014**, 122, 684; b) T. B. Qiang Wei, Radu-Cristian Mutihac, Paul-Ludwig Michael Noeske, Florian Paulus, Rainer Haag, and Ingo Grunwald, *Biomacromolecules* **2014**, 15, 3061.
[27] a) E. Moore, B. Delalat, R. Vasani, G. McPhee, H. Thissen, N. H. Voelcker, *ACS Applied Materials & Interfaces* **2014**, 6, 15243; b) M. Khan, W. T. S. Huck, *Macromolecules* **2003**, 36, 5088.
[28] T. Weber, M. Bechthold, T. Winkler, J. Dauselt, A. Terfort, *Colloids and Surfaces B: Biointerfaces* **2013**, 111, 360.
[29] A. Sunder, R. Hanselmann, H. Frey, R. Mülhaupt, *Macromolecules* **1999**, 32, 4240.

[30] P. Louette, F. Bodino, J.-J. Pireaux, *Surface Science Spectra* **2005**, 12, 38.
[31] C. Schlaich, L. Cuellar Camacho, L. Yu, K. Achazi, Q. Wei, R. Haag, *ACS Applied Materials & Interfaces* **2016**, 8, 29117.

Supporting Information for

Surface-Initiated Grafting of Dendritic Polyglycerol from Mussel-Inspired Adhesion Layers for the Creation of Biocompatible Cell-Repelling Coatings

Michaël W. Kulka,[a] Chuanxiong Nie,[a] Philip Nickl,[a,b] Yannic Kerkhoff,[a] Arushi Garg,[a] Dirk Salz,[c] Jörg Radnik,[b] Ingo Grunwald,[c,d] Rainer Haag*,[a]

[a] Institute for Chemistry and Biochemistry, Freie Universität Berlin, Takustraße 3, 14195 Berlin, Germany

[b] BAM – Federal Institute for Material Research and Testing, Division of Surface Analysis and Interfacial Chemistry, Unter den Eichen 44-46, 12205 Berlin, Germany

[c] Fraunhofer Institute for Manufacturing Technology and Advanced Materials IFAM, Wiener Straße12, 28359 Bremen, Germany

[d] Hochschule Bremen – City University of Applied Sciences, Department of Industrial and Environmental Biology, Neustadtswall 30, 28199 Bremen, Germany

1. EXPERIMENTAL SECTION

1.1. CHEMICALS & LAB TECHNIQUES

The chemicals were purchased from Merck (Darmstadt, Germany) and were used as received without further purification, unless mentioned otherwise. Besides, NaOH pellets bought from VWR International (Darmstadt, Germany). Non-protic solvents were either purchased in an extra-dry form or were dried with the help of CaH_2, prior to use. Dialysis was performed using benzoylated cellulose tubes (D7884, width: 32 mm; molecular-weight cutoff (MWCO): 2 kDa) purchased from Merck (Darmstadt, Germany). Deionized water was purified using a water purification system by Millipore (Burlington, Massachusetts, USA), with a minimum resistivity of 18.0 MΩ cm. All grafting reactions were performed under dry and inert conditions (argon atmosphere), using Schlenk technique and custom-made glassware (**Figure S1**).

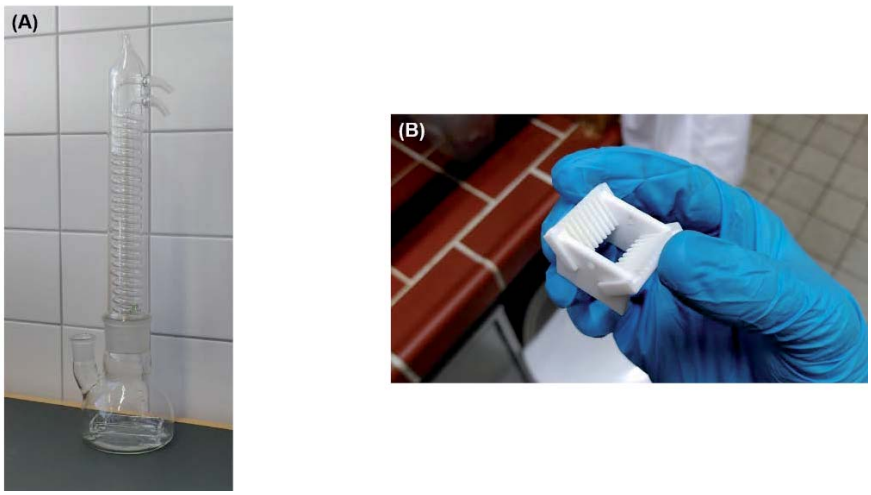

Figure S1. (A) Custom-made glassware for the incubation of the substrates with glycidol. The glassware was fabricated in such a manner that it could withstand the high vacuum (1 x 10^{-3} bar)

conditions that were required for the drying process of the flask. The cooler was necessary because glycidol tends to evaporate at elevated temperatures (> 100 °C). The glass flask contained a glass rack at the bottom, which was used for the placement of the substrate holders. (B) A picture of one of the custom-made Teflon substrate holders that were used to place the (MI-dPG-coated) substrates into the reaction flask.

1.1.1. Static Water Contact Angle Measurements

Static water contact angle (CA) measurements were performed by applying a Dataphysics Instruments GmbH (Filderstadt, Germany) OCA 20 contact-angle measure device, according to the sessile drop method. The OCA 20 system was equipped with a six-fold zoom lens with integrated fine focus (+/- 6 mm) and a high light-transmitting-capacity CCD-camera, with a resolution of max 768 x 576 pixels. The used video system was a high performance imaging processing system, with a 132 Mbytes/s data transfer rate, and a digitizing speed up to 50 images/s. Image processing was performed by applying SCA 202 software also by Dataphysics Instruments GmbH.

1.1.2. Scanning Electron Microscopy

The surface morphology was investigated using a field emission scanning electron microscope (FE-SEM) model SU8030 by Hitachi (Chiyoda, Japan), at an accelerating voltage (V_{ac}) of 20 kV, a current of 15 μA, and a working distance of 8.5 inches. The substrates were sputtered with a 5

nm conductive gold layer prior to the SEM measurements, using a CCU-010 sputter machine by Safematic GmbH (Bad Ragaz, Switzerland).

1.1.3. X-Ray Photoelectron Spectroscopy

X-ray photoelectron spectroscopy (XPS) spectra were recorded on a Kratos (Manchester, UK) Axis Ultra DLD spectrometer, equipped with a monochromatic Al Kα X-ray source. The spectra were measured in normal emission, and a source-to-sample angle 60° was used. All spectra were recorded utilizing the fixed analyzer transmission (FAT) mode. The binding energy scale of the instrument was calibrated, following a technical procedure provided by Kratos Analytical Ltd (calibration was performed according to ISO 15472). The spectra were recorded utilizing the instrument's slot and hybrid lens modes. An analysis area of approximately a 300 μm x 700 μm was investigated; charge neutralization was applied. For quantification, the survey spectra were measured with a pass energy of 80 electron volt (eV), and the spectra were quantified utilizing the empirical sensitivity factors that were provided by KRATOS (the sensitivity factors were corrected with the transmission function of the spectrometer).

The high-resolution XPS spectra were measured with a pass energy of 20 eV, and the respective data were processed using UNIFIT spectrum processing software.[1] For fitting, a Shirley background and a Gaussian/Lorentzian sum function (peak shape model GL (30)) were used. If not denoted otherwise, the L-G mixing component was set to 0.35 for all peaks. In case of the C1s spectra, peak fitting was performed in such a manner that all residual structures were

removed, and all binding energies were calibrated to the signal observed for the aliphatic C–C bond component (observed at 248.8 eV).

1.1.4. MI-dPG Synthesis

Dendritic polyglycerol (dPG) with M_n: 12,000 and M_w: 16,000 was polymerized in a one-step ring-opening anionic polymerization, as described in earlier work by Sunder et al.[2] The amine-functionalized dPG (dPG–NH_2) was produced by mesylation, azidation, and subsequent Staudinger reduction of the introduced azides, according to procedures that were earlier published by our group.[3] The dPG–NH_2 (4 g, 0.38 mmol) was dissolved in MeOH (100 ml), and 10% HCl-solution was added until a neutral pH was obtained. Subsequently, an aqueous buffer solution of 2–(N–morpholino) ethane sulfonic acid (MES) (0.1 M, pH: 4.8) was added, so that a 1:1 (V:V) ratio of MeOH to buffer was obtained. Next, 3,4–dihydroxy–hydrocinnamic acid (DHHA) (20 g, 110 mmol, 2 equivalent respectively to 100% of the –NH_2 groups), 1–ethyl–3–(3–dimethylamino)propyl)carboiimide (21 g, 110 mmol, 2.0 equivalent respective to 100% of the –NH_2 groups) were added, and the resulting reaction mixture was stirred for 16 h at room temperature. The reaction mixture was then purified by dialysis in MeOH. In order to increase product stability (i.e., to prevent polymerization), 37% HCl-solution was added to the dialysis-solution (1 drop per gram of product). The pure product was obtained upon removal of the solvent by means of rotary evaporation. The product was stored under argon atmosphere at -20 °C.

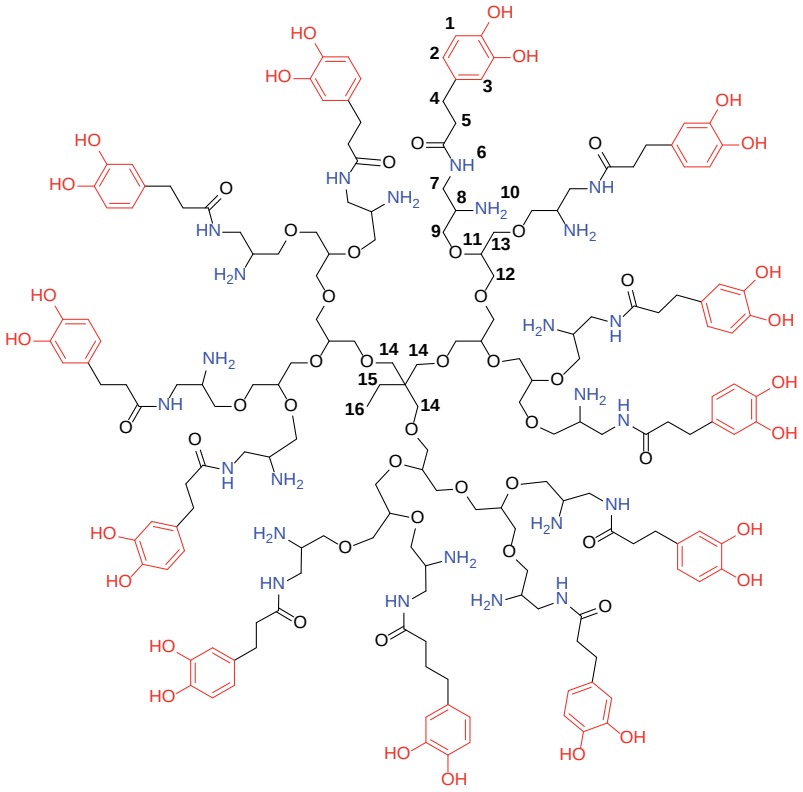

Figure S2. The molecular structure of MI-dPG. The depicted figure is an idealized dendrimer. The dPG-backbone structure shown in black varies with the molecular size of the MI-dPG and also contains unfunctionalized –OH moieties, resulting from chain termination during the polymerization process.

^{1}H NMR (500 MHz; CD_3OD): δ= 6.68-6.53 (**1-3**, m, aromatic protons); 4.21-3.02 (**7-14**, m, dPG-backbone); 2.74 (**5**, m, –RCO**C**$H_2$$CH_2$CR–); 2.44 (**4**, m, –$COCH_2$**C**$H_2$R–).[4]

^{13}C NMR (700 MHz; CD_3OD): δ= 175.19, 174.27, and 172.13 (carboxylic carbons); 148.46-115.47 (aromatic carbons); 78.32-51.19 (dPG-backbone carbons); 37.532 and 35.582 (–CO**C**$H_2$$CH_2$C–); 30.589 and 30.007 (–$COCH_2$**C**H_2C–) ppm.[5]

1.2. SURFACE CHEMISTRY

1.2.1. Coating glass with TiO_2 via Physical Vapor Deposition

Glass microscope slides (76 mm x 26 mm, thickness 1 mm) purchased from VWR International (Radnor, Pennsylvania, USA) were coated with a transparent titanium dioxide (TiO_2) layer (ca. 30 nm) by means of physical vapor deposition (PVD). The TiO_2 coatings were prepared using radio frequency (13.56 MHz) reactive sputtering. Oxygen 5.0 and argon 4.6 purchased from Linde plc (Munich, Germany), and a titanium target (99.9 % purity) purchased from Sindlhauser Materials GmbH (Kempten, Germany) were used as source materials. The sputtering chamber (50 cm x 50 cm x 50 cm) was evacuated to a base pressure of 1 x 10^{-5} mbar. Subsequently, the substrates were plasma cleaned with oxygen (60 standard cubic centimeter per minute (sccm)) and argon (60 sccm) for 5 min (sputtering power: 2380 W). Without venting the chamber, the target was sputtered using an Ar-flux (120 sscm, sputter power: 2380 W). After the sputter plasma showed a blue color, an additional 9 sccm of oxygen was added to the chamber. The blue color indicated metallic titanium on the surface of the target, i.e., the absence of a TiO_2-layer. After a reactive sputtering time of 10 min, a 25 nm thick TiO_2-coating was obtained on the substrates. To get fully oxidized TiO_2, the distance between target and substrate was maximized (58 cm).

1.2.2. PDMS Spin Coating

Glass microscope slides (76 mm x 26 mm, thickness 1 mm) purchased from VWR International (Radnor, Pennsylvania, USA) were spin coated with a solution of PDSM in xylol (1 wt%). The glass slides (cut in ca. 1 x 1 cm) were spin coated at 3,000 rpm for 1 min. Spin coating was performed using a WS-650Mz-23NPPB spin coater by Laurell Technologies corporation (North Wales, Pennsylvania, USA).

1.2.3. MI-dPG Coating

TiO_2-coated glass substrates were cleaned by ultrasonic treatment in EtOH for 10 min, prior the coating procedure. The cleaned surfaces were then immerged in a solution of MI-dPG (4 mg, 1.33 x 10^{-4} mmol) in MeOH (2 ml) to which an aqueous solution of 3–(*N*–morpholino)propane sulfonic acid (MOPS) buffer (2 ml, 0.1 M, pH: 8.5) was added, initiating the polymerization reaction of MI-dPG. The surfaces were immersed in the polymerizing solution for 10 min (immersion depth ca 1 cm), after which they were removed from the solution and thoroughly rinsed with EtOH. Subsequently, the substrates were dried under a N_2-flow and placed in a custom glass flask (**Figure S1**) at 110 °C under high vacuum conditions (1 x 10^{-3} bar) for > 10 h. The PDMS-spin-coated substrates were functionalized with MI-dPG according to the same procedure.

1.2.4. dPG Grafting

Prior to the grafting reaction, glycidol was dried overnight in a pre-dried Schlenk-flask containing molecular sieve (type 562 C, pore size 3 Å) by Carl Roth GmbH (Karlsruhe, Germany). Additionally, the (MI-dPG-coated) substrates were dried overnight at 110 °C under high vacuum conditions (1 x 10^{-3} bar) using custom glassware (**Figure S1**). The flask was removed from the oil bath and was cooled down to room temperature. The flask was then flushed with argon, and subsequently glycidol was added to the flask under argon backflow. Next, the flask was placed back in the oil bath at 80 °C, 100 °C, or 120 °C for 30 min, 1 h, 3 h, or 24 h, allowing the grafting of dendritic polyglycerol (dPG) from the surface. After the grafting reaction, the substrates were removed from the system, thoroughly rinsed with EtOH (3x), and subsequently placed in a beaker glass containing in EtOH for > 10 h. Next, the substrates were dried under N_2 flow and dried at 50 °C for 1 h prior to any further measurements.

1.3. BIOLOGICAL ASSAYS

1.3.1. LIVE/DEAD Staining of A549 and DF-1 Cells

Human adenocarcinoma cells (A549 cells) and chicken fibroblast cells (DF-1 cells) were maintained as a monolayer culture in tissue culture polystyrene (TCPS) petri dishes containing Dulbecco's Modified Eagle's Medium (DMEM) supplemented with fetal bovine serum (FBS) (10 v%), streptomycin (100 mg/ml), and penicillin (100 units/ml). The cell lines were cultured under 5% CO_2 at 37 °C, using a laboratory CO_2 incubator by Heraeus Holding GmbH (Hanau, Germany). MI-dPG coated substrates were prepared according to the procedure described in

Section 1.2.3. of this document. Subsequently, the samples were sterilized with EtOH (75 vol% in Milli-Q) for 10 min and washed with cell culture medium before the seeding. The cells were seeded at a concentration of 1 x 10^6 cells/mL. After 24 h of culturing, the cells were stained utilizing a commercially available LIVE/DEAD™ Viability/Cytotoxicity Kit (Order No: L3224) by Thermo Fisher Scientific Inc. (Waltham, Massachusetts, USA) and visualized using AxioObserver Z.1 microscope by the Carl Zeiss AG (Oberkochen, Germany). Zen blue software (also provided by the Carl Zeiss AG) was applied for image capturing.

1.3.2. Automated LIVE/DEAD™ Quantification

Automatic image analysis was performed with the Java-based image processing program "ImageJ" developed by the Laboratory for Optical and Computational Instrumentation of the University of Wisconsin (Madison, Wisconsin, USA).[6] Cell recognition was achieved via distinctive assessment of fluorescence signals from live and dead cells. First, the cells were separated from the background utilizing the "subtract background" function of "ImageJ". In this process, a rolling ball radius of 50 pixels was chosen. The cells were separated from the background by thresholding the fluorescence value of the 16-bit images (threshold $_{Live}$: 1510, threshold $_{Dead}$: 150). After binarization, cell clusters were segmented utilizing a "watershed algorithm" for the separation of different objects in an image (coefficient: 0.1). Subsequently, the particle analyzer function of ImageJ was utilized for cell quantification and morphology analysis. To avoid counting single pixels or cell fragments, only objects above a specific size were analyzed (i.e., only objects bigger than 10 pixels were analyzed). Finally, the results were

manually evaluated by comparing the outlines of the analyzed particles with the original fluorescence images. Insufficiently segmented cell clusters were manually recounted.

2. RESULTS

2.1. CA Results

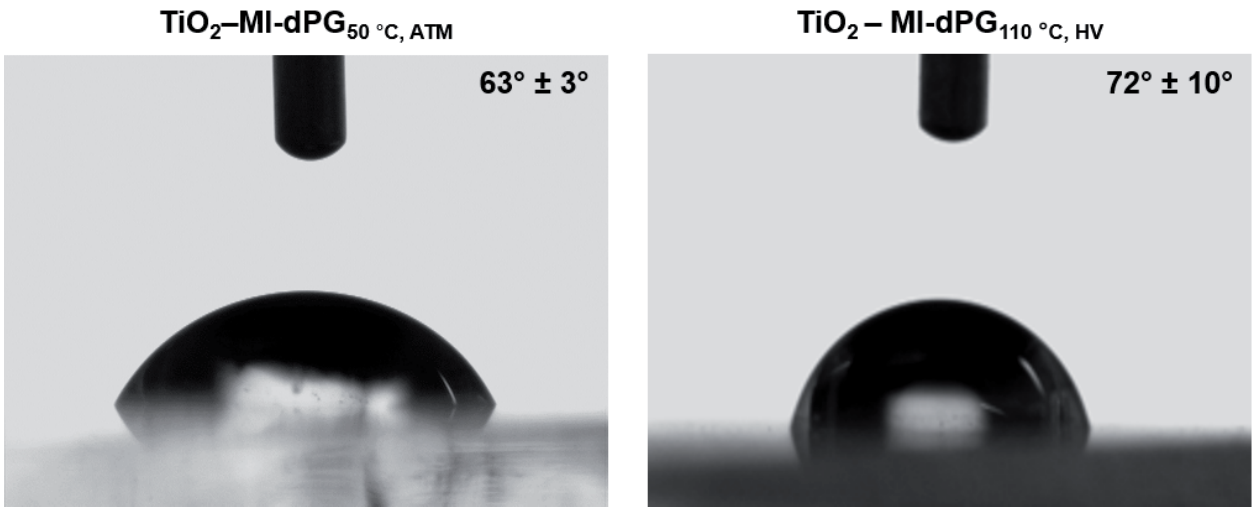

Figure S3. CA Pictures of TiO_2–MI-$dPG_{50\ °C,\ ATM}$ (left) and TiO_2–MI-$dPG_{110\ °C,\ HV}$ (right). An increase in the CA was observed after drying of the coating at elevated temperatures under high vacuum conditions.

Table S1. CA values for TiO_2–MI-dPG$_{50\ °C,\ ATM}$ and TiO_2–MI-dPG$_{110\ °C,\ HV}$.

S[A]		**TiO$_2$–MI-dPG$_{50\ °C,\ ATM}$**		**Mean (μ)**	**STDV[B] (σ)**
I	65.8°	64.1°	64.5°		
II	59.6°	63.2°	64.6°	62.6°	2.9°
III	56.1°	61.4°	64.0°		
		TiO$_2$–MI-dPG$_{110\ °C,\ HV}$			
I	60.1°	52.1°	62.6°		
II	79.6°	77.6°	79.8°	71.9°	10.0°
III	79.1°	78.3°	78.2°		

Note for A, S = Substrate. Note for B, STDV = Standard deviation from the mean.

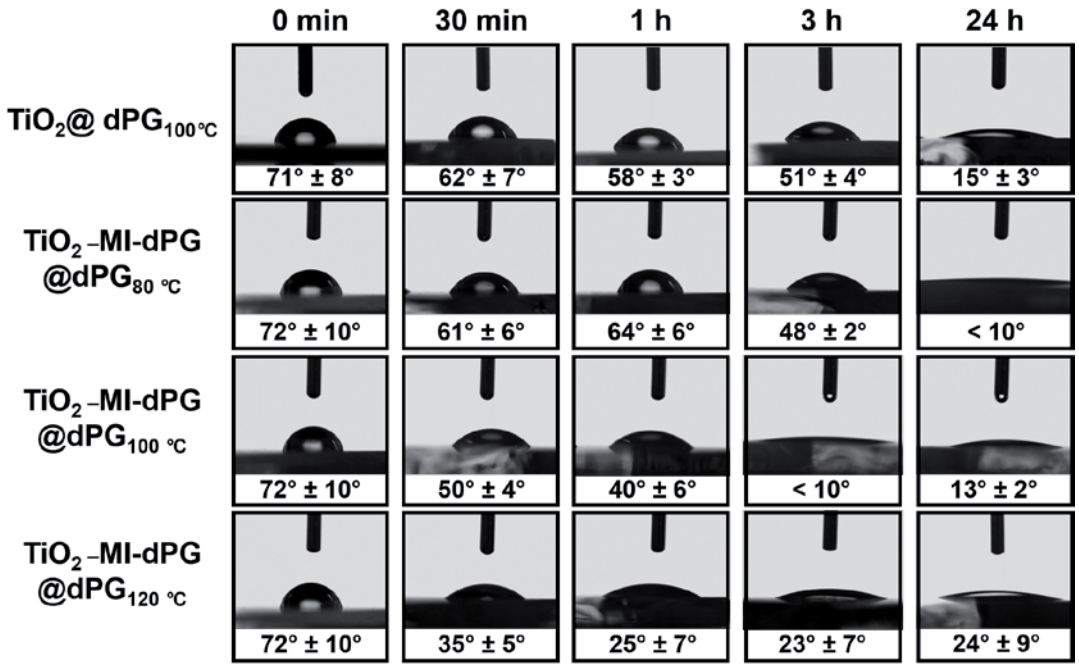

Figure S4. The images and the average CA values obtained for TiO_2@dPG and TiO_2–MI-dPG@dPG at various dPG grafting times and temperatures.

Table S2. CA values for TiO_2 and TiO_2–MI-dPG after dPG grafting at various times and temperatures.

S^A	Bare TiO_2			Mean (μ)	STDV^B (σ)
I	72.4°	69.0°	79.5°		
II	80.1°	73.5°	78.3°	71.9°	6.1°
III	67.5°	63.9°	63.0°		

		TiO_2@dPG$_{30\ min,\ 100\ °C}$			
I	60.2°	65.2°	62.6°		
II	66.9°	64.7°	64.2°	62.3°	7.3°
III	42.6°	68.0°	66.2°		
		TiO_2@dPG$_{1\ h,\ 100\ °C}$			
I	61.2°	58.0 °	55.7°		
II	55.3°	56.3°	59.0°	57.7°	2.5°
III	53.6°	58.4°	61.4°		
		TiO_2@dPG$_{3\ h,\ 100\ °C}$			
I	53.5°	54.2°	52.4°		
II	54.2°	41.2°	51.2°	51.4°	3.9°
III	54.2°	51.6°	50.0°		
		TiO_2@dPG$_{24\ h,\ 100\ °C}$			
I	17.0°	12.2°	11.5°		
II	16.6°	15.1°	16.7°	15.1°	2.5°
III	11.4°	17.3°	18.2°		

		TiO_2–MI-dPG			
I	60.1°	52.1°	62.6°		
II	79.6°	77.6°	79.8°	71.9°	10.0°
III	79.1°	78.3°	78.2°		
		TiO_2–MI-dPG@dPG$_{30\ min,\ 80\ °C}$			
I	63.2°	47.0°	62.2°		
II	63.7°	62.1°	58.4°	61.3°	5.6°
III	63.3°	67.9°	64.0°		
		TiO_2–MI-dPG@dPG$_{1\ h,\ 80\ °C}$			
I	72.0°	69.1°	70.8°		
II	54.4°	55.8°	57.3°	64.0°	6.2°
III	66.4°	63.9°	66.3°		
		TiO_2–MI-dPG@dPG$_{3\ h,\ 80\ °C}$			
I	50.7°	46.9°	49.6°		
II	47.6°	44.8°	44.8°	47.8°	1.9°
III	48.1°	49.1°	48.6°		

	TiO_2–MI-dPG@dPG$_{24\ h,\ 80\ °C}$				
I	9.3°	5.9°	< 10°		
II	3.1°	< 10°	< 10°	< 10°	N.A.
III	4.5°	8.8°	< 10°		
	TiO_2–MI-dPG@dPG$_{30\ min,\ 100\ °C}$				
I	57.8°	54.8°	47.4°		
II	48.9°	46.5°	53.7°	50.1°	4.0°
III	48.0°	46.2°	47.4°		
	TiO_2–MI-dPG@dPG$_{1\ h,\ 100\ °C}$				
I	44.2°	44.4°	42.5°		
II	39.1°	47.5°	33.3°	40.1°	5.6°
III	42.3°	39.1°	28.8°		
	TiO_2–MI-dPG@dPG$_{3\ h,\ 100\ °C}$				
I	< 10°	< 10°	10.7°		
II	< 10°	< 10°	< 10°	< 10°	N.A.
III	< 10°	< 10°	< 10°		

	TiO_2–MI-dPG@dPG$_{24\ h,\ 100\ °C}$				
I	12.1°	12.5°	13.3°		
II	< 10°	13.8°	11.6°	12.5°	1.5°
III	13.4°	14.7°	11.9°		
	TiO_2–MI-dPG@dPG$_{30\ min,\ 120\ °C}$				
I	32.8°	40.3°	34.6°		
II	28.7°	26.6°	39.4°	35.0°	4.5°
III	36.3°	36.9°	38.9°		
	TiO_2–MI-dPG@dPG$_{1\ h,\ 120\ °C}$				
I	33.5°	14.9°	27.3°		
II	31.7°	21.6°	33.6°	25.4°	6.5°
III	19.3°	27.4°	19.0°		
	TiO_2–MI-dPG@dPG$_{3\ h,\ 120\ °C}$				
I	30.7°	20.1°	14.6°		
II	22.4°	13.7°	15.3°	23.1°	7.2°
III	26.9°	29.9°	34.1°		

	TiO_2–MI-dPG@dPG$_{24\ h,\ 120\ °C}$				
I	24.2°	11.8°	13.7°		
II	37.8°	24.3°	15.9°	24.1°	9.2°
III	22.5°	27.5°	39.6°		
	Bare PDMS				
I	111.5°	112.3°	110.8°		
II	102.6°	113.9°	106.4°	108.1°	3.8°
III	106.0°	103.7°	105.8°		

Note for A, S = Substrate. Note for B, STDV = Standard deviation from the mean.

2.2. XPS Results

Table S3. Highly resolved C1s spectra for TiO_2, TiO_2–MI-dPG$_{50\ °C,\ ATM}$, TiO_2–MI-dPG$_{110\ °C,\ HV}$ as determined by XPS**.**

Substrate	*Spectrum*	*Binding energy*	*L-G Mixing*	*FWHM*	*Chemical state*	*Rel. Area*
TiO_2	**C 1s**	284.8	0.35	1.4	C–C	0.78
		286.1	0.35	1.0	C–O	0.15
		288.2	0.35	1.0	C=O	0.07
TiO_2 – MI-dPG$_{50\ °C,\ ATM}$	**C1s**	284.8	0.35	1.2	C–C	0.40
		286.3	0.35	1.1	C–O	0.54
		288.1	0.35	1.1	C=O	0.06
TiO_2 – MI-dPG$_{110\ °C,\ HV}$	**C1s**	284.8	0.35	1.2	C–C	0.44
		286.2	0.35	1.1	C–O	0.48
		288.1	0.35	1.1	C=O	0.08
		289.2	0.35	1.1	O–C=O	0.00

Fitting parameters and the relative areas for C1s component peaks at various binding energies in XPS. The values reported for the C–O component include the C–N component resulting from peak overlap.

Table S4. The C–O/C–C component peak area ratios for TiO_2, TiO_2–MI-$dPG_{50\ °C,\ ATM}$, and TiO_2–MI-$dPG_{110\ °C,\ HV}$ as determined by XPS.

Substrate	*C–O/C–C*
TiO_2	0.19
TiO_2–MI-$dPG_{50\ °C,\ ATM}$	1.35
TiO_2 –MI-$dPG_{110\ °C,\ HV}$	1.09

The C–O/C–C component peak area ratios were calculated by dividing the relative area of the peak fitted at ~286.5 eV (for the C–O component) by the relative area for the peak fitted at ~285.0 eV (for the C–C and C=C components). The values reported for the C–O component include the C–N component resulting from peak overlap.

Table S5. Atomic C-, O-, N- and Ti-fractions of TiO_2, TiO_2–MI-$dPG_{50\ °C,\ ATM}$ and TiO_2–MI-$dPG_{110\ °C,\ HV}$ as determined by XPS.

Substrate	*C(at.%)[A]*	*O (at.%)[A]*	*N (at.%)[A]*	*Ti (at.%)[A]*
TiO_2	22.3	52.3	0.6	12.9
TiO_2–MI-$dPG_{50\ °C,\ ATM}$	67.4	23.3	7.3	0.6
TiO_2–MI-$dPG_{110\ °C,\ HV}$	66.6	24.2	5.8	0.8

The elemental contents were extracted from the respective survey spectra (**Figure S9** of the appendix). Note for A, at.% = atomic percentage.

Table S6. Highly resolved C1s spectra for TiO_2 and TiO_2–MI-dPG after dPG grafting at varying reaction times and temperatures as determined by XPS.

Substrate	*Spectrum*	*Binding energy*	*L-G Mixing*	*FWHM*	*Chemical state*	*Rel. Area*
TiO_2	**C 1s**	284.8	0.35	1.4	C–C	0.78
		286.1	0.35	1.0	C–O	0.15
		288.2	0.35	1.0	C=O	0.07

TiO$_2$ @dPG$_{30\ min,\ 100\ °C}$	**C1s**	284.8	0.35	1.2	C–C	0.41
		286.2	0.35	1.2	C–O	0.50
		288.1	0.35	1.1	C=O	0.05
		289.0	0.35	1.1	O–C=O	0.04
TiO$_2$ @dPG$_{1\ h,\ 100\ °C}$	**C1s**	284.8	0.35	1.2	C–C	0.36
		286.2	0.35	1.2	C–O	0.58
		288.1	0.35	1.1	C=O	0.04
		289.0	0.35	1.1	O–C=O	0.02
TiO$_2$ @dPG$_{3\ h,\ 100\ °C}$	**C1s**	284.8	0.35	1.1	C–C	0.31
		286.0	0.35	1.3	C–O	0.60
		287.8	0.35	1.1	C=O	0.03
		288.8	0.35	1.1	O–C=O	0.06
TiO$_2$ @dPG$_{24\ h,\ 100\ °C}$	**C1s**	284.8	0.35	1.0	C–C	0.17
		286.3	0.35	1.1	C–O	0.77
		287.8	0.35	1.1	C=O	0.04
		289.1	0.35	1.1	O–C=O	0.02

	C1s	284.8	0.35	1.2	C–C	0.34
TiO_2 – MI-dPG @$dPG_{30\ min,\ 80\ °C}$		286.2	0.35	1.1	C–O	0.58
		288.0	0.35	1.1	C=O	0.08
		289.1	0.35	1.1	O–C=O	0.01
	C1s	284.8	0.35	1.3	C–C	0.34
TiO_2 – MI-dPG @$dPG_{1\ h,\ 80\ °C}$		286.2	0.35	1.1	C–O	0.56
		288.0	0.35	1.1	C=O	0.04
		283.6	0.35	1.1	Charge[A]	0.06
	C1s	284.8	0.35	1.2	C–C	0.28
TiO_2 – MI-dPG @$dPG_{3\ h,\ 80\ °C}$		286.2	0.35	1.2	C–O	0.68
		288.1	0.35	1.2	C=O	0.03
		283.9	0.35	1.2	Charge[A]	0.06
	C1s	284.8	0.35	1.0	C–C	0.29
TiO_2 – MI-dPG @$dPG_{24\ h,\ 80\ °C}$		286.3	0.35	1.1	C–O	0.67
		287.8	0.35	1.1	C=O	0.03
		289.0	0.35	1.1	O–C=O	0.01

TiO_2 – MI-dPG @$dPG_{30\ min,\ 100\ °C}$	**C1s**	284.8	0.35	1.0	C–C	0.24
		286.3	0.35	1.1	C–O	0.70
		287.9	0.35	1.1	C=O	0.05
		289.0	0.35	1.1	O–C=O	0.01
TiO_2 – MI-dPG @$dPG_{1\ h,\ 100\ °C}$	**C1s**	284.8	0.35	1.0	C–C	0.18
		286.3	0.35	1.1	C–O	0.77
		287.9	0.35	1.1	C=O	0.04
		289.1	0.35	1.1	O–C=O	0.01
TiO_2 – MI-dPG @$dPG_{3\ h,\ 100\ °C}$	**C1s**	284.8	0.35	1.0	C–C	0.16
		286.3	0.35	1.1	C–O	0.80
		287.9	0.35	1.1	C=O	0.04
		289.0	0.35	1.1	O–C=O	0.01
TiO_2 – MI-dPG @$dPG_{24\ h,\ 100\ °C}$	**C1s**	284.8	0.35	1.0	C–C	0.09
		286.4	0.35	1.1	C–O	0.86
		287.8	0.35	1.1	C=O	0.04
		289.1	0.35	1.1	O–C=O	0.01

	C1s	284.8	0.35	1.0	C–C	0.22
TiO_2 – MI-dPG @$dPG_{30\ min,\ 120\ °C}$		286.3	0.35	1.1	C–O	0.73
		287.9	0.35	1.1	C=O	0.04
		289.0	0.35	1.1	O–C=O	0.01
	C1s	284.8	0.35	1.0	C–C	0.20
TiO_2 – MI-dPG @$dPG_{1\ h,\ 120\ °C}$		286.3	0.35	1.1	C–O	0.75
		287.9	0.35	1.1	C=O	0.04
		289.0	0.35	1.1	O–C=O	0.01
	C1s	284.8	0.35	1.0	C–C	0.18
TiO_2 – MI-dPG @$dPG_{3\ h,\ 120\ °C}$		286.3	0.35	1.1	C–O	0.78
		287.8	0.35	1.1	C=O	0.04
		289.1	0.35	1.1	O–C=O	0.01
	C1s	284.8	0.35	1.0	C–C	0.06
TiO_2 – MI-dPG @$dPG_{24\ h\ ,120\ °C}$		286.4	0.35	1.1	C–O	0.90
		287.8	0.35	1.1	C=O	0.03
		289.1	0.35	1.1	O–C=O	0.01

Fitting parameters and the relative areas for C1s component peaks at various binding energies in XPS. The values reported for the C–O component include the C–N component resulting from peak overlap. Note for A, during XPS-measurements the substrates might electrostatically charge, due to the removal of electrons in proximity of the atomic nuclei. This charge is automatically corrected via charge correction procedures, but might still lead to observable peaks in the highly resolved C1s spectra.

Table S7. The C–O/C–C component peak area ratios for TiO_2, TiO_2–MI-dPG with dPG grafting at varying reaction times and temperatures as determined by XPS

Substrate	*C–O/C–C*
TiO_2	0.19
TiO_2@dPG$_{30\ min,\ 100\ °C}$	1.22
TiO_2@dPG$_{1\ h,\ 100\ °C}$	1.61
TiO_2@dPG$_{3\ h,\ 100\ °C}$	1.94
TiO_2@dPG$_{24\ h,\ 100\ °C}$	4.53
TiO_2–MI-dPG@dPG$_{30\ min,\ 80\ °C}$	1.71
TiO_2–MI-dPG@dPG$_{1\ h,\ 80\ °C}$	1.65
TiO_2–MI-dPG@dPG$_{3\ h,\ 80\ °C}$	2.43

TiO_2–MI-dPG@dPG$_{24\ h,\ 80\ °C}$	2.31
TiO_2–MI-dPG@dPG$_{30\ min,\ 100\ °C}$	2.92
TiO_2–MI-dPG@dPG$_{1\ h,\ 100\ °C}$	4.28
TiO_2–MI-dPG@dPG$_{3\ h,\ 100\ °C}$	5.00
TiO_2–MI-dPG@dPG$_{24\ h,\ 100\ °C}$	9.56
TiO_2–MI-dPG@dPG$_{30\ min,\ 120\ °C}$	3.32
TiO_2–MI-dPG@dPG$_{1\ h,\ 120\ °C}$	3.75
TiO_2–MI-dPG@dPG$_{3\ h,\ 120\ °C}$	4.33
TiO_2–MI-dPG@dPG$_{24\ h,\ 120\ °C}$	15.00

The obtained ratios were calculated by dividing the relative area of the peak fitted at ~286.5 eV (for C–O component) by the relative area for the peak fitted at ~285.0 eV (C–C and C=C components). The values reported for the C–O component include the C–N component, resulting from peak overlap.

Table S8. The atomic C-, O-, N-, and Ti-fractions for TiO_2, TiO_2–MI-dPG after dPG grafting at varying reaction times and temperatures as determined by XPS.

Substrate	*C(at.%)*	*O (at.%)*	*N (at.%)*	*Ti (at.%)*
TiO_2	22.3	52.3	0.6	12.9
TiO_2@dPG$_{30\ min,\ 100\ °C}$	30.5	51.6	0.3	16.3
TiO_2@dPG$_{1\ h,\ 100\ °C}$	29.3	52.6	0.2	15.6
TiO_2@dPG$_{3\ h,\ 100\ °C}$	36.8	49.3	0.4	12.4
TiO_2@dPG$_{24\ h,\ 100\ °C}$	59.8	37.7	0	1.8
TiO_2–MI-dPG	66.6	24.2	5.8	0.8
TiO_2 – MI-dPG@dPG$_{30\ min,\ 80\ °C}$	66.7	27.2	5.0	0.4
TiO_2 – MI-dPG@dPG$_{1\ h,\ 80\ °C}$	68.2	27.3	3.6	0.2
TiO_2 – MI-dPG@dPG$_{3\ h,\ 80\ °C}$	64.9	32.2	2.2	0.5
TiO_2 – MI-dPG@dPG$_{24\ h,\ 80\ °C}$	70.2	29.2	0.5	0.0

TiO_2 – MI-dPG@dPG$_{30\ min,\ 100\ °C}$	66.1	30.6	2.9	0.0
TiO_2 – MI-dPG@dPG$_{1\ h,\ 100\ °C}$	64.9	33.3	1.5	0.1
TiO_2 – MI-dPG@dPG$_{3\ h,\ 100\ °C}$	65.3	33.8	0.8	0.0
TiO_2 – MI-dPG@dPG$_{24\ h,\ 100\ °C}$	64.0	35.8	0.0	0.0
TiO_2 – MI-dPG@dPG$_{30\ min,\ 120\ °C}$	65.5	32.3	1.7	0.3
TiO_2 – MI-dPG@dPG$_{1\ h,\ 120\ °C}$	66.3	32.1	1.0	0.0
TiO_2 – MI-dPG@dPG$_{3\ h,\ 120\ °C}$	66.9	32.3	0.4	0.0
TiO_2 – MI-dPG@dPG$_{24\ h,\ 120\ °C}$	62.7	36.9	0.2	0.0

The elemental contents were extracted from the C1s, O1s, N1s and Ti2p peaks of the respective survey spectra (**Figure S9**, **S10**, and **S11** of the appendix).

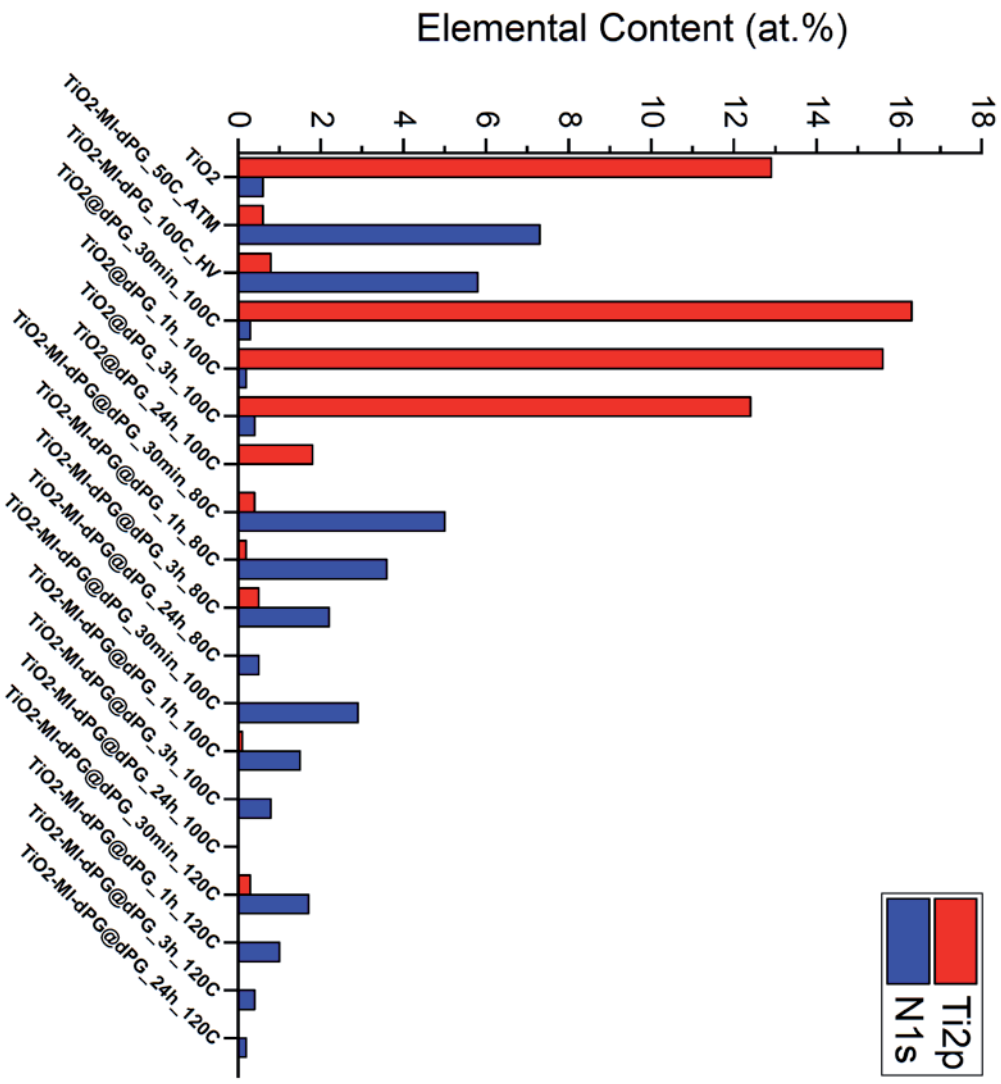

Figure S5. A graph showing the Ti2p and N1s elemental content (in at.%) for TiO_2 and TiO_2–MI-dPG after dPG grafting at varying reaction times and temperatures as determined by XPS. The elemental contents were extracted from the respective survey spectra (**Figures S9**, **S10** and **S11** of the appendix).

Table S9. Highly resolved C1s spectra for PDMS and PDMS–MI-dPG after dPG grafting at 100 °C for 3 h as determined by XPS.

Substrate	*Spectrum*	*Binding energy*	*L-G Mixing*	*FWHM*	*Interpretation*	*Rel. Area*
PDMS	**C1s**	284.8	0.35	1.1	Si–C	1.00
PDMS @dPG$_{3\ h,\ 100\ °C}$	**C1s**	284.8	0.35	1.0	Si–C	0.99
		286.3	0.35	1.0	C–O	0.01
PDMS – MI-dPG	**C1s**	284.8	0.35	1.0	Si–C & C–C	0.90
		286.4	0.35	1.0	C–O	0.09
		287.9	0.35	1.0	C=O	0.01
PDMS – MI-dPG @dPG$_{3\ h,\ 100\ °C}$	**C1s**	284.8	0.35	1.1	Si–C & C–C	0.36
		286.6	0.35	1.0	C–O	0.63
		288.1	0.35	1.0	C=O	0.02

Fitting parameters and the relative areas for C1s component peaks at various binding energies in XPS. The values reported for the C–O component include the C–N component resulting from peak overlap.

Table S10. The C–O/(Si–C & C–C) component peak area ratios for PDMS and PDMS–MI-dPG after dPG grafting at 100 °C for 3 h determined from XPS.

Substrate	*C–O/(Si–C & C–C)*
PDMS	0.00
PDMS@dPG$_{3\ h,\ 100\ °C}$	0.01
PDMS–MI-dPG	0.10
PDMS–MI-dPG@dPG$_{3\ h,\ 100\ °C}$	1.75

The obtained ratios were calculated by dividing the relative area of the peak fitted at ~286.5 eV (for C–O component) by the relative area for the peak fitted at ~285.0 eV (Si–C, C–C and C=C components). The values reported for the C–O component include C–N component resulting from peak overlap.

Table S11. Atomic C, O, N and Si fractions of PDMS and PDMS–MI-dPG after dPG grafting at 100 °C for 3 h as determined by XPS.

Substrate	*C(at.%)*	*O (at.%)*	*N (at.%)*	*Si (at.%)*
PDMS	30.0	45.1	0.1	23.1
PDMS@dPG$_{3\ h,\ 100\ °C}$	51.5	25.5	0.3	22.7
PDMS–MI-dPG	61.5	23.6	1.4	13.5
PDMS–MI-dPG@dPG$_{3\ h,\ 100\ °C}$	60.2	32.1	0.3	7.5

The elemental contents were extracted from the C1s, O1s, N1s and Si2p peaks of the respective survey spectra (**Figure S11** of the appendix).

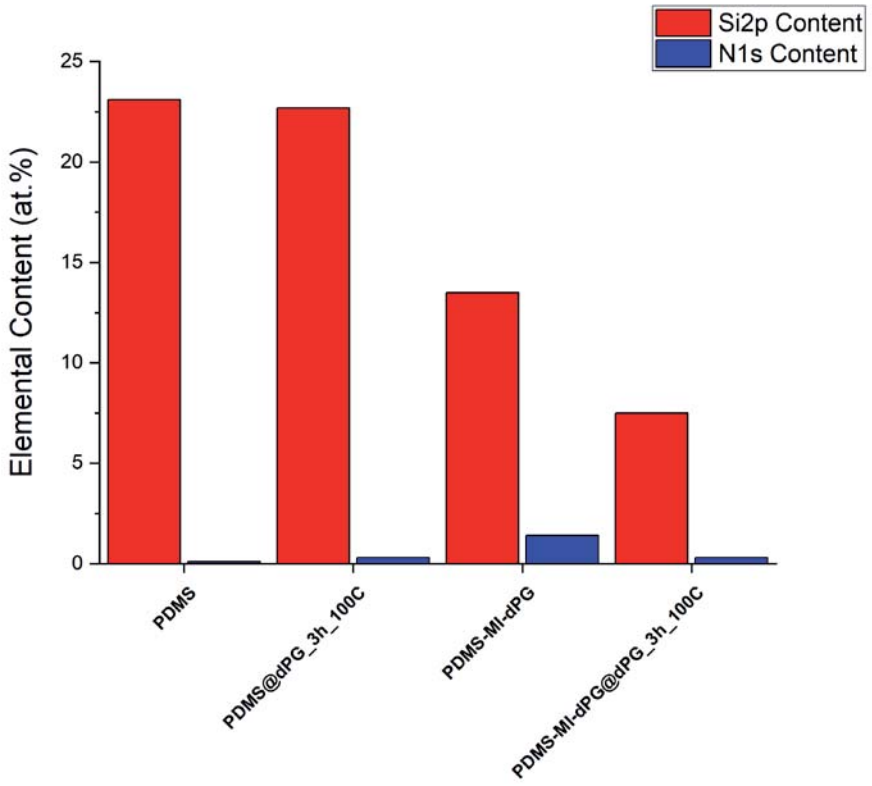

Figure S6. A graph showing the Si2p and N1s' elemental content for PDMS, PDMS@dPG$_{3\ h,\ 100\ °C}$, PDMS–MI-dPG, and PDMS–MI-dPG@dPG$_{3\ h,\ 100\ °C}$ as determined by XPS. The elemental contents were extracted from the respective survey spectra (**Figure S11** of the appendix).

2.3. SEM Results

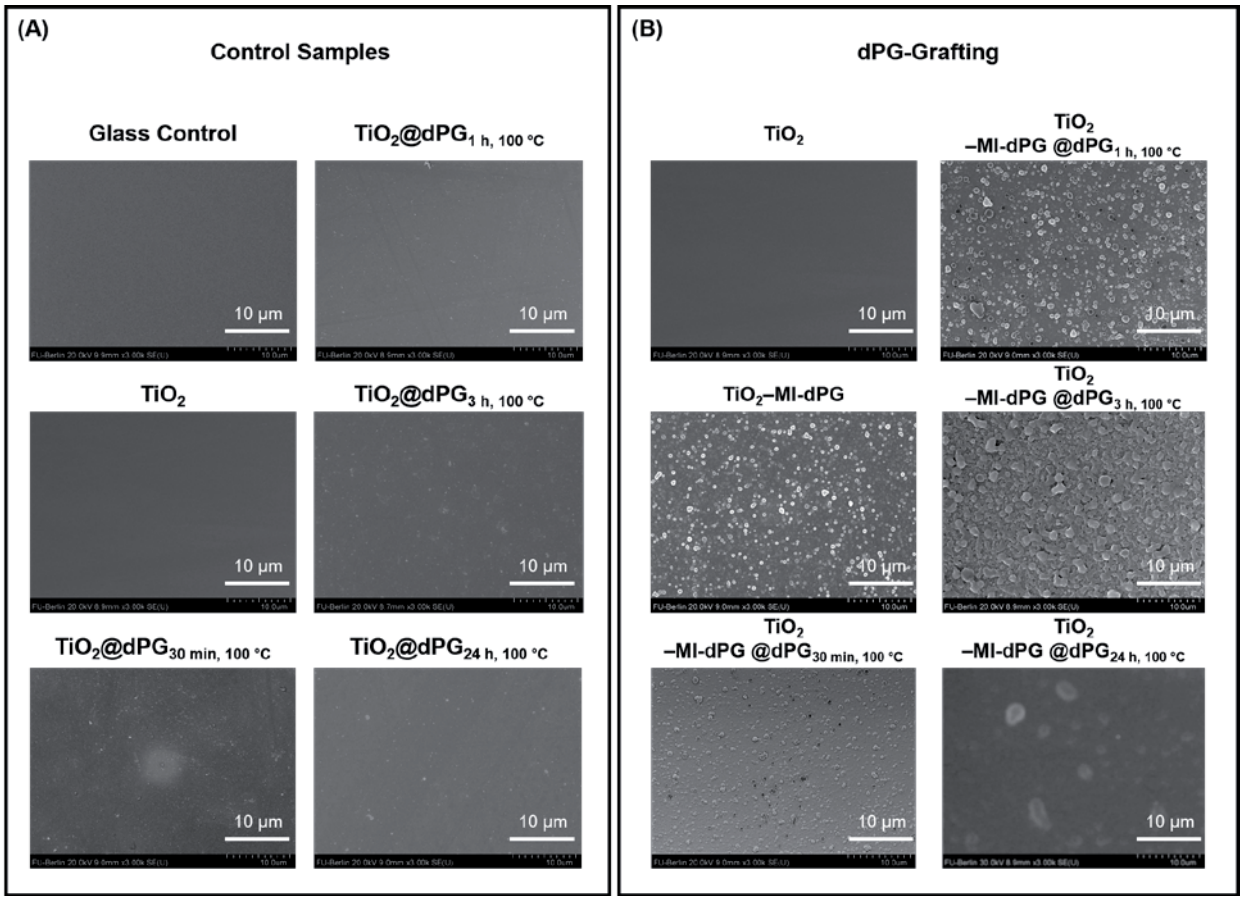

Figure S7. SEM Images showing the dPG grafting process from TiO_2 and TiO_2–MI-dPG at 100 °C. (A) For the bare TiO_2 substrate, only slight changes in the surface morphology were observed after incubation with glycidol under elevated temperatures. (B) In contrast, for the TiO_2–MI-dPG substrate, it was clearly observed that the roughness increased as a function of the reaction time resulting from the dPG grafting process.

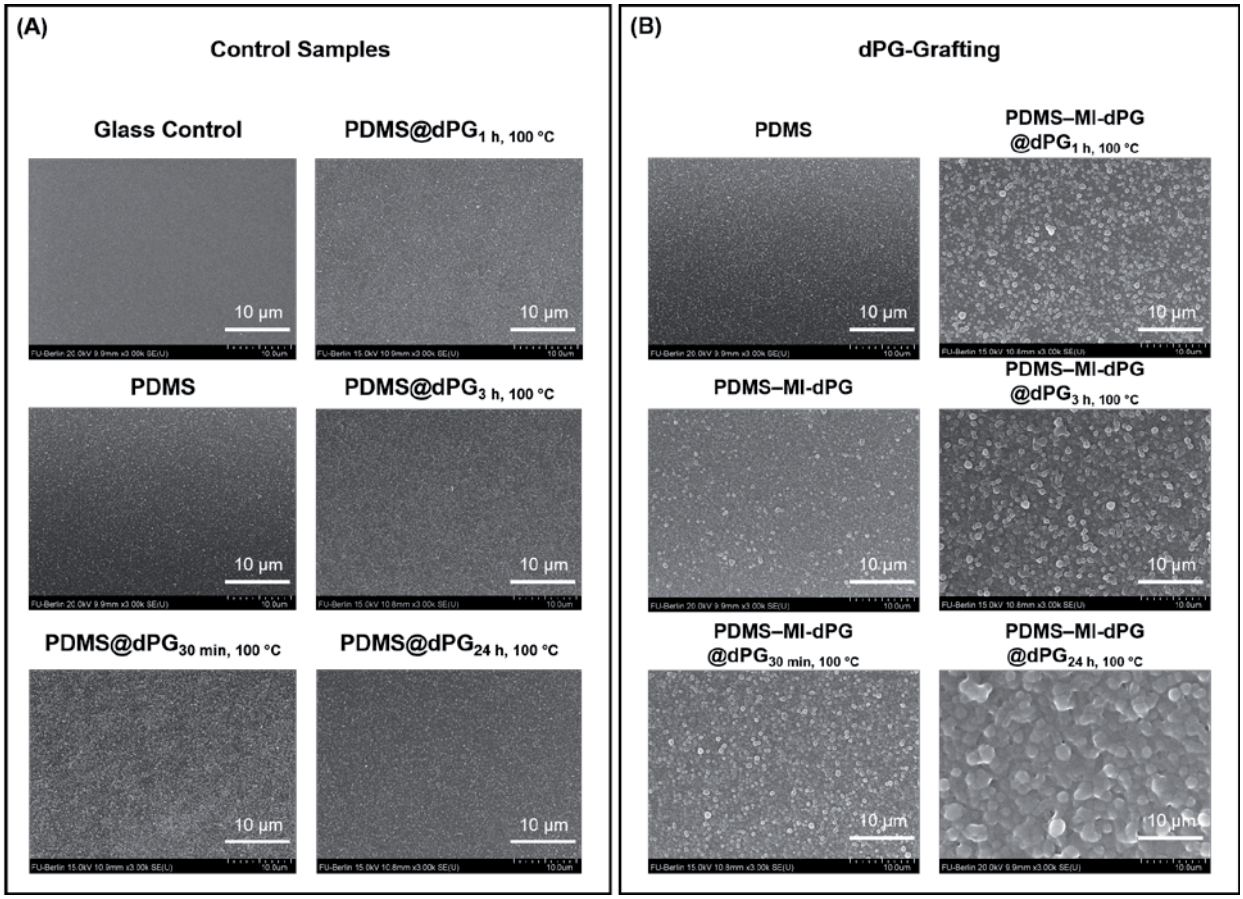

Figure S8. SEM Images showing the dPG grafting process from PDMS and PDMS–MI-dPG at 100 °C. (A) For the bare PDMS substrate, no obvious change in the morphology of the surface was observed after incubation with glycidol at elevated temperatures. (B) In contrast, for the PDMS–MI-dPG substrate, it was clearly observed that the surface roughness increased as a function of the reaction time resulting from the dPG grafting process.

2.4. Cell Viability Results

Table S12. Cell number and viability quantification via LIVE/DEAD™ staining.

Substrate		Live Cells		Dead Cells		Total Cell Number		Viability (%)	
		A549	*DF-1*	*A549*	*DF-1*	*A549*	*DF-1*	*A549*	*DF-1*
TCPS	**I**	962	306	3	12	965	318	0.99	0.96
TCPS	**II**	1044	333	7	12	1051	345	0.99	0.97
TCPS	**III**	1129	295	0	4	1129	299	1	0.99
TCPS	**IV**	1076	332	6	11	1082	343	0.99	0.97
TCPS	**V**	919	- [B]	2	- [B]	921	- [B]	0.99	- [B]
TiO_2	**I**	1031	78	2	11	1033	89	0.99	0.88
TiO_2	**II**	956	86	5	8	961	94	0.99	0.91
TiO_2	**III**	1098	92	5	3	2003	95	0.99	0.97
TiO_2	**IV**	1205	75	3	5	1208	80	0.99	0.94
TiO_2@dPG[A]	**I**	935	207	2	11	937	218	0.99	0.95
TiO_2@dPG[A]	**II**	1088	110	2	13	1090	123	0.99	0.89
TiO_2@dPG[A]	**III**	861	172	1	23	862	195	0.99	0.88

TiO_2@dPG[A]	**IV**	855	249	9	11	864	260	0.99	0.96
TiO_2–MI-dPG	**I**	867	114	1	0	868	114	0.99	1.00
TiO_2–MI-dPG	**II**	840	179	0	6	840	185	1.00	0.97
TiO_2–MI-dPG	**III**	866	124	5	3	871	127	0.99	0.98
TiO_2–MI-dPG	**IV**	1110	183	9	1	1119	184	0.99	0.99
TiO_2–MI-dPG @dPG[A]	**I**	6	5	0	0	6	5	1.00	1.00
TiO_2–MI-dPG @dPG[A]	**II**	1	4	0	1	1	5	1.00	0.80
TiO_2–MI-dPG @dPG[A]	**III**	4	2	0	0	4	2	1.00	1.00
TiO_2–MI-dPG @dPG[A]	**IV**	3	2	0	0	3	2	1.00	1.00
PDMS	**I**	1233	73	5	6	1238	79	0.99	0.92
PDMS	**II**	1088	114	11	12	1099	126	0.99	0.90
PDMS	**III**	1123	136	2	7	1125	143	0.99	0.95
PDMS	**IV**	976	130	5	3	981	133	0.99	0.98
PDMS	**V**	922	-[B]	7	-[B]	929	-[B]	0.99	-[B]
PDMS@dPG[A]	**I**	881	407	40	33	921	440	0.95	0.93
PDMS@dPG[A]	**II**	188	308	17	19	205	327	0.92	0.94

PDMS@dPG[A]	**III**	976	319	48	25	1024	344	0.95	0.93
PDMS@dPG[A]	**IV**	851	109	49	26	900	135	0.95	0.81
PDMS@dPG[A]	**V**	635	-[B]	41	-[B]	676	-[B]	0.94	-[B]
PDMS–MI-dPG	**I**	860	204	3	12	863	216	0.99	0.94
PDMS–MI-dPG	**II**	992	186	5	32	997	218	0.99	0.85
PDMS–MI-dPG	**III**	1186	146	3	28	1189	174	0.99	0.84
PDMS–MI-dPG	**IV**	1121	244	10	14	1131	258	0.99	0.95
PDMS–MI-dPG @dPG[A]	**I**	2	6	0	1	2	7	1.00	0.86
PDMS–MI-dPG @dPG[A]	**II**	6	2	0	0	6	2	1.00	1.00
PDMS–MI-dPG @dPG[A]	**III**	8	1	0	0	8	1	1.00	1.00
PDMS–MI-dPG @dPG[A]	**IV**	2	2	0	1	2	3	1.00	0.67

The cell numbers were determined on a 920 µm x 720 µm surface; the cell numbers per cm^2 as reported in the main text were calculated accordingly. Note for A, dPG grafting was performed for 3 h at 100 °C. Note for B, for the DF-1 cells only 4 TCPS samples were taken.

3. LITERATURE

[1] A. O. Fitton, J. Hill, D. E. Jane, R. Millar, *Synthesis* **1987**, 1987, 1140.

[2] A. Sunder, R. Hanselmann, H. Frey, R. Mülhaupt, *Macromolecules* **1999**, 32, 4240.

[3] S. Roller, H. Zhou, R. Haag, *Molecular Diversity* **2005**, 9, 305.

[4] H. e. al., *ACS Applied Materials & Interfaces* **2016**, 8, 29117.

[5] Q. Wei, K. Achazi, H. Liebe, A. Schulz, P.-L. M. Noeske, I. Grunwald, R. Haag, *Angewandte Chemie International Edition* **2014**, 53, 11650.

[6] M. D. Abràmoff, P. J. Magalhães, S. J. Ram, *Biophotonics international* **2004**, 11, 36.

4. APPENDIX

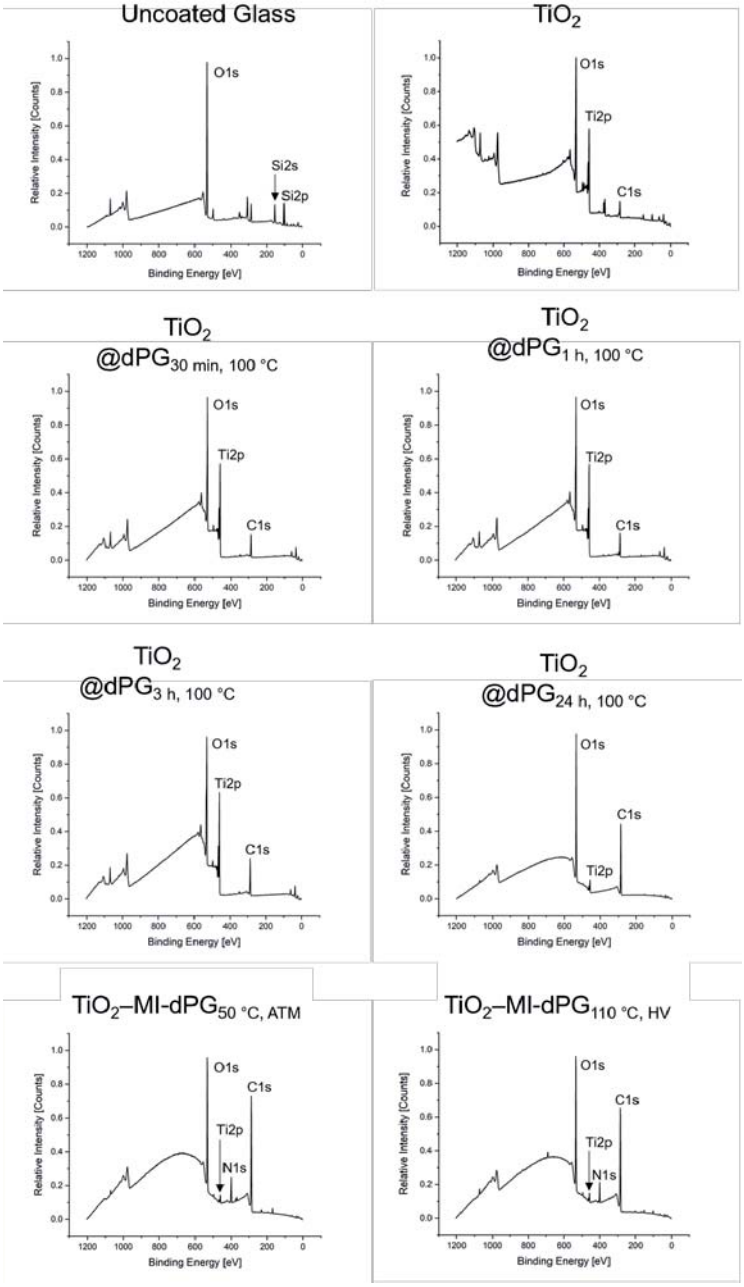

Figure S9. The XPS survey spectra of bare glass (which was used as the substrate material for the immobilization of TiO_2 and PDMS), TiO_2, TiO_2@$dPG_{\Delta t,\ 100\ °C}$, TiO_2–MI-$dPG_{50\ °C,\ ATM}$, and TiO_2–MI-$dPG_{110\ °C,\ HV}$.

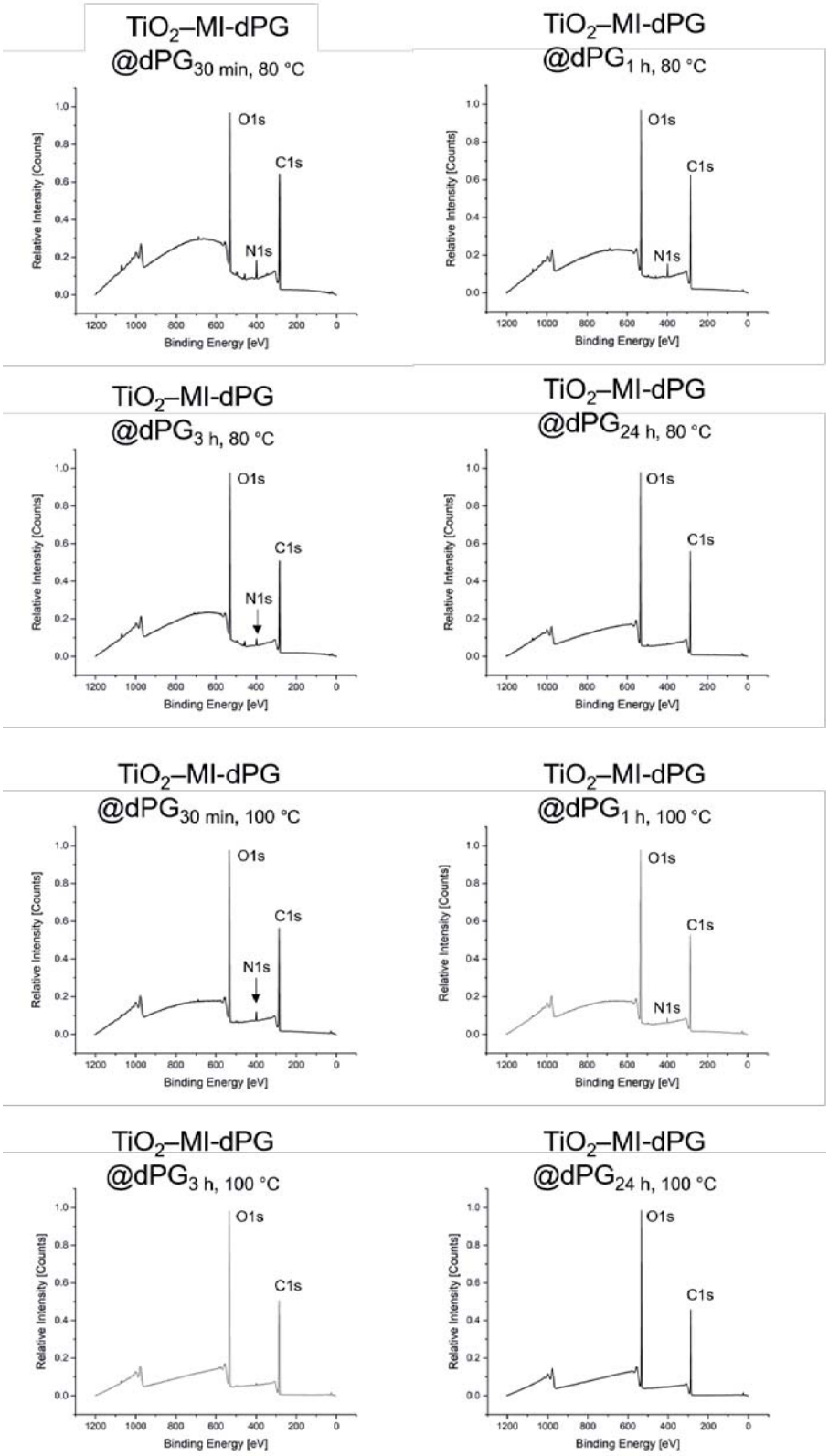

Figure S10. The XPS survey spectra of TiO_2–MI-dPG@$dPG_{\Delta t,\ 80\ °C/100\ °C}$.

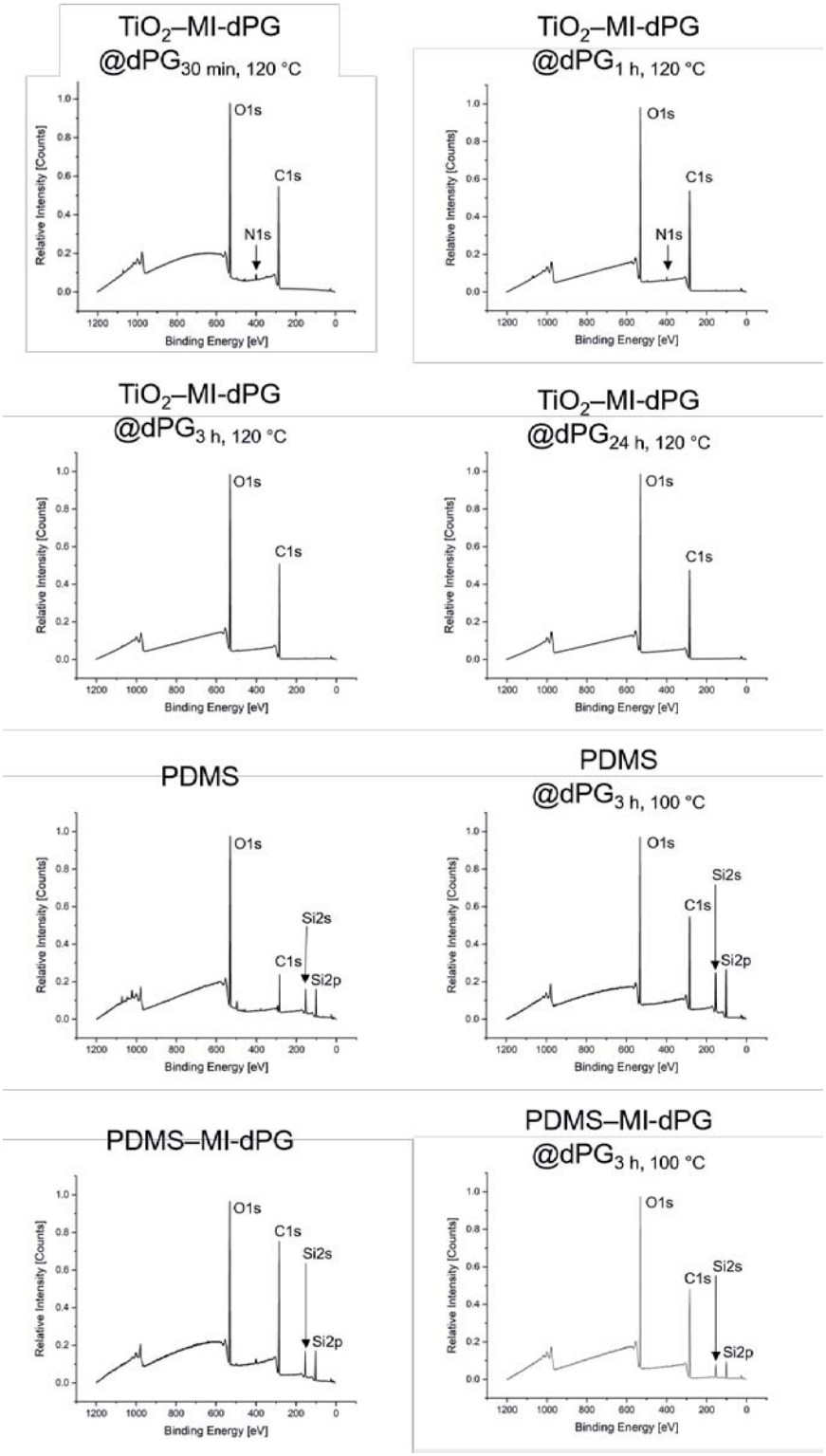

Figure S11. The XPS survey spectra of TiO_2–MI-dPG@$dPG_{\Delta t,\ 120\ °C}$, PDMS, PDMS@$dPG_{3\ h,\ 120\ °C}$, PDMS–MI-dPG, and PDMS–MI-dPG@$dPG_{3\ h,\ 120\ °C}$.

5. SUMMARY AND CONCLUSIONS

In this doctoral thesis novel mussel-inspired coatings for the prevention of biomaterial- and shear-induced fouling were successfully developed. The formation of the MI-dPG coating on TiO_2 and its subsequent post-functionalization with lPG–b–OA_{11} or HO–PEG–NH_2 substrates were confirmed via CA, AFM, SEM, X-ray photoelectron spectroscopy (XPS), and streaming current measurements. Furthermore, CA and XPS measurements confirmed the stability of the lPG-functionalized system for at least one month in phosphate buffered saline and sodium dodecyl sulfate solution at room temperature.

The bio- and hemocompatibility of the developed materials were assessed by investigating the cytotoxicity, complement activating properties, and antifouling properties of the novel coatings. Most importantly, the adhesion and activation of blood platelets was investigated on the various substrates under static and flow conditions. When the proliferation and viability of adenocarcinomic human alveolar basal epithelial cells (A549 cells) and chicken fibroblast cells (DF-1 cells) were studied on the different coatings via LIVE/DEAD™ staining, it was clearly observed that the introduction of lPG to MI-dPG-coated TiO_2 prevented the adhesion of both cell types. Furthermore, all lPG-functionalized samples showed high cell viability, indicating that cell-repelling but highly biocompatible coatings were obtained. Quantification of the C5a levels in PRP solutions that were exposed to the various coatings showed slightly increased C5a levels in comparison to the negative control in all cases. However, all observed C5a levels were significantly lower than those of the positive control, indicating that the coatings did not induce any apparent complement activation. When the protein fouling characteristics of the coatings were assessed by means of QCM-D, the strongest reduction in unspecific protein adhesion was observed for the lPG-functionalized MI-dPG coating (96% reduction for albumin and 99% reduction for fibrinogen in comparison to the bare TiO_2 substrate). Furthermore, SEM investigations clearly showed that the lPG-functionalized surface inhibited the activation of platelets from PRP under static conditions. The adhesion of platelets from whole blood under flow conditions was investigated using the stagnation point flow model developed by Affeld et al.[111-112, 274] The lowest platelet adhesion was clearly observed for the lPG-functionalized MI-dPG coating (60% reduction in respect to the native MI-dPG coating, 77% reduction in respect to the bare TiO_2 substrate, and 86% reduction in respect to the collagen positive control). The coating of a VAD with MI-dPG under flow conditions was successfully performed. Visualization of the MI-dPG coating was achieved by reacting the coating with a commercially available fluorophore under optimized

reaction conditions. The combined results showed that highly biocompatible, cell-, protein-, and platelet-repelling surface coatings were obtained via the introduction of lPG–b–OA_{11} to the MI-dPG coating. Furthermore, MI-dPG has proven itself as a suitable coating material for the functionalization of VAD systems.

When MI-dPG-coated hydrophilic TiO_2 and MI-dPG-coated hydrophobic PDMS were incubated with bulk glycidol under elevated temperatures, a clear decrease in the CA as a function of the reaction time and temperature was observed. Additionally, XPS confirmed the increase of the C–O bond content as a result of the grafting process. Furthermore, when the morphology of the surface was studied by means of SEM, a clear increase in the surface roughness was observed resulting from the grafting process. The combined results showed the successful grafting of dPG from the MI-dPG coating on hydrophilic TiO_2 and hydrophobic PDMS substrates. Furthermore, CA and XPS measurements showed that in the absence of the MI-dPG coating, the grafting of dPG did not occur sufficiently. When the proliferation and viability of A549 and DF-1 cells were investigated on the dPG-grafted MI-dPG coatings by means of LIVE/DEAD™ staining, a strong reduction in the cell numbers of both cell types was observed (> 95% in all cases) in respect to the uncoated TiO_2 and PDMS substrates. However, the observed cells showed high viability on the dPG-functionalized MI-dPG-coatings (> 88% viability in all cases), showing that cell-repelling but highly biocompatible surfaces were obtained.

To summarize, the hypothesis of the first paper of the thesis was confirmed: i.e., stable substrate-independent antifouling systems were successfully created via the introduction of lPG–b–OA_{11} and HO–PEG–NH_2 to MI-dPG-coated TiO_2. The hypothesis of the second paper was also confirmed: i.e., the lPG-functionalized MI-dPG coating proofed itself as a highly biocompatible antifouling coating for the effective inhibition platelet adhesion and activation under static and flow conditions. Furthermore, the MI-dPG coating was identified as a suitable coating material for the functionalization of VADs under flow conditions. Finally, the hypothesis of the third paper was also confirmed: i.e., dPG was effectively grafted from MI-dPG-coated hydrophilic TiO_2 and from MI-dPG-coated hydrophobic PDMS, for the creation of highly biocompatible but cell-repelling surfaces. Furthermore, the surface wettability and surface roughness were precisely controlled by carefully adjusting the reaction times and temperatures.

6. OUTLOOK

In the first project of this thesis, the stability of multivalently bound lPG–b–OA_{11} was clearly demonstrated.[180] However, the relation between the number of surface tethering groups and the surface chain density was not investigated in the current work. Future works could utilize the MI-dPG coating as a platform for the direct comparison of the antifouling properties of a wide variety of hydrophilic polymers. The grafting density of these hydrophilic polymers could potentially be tuned on the MI-dPG coating, by varying the amount of surface tethering groups and by adjusting the polymer concentration of the secondary reagent during the post-functionalization step. It is important to notice, that a direct comparison of the antifouling surface properties of different hydrophilic polymers can only be made once surfaces with identical surface chain densities are obtained.[163] To the best of our knowledge, such a direct comparison of the antifouling surface properties for multi-layer hydrophilic polymeric systems has not been performed yet.

The second project of this thesis gave a proof-of-concept for the use of mussel-inspired PG-based coatings for the prevention of biomaterial- and shear-induced thrombosis. However, the efficiency of these coatings was only shown *in vitro* so far. Future works might focus on the functionalization of shunts and/or metallic stents for *in vivo* applications. Next, a VAD could be coated with an optimized version of the PG-based system for further *in vivo* testing under high shear conditions. Future studies could also assess the use of lPG and dPG monolayers as hydrophilic bioinert antithrombogenic surface coatings.[14, 181, 195]

In the third project of this thesis, MI-dPG was utilized as a platform for the grafting of dPG from the surface. Besides glycidol, other glycidyl ether such as dodecyl glycidyl ether (DGE) or glycidyl 2,2,3,3,4,4,5,5-octafluoropentyl ether (GOFE) could potentially be grafted from the MI-dPG coating, for the creation of surfaces with superhydrophobic wetting properties. Furthermore, the catechol moieties of the MI-dPG coating could be utilized for the immobilization of antibacterial AgNPs, prior to the grafting of hydrophobic glycidyl ether monomers. By applying this strategy, the AgNPs would be protected from aqueous media by a grafted hydrophobic layer, potentially preventing the removal of the AgNPs in the form of Ag^+ ions (resulting from oxidation). As a result, the AgNPs could reside longer on the surface, possibly leading to sustained antibacterial activity via the release of reactive oxygen species.

7. KURZZUSAMMENFASSUNG

Diese Doktorarbeit beschreibt die erfolgreiche Entwicklung neuartiger, von Muscheln inspirierter Beschichtungen zur Verhinderung von biomaterial- und scherinduziertem Fouling. Die Bildung der MI-dPG-Beschichtung auf TiO_2 und ihre anschließende Funktionalisierung mit lPG–b–OA_{11}- oder HO–PEG–NH_2-Substraten wurde mittels Kontaktwinkelmessungen, Rasterkraftmikroskopie (AFM), Rasterelektronenmikroskopie (REM), Röntgen-Photoelektronen-spektroskopie (XPS) und Strömungsstrommessungen nachgewiesen. Darüber hinaus bestätigten Kontaktwinkel- und XPS-Messungen die Stabilität des lPG-funktionalisierten Systems für mindestens einen Monat in phosphatgepufferter Kochsalz- und Natrium-laurylsulfatlösung bei Raumtemperatur.

Die Bio- und Hämokompatibilität der neuentwickelten Materialien wurde mittels Untersuchung der Zytotoxizität, komplementaktivierender Eigenschaften und Antifouling-Eigenschaften bestimmt. Weiterhin standen vor allem die Adhäsion und Aktivierung von Blutplättchen auf den verschiedenen Substraten unter statischen und Fließbedingungen im Fokus. Bei der Charakterisierung von Proliferation und Lebensfähigkeit von adenokarzinomischen humanen alveolären Basalepithelzellen (A549-Zellen) und Hühnerfibroblastenzellen (DF-1-Zellen) auf den verschiedenen Beschichtungen mittels LIVE/DEAD™-Färbung, konnte gezeigt werden, dass die Adhäsion dieser beiden Zelltypen durch Einführung von lPG auf MI-dPG-beschichtetem TiO_2 verhindert wird. Darüber hinaus zeigten alle lPG-funktionalisierten Proben eine hohe Zellviabilität, was darauf hinweist, dass zellabweisende, aber hoch biokompatible Beschichtungen erhalten wurden. Die Quantifizierung der C5a-Gehalte in PRP (thrombozytenreiches Plasma) Lösungen, die den verschiedenen Beschichtungen ausgesetzt waren, zeigte in allen Fällen leicht erhöhte C5a-Gehalte im Vergleich zur Negativkontrolle. Alle beobachteten C5a-Gehalte waren jedoch signifikant niedriger als die der Positivkontrolle, was darauf hindeutet, dass die Beschichtungen keine offensichtliche Komplementaktivierung induzierten. Bei der Beurteilung der Proteinfouling der Beschichtungen mit Hilfe von Quarzkristall-Mikrowaagenmessungen mit Dissipationsmonitoring (QCM-D) wurde die stärkste Reduktion der unspezifischen Proteinadhäsion bei der lPG-funktionalisierten MI-dPG-Beschichtung beobachtet (96% Reduktion für Albumin und 99% Reduktion für Fibrinogen im Vergleich zum blanken TiO_2-Substrat). Darüber hinaus zeigten REM-Untersuchungen eindeutig, dass die lPG-funktionalisierte Oberfläche die Aktivierung von Thrombozyten aus thrombozytenreichem Plasma unter statischen Bedingungen hemmt. Die Adhäsion von

Thrombozyten aus Vollblut unter Flussbedingungen wurde mit dem von Affeld et al. entwickelten Stagnationspunkt-Flussmodell untersucht. Die geringste Thrombozytenadhäsion wurde eindeutig für die lPG-funktionalisierte MI-dPG-Beschichtung beobachtet (60% Reduktion gegenüber der nativen MI-dPG-Beschichtung, 77% Reduktion gegenüber dem blanken TiO_2-Substrat und 86% Reduktion gegenüber der Kollagenpositivkontrolle). Die Beschichtung eines Ventrikelunterstützungssystems (VAD) mit MI-dPG unter Fließbedingungen wurde erfolgreich durchgeführt. Die Visualisierung der MI-dPG-Beschichtung wurde durch Reaktion der Beschichtung mit einem kommerziell erhältlichen Fluorophor unter optimierten Reaktionsbedingungen erreicht. Die kombinierten Ergebnisse zeigten, dass durch die Immobilisierung von lPG auf die MI-dPG-Beschichtung hoch biokompatible, zell-, protein- und plättchenabweisende Oberflächenbeschichtungen erzielt wurden. Darüber hinaus hat sich MI-dPG als geeignetes Beschichtungsmaterial für die Funktionalisierung von VAD-Systemen bewährt.

Bei der Inkubation von MI-dPG-beschichtetem hydrophilem TiO_2 und MI-dPG-beschichtetem hydrophobem PDMS mit Bulkglycidol unter erhöhten Temperaturen, konnte eine deutliche Abnahme der Kontaktwinkel in Abhängigkeit von der Reaktionszeit und Temperatur beobachtet werden. Zusätzlich bestätigte XPS den Anstieg des C–O-Bindungsgehalts als Folge des Grafting-Prozesses. Darüber hinaus wurde bei der Untersuchung der Oberflächenmorphologie mittels REM eine deutliche Zunahme der Oberflächenrauhigkeit als Folge des Graftings beobachtet. Die kombinierten Ergebnisse zeigten das erfolgreiche Grafting von dPG der MI-dPG-Beschichtung auf hydrophile TiO_2- und hydrophobe PDMS-Substrate. Darüber hinaus zeigten Kontaktwinkel- und XPS-Messungen, dass in Abwesenheit der MI-dPG-Beschichtung die Grafting von dPG nicht ausreichend erfolgte. Bei der Untersuchung der Proliferation und Lebensfähigkeit von A549- und DF-1-Zellen auf den dPG-funktionalisierten MI-dPG-Beschichtungen mittels LIVE/DEAD™-Färbung wurde eine starke Reduktion der Zellzahlen beider Zelltypen (> 95% in allen Fällen) im Vergleich zu den unbeschichteten TiO_2- und PDMS-Substraten beobachtet. Die untersuchten Zellen zeigten jedoch eine hohe Viabilität auf den dPG-funktionalisierten MI-dPG-Beschichtungen (> 88% Viabilität in allen Fällen), sodass zellabweisende, aber hoch biokompatible Oberflächen erzielt wurden.

Zusammenfassend konnte die Hypothese aus der ersten Veröffentlichung dieser Arbeit bestätigt werden: durch die Einführung von lPG–b–OA_{11} und HO–PEG–NH_2 zu MI-dPG-beschichtetem TiO_2 wurden erfolgreich stabile substratunabhängige Antifoulingsysteme

geschaffen. Auch die Hypothese des zweiten Manuskripts wurde bestätigt: die lPG-funktionalisierte MI-dPG-Beschichtung erwies sich als hoch biokompatible Antifouling-Beschichtung für die effektive Inhibierung der Plättchenhaftung und -aktivierung unter statischen und Fließbedingungen. Darüber hinaus wurde die MI-dPG-Beschichtung als ein geeignetes Beschichtungsmaterial für die Funktionalisierung von VADs unter Fließbedingungen identifiziert. Schließlich wurde auch die Hypothese des dritten Manuskripts bestätigt: dPG wurde effektiv aus MI-dPG-beschichtetem hydrophilem TiO_2 und aus MI-dPG-beschichtetem hydrophoben PDMS gegrafted, um stark biokompatible, aber zellabweisende Oberflächen zu erzeugen. Darüber hinaus konnten die Oberflächenbenetzbarkeit und die Oberflächenrauhigkeit durch sorgfältige Einstellung der Reaktionszeiten und Temperaturen präzise gesteuert werden.

8. ABBREVIATION LIST

A549: adenocarcinomic human alveolar basal epithelial cells
AC: alternating current
ADP: adenosine diphosphate
AFM: atomic force microscopy
AgNP: silver nanoparticle
CA: contact angle
CF8: fluoroundecanoyl chloride
CVD: cardiovascular disease
DF-1: chicken fibroblast cells
DGE: dodecyl glycidyl ether
DLC: diamond-like carbon
DOPA: 3,4–dihydroxyphenyl-L-alanine
dPG: dendritic polyglycerol
dPG-Cat(x): x% catechol functionalized dendritic polyglycerol
ELISA: enzyme-linked immunosorbent assay
GOFE: glycidyl 2,2,3,3,4,4,5,5-octa fluoropentyl ether
GPIIb/IIIa: glycoprotein IIb/IIIa
HMWK: high molecular weight kininogen
KK: kallikrein
LBL: layer-by-layer
lPG: linear polyglycerol
MAC: membrane attack complex
mfp: mussel-foot protein
MI-dPG: mussel-inspired dPG
NO: nitric oxide
OA: oligo-amine
PDA: polydopamine
PDMS: polydimethylsiloxane
PEG: poly(ethylene glycol)
PES: polyethersulfone
PF4: platelet factor 4
PG: polyglycerol
PK: prekallikrein
PMN: polymorphonuclear
PRP: platelet rich plasma
PS: Polystyrene
PTFE: polytetrafluoroethylene
PU: polyurethane
QCM-D: quartz crystal microbalance with dissipation monitoring
SAM: self-assembled monolayer
SEM: scanning electron microscopy
TF: tissue factor
TiN: titanium nitride
TiO_2: titanium dioxide
TXA2: thromboxane A2
UV: ultraviolet
VAD: ventricular assist device
vWF: von Willebrand factor
XPS: X-ray photoelectron spectroscopy

9. LITERATURE

1. E. Wilkins, L. Wilson, K. Wickramasinghe, P. Bhatnagar, J. Leal, R. Luengo-Fernandez, R. Burns, M. Rayner, N. Townsend, *European cardiovascular disease statistics 2017* **2017**.
2. P. Shah, U.S. Tantry, K. P. Bliden, P. A. Gurbel, *J. Heart Lung Transpl.* **2017**, *36*, 1164.
3. L. D. C. Casa, D. N. Ku, *Annu. Rev. Biomed. Eng.* **2017**, *19*, 415.
4. C. Cheng, S. Sun, C. Zhao, *J. Mater. Chem. B* **2014**, *2*, 7649.
5. J. Zhu, R. E. Marchant, *Biomacromolecules* **2006**, *7*, 1036.
6. N. Hadjesfandiari, M. Weinhart, J. N. Kizhakkedathu, R. Haag, D. E. Brooks, *Adv. Healthc. Mater.* **2018**, *7*, 1700839.
7. X. Ding, C. Yang, T. P. Lim, L. Y. Hsu, A. C. Engler, J. L. Hedrick, Y.-Y Yang, *Biomaterials* **2012**, *33*, 6593.
8. D.-C. Sin, H.-L Kei, X. Miao, *Expert Rev. of Med. Devices* **2009**, *6*, 51.
9. C. D. Bain, E. B. Troughton, Y. T. Tao, J. Evall, G. M. Whitesides, R. G. Nuzzo, *J. Am. Chem. Soc.* **1989**, *111*, 321.
10. A. Y. Fadeev, Y. V. Kazakevich, *Langmuir* **2002**, *18*, 2665.
11. D. Kubies, L. Machová, E. Brynda, J. Lukáš, F. Rypáček, *J. Mater. Sci. Mater. Med.* **2003**, *14*, 143.
12. C. Boura, P. Menu, E. Payan, C. Picart, J. C. Voegel, S. Muller, J. F. Stoltz, *Biomaterials* **2003**, *24*, 3521.
13. P. Petrov, G. Georgiev, D. Momekova, G. Momekov, C. B. Tsvetanov, *Polymer* **2010**, *51*, 2465.
14. L. Yu, Y. Hou, C. Cheng, C. Schlaich, P.-L M. Noeske, Q. Wei, R. Haag, *ACS Appl. Mater. Inter.* **2017**, *9*, 44281.
15. P. Bertrand, A. Jonas, A. Laschewsky, R. Legras, *Macromol. Rapid Commun.* **2000**, *21*, 319.
16. C. Freij-Larsson, T. Nylander, P. Jannasch, B. Wesslén, *Biomaterials* **1996**, *17*, 2199.
17. N. Uriel, J. Han, K. A. Morrison, N. Nahumi, M. Yuzefpolskaya, A. R. Garan, J. Duong, P. C. Colombo, H. Takayama, S. Thomas, *J. Heart Lung Transpl.* **2014**, *33*, 51.
18. W.-T. Wu, F. Yang, J. Wu, N. Aubry, M. Massoudi, J. F. Antaki, *Sci. Rep.* **2016**, *6*, 38025.
19. F. Yin, H.-K. Shin, Y.-S. Kwon, *Thin Solid Films* **2006**, *499*, 1.
20. C. Qiu, S. Qi, C. Y. Tang, *J. Membr. Sci.* **2011**, *381*, 74.

21. H. Lee, S. M. Dellatore, W. M. Miller, P. B. Messersmith, *Science* **2007**, *318*, 426.
22. H.-C. Yang, J. Luo, Y. Lv, P. Shen, Z.-K. Xu, *J. Membr. Sci.* **2015**, *483*, 42.
23. Y. Cho, S. Y. Seo, B. J. Park, Y. K. Joung, D. K. Han, *Macromol. Res.* **2017**, *25*, 841.
24. Q. Wei, B. Li, N. Yi, B. Su, Z. Yin, F. Zhang, J. Li, C. Zhao, *J. Biomed. Mater. Res. A* **2011**, *96A*, 38.
25. R. Biran, D. Pond, *Adv. Drug Deliv. Rev.* **2017**, *112*, 12.
26. H.-Y. Mi, X. Jing, J. A. Thomsom, L.-S. Turng, *J. Mater. Chem. B* **2018**, *6*, 3475.
27. R. Luo, X. Wang, J. Deng, H. Zhang, M. F. Maitz, L. Yang, J. Wang, N. Huang, Y. Wang, *Colloids Surface. B* **2016**, *144*, 90.
28. M. Irfan, A, Idris, *Mater. Sci. Eng. C* **2015**, *56*, 574.
29. M. Navarro, A. Michiardi, O. Castaño, J. A. Planell, *J. R. Soc. Interface* **2008**, *5*, 1137.
30. L. Xue, H. P. Greisler, *J. Vasc. Surg.* **2003**, *37*, 472.
31. I. H. Jaffer, J. C. Fredenburgh, J. Hirsh, J. I. Weitz, *J. Thromb. Haemost.* **2015**, *13*, S72.
32. M. Weber, H. Steinle, S. Golombek, L. Hann, C. Schlensak, H. P. Wendel, M. Avci-Adali, *Front. Bioeng. Biotechnol.* **2018**, *6*, 99.
33. R. Paniccia, R. Priora, A. A. Liotta, R. Abbate, *Vasc. Health Risk Manag.* **2015**, *11*, 133.
34. B. P. Nuyttens, T. Thijs, H. Deckmyn, K. Broos, *Thromb. Res.* **2011**, *127*, S26.
35. L. Yang, L. Han, Q. Liu, Y. Xu, L. Jia, *Acta Biomater.* **2017**, *64*, 187.
36. L.-C. Xu, J. W. Bauer, C. A. Siedlecki, *Colloid Surface. B* **2014**, *124*, 49.
37. W.-B. Tsai, J. M. Grunkemeier, T. A. Horbett, *J. Biomed. Mater. Res.* **1999**, *44*, 130.
38. L. Zhang, B. Casey, D. K. Galanakis, C. Marmorat, S. Skoog, K. Vorvolakos, M. Simon, M. H. Rafailovich, *Acta Biomater.* **2017**, *54*, 164.
39. A. J. Gale, *Toxicol. Pathol.* **2011**, *39*, 273.
40. R. D. Allen, L. R. Zacharski, S. T. Widirstky, R. Rosenstein, L. M. Zaitlin, D. R. Burgess, *J. Cell Biol.* **1979**, *83*, 126.
41. S. N. Rodrigues, I. C. Gonçalves, M. C. L. Martins, M. A. Barbosa, B. D. Ratner, *Biomaterials* **2006**, *27*, 5357.
42. T. Xiang, T. Lu, Y. Xie, W.-F. Zhao, S.-D. Sun, C.-S. Zhao, *Acta Biomater.* **2016,** *40*, 162.
43. I. C. Gonçalves, M. C. L. Martins, M. A. Barbosa, E. Naeemi, B. D. Ratner, *J. Biomed. Mater. Res. A* **2009**, *89A*, 642.
44. C. J. Nonckreman, S. Fleith, P. G. Rouxhet, C. C. Dupont-Gillain, *Colloid. Surface. B* **2010**, *77*, 139.

45. B. Sivaraman, R. A. Latour, *Biomaterials* **2010**, *31*, 832.
46. Y. Hu, J. Jin, H. Liang, X. Ji, J. Yin, W. Jiang, *Langmuir* **2016**, *32*, 4086.
47. S. P. Grover, N. Mackman, *Arterioscler. Thromb. Vasc. Biol.* **2019**, *39*, 331.
48. H. E. Caputo, J. E. Straub, M. W. Grinstaff, *Chem. Soc. Rev.* **2019**, *48*, 2338.
49. J. Bäck, J. Sanchez, G. Elgue, K. N. Ekdahl, B. Nilsson, *Biochem. Bioph. Res. Co.* **2010**, *391*, 11.
50. L. F. Brass, *Chest* **2003**, *124*, 18S.
51. Z. Hofman, S. de Maat, C. E. Hack, C. Maas, *Clin. Rev. Allerg. Immu.* **2016**, *51*, 152.
52. R. C. Wiggins, B. N. Bouma, C. G. Cochrane, J. H. Griffin, *PNAS* **1977**, *74*, 4636.
53. L. Faxälv, T. Lindahl, http://platelets.se/biomaterial/, Accessed 28.05.20.
54. O. D. Ratnoff, J. M. Rosenblum, *Am. J. Med. Sci.* **1958**, *25*, 160.
55. J. Margolis, *Aust. J. Exp. Biol. Med. Sci.* **1961**, *39*, 249.
56. F. van der Graaf, F. Keus, R. Vlooswijk, B. N. Bouma, *Blood* **1982**, *59*, 1225.
57. D. L. Tankersley, B. M. Alving, J. Finlayson, *Blood* **1983**, *62*, 448.
58. R. C. Wiggins, C. C. Cochrane, *J. Exp. Med.* **1979**, *150*, 1122.
59. D. Kudela, S. A. Smith, A. May-Masnou, G. B. Braun, A. Pallaoro, C. K. Nguyen, T. T. Chuong, S. Nownes, R. Allen, N. R. Parker, H. H. Rashidi, J. H. Morrissey, G. D. Stucky, *Angew. Chem. Int. Ed.* **2015**, *54*, 4018.
60. S. A. Smith, N. J. Mutch, D. Baskar, P. Rohloff, R. Docampo, J. H. Morrissey, *PNAS* **2006**, *103*, 903.
61. P. E. J. van der Meijden, I. C. A. Munnix, J. M. Auger, J. W. P. Govers-Riemslag, J. M. E. M. Cosemans, M. J. E. Kuijpers, H. M. Spronk, S. P. Watson, T. Renné, J. W. M. Heemskerk, *Blood* **2009**, *114*, 881.
62. Y. Yan, L. C. Xu, E. A. Vogler, C. A. Siedlecki, *Hemocompatibility of Biomaterials for Clinical Applications* **2018**, 1 Ed., 3.
63. Y. Wu, *Thromb. J.* **2015**, *13*, 17.
64. J. D. Loike, B. Sodeik, L. Cao, S. Leucona, J. I. Weitz, P. A. Detmers, S. D. Wright, S. C. Silverstein, *PNAS* **1991**, *88*, 1044.
65. S. D. Wright, J. I. Weitz, A. J. Huang, S. M. Levin, S. C. Silverstein, J. D. Loike, *PNAS* **1988**, *85*, 7734.
66. D. Morley, I. Feuerstein, *Thromb. Haemost.* **1989**, *62*, 1023.
67. T. Imamura, H. Kaneda, S. Nakamura, *Lab. Investig.* **2002**, *82*, 1287.
68. H. Todoroki, S. Nakamura, A. Higure, K. Okamoto, S. Takeda, N. Nagata, H. Itoh, K. Ohsato, *Surgery* **2000**, *127*, 209.

69. T. Lisman, *Cell Tissue Res.* **2018**, *371*, 567.
70. L. Vroman, A. L. Adams, *Surf. Sci.* **1969**, *16*, 438.
71. J. Andersson, K. N. Ekdahl, R. Larsson, U. R. Nilsson, B. Nilsson, *J. Immunol.* **2002**, *168*, 5786.
72. M. Noris, G. Remuzzi, *Semin. Nephrol.* **2013**, *33*, 479.
73. H. Rus, C. Cudrici, F. Niculescu, *Immunol. Res.* **2005**, *33*, 103.
74. Y. N. V. Reddy, A. M. Siedlecki, J. M. Francis, *Curr. Opin. Nephrol. Hy.* **2017**, *26*, 123.
75. B. Nilsson, K. N. Ekdahl, T. E. Mollnes, J. D. Lambris, *Mol. Immunol.* **2007**, *44*, 82.
76. S. P. Jackson, W. S. Nesbitt, E. Westein, *J. Thromb. and Haemost.* **2009**, *7*, 17.
77. W. S. Nesbitt, E. Westein, F. J. Tovar-Lopez, E. Tolouei, A. Mitchell, J. Fu, J. Carberry, A. Fouras, S. P. Jackson, *Nat. Med.* **2009**, *15*, 665.
78. C. C. Helms, M. Marvel, W. Zhao, M. Stahle, R. Vest, G. J. Kato, J. S. Lee, G. Christ, M. T. Gladwin, R. R. Hantgan, D. B. Kim-Shapiro, *J. Thromb. and Haemost.* **2013**, *11*, 2148.
79. A. Gaarder, J. Jonsen, S. Laland, A. Hellem, P. A. Owren, *Nature* **1961**, *192*, 531.
80. S. Sinn, T. Scheuermann, S. Deichelbohrer, G. Ziemer, H. P. Wendel, *J. Mater. Sci. Mater. Med.* **2011**, *22*, 1521.
81. K. Stang, S. Krajewski, B. Neumann, J. Kurz, M. Post, S. Stoppelkamp, S. Fennrich, M. Avci-Adali, D. Armbruster, C. Schlensak, I. A. Burgener, H. P. Wendel, T. Walker, *Mater. Sci. Eng. C* **2014**, *42*, 422.
82. M. V. Homann, D. Johansson, H. Wallen, J. Sanchez, *J. Biomed. Mater. Res. B* **2016**, *104*, 1359.
83. B. I. Cerda-Cristerna, H. Flores, A. Pozos-Guillén, E. Pérez, C. Sevrin, C. Grandfils, *J. Control. Release* **2011**, *153*, 269.
84. H. Stoll, H. Steinle, K. Stang, S. Kunnakattu, L. Scheideler, B. Neumann, J. Kurz, I. Degenkolbe, N. Perle, C. Schlensak, H. P. Wendel, M. Avci-Adali, *Macromol. Biosci.* **2017**, *17*, 1600252.
85. L. D. C. Casa, D. H. Deaton, D. N. Ku, *J. Vasc. Surg.* **2015**, *61*, 1068.
86. Y. Cadroy, T. Horbett, S. Hanson, *J. Lab. Clin. Med.* **1989**, *113*, 436.
87. D. M. Wootton, D. N. Ku, *Annu. Rev. Biomed. Eng.* **1999**, *1*, 299.
88. D. N. Ku, C. J. Flannery, *Biorheology* **2007**, *44*, 273.
89. D. L. Bark Jr., A. N. Para, D. N. Ku, *Biotechnol. Bioeng.* **2012**, *109*, 2642.

90. K. B. Neeves, A. A. Onasoga, R. R. Hansen, J. J. Lilly, D. Venckunaite, M. B. Sumner, A. T. Irish, G. Brodsky, M. J. Manco-Johnson, J. A. Di Paola, *PloS one* **2013**, *8*, e54680.
91. A. Para, D. Bark, D., A. Lin, D. Ku, *Ann. Biomed. Eng.* **2011**, *39*, 1961.
92. M. Mehrabadi, L. D. C. Casa, C. K. Aidun, D. N. Ku, *Ann. Biomed. Eng.* **2016**, *44*, 2339.
93. A. Zydney, C. K. Colton, *PCH* **1988**, *10*, 77.
94. S. W. Schneider, S. Nuschele, A. Wixforth, C. Gorzelanny, A. Alexander-Katz, R. R. Netz, M. F. Schneider, *PNAS* **2007**, *104*, 7899.
95. P. A. Holme, U. Ørvim, M. J. A. G. Hamers, N. O. Solum, F. R. Brosstad, R. M. Barstad, K. S. Sakariassen, *Arterioscler. Thromb. Vasc. Biol.* **1997**, *17*, 646.
96. A. Jordan, T. David; S. Homer-Vanniasinkam, A. Graham, P. Walker, *Biorheology* **2004**, *41*, 641.
97. P. Aarts, S. Van Den Broek, G. W. Prins, G. Kuiken, J. J. Sixma, R. M. Heethaar, *Arteriosclerosis* **1988**, *8*, 819.
98. J. E. Sadler, *Annu. Rev. Biochem.* **1998**, *67*, 395.
99. Y. Ikeda, M. Handa, K. Kawano, T. Kamata, M. Murata, Y. Araki, H. Anbo, Y. Kawai, K. Watanabe, I. Itagaki, *J. Clin. Invest.* **1991**, *87*, 1234.
100. Z. M. Ruggeri, J. N. Orje, R. Habermann, A. B. Federici, A. J. Reininger, *Blood* **2006**, *108*, 1903.
101. T. V. Colace, S. L. Diamond, *Arterioscler. Thromb. Vasc. Biol.* **2013**, *33*, 105.
102. C. C. Mohan, K. P. Chennazhi, D. Menon, *Acta Biomater.* **2013**, *9*, 9568.
103. C. L. Haycox, B. D. Ratner, *J. Biomed. Mater.* **1993**, *27*, 1181.
104. U. Streller, C. Sperling, J. Hübner, R. Hanke, C. Werner, *J. Biomed. Mater. Res. B* **2003**, *66B*, 379.
105. M. F. Maitz, C. Sperling, T. Wongpinyochit, M. Herklotz, C. Werner, F. P. Seib, *Nanomed.-Nanotechnol.* **2017**, *13*, 2633.
106. W. G. McClung, D. E. Babcock, J. L. Brash, *J. Biomed. Mater. Res. A* **2007**, *81A*, 644.
107. D.-A. Wang, J. Ji, C.-Y. Gao, G.-H. Yu, L.-X. Feng, *Biomaterials* **2001**, *22*, 1549.
108. R. Van Kruchten, J. M. E. M. Cosemans, J. W. M. Heemskerk, *Platelets* **2012**, *23*, 229.
109. J. M. Lackner, W. Waldhauser, P. Hartmann, F. Bruckert, M. Weidenhaupt, R. Major, M. Sanak, M. Wiesinger, D. Heim, *J. Funct. Biomater.* **2012**, *3*, 283.
110. E. Gutierrez, B. G. Petrich, S. J. Shattil, M. H. Ginsberg, A. Groisman, A. Kasirer-Friede, *Lab on a Chip* **2008**, *8*, 1486.

111. K. Affeld, A. J. Reininger, J. Gadischke, K. Grunert, S. Schmidt, F. Thiele, *Artif. Organs* **1995**, *19*, 597.
112. K. Affeld, S. Stefansdottir, J. Schaller, U. Kertzscher, *Biomed. Tech.* **2014**, *59*, 11.
113. L. J. Wurzinger, P. Blasberg, F. Horii, H. Schmid-Schöbein, *Thromb. Res.* **1986**, *44*, 401.
114. L. Wurzinger, P. Blasberg, M. Van de Loecht, W. Suwelack, H. Schmid-Schönbein, *Biorheology* **1984**, *21*, 649.
115. J. Deng, X. Liu, L. Ma, C. Cheng, W. Shi, C. Nie, C. Zhao, *ACS Appl. Mater. Inter.* **2014**, *6*, 21603.
116. L. Ma, C. Cheng, C. He, C. Nie, J. Deng, S. Sun, C. Zhao, C., *ACS Appl. Mater. Inter.* **2015**, *7*, 26050.
117. L. Ma, C. Cheng, C. Nie, C. He, J. Deng, L. Wang, Y. Xia, C. Zhao, *J. Mater. Chem. B* **2016**, *4*, 3203.
118. N. Hadjesfandiari, P. Schubert, S. Fallah Toosi, Z. Chen, B. Culibrk, S. Ramirez-Arcos, D. V. Devine, D. E. Brooks, *Transfusion* **2016**, *56*, 2808.
119. B. Balakrishnan, D. Kumar, Y. Yoshida, A. Jayakrishnan, *Biomaterials* **2005**, *26*, 3495.
120. K. Affeld, J. Schaller, T. Wölken, T. Krabatsch, U. Kertzscher, *Biointerphases* **2016**, *11*, 029804.
121. I. H. A. Badr, M. Gouda, R. Abdel-Sattar, H. E. M. Sayour, *Carbohydr. Polym.* **2014**, *99*, 783.
122. W. J. Sung, K. Na, Y. H. Bae, *Sensors Actuat. B-Chem.* **2004**, *99*, 393.
123. L. K. Von Segesser, *Coatings for Biomedical Applications*, **2012**, 1 Ed., 251.
124. S. Thelin, L. Bagge, J. Hultman, J. Borowiec, L. Nilsson, J. Thorelius, *Eur. J. Cardiothorac. Surg.* **1991**, *5*, 486.
125. X. Wang, N. Shi, Y. Chen, C. Li, X. Du, W. Jin, Y. Chen, P. R. Chang, *Bio.-Med. Mater. Eng.* **2012**, *22*, 143.
126. M. F. Maitz, U. Freudenberg, M. V. Tsurkan, M. Fischer, T. Beyrich, C. Werner, *Nat. Commun.* **2013**, *4*, 2168.
127. J. Li, X.-J. Huang, J. Ji, P. Lan, J. Vienken, T. Groth, Z.-K. Xu, *Macromol. Biosci.* **2011**, *11*, 1218.
128. P.-Y. Tseng, S. M. Rele, X.-L. Sun, E. L. Chaikof, *Biomaterials* **2006**, *27*, 2627.
129. M.-C. Yang, W.-C. Lin, *J. Polym. Res.* **2002**, *9*, 201.
130. F. Y. Mahlicli, S. A. Altinkaya, *J. Mater. Sci. Mater. Med.* **2013**, *24*, 533.

131. S. Claudia, H. Milan, B. Eduard, S. Uwe, W. Carsten, *J. Biomed. Mater. Res. A* **2006**, *76A*, 681.
132. C. Sperling, U. Konig, G. Hermel, C. Werner, M. Muller, F. Simon, K. Grundke, H. J. Jacobasch, V. N. Vasilets, Y. Ikada, *J. Mater. Sci. Mater. Med.* **1997**, *8*, 789.
133. S. Alibeik, S. Zhu, J. W. Yau, J. I. Weitz, J. L. Brash, *Acta Biomaterialia* **2011**, *7*, 4177.
134. M. Hoffmann, B. Huppertz, R. Horres, H. Baumann, R. Keller, *Materwiss. Werksttech.* **2001**, *32*, 110.
135. S. Sarrazin, W. C. Lamanna, J. D. Esko, *CSH Perspect. Biol.* **2011**, *3*, a004952.
136. J. Lahann, D. Klee, W. Pluester, H. Hoecker, *Biomaterials* **2001**, *22*, 817.
137. Z. Yang, Q. Tu, M. F. Maitz, S. Zhou, J. Wang, N. Huang, *Biomaterials* **2012**, *33*, 7959.
138. S. C. Freitas, T. B. Cereija, A. C. Figueiredo, H. Osório, P. J. B. Pereira, M. A. Barbosa, M. C. L. Martins, *Acta Biomater.* **2012**, *8*, 4101.
139. R. Xu, Q. Feng, Y. He, F. Yan, L. Chen, Y. Zhao, *J. Biomed. Mater. Res. A* **2017**, *105*, 178.
140. M. C. Porté-Durrieu, C. Aymes-Chodur, N. Betz, C. Baquey, *J. Biomed. Mater. Res.* **2000**, *52*, 119.
141. J. Gu, X. Yang, H. Zhu, *Mater. Sci. Eng. C* **2002**, *20*, 199.
142. C. Nie, L. Ma, Y. Xia, C. He, J. Deng, L. Wang, C. Cheng, S. Sun, C. Zhao, *J. Membr. Sci.* **2015**, *475*, 455.
143. T. Xiang, L.-S. Zhang, R. Wang, Y. Xia, B.-H. Su, C.-S Zhao, *J. Colloid Interface Sci.* **2014**, *432*, 47.
144. L. Ma, H. Qin, C. Cheng, Y. Xia, C. He, C. Nie, L. Wang, C. Zhao, *J. Mater. Chem. B* **2014**, *2*, 363.
145. F. Ran, S. Nie, J. Li, B. Su, S. Sun, C. Zhao, *Macromol. Biosci.* **2012**, *12*, 116.
146. K. A. Woodhouse, P. Klement, V. Chen, M. B. Gorbet, F. W. Keeley, R. Stahl, J. D. Fromstein, C. M. Bellingham, *Biomaterials* **2004**, *25*, 4543.
147. E. M. Srokowski, P. H. Blit, W. G. McClung, J. L. Brash, J. P. Santerre, K. A. Woodhouse, *J. Biomater. Sci. Polym. Ed.* **2011**, *22*, 41.
148. S. W. Jordan, C. A. Haller, R. E. Sallach, R. P. Apkarian, S. R. Hanson, E. L. Chaikof, *Biomaterials* **2007**, *28*, 1191.
149. V. N. Varu, N. D. Tsihlis, M. R. Kibbe, *Vasc. Endovasc. Surg.* **2009**, *43*, 121.
150. C. R. Arciola, D. Campoccia, L. Montanaro, *Nat. Rev. Microbiol.* **2018**, *16*, 397.
151. M. R. Beresford, P. W. Andrew, G. Shama, *J. Appl. Microbiol.* **2001**, *90*, 1000.
152. J. Genzer, K. Efimenko, *Biofouling* **2006**, *22*, 339.

153. M. Elimelech, W. A. Phillip, *Science* **2011**, *333*, 712.
154. J. Y. Lichtenberg, Y. Ling, S. Kim, *Sensors* **2019**, *19*, 2488.
155. N. Wisniewski, M. Reichert, *Colloid. Surface. B* **2000**, *18*, 197.
156. W. Zimmerli, *Best Pract. Res. Cl. Rh.* **2006**, *20*, 1045.
157. K. Prime, G. Whitesides, *Science* **1991**, *252*, 1164.
158. H. Lee, S. M. Dellatore, W. M. Miller, P. B. Messersmith, *Science* **2007**, *318*, 426.
159. Y. Gidi, S. Bayram, C. J. Ablenas, A. S. Blum, G. Cosa, *ACS Appl. Mater. Inter.* **2018**, *10*, 39505.
160. M. Huebner, M. Ben Haddada, C. Méthivier, R. Niessner, D. Knopp, S. Boujday, *Biosens. Bioelectron.* **2015**, *67*, 334.
161. H. Lee, K. D. Lee, K. B. Pyo, S. Y. Park, H. Lee *Langmuir* **2010**, *26*, 3790.
162. S. Chen, L. Li, C. Zhao, J. Zheng, *Polymer* **2010**, *51*, 5283.
163. S. Sharma, R. W. Johnson, T. A. Desai, *Biosens. Bioelectron.* **2004**, *20*, 227.
164. X. Chen, Y. Su, F. Shen, Y. Wan, *J. Membr. Sci.* **2011**, *384*, 44.
165. L. D. Unsworth, H. Sheardown, J. L. Brash, *Langmuir* **2005**, *21*, 1036.
166. M. Penna, K. J. Ley, A. Belessiotis-Richards, S. MacLaughlin, D. A. Winkler, I. Yarovsky, *J. of Phys. Chem. C* **2019**, *123*, 30360.
167. P. Zhang, F. Sun, S. Liu, S. Jiang, *J. Control. Release* **2016**, *244*, 184.
168. J. K. Armstrong, G. Hempel, S. Koling, L. S. Chan, T. Fisher, H. J. Meiselman, G. Garratty, *Cancer* **2007**, *110*, 103.
169. M. Imran al-haq, B. F. L. Lai, R. Chapanian, J. N. Kizhakkedathu, *Biomaterials* **2012**, *33*, 9135.
170. A. R. Statz, R. J. Meagher, A. E. Barron, P. B. Messersmith, *J. Am. Chem. Soc.* **2005**, *127*, 7972.
171. J. Y. Park, J. S. Kim, Y. S. Nam, *Carbohydr. Polym.* **2013**, *97*, 753.
172. T. He, D. Jańczewski, S. Jana, A. Parthiban, S. Guo, X. Zhu, S. S.-C. Lee, F. J. Parra-Velandia, S. L.-M. Teo, G. J. Vancso, *J. Polym. Sci Pol. Chem.* **2016**, *54*, 275.
173. R. Konradi, B. Pidhatika, A. Mühlebach, M. Textor, *Langmuir* **2008**, *24*, 613.
174. B. Pidhatika, J. Möller, V. Vogel, R. Konradi, *Int. J. Chem.* **2008**, *62*, 264.
175. L. Deng, M. Mrksich, G. M. Whitesides, *J. Am. Chem. Soc.* **1996**, *118*, 5136.
176. M. Sun, Q. Wu, J. Xu, F. He, A. P. Brown, Y. Ye, *J. Mater. Chem. B* **2016,** *4*, 2669.
177. X. Liu, W. Tong, Z. Wu, W. Jiang, *RSC Advances* **2013**, *3*, 4716.
178. M. Weinhart, I. Grunwald, M. Wyszogrodzka, L. Gaetjen, A. Hartwig, R. Haag, *Chem. Asian J.* **2010**, *5*, 1992.

179. Q. Wei, T. Becherer, R.-C. Mutihac, P.-L. M. Noeske, F. Paulus, R. Haag, I. Grunwald, *Biomacromolecules* **2014**, *15*, 3061.
180. M. W. Kulka, I. S. Donskyi, N. Wurzler, D. Salz, Ö. Ozcan, W. E. S. Unger, R. Haag, *ACS Appl. Bio Mater.* **2019**, 2, 5749.
181. L. Yu, C. Cheng, Q. Ran, C. Schlaich, P.-L. M. Noeske, W. Li, Q. Wei, R. Haag, *ACS Appl. Mater. Interfaces* **2017**, *9*, 6624.
182. E. S. Gil, S. M. Hudson, *Prog. Polym. Sci.* **2004**, *29*, 1173.
183. D. J. Vanderah, H. La, J. Naff, V. Silin, K. A. Rubinson, *JACS* **2004**, *126*, 13639.
184. S. Herrwerth, W. Eck, S. Reinhardt, M. Grunze, *JACS* **2003**, *125*, 9359.
185. D. Leckband, S. Sheth, A. Halperin, *J. Biomater. Sci. Polym. Ed.* **1999**, *10*, 1125.
186. J.-F. Lutz, Ö Akdemir, A. Hoth, *JACS* **2006**, *128*, 13046.
187. M. Imran al-haq, B. F. L. Lai, R. Chapanian, J. N. Kizhakkedathu, *Biomaterials* **2012**, *33*, 9135.
188. M. Gervais, A.-L. Brocas, G. Cendejas, A. Deffieux, S. Carlotti, *Macromol. Symp.* **2011**, *308*, 101.
189. M. Gervais, A.-L. Brocas, G. Cendejas, A. Deffieux, S. Carlotti, *Macromolecules* **2010**, *43*, 1778.
190. A. Sunder, R. Hanselmann, H. Frey, R. Mülhaupt, *Macromolecules* **1999**, *32*, 4240.
191. M. Wyszogrodzka, R. Haag, *Biomacromolecules* **2009**, *10*, 1043.
192. C. Siegers, M. Biesalski, R. Haag, *Chem. Eur. J.* **2004**, *10*, 2831.
193. K. Höger, T. Becherer, Q. Wei, R. Haag, W. Frieß, S. Küchler, *Eur. J. Pharm. Biopham.* **2013**, *85*, 756.
194. M. Weinhart, T. Becherer, N. Schurbusch, K. Schwibbert, H. J. Kunte, R. Haag, *Adv. Eng. Mater.* **2011**, *13*, 501.
195. Q. Wei, S. Krysiak, K. Achazi, T. Becherer, P.-L. M. Noeske, F. Paulus, H. Liebe, I. Grunwald, J. Dernedde, A. Hartwig, T. Hugel, R. Haag, *Colloid. Surface. B* **2014**, *122*, 684.
196. G. Zhai, W. H. Yu, E. T. Kang, K. G. Neoh, C. C. Huang, D. J. Liaw, *Ind. Eng. Chem. Res.* **2004**, *43*, 1673.
197. T. Tah, M. T. Bernards, *Colloid. Surface. B* **2012**, *93*, 195.
198. R.E. Holmlin, X. Chen, R. G. Chapman, S. Takayama, G. M. Whitesides, *Langmuir* **2001**, *17*, 2841.
199. S. Chen, J. Zheng, L. Li, S. Jiang, *JACS* **2005**, *127*, 14473.

200. J.-G. Piao, F. Gao, Y. Li, L. Yu, D. Liu, Z.-B. Tan, Y. Xiong, L. Yang, Y.-Z You, *Nano Res.* **2018**, *11*, 3193.
201. Y. Chang, S. Chen, Z. Zhang, S. Jiang, S., *Langmuir* **2006**, *22*, 2222.
202. W. Yang, S. Chen, G. Cheng, H. Vaisocherová, H. Xue, W. Li, J. Zhang, S. Jiang, *Langmuir* **2008**, *24*, 9211.
203. Y. Terayama, M. Kikuchi, M. Kobayashi, A. Takahara, *Macromolecules* **2011,** *44*, 104.
204. Z. Zhang, H. Vaisocherová, G. Cheng, W. Yang, H. Xue, S. Jiang, *Biomacromolecules* **2008**, *9*, 2686.
205. W. Feng, J. L. Brash, S. Zhu, *Biomaterials* **2006**, *27*, 847.
206. M. Sponchioni, U. C. Palmiero, N. Manfredini, D. Moscatelli, *Reac. Chem. Eng.* **2019**, *4*, 436.
207. S. Nishimoto, B. Bhushan, *RSC Adv.* **2013**, *3*, 671.
208. S. Movafaghi, V. Leszczak, W. Wang, J. A. Sorkin, L. P. Dasi, K. C. Popat, A. K. Kota, *Adv. Healthc. Mater.* **2017**, *6*, 1600717.
209. T. Sun, H. Tan, D. Han, Q. Fu, L. Jiang, *Small* **2005**, *1*, 959.
210. Y. Ding, Y. Leng, N. Huang, P. Yang, X. Lu, X. Ge, F. Ren, K. Wang, L. Lei, X. Guo, *J. Biomed. Mater. Res.* **2013**, *101*, 622.
211. H. Fan, P. Chen, R. Qi, J. Zhai, J. Wang, L. Chen, L. Chen, Q. Sun, Y. Song, D. Han, L. Jiang, *Small* **2009**, *5*, 2144.
212. T. T. Pham, S. Wiedemeier, S. Maenz, G. Gastrock, U. Settmacher, K. D. Jandt, J. Zanow, C. Lüdecke, J. Bossert, *Colloid. Surface. B* **2016**, *145*, 502.
213. P. Roach, D. Farrar, C. C. Perry, *JACS* **2006**, *128*, 3939.
214. E. S. Leibner, N. Barnthip, W. Chen, C. R. Baumrucker, J. V. Badding, M. Pishko, E. A. Vogler, *Acta Biomater.* **2009**, *5*, 1389.
215. V. Jokinen, E. Kankuri, S. Hoshian, S. Franssila, R. H. A. Ras, *Adv. Mater.* **2018**, *30*, e1705104
216. G. B. Hwang, K. Page, A. Patir, S. P. Nair, E. Allan, I. P. Parkin, *ACS Nano* **2018**, *12*, 6050.
217. T. Lucas, B. Stanczewski, N. Ramasamy, S. Srinivasan, G. Kammlott, P. Sawyer, *Biomater. Med. Dev. Artif. Organs* **1975**, *3*, 215.
218. V. V. Nikolaychik, D. M. Wankowski, M. M. Samet, P. I. Lelkes, *ASAIO Journal* **1996**, *42*, M487.
219. T. Scott-Burden, C. L. Tock, J. P. Bosely, F. J. Clubb, S. M. Parnis, J. J. Schwarz, D. A. Engler, O. H. Frazier, S. W. Casscells, *Circulation* **1998**, *98*, II339.

220. I. Dion, F. Rouais, L. Trut, C. Baquey, J. R. Monties, P. Havlik, *Biomaterials* **1993**, *14*, 169.
221. J. R. Montiès, I. Dion, P. Havlik, F. Rouais, J. Trinkl, C. Baquey, *Artif. Organs* **1997**, *21*, 730.
222. J. F. Antaki, G. W. Burgreen, Z. J. Wu, D. Borzelleca, M. V. Kameneva, J. A. Holmes, P. Litwak, K. Litwak, M. Watach, B. E. Paden, T. Dragnes, N. J. Groom, B. P. Griffith, B. P., *ASAIO Journal* **2000**, *46*, 194.
223. E. Benrashid, C. C. McCoy, L. M. Youngwirth, J. Kim, R. J. Manson, J. C. Otto, J. H. Lawson, *Methods* **2016**, *99*, 13.
224. S. P. Pujari, L. Scheres, A. T. M. Marcelis, H. Zuilhof, *Angew. Chem. Int. Ed.* **2014**, *53*, 6322.
225. R. G. Nuzzo, D. L. Allara, *JACS* **1983**, *105*, 4481.
226. Q. Wei, R. Haag, *Mater. Horiz.* **2015**, *2*, 567.
227. M. D. Porter, T. B. Bright, D. L. Allara, C. E. D. Chidsey, *JACS* **1987**, *109*, 3559.
228. N. Saito, S. Yamashita, T. Matsuda, *J. Polym. Sci. A Polym. Chem.* **1997**, *35*, 747.
229. G. R. Xu, S.-H. Wang, H.-L. Zhao, S.-B. Wu, J.-M. Xu, L. Li, X.-Y. Liu, *J. Membrane Sci.* **2015**, *493*, 428.
230. D. Y. Ryu, K. Shin, E. Drockenmuller, C. J. Hawker, T. P. Russell, T. P., *Science* **2005**, *308*, 236.
231. K. K. Goli, O. J. Rojas, J. Genzer, *Biomacromolecules* **2012**, *13*, 3769.
232. D. G. Barrett, T. S. Sileika, P. B. Messersmith, *ChemComm* **2014**, *50*, 7265.
233. J. H. Waite, *J. Exp. Biol.* **2017**, *220*, 517.
234. J. H. Waite, M. L. Tanzer, *Science* **1981**, *212*, 1038.
235. H. Lee, N. F. Scherer, P. B. Messersmith, *PNAS* **2006**, *103*, 12999.
236. H. Gulley-Stahl, P. A. Hogan, W. L. Schmidt, S. J. Wall, A. Buhrlage, H. A. Bullen, *Environ. Sci. Technol.* **2010**, *44*, 4116.
237. J. Saiz-Poseu, J. Mancebo-Aracil, F. Nador, F. Busqué, D. Ruiz-Molina,. *Angew. Chem. Int. Ed.* **2019**, *58*, 696.
238. J. Yang, V. Saggiomo, A. H. Velders, M. A. C. Stuart, M. Kamperman, *PLoS One* **2016,** *11*, e0166490.
239. Q. Wei, T. Becherer, P.-L. M. Noeske, I. Grunwald, R. Haag, *Adv. Mater.* **2014**, *26*, 2688.
240. J. H. Waite, X. Qin, *Biochemistry* **2001**, *40*, 2887.

241. H. Lee, Y. Lee, A. R. Statz, J. Rho, T. G. Park, P. B. Messersmith, *Adv. Mater.* **2008**, *20*, 1619.
242. M. Shin, S.-G. Park, B.-C. Oh, K. Kim, S. Jo, M. S. Lee, S. S. Oh, S.-H. Hong, E.-C. Shin, K.-S. Kim, S.-W. Kang, H. Lee, *Nat. Mater.* **2016**, *16*, 147.
243. J.-H. Jiang, L.-P. Zhu, X.-L. Li, Y.-Y. Xu, B.-K. Zhu, *J. Membrane Sci.* **2010**, *364*, 194.
244. M. Li, L. Gao, C. Schlaich, J. Zhang, I. S. Donskyi, G. Yu, W. Li, Z. Tu, J. Rolff, T. Schwerdtle, R. Haag, N. Ma, *ACS Appl. Mater.* **2017**, *9*, 35411.
245. J. H. Ryu, P. B. Messersmith, H. Lee, *ACS Appl. Mater.* **2018**, *10*, 7523.
246. J. Yang, M. A. C. Stuart, M. Kamperman, *Chem. Soc. Rev.* **2014**, *43*, 8271.
247. A. Stepuk, J. G. Halter, A. Schaetz, R. N. Grass, W. J. Stark, *ChemComm* **2012**, *48*, 6238.
248. B. Mizrahi, X. Khoo, H. H. Chiang, K. J. Sher, R. G. Feldman, J.-J. Lee, S. Irusta, D. S. Kohane, *Langmuir* **2013**, *29*, 10087.
249. Q. Wei, F. Zhang, J. Li, B. Li, C. Zhao, *Polym. Chem.* **2010**, *1*, 1430.
250. X. Du, L. Li, J. Li, C. Yang, N. Frenkel, A. Welle, S. Heissler, A. Nefedov, M. Grunze, P. A. Levkin, *Adv. Mater.* **2014**, *26*, 8029.
251. Q. Wei, K. Achazi, H. Liebe, A. Schulz, P.-L. M. Noeske, I. Grunwald, R. Haag, *Angew. Chem. Int. Ed.* **2014**, *53*, 11650.
252. C. Schlaich, L. C. Camacho, L. Yu, K. Achazi, Q. Wei, R. Haag, *ACS Appl. Mater.* **2016**, *8*, 29117.
253. C. Schlaich, Q. Wei, R. Haag, *Langmuir* **2017**, *33*, 9508.
254. T. G. Kim, H. Lee, Y. Jang, T. G. Park, *Biomacromolecules* **2009**, *10*, 1532.
255. I. You, S. M. Kang, Y. Byun, H. Lee, *Bioconjug. Chem.* **2011**, *22*, 1264.
256. Y. Yang, P. Qi, F. Wen, X. Li, Q. Xia, M. F. Maitz, Z. Yang, R. Shen, Q. Tu, N. Huang, *ACS Appl. Mater.* **2014**, *6*, 14608.
257. A. Gao, F. Liu, L. Xue, *J. Membr. Sci* **2014**, *452*, 390.
258. L. Li, M. Li, D. Li, P. He, H. Xia, Y. Zhang, C. Mao, *J. Mater. Chem. B* **2014**, *2*, 5952.
259. C. Cheng, S. Nie, S. Li, H. Peng, H. Yang, L. Ma, S. Sun, C. Zhao, *J. Mater. Chem. B* **2013**, *1*, 265.
260. H. Wei, L. Han, J. Ren, L. Jia, *ACS Appl. Mater.* **2013**, *5*, 12571.
261. D.-G. Yu, C.-H. Jou, W.-C. Lin, M.-C. Yang, *Colloid. Surface. B* **2007**, *54*, 222.
262. C. S. Campelo, P. Chevallier, J. M. Vaz, R. S. Vieira, D. Mantovani, *Mater. Sci. Eng. C* **2017**, *72*, 682.

263. Y. Xia, C. Cheng, R. Wang, H. Qin, Y. Zhang, L. Ma, H. Tan, Z. Gu, C. Zhao, *Polym. Chem.* **2014**, *5*, 5906.
264. M. Li, C. Schlaich, M. W. Kulka, I. S. Donskyi, T. Schwerdtle, W. E. Unger, R. Haag, *J. Mater. Chem. B* **2019**, *7*, 3438.
265. S. Kim, T. Gim, S. M. Kang, *ACS Appl. Mater.* **2015**, *7*, 6412.
266. S. Chen, Y. Xie, T. Xiao, W. Zhao, J. Li, C. Zhao, *Chem. Eng. J.* **2018**, *337*, 122.
267. H. Thissen, A. Koegler, M. Salwiczek, C. D. Easton, Y. Qu, T. Lithgow, R. A. Evans, *NPG Asia Mater.* **2015**, *7*, e225.
268. Z. Li, W. Wang, K. Kratz, J. Kuechler, X. Xu, J. Zou, Z. Deng, X. Sun, M. Gossen, N. Ma, *Clin. Hemorheol. Microcirc.* **2016**, *64*, 355.
269. M. K. Chaudhury, G. M. Whitesides, *Science* **1992**, *256*, 1539.
270. Q. Wei, T. Becherer, R.-C. Mutihac, P.-L. M. Noeske, F. Paulus, R. Haag, I. Grunwald, *Biomacromolecules* **2014**, *15*, 3061.
271. H. Qian, M. Li, Z. Li, Y. Lou, L. Huang, D. Zhang, D. Xu, C. Du, L. Lu, J. Gao, *Mater. Sci. Eng.* **2017**, *80*, 566.
272. S. Liu, T. Cai, X. Shen, E. Huang, Z. Wang, Q. Sun, *Ceram. Int.* **2019**, *45*, 21263.
273. L. Chen, Z. Guo, *Colloids Surf.* **2018**, *554*, 253.
274. K. Affeld, J. Schaller, T. Wölken, T. Krabatsch, U. Kertzscher, *Biointerphases* **2016**, *11*, 029804.
275. M. Calderón, M. A. Quadir, S. K. Sharma, R. Haag, *Adv. Mater.* **2010**, *22*, 190.
276. R. K. Kainthan, J. Janzen, E. Levin, D. V. Devine, D. E. Brooks, *Biomacromolecules* **2006,** *7*, 703.
277. M. Khan, W. T. S. Huck, *Macromolecules* **2003**, *36*, 5088.
278. E. Moore, B. Delalat, R. Vasani, G. McPhee, H. Thissen, N. H. Voelcker, *ACS Appl. Mater.* **2014**, *6*, 15243.
279. T. Weber, M. Bechthold, T. Winkler, J. Dauselt, A. Terfort, *Colloid. Surface. B* **2013**, *111*, 360.
280. M. W. Kulka, S. Smatty., F. Hehnen, T. Bierewirtz, K. Silberreis, C. Nie, Y. Kerkhoff, C. Grötzinger, S. Friedrich, L. I. Dahms, J. Dernedde, I. Grunwald, M. Schirner, U. Kertzscher, K. Affeld, R. Haag, *Wiley Adv. Mater. Interfaces* **2020**, *Accepted.*
281. M. W. Kulka, C. Nie, P. Nickl, Y. Kerkhoff, A. Garg, D. Salz, J. Radnik, I. Grunwald, R. Haag, *Wiley Adv. Mater. Interfaces* **2020**, *Submitted.*

10. PUBLICATION LIST

I. R. R. Steendam, M. C. Brouwer, E. M. Huijs, M. W. Kulka, H. Meekes, W. J. van Enckevort, J. Raap, F. P. Rutjes, E. Vlieg, *Chem. Eur. J.* **2014**, *20*, 13527. DOI:10.1002/chem.201404320

II. R. R. Steendam, M. W. Kulka, H. Meekes, W. J. van Enckevort, J. Raap, E. Vlieg, F. P. Rutjes, *Eur. J. Org. Chem.* **2015**, *2015*, 7249. DOI:10.1002/ejoc.201501191

III. M. Li, C. Schlaich, M. W. Kulka, I. S. Donskyi, T. Schwerdtle, W. E. S. Unger, R. Haag, *J. Mater. Chem. B* **2019**, *7*, 3438. DOI: 10.1039/c9tb00534j

IV. R. Randriantsilefisoa, Y. Hou, Y. Pan, J. L. C. Camacho, M. W. Kulka, J. Zhang, R. Haag, *Adv. Funct. Mater.* **2019**, *30*, 1905200. DOI: 10.1002/adfm.201905200

V. M. W. Kulka, I. S. Donskyi, N. Wurzler, D. Salz, Ö. Özcan, W. E. S. Unger, R. Haag, *ACS Appl. Bio Mater.* **2019**, *2*, 5749. DOI: 10.1021/acsabm.9b00786

VI. M. W. Kulka, S. Smatty, K. Silberreis, F. Hehnen, T. Bierewirtz, Y. Kerkhoff, C. Nie, C. Grötzinger, S. Friedrich, L. I. Dahms, J. Dernedde, I. Grunwald, U. Kertzscher, K. Affeld, M. Schirner, R. Haag, *Adv. Mater. Interfaces* **2020**, *Accepted.*

VII. M. Czuban, M. W. Kulka, L. Wang, A. Koliszak, K. Achazi, C. Schlaich, I. S. Donskyi, M. Di Luca, J. M. Mejia Oneto, M. Royzen, R. Haag, A. Trampuz, *Mater. Sci. Eng. C.* **2020**, *Accepted.*

VIII. M. W. Kulka, C. Nie, P. Nickl, Y. Kerkhoff, A. Garg, D. Salz, J. Radnik, I. Grunwald, R. Haag *Adv. Mater. Interfaces* **2020**, *Submitted.*

11. CURRICULUM VITAE

Der Lebenslauf ist in der Online-Version aus Gründen des Datenschutzes nicht enthalten.